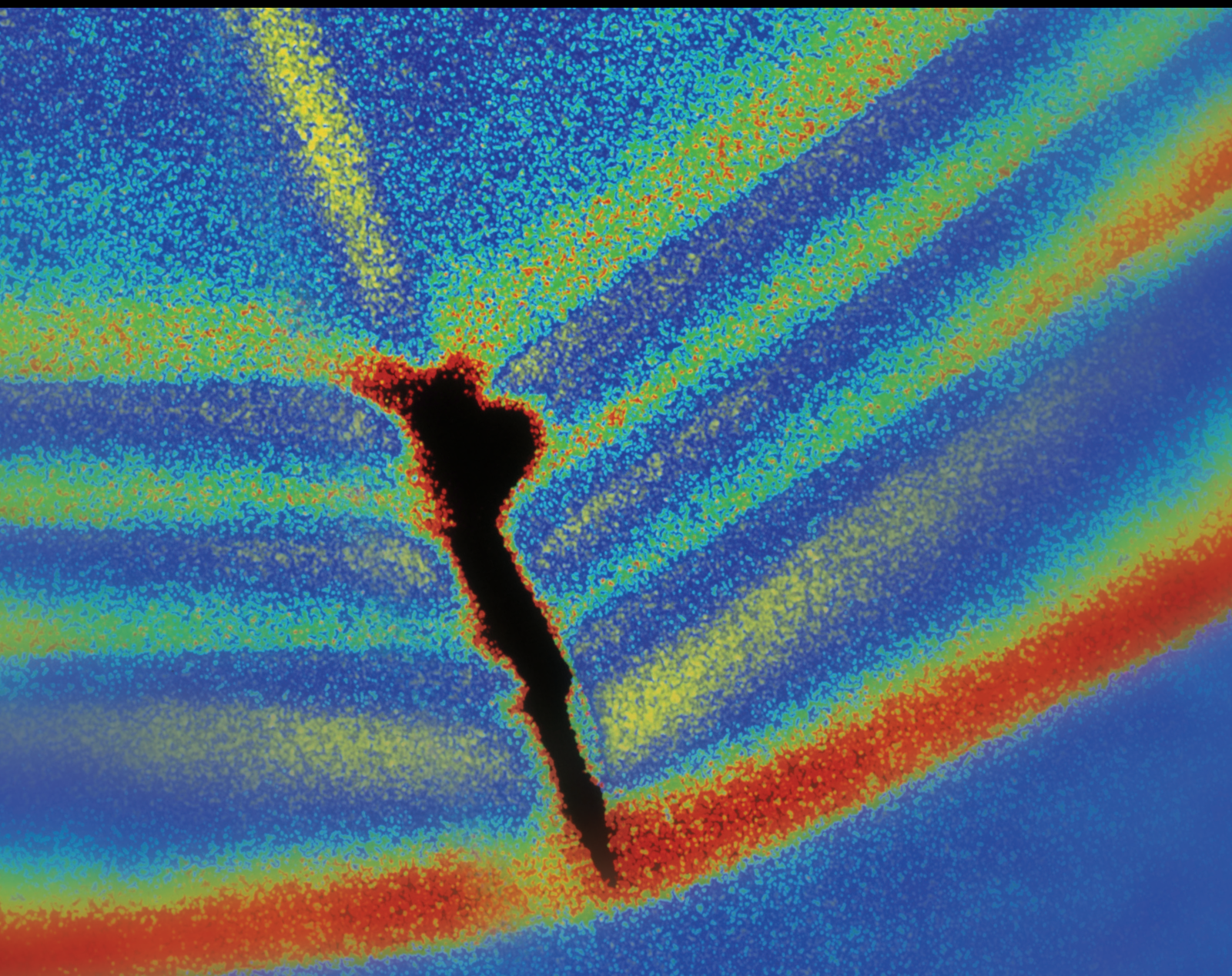


Shock and Vibration

Mechanical Vibrations Applied to Nondestructive Evaluation of Materials and Structures

Lead Guest Editor: Luca Collini

Guest Editors: Salvatore Russo, Giada Gasparini, and Michele Palermo





**Mechanical Vibrations Applied
to Nondestructive Evaluation of
Materials and Structures**

Shock and Vibration

**Mechanical Vibrations Applied
to Nondestructive Evaluation of
Materials and Structures**

Lead Guest Editor: Luca Collini

Guest Editors: Salvatore Russo, Giada Gasparini,
and Michele Palermo



Copyright © 2017 Hindawi. All rights reserved.

This is a special issue published in "Shock and Vibration." All articles are open access articles distributed under the Creative Commons Attribution License, which permits unrestricted use, distribution, and reproduction in any medium, provided the original work is properly cited.

Editorial Board

Brij N. Agrawal, USA
Marco Alfano, Italy
Sumeet S. Aphale, UK
Hassan Askari, Canada
Lutz Auersch, Germany
Matteo Aureli, USA
Mahmoud Bayat, Iran
Marco Belloli, Italy
Giosuè Boscato, Italy
Francesco Braghin, Italy
Ivo Caliò, Italy
Antonio Carcaterra, Italy
Dumitru I. Caruntu, USA
Cristina Castejón, Spain
Gabriele Cazzulani, Italy
Noel Challamel, France
Athanasios Chasalevris, UK
Simone Cinquemani, Italy
Giorgio Dalpiaz, Italy
Farhang Daneshmand, Canada
Sergio De Rosa, Italy
Dario Di Maio, UK
Luigi Di Sarno, Italy
Longjun Dong, China
Lorenzo Dozio, Italy
Mohamed El Badaoui, France
Mohammad Elahinia, USA
Fiorenzo A. Fazzolari, UK
Matteo Filippi, Italy

Francesco Franco, Italy
Juan C. G. Prada, Spain
Pedro Galvín, Spain
Gianluca Gatti, Italy
Anindya Ghoshal, USA
Nere Gil-Negrete, Spain
Hassan Haddadpour, Iran
M.I. Herreros, Spain
Hamid Hosseini, Japan
Reza Jazar, Australia
Sakdirat Kaewunruen, UK
Yuri S. Karinski, Israel
Jeong-Hoi Koo, USA
Georges Kouroussis, Belgium
Mickaël Lallart, France
Nuno M. Maia, Portugal
Giuseppe Carlo Marano, Italy
Laurent Mevel, France
Emiliano Mucchi, Italy
Sara Muggiasca, Italy
Tony Murmu, UK
Pedro Museros, Spain
Sundararajan Natarajan, India
Toshiaki Natsuki, Japan
Miguel Neves, Portugal
Nicola Nisticò, Italy
Roberto Palma, Spain
Francesco Pellicano, Italy
Evgeny Petrov, UK

Giuseppe Piccardo, Italy
Antonina Pirrotta, Italy
Carlo Rainieri, Italy
Didier Rémond, France
Francesco Ripamonti, Italy
Salvatore Russo, Italy
Edoardo Sabbioni, Italy
Onome E. Scott-Emuakpor, USA
Vadim V. Silberschmidt, UK
Kumar V. Singh, USA
Isabelle Sochet, France
Alba Sofi, Italy
Jussi Sopanen, Finland
Stefano Sorace, Italy
Chao Tao, China
Mario Terzo, Italy
Tai Thai, Australia
Marc Thomas, Canada
Carlo Trigona, Italy
Federica Tubino, Italy
Nerio Tullini, Italy
Jens Twiefel, Germany
Filippo Ubertini, Italy
Marcello Vanali, Italy
Jörg Wallaschek, Germany
Matthew J. Whelan, USA
Enrico Zappino, Italy

Contents

Mechanical Vibrations Applied to Nondestructive Evaluation of Materials and Structures

Luca Collini, Giada Gasparini, Michele Palermo, and Salvatore Russo
Volume 2017, Article ID 3769401, 2 pages

Damage Identification of Unreinforced Masonry Panels Using Vibration-Based Techniques

Claudio Oyarzo-Vera and Nawawi Chouw
Volume 2017, Article ID 9161025, 14 pages

The Monitoring of Palazzo Lombardia in Milan

Marta Berardengo, Giorgio Busca, Simone Grossi, Stefano Manzoni, and Marcello Vanali
Volume 2017, Article ID 8932149, 13 pages

Damage Identification of a Derrick Steel Structure Based on the HHT Marginal Spectrum Amplitude Curvature Difference

Dongying Han, Shimin Wei, Peiming Shi, Ying Zhang, Kai Gao, and Nengyuan Tian
Volume 2017, Article ID 1062949, 9 pages

A Signal Decomposition Method for Ultrasonic Guided Wave Generated from Debonding Combining Smoothed Pseudo Wigner-Ville Distribution and Vold-Kalman Filter Order Tracking

Junhua Wu, Xinglin Chen, and Zheshu Ma
Volume 2017, Article ID 7283450, 13 pages

Optimization Method of the Car Seat Rail Abnormal Noise Problem Based on the Finite Element Method

Huijie Yu, Xinkan Zhang, and Chen Zhang
Volume 2017, Article ID 4132092, 13 pages

Vibration Analysis for Monitoring of Ancient Tie-Rods

L. Collini, R. Garziera, and K. Riabova
Volume 2017, Article ID 7591749, 11 pages

Experimental Research on Seismic Performance of a New-Type of R/C Beam-Column Joints with End Plates

Shufeng Li, Qingning Li, Haotian Jiang, Hao Zhang, and Lizhong Zhang
Volume 2017, Article ID 3823469, 11 pages

Experimental Evaluation for the Microvibration Performance of a Segmented PC Method Based High Technology Industrial Facility Using 1/2 Scale Test Models

Sijun Kim and Se Woon Choi
Volume 2017, Article ID 2452598, 9 pages

The Absolute Deviation Rank Diagnostic Approach to Gear Tooth Composite Fault

Guangbin Wang, Wenhui Deng, Xiaoyang Du, and Xuejun Li
Volume 2017, Article ID 7285216, 10 pages

Editorial

Mechanical Vibrations Applied to Nondestructive Evaluation of Materials and Structures

Luca Collini,¹ Giada Gasparini,² Michele Palermo,³ and Salvatore Russo⁴

¹*Department of Engineering and Architecture, University of Parma, 43124 Parma, Italy*

²*Department of Civil, Chemical, Environmental, and Materials Engineering, University of Bologna, 40126 Bologna, Italy*

³*Interdepartmental Centre for Industrial Research in Building and Construction, University of Bologna, 40126 Bologna, Italy*

⁴*Iuav University of Venice, 0123 Venice, Italy*

Correspondence should be addressed to Luca Collini; lucaferdinando.collini@gmail.com

Received 20 November 2017; Accepted 21 November 2017; Published 18 December 2017

Copyright © 2017 Luca Collini et al. This is an open access article distributed under the Creative Commons Attribution License, which permits unrestricted use, distribution, and reproduction in any medium, provided the original work is properly cited.

Since the first vibration-based damage detection technology in the monitoring of rotating machinery, up-to-date mechanical vibrations are successfully used in many other applications in the field of NDT and NDE, and we think that many open questions and possibilities are still left to be found. Vibrations are relatively simple measurable quantities, containing a set of information that is peculiar of the system we examine. Further, repeated measures, even after years, are precious witnesses of an evolving situation over the time for those ambits in which aging is critical as health and restoration problems in artistic heritage.

In this special issue devoted to applications of mechanical vibration methods in NDT and NDE, we tried to collect contributions from researchers and experts from the academic world and also belonging to the industrial world. The valuable contributions, 9 in number, have been selected in such a way that some of the most important themes of the main topic are touched, and even though ranging from industrial diagnostics to civil construction dynamical performance, in the whole they appear in a harmonious form.

The works are of high scientific level and introduce to the researches community of remarkable novelty. The issue contains a classical application of the frequency-based diagnosis method treated in the paper “The Absolute Deviation Rank Diagnostic Approach to Gear Tooth Composite Fault” by G. Wang et al. from the Hunan University of Science & Technology of Xiangtan, China. In this work, the authors apply with success the absolute deviation rank approach for

determining damage occurring in transmission gears, as teeth breakage or pitting. The frequency response of gears is shown to indicate different degrees and different types of damage.

Another contribution deals with the NDT methods for civil structures and is about the “Experimental Evaluation for the Microvibration Performance of a Segmented PC Method Based High Technology Industrial Facility Using 1/2 Scale Test Models” proposed by S. Kim and S. W. Choi from the Kyonggi University, Kyonggido, and the Catholic University of Daegu, Kyeongsan-si, both in Korea. In this work, the authors present an experimental work on a half-scale model of a bridge system built and assembled in segments to facilitate transportation due to the dimensions.

In the paper entitled “Experimental Research on Seismic Performance of a New-Type of R/C Beam-Column Joints with End-Plates” the authors S. Li et al. from the Xi’an University of Architecture and Technology, China, present the design of an end-plate for the connection of civil structures. Via a dynamical testing campaign, they calculate the dissipation of the joint that is a crucial parameter when in presence of seismic excitation.

Again from China, University of Shanghai for Science and Technology, there comes the research “Optimization Method of the Car Seat Rail Abnormal Noise Problem Based on the Finite Element Method” by H. Yu et al., in which experiments in conjunction with finite element analysis are used within the design of car seat supports; here stiffness and damping of the system are optimized for the comfort and safety.

In another contribution to the special issue, D. Han et al. from the School of Vehicles and Energy, Yanshan University, Qinhuangdao (China), the School of Electrical Engineering, Yanshan University, Qinhuangdao (China), and the School of Electrical and Computer Engineering, Georgia Institute of Technology, Atlanta (USA), introduce a vibration-based method for damage monitor with the paper “Damage Identification of Derrick Steel Structure Based on HHT Marginal Spectrum Amplitude Curvature Difference.” In this interesting paper, the Hilbert-Huang transform marginal spectrum amplitude curvature is successfully applied for the damage sensitivity index to identify the damage in a derrick structure; the results show that the index can accurately determine the location of the damage element and weak damage element.

The paper “Vibration Analysis for Monitoring of Ancient Tie-Rods” by L. Collini et al. from the University of Parma (Italy) instead is devoted to the indirect monitoring of the axial load, which is commonly unknown especially after many years, in structural tie-rods placed as reinforcing elements in historical buildings. The problem of assessing the healthy condition of such elements is crucial for determining the building stability and a ND method based on the measure of vibrations looks very useful.

In the paper “Damage Identification of Unreinforced Masonry Panels Using Vibration-Based Techniques” by C. Oyarzo-Vera and Nawawi Chouw from the Universidad Católica de la Santísima Concepción, Concepción, Chile, and from the University of Auckland, New Zealand, the changing of modal parameters is analyzed to detect damage in a masonry specimen; the experimental method works properly, even if a large number of measurement points need to be considered to obtain an acceptable level of resolution.

One paper is entitled “A Signal Decomposition Method for Ultrasonic Guided Wave Generated from Debonding Combining Smoothed Pseudo Wigner-Ville Distribution and Vold-Kalman Filter Order Tracking” and is presented by J. Wu et al. from the Nanjing Forestry University, Nanjing, China. In this work, the wave packets of ultrasonic nondestructive evaluation and testing applied to carbon fiber composites are analyzed via a signal decomposition method in order to detect the debonding damage, which are characteristic of these materials, in terms of size and location.

Another paper, entitled “The Monitoring of Palazzo Lombardia in Milan” is presented by an Italian team of researchers from the Polytechnic of Milan and from the University of Parma, Italy, M. Berardengo et al., and deals with the estimation of modal parameters of Palazzo Lombardia, one of the tallest high-rise buildings in Italy, through operational modal analysis. The work conjugates an extensive experimental monitoring activity through transducers and accelerometers positioned ad hoc along the building, with a statistical analysis of data allowing the draft of a model for the relationships between eigenfrequencies and environmental variables aiming at a general structural health monitoring procedure which is based on the evolution of the building modal parameters.

Hoping the issue results are of interest for academic and technical readers, we wish a fruitful reading.

*Luca Collini
Giada Gasparini
Michele Palermo
Salvatore Russo*

Research Article

Damage Identification of Unreinforced Masonry Panels Using Vibration-Based Techniques

Claudio Oyarzo-Vera¹ and Nawawi Choww²

¹*Departamento de Ingeniería Civil, Universidad Católica de la Santísima Concepción, Concepción, Chile*

²*Department of Civil and Environmental Engineering, University of Auckland, Auckland, New Zealand*

Correspondence should be addressed to Claudio Oyarzo-Vera; coyarzov@ucsc.cl

Received 8 May 2017; Revised 30 September 2017; Accepted 8 October 2017; Published 26 October 2017

Academic Editor: Salvatore Russo

Copyright © 2017 Claudio Oyarzo-Vera and Nawawi Choww. This is an open access article distributed under the Creative Commons Attribution License, which permits unrestricted use, distribution, and reproduction in any medium, provided the original work is properly cited.

Several damage indicators based on changes in modal properties validated for homogeneous materials were applied to detect damage in an unreinforced masonry cantilever panel. Damage was created by a “clean diagonal cut” at the center of the specimen which length was progressively extended towards the specimen’s corners. Numerical simulations were employed to determine the modal response at several damage states and this data was used to calculate the damage indicators. Those indicators presenting a good performance were then applied to identify damage on a physical specimen tested in the laboratory. The outcomes of this study demonstrated that vibration-based damage detection in unreinforced masonry structures can be satisfactorily performed. However, the identification of the damage spatial distribution using vibration-based methods in unreinforced masonry structures is still difficult. To improve the prediction of damage distribution, a large number of measurement points need to be considered to obtain an acceptable level of resolution.

1. Introduction

Damage has been defined as any change that adversely affects current or future performance of a system [1]. Damage is usually related to structural responses that cause material nonlinearity. However, the effect of damage is not only observed in postelastic behavior of structures. The linear response might also be perturbed due to degradation of elastic stiffness and loss of mass or in forms of changes in the system boundary conditions.

A number of nondestructive techniques have been developed in the last three decades to detect damage beyond human naked-eye capacities (e.g., acoustic emissions, ultrasonic emissions, or X-ray inspections). Most of these methods focus on assessing the local condition of structural elements, and they require a prior localization of the damage and access to the damaged area. Nevertheless, there are other kinds of nondestructive methods based on the global vibration response of the structure that have been demonstrated to be effective in detecting and localizing damage.

Modal testing and system identification are techniques usually employed to extract the modal properties, that is, modal frequencies, mode shapes, and modal damping from the vibration response of a structure. Assuming that ambient conditions do not significantly affect the system properties, changes in the dynamic response can be associated with alteration of the mass, stiffness, and/or damping distribution and, consequently, they can be interpreted as a symptom of structural damage. An advantage of these techniques is that they do not require direct access to the damaged zone. That is particularly convenient from an economical and practical point of view, because damage can be early detected and “prelocalized” by applying vibration-based techniques. The information obtained can then be used to decide whether a more detailed local analysis is necessary.

Traditionally, modal data has been obtained from measurements of the excitation applied to the structure (input) and the structural response (output). This approach is known as experimental modal analysis (EMA). However, since the early 1990s, operational modal analysis (OMA) [2] has drawn great attention in the civil engineering community. OMA

utilizes only measurements of the structural response to identify modal characteristics. The main requisite of OMA techniques is that the excitation signal corresponds to a stationary random process, for example, impacts, ambient vibrations, or any other excitation that has white-noise characteristics in a range of frequencies wide enough to cover the entire range of modal frequencies that need to be identified. The increasing popularity of this method is due to the fact that measurements of excitation are not necessary. In addition, in the case of massive structures, usually it is very difficult to artificially excite the structure, and the only practical option is to consider its operational response due to ambient excitations.

Damage identification can be performed at five different levels: detection, localization, classification, assessment, and prognosis [3, 4]. Qualitative information about the presence or nonpresence of damage is given when methods at the *detection level* are applied. With *localization level* approaches, it is possible both to detect damage and to determine a probable position of the damage. The type of damage generated in the system is characterized by the use of *classification level* procedures. When the extent of the damage is also determined, the damage identification method is performed at an *assessment level*. Finally, with *prognosis level* methods, a prediction of structural safety and residual operating lifespan is inferred.

Most vibration-based damage identification studies have focused on structures built using relatively homogeneous materials (e.g., steel and concrete) and only few have taken on the challenge of investigating damage to structures made of composite material such as masonry (assembly of bricks and mortar). Recently, several studies have addressed the problem of assessing damage to heritage buildings [5–12]. A number of these studies have implemented vibration-based techniques because of their nondestructive nature, especially attractive for applying to structures of high historical and/or architectural value.

Several initiatives have been implemented to perform vibration-based structural assessment of heritage buildings at national, regional, or single structure scale. For example, the article of Gattulli et al. [13] presented recent experiences in Italy; many of them triggered after the LAquila earthquake in 2009. Most of these initiatives combine historical and architectural surveys, dynamics investigations, and numerical modeling. In general, the goal of these studies is generating reliable numerical models, updated by information obtained from tests on actual buildings. Then, the updated models can be used to predict future structural behavior or diagnose potential damage, when dynamics alterations are detected on buildings [14]. One example of these kinds of study is reported by Gentile et al. [15]. They performed an extensive structural assessment program on a historic bell tower. This study combined vibration-based methodologies with the calibration of a three-dimensional finite element model. The model calibration process incorporated manual tuning, sensitivity analysis, and simple system identification algorithm. At the end of this study a reliable and verified model of the structure was obtained that can be used in future structural performance studies.

In our study, the pertinence of applying global damage identification methods based on vibration response for detecting and determining the spatial distribution of damage to unreinforced masonry (URM) structures was evaluated. Several damage indicators proposed by different authors were considered and applied to the results obtained from modal test conducted on a URM cantilever panel. These indicators have been demonstrated to be effective in identifying damage to structures built of homogeneous materials (steel, aluminum, or concrete), but their performance has not been examined in nonhomogeneous materials such as masonry.

Damage was created in a masonry panel by a “clean diagonal cut” at the center of the specimen which length was progressively extended towards the corners of the specimen. The modal response of the panel was extracted for the healthy condition and for different states of damage to detect correlations between variations in the modal properties (modal frequency and mode shapes) and the damage defined by the length of the cut. The purpose of this damage configuration was to obtain controlled, well-characterized, and easily quantifiable damage to facilitate the subsequent analysis that correlates damage with variations in the damage indicators.

In the first half of this paper, the results of numerical simulations of the experiment were employed to evaluate the effectiveness of a set of existing damage identification approaches based on changes in modal properties. While in second half of the paper, the experimental procedure is extensively described.

To the authors’ best knowledge, investigation of damage identification using results of experiments with this kind of artificially generated damage, that is, a clean cut of a defined length, has never been reported in investigation of URM structures. Only preliminary and partial results of this study have been previously introduced by the authors [16], but this article presents the definitive and complete outcomes of this research.

2. Damage Indicators Based on Vibration Response

Previous experiences in damage identification applied to URM structures [17] have demonstrated that usually one single damage indicator is not able to identify damage under different conditions, because damage can affect structures and, therefore, alters modal parameters in different ways. Hence, the common practice is to use several damage indicators based on different modal parameters to cover a wider range of damage effects. Five vibration-based damage indicators related to different modal parameters (i.e., modal frequencies, mode shapes, and mode shape curvatures) were considered in this study.

2.1. Variation in Modal Frequencies. The relationship observed between degradation of structural properties (stiffness and mass) and changes in modal frequencies was a main promoter for developing vibration-based damage identification techniques. Because frequency measurements can be quickly conducted and have a lower data scatter than mode shapes

and damping measurements, damage parameters related to modal frequencies have historically been preferred [18]. In the study presented here, statistically significant differences in the modal frequencies, calculated before and after damage, were employed to detect damage. Particularly for this study, the frequency database obtained from different damage states were analyzed considering a method known as “two-sample t -test for equal means” [19]. This method is utilized to verify whether the mean values of two populations are equal.

The null hypothesis (H_0) for unpaired data considered in this analysis was

$$H_0: u_1 = u_2 \quad (1)$$

and the alternative hypothesis (H_a) was

$$H_a: u_1 \neq u_2. \quad (2)$$

The test statistic was defined by

$$T = \frac{(\bar{y}_1 - \bar{y}_2)}{S_p \sqrt{1/N_1 + 1/N_2}}, \quad (3)$$

where N_1 and N_2 were the sample sizes, \bar{y}_1 and \bar{y}_2 were the sample means, and S_p was defined as

$$S_p^2 = \frac{[(N_1 - 1)s_1] + [(N_2 - 1)s_2]}{[N_1 + N_2 - 2]} \quad (4)$$

in which s_1 and s_2 are the sample variances.

The level of significance (α) desired for the analysis being defined and the number of degrees of freedom (v) computed, the T statistic is compared to the tabulated value of the t -distribution ($t_{(\alpha/2, v)}$). If T is smaller than the negative of $t_{(\alpha/2, v)}$, then the null hypothesis must be rejected, which signify that it can be ensured with a level of certainty of $(1 - \alpha)$ that the means values of both database are not equal.

2.2. Modal Assurance Criteria. The Modal Assurance Criteria (MAC) is an indicator that quantifies the degree of similarity between two mode shape vectors (see (5)). A low value of MAC represents low correspondence between the compared mode shape vectors. MAC is therefore used to detect differences between mode shapes measured before and after damage. Previous studies [20] have confirmed that a good result can be achieved, even in the case when frequency based indicators were not able to identify structural deterioration.

$$MAC_j = \frac{\left(\{\phi_j^0\}^T \{\phi_j^D\} \right)^2}{\left(\{\phi_j^0\}^T \{\phi_j^0\} \right) \left(\{\phi_j^D\}^T \{\phi_j^D\} \right)}, \quad (5)$$

where $\{\phi_j^0\}$ and $\{\phi_j^D\}$ correspond to the mode shapes vectors of j th mode for the undamaged and damaged condition, respectively.

2.3. Coordinate Modal Assurance Criterion. A more effective method for determining the spatial distribution of damage can be achieved by using the Coordinate Modal Assurance

Criterion (COMAC) [21]. This indicator detects differences between two mode shape vectors. However, it also shows where these differences are located. COMAC is defined as the mode correlation evaluated at each degree of freedom averaged over a set of correlated mode pairs (see (6)). A COMAC value close to zero represents low correspondence between the modal displacements recorded before and after damage at the degree of freedom under investigation. The discrepancy detected by COMAC can be related to damage at the location considered.

$$COMAC_i = \frac{\left(\sum_{j=1}^m (\phi_{i,j}^0 \phi_{i,j}^D) \right)^2}{\left(\sum_{j=1}^m (\phi_{i,j}^0)^2 \right) \left(\sum_{j=1}^m (\phi_{i,j}^D)^2 \right)}, \quad (6)$$

where $\phi_{i,j}^0$ and $\phi_{i,j}^D$ are the modal displacements of the j th mode at the i th degree of freedom evaluated for the undamaged and damaged condition, respectively; and m represents the number of modes taken into account in the analysis.

2.4. Curvature Damage Factor. For detecting early stages of damage, mode shape curvatures (second derivative of the mode shape) have proved to be more sensitive than mode shapes. Pandey et al. [22] verified that changes observed in modal curvature are inversely proportional to flexural stiffness variation. Consequently, modal curvature can be employed to determine the spatial distribution of damage. The Curvature Damage Factor (CDF) [23] corresponds to the average absolute change of the modal curvatures considering several modes:

$$CDF = \frac{1}{m} \sum_{k=1}^m \left| \phi_{k,0}'' - \phi_{k,D}'' \right|, \quad (7)$$

where $\phi_{k,0}''$ and $\phi_{k,D}''$ are the modal curvatures of the k th mode measured for the undamaged and damaged state, respectively, and m is the number of modes considered in the analysis. The logic behind CDF is that for different modes different parts of the structure are activated. If a damaged zone is not strained by a vibration mode, other modes would be able to strain that damaged section. Hence, when several modes are considered, the curvature change at the damaged location will be different than zero and damage identification is then possible. In this study, CDF was separately calculated in two orthogonal directions for each measuring grid point and the superposition of these factors ($CDF_X + CDF_Y$) was considered to capture the combined effect of damage in both directions.

2.5. Stubbs-Cornwell Damage Index. Stubbs et al. [24] proposed a more sophisticated damage index based on the strain energy loss in a beam segment. More recently, Cornwell et al. [25] extended this formulation to bidimensional elements (plates). This method creates a fractional ($f_{i,jk}$) that represents the ratio between the strain energy generated by a mode at one of the finite elements compared to the total strain energy generated in the whole plate-like member with undamaged and damaged conditions:

$$f_{i,jk} = \frac{\int_{y_k}^{y_{k+1}} \int_{x_j}^{x_{j+1}} \left[(\partial^2 \phi_i / \partial x^2)^2 + (\partial^2 \phi_i / \partial y^2)^2 + 2\nu (\partial^2 \phi_i / \partial x^2) (\partial^2 \phi_i / \partial y^2) + 2(1-\nu) (\partial^2 \phi_i / \partial x \partial y)^2 \right] dx dy}{\int_{y_0}^{y_{Ny}} \int_{x_0}^{x_{Nx}} \left[(\partial^2 \phi_i / \partial x^2)^2 + (\partial^2 \phi_i / \partial y^2)^2 + 2\nu (\partial^2 \phi_i / \partial x^2) (\partial^2 \phi_i / \partial y^2) + 2(1-\nu) (\partial^2 \phi_i / \partial x \partial y)^2 \right] dx dy}, \quad (8)$$

where ν is the Poisson's ratio and ϕ_i is the modal deflection at the i th degree of freedom in the jk element. In order to use all m measured modes in the calculation, the damage index for subregion jk was defined to be

$$\beta_{jk} = \frac{\sum_{i=1}^m f_{i,jk}^D}{\sum_{i=1}^m f_{i,jk}}, \quad (9)$$

where $f_{i,jk}$ and $f_{i,jk}^D$ denote the fractions defined in (4) considering the mode shapes extracted from the undamaged and damaged system, respectively. Assuming that the collection of the damage indices, β_{jk} , represented a sample population of a normally distributed random variable, a normalized damage index was obtained using (10), where $\overline{\beta_{jk}}$ and σ_{jk} represent the mean and standard deviation of the damage indices, respectively.

$$DI_{\text{Stubbs},jk} = \frac{(\beta_{jk} - \overline{\beta_{jk}})}{\sigma_{jk}}. \quad (10)$$

In both CDF and DI_{Stubbs} , the mode shape curvature at each grid point was calculated from the computed modal displacements by applying a central difference approximation. In the case of DI_{Stubbs} , the number of degrees of freedom was artificially expanded by fitting a polynomial function to the data computed at the different grid points. The use of numerical estimations for curvatures makes it impossible to evaluate the damage indicators at the edges of the specimen and, consequently, damage that occurred close to the border of the panels would be not detected by these two indicators.

The effectiveness of all the above introduced indicators (i.e., significant variation of modal frequencies, MAC, COMAC, CDF, and DI_{Stubbs}) to identify damage in URM structures under ideal conditions (e.g., homogeneous properties of bricks and mortar and perfect connection in the brick-mortar interface) was assessed using numerical simulations.

3. Numerical Simulation

The specimen selected for this study corresponded to a cantilever URM panel embedded at the base in a reinforced concrete foundation to replicate fully fixed support conditions. The panel dimensions were 1150 mm high and 1150 mm long, with a nominal thickness of 230 mm (two leafs of bricks). The foundation block was 2050 mm long, 400 mm high, and 640 mm thick. A finite element model was generated to represent the physical specimen. This numerical analysis was conducted simultaneously with the physical test; hence, the results obtained from the simulations were not available when the laboratory trials were performed and could not be used to improve the design of the experiment (e.g., optimization of the sensors distribution).

3.1. Numerical Model. The finite element model was generated using FEMtools [26] considering QUAD4 shell elements, with an effective thickness of 198 mm, a density equal to 1790 kg/m³, and Young's modulus of 0.53 GPa. The wall thickness and Young's modulus were adjusted to better replicate the specimen's nondamage dynamic properties. The calibration process applied for this purpose is described in detail in Oyarzo Vera [27]. It was based on the studies by Derakhshan et al. [28] that calculated the equivalent section of a URM wall for out-of-plane bending analysis. The foundation block was simply supported to replicate laboratory real conditions.

The damage to the panel was simulated by eliminating the finite elements along the diagonal line (10 mm wide), initiated at the center of the panel and progressively extended towards the corners. Six damage states (DS) were defined according to the length of the cut. The specimen dimensions and damage distribution for the different DS are illustrated in Figure 1 and Table 1.

For each damage state, the modal frequency and mode shapes were calculated. The modal displacements were recorded at 16 different nodes (16-dof model). However, another model, considering modal displacements at 49 different locations (49-dof model), was also analyzed to investigate the performance of the damage location indicators (i.e., COMAC, CDF, and DI_{Stubbs}) when the number of points considered in the analysis (degrees of freedom) is increased. Figure 2 shows schematically the grid of point considered in each case. Only out-of-plane modes were considered in the numerical simulation, because in the physical experiments the sensors only measured acceleration oriented normal to the panel surface. It was assumed that the loss of mass due to the cut was insignificant.

The effect of inexact and spurious measurements of modal displacements during the physical experiment (noise) was represented in the simulated mode shape by the addition of random error equivalent to 5% and 10% of the exact mode shape norm in each degree of freedom.

3.2. Results of the Simulation. The modal frequencies obtained for each damage state model are presented in Table 2. The first mode was omitted in the analysis, because it was related to a rigid-body response of the entire specimen with its foundation block (rocking). Rocking response was only sensitive to changes in the inertial properties (loss mass) and did not depend on variations in panel stiffness. In general, modal frequencies dropped from their initial values computed at DS0 as the damage progressed.

3.2.1. Variation in Modal Frequencies. In the simulation, the frequency variation usually exceeded 5%, which is the

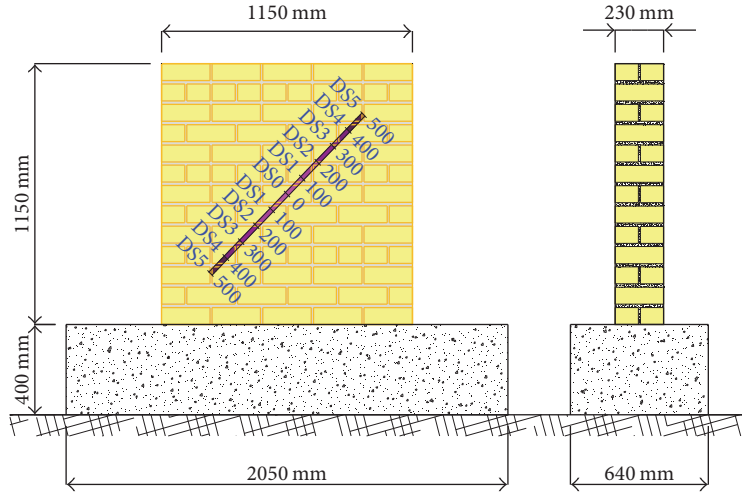


FIGURE 1: Specimen dimensions and damage distribution at different DS.

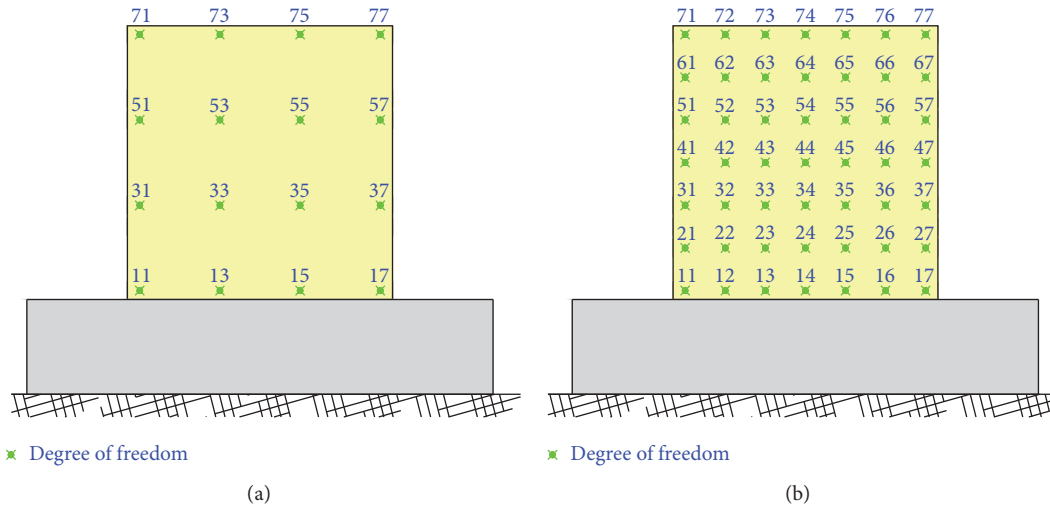


FIGURE 2: Reduced degree-of-freedom models.

TABLE 1: Cut length at different damage states.

Damage state	Total length of the cut [mm]
DS0	0
DS1	200
DS2	400
DS3	600
DS4	800
DS5	1000

typical data scatter computed in experimental studies. These frequency variations were therefore considered as potentially effective in detecting damage. The most significant frequency drop occurred at DS3 and DS4.

3.2.2. *Modal Assurance Criteria.* MAC was also able to detect damage (Figure 3) and the influence of noise was insignificant. The most significant damage was identified

at DS3, similar to that observed in the case of frequency variations.

Considering that damage produced after DS3 was less noteworthy, only the results of DS3 compared to DS0 are presented for COMAC, CDF, and DI_{Stubbs} to illustrate the performance of these indicators that describe spatial distribution of damage. The entire set of plots is available in Oyarzo Vera [27].

3.2.3. *Coordinate Modal Assurance Criterion.* COMAC was able to identify damage from DS3 onwards, and no substantial differences were observed in the subsequent states of damage. The method identified a damage concentration at the center of the panel, but it is sensitive to noise content, leading to many false damage detections especially when levels of noise exceed 5% (Figure 4). The performance of COMAC was significantly improved when the number of degrees of freedom was increased (Figure 7(a)). However, the 49-dof model was equally sensitive to noise.

TABLE 2: Modal frequencies (Hz) at different DS and their variation relative to DS0.

Mode	DS0	DS1	DS2	DS3	DS4	DS5
(2)	27.20	26.84 (1%)	25.91 (5%)	24.14 (11%)	21.49 (21%)	20.15 (26%)
(3)	31.45	31.03 (1%)	30.22 (4%)	29.29 (7%)	28.27 (10%)	27.73 (12%)
(4)	88.47	87.41 (1%)	85.73 (3%)	79.80 (10%)	67.39 (24%)	62.73 (29%)
(5)	99.12	96.21 (3%)	89.63 (10%)	83.95 (15%)	80.48 (19%)	78.77 (21%)
(6)	106.18	105.81 (0%)	104.40 (2%)	100.16 (6%)	94.92 (11%)	93.68 (12%)
(7)	172.98	169.76 (2%)	155.09 (10%)	126.58 (27%)	116.48 (33%)	114.67 (34%)

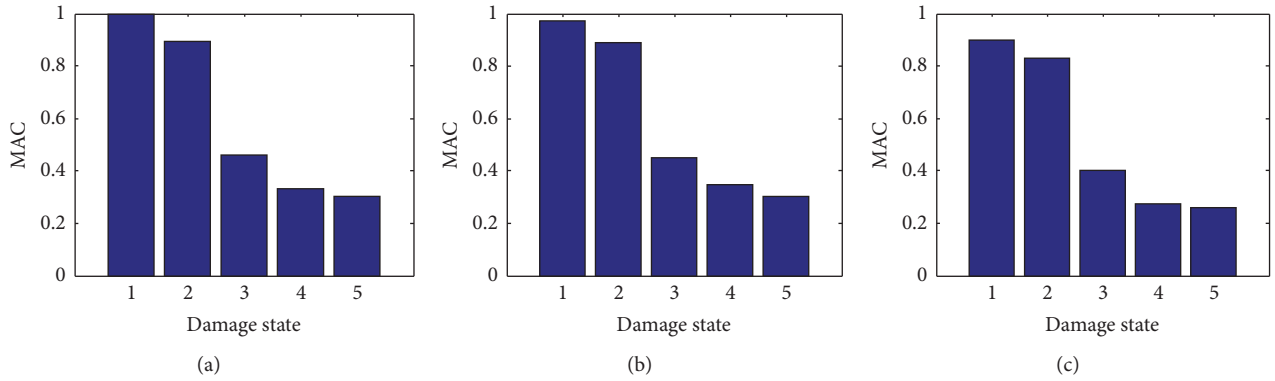


FIGURE 3: Effect of the noise in MAC relative to DS0 of a 16-dof model. (a) 0% noise, (b) 5% noise, and (c) 10% noise.

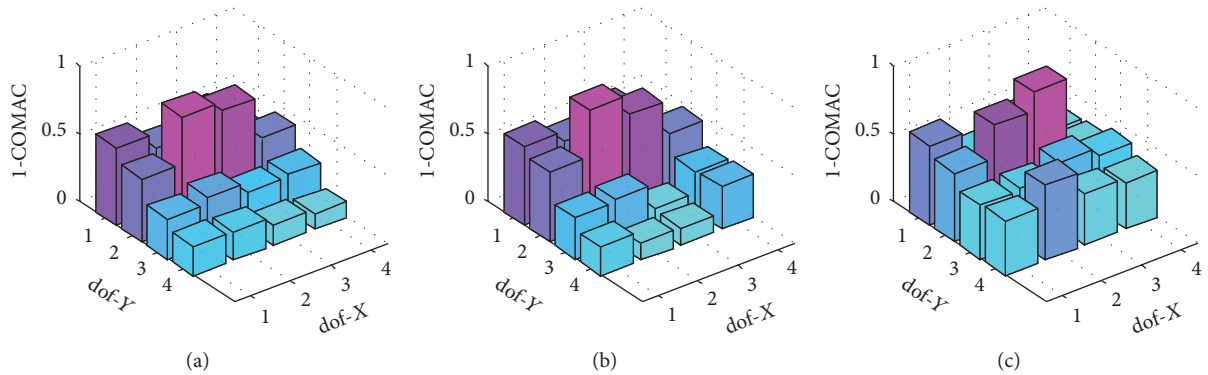


FIGURE 4: Effect of the noise in COMAC calculated for DS3 versus DS0 for a 16-dof model. (a) 0% noise, (b) 5% noise, and (c) 10% noise.

3.2.4. Curvature Damage Factor. CDF was capable of effectively detecting the damage concentration at the center of the panel at early stages. However, the damage evolution was not captured with sufficient resolution (Figure 5(a)). The inclusion of measurement error (noise) in the modal displacement was significant in the case of the 16-dof models (Figures 5(b) and 5(c)), resulting in an unreliable damage identification. Damage identification was significantly improved when the 49-dof model was considered (Figure 7(b)). In that case, the method was able to capture the damage evolution showing peaks at the degrees of freedom affected by the growing cut length at the different stages of the damage. The magnitude of the peaks at a degree of freedom already identified as damaged in a previous DS did not significantly change due to the extension of the damage to other degrees of freedom. The damage misidentification problems generated by noise were drastically reduced when the 49-dof model was used in the simulation.

3.2.5. Stubbs-Cornwell Damage Index. DI_{Stubbs} was able to determine the damage distribution using the data obtained from the 16-dof model. However, it was not accurate in capturing the damage evolution (Figure 6(a)). No significant difference was observed between DS1, DS2, and DS3, nor between DS4 and DS5. It can be even argued that the 16-dof model prematurely detected the damage condition (false damage detection). The main problem observed in applying this method was its sensitivity to noise (Figures 6(b) and 6(c)). Spurious mode shape calculations affected the damage detection even at a low level of noise (5%) giving several false identifications of damage. This misidentification was associated with the interpolations performed to artificially expand the number of degrees of freedom of the system. When the number of degrees of freedom considered for the analysis was increased from 16 dof to 49 dof (Figure 7(c)), the method was capable of depicting the damage growth, but many false identifications of damage persist.

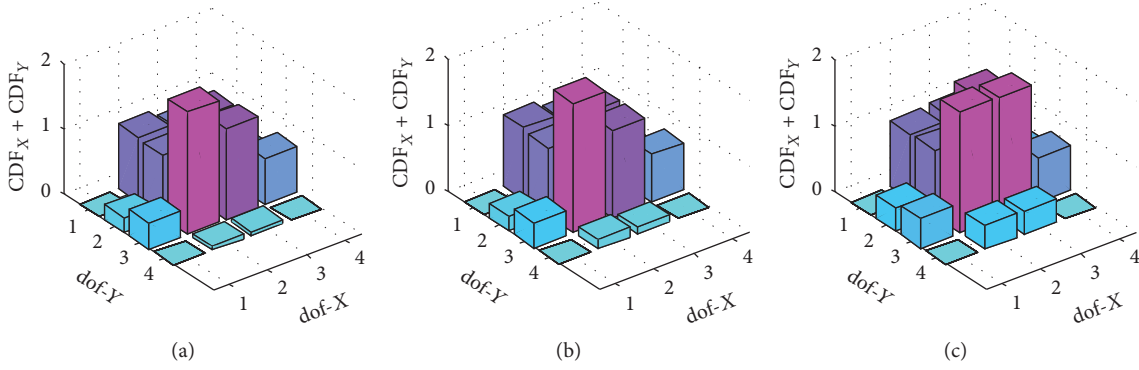


FIGURE 5: Effect of the noise in CDF calculated for DS3 versus DS0 for a 16-dof model. (a) 0% noise, (b) 5% noise, and (c) 10% noise.

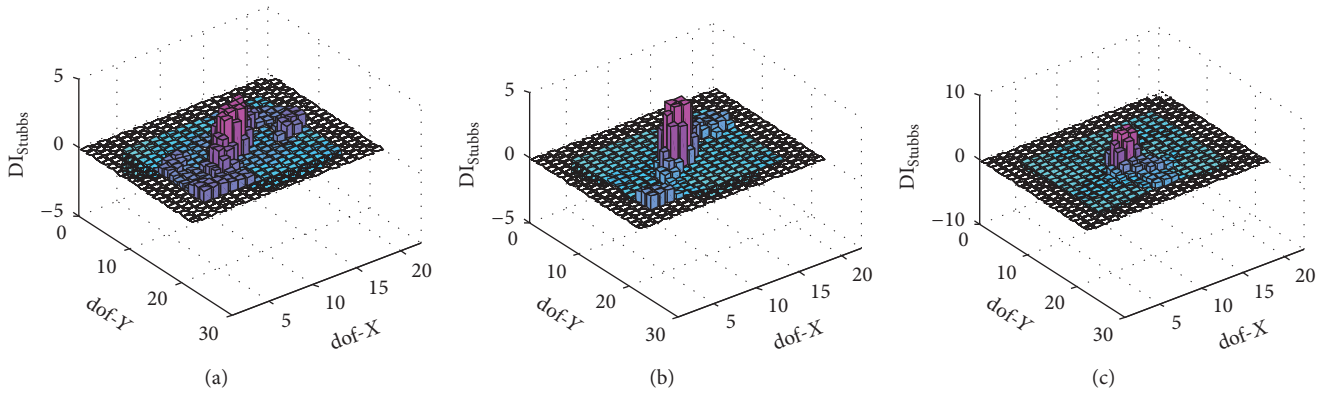


FIGURE 6: Effect of the noise in DI_{Stubbs} calculated for DS3 versus DS0 for a 16-dof model. (a) 0% noise, (b) 5% noise, and (c) 10% noise.

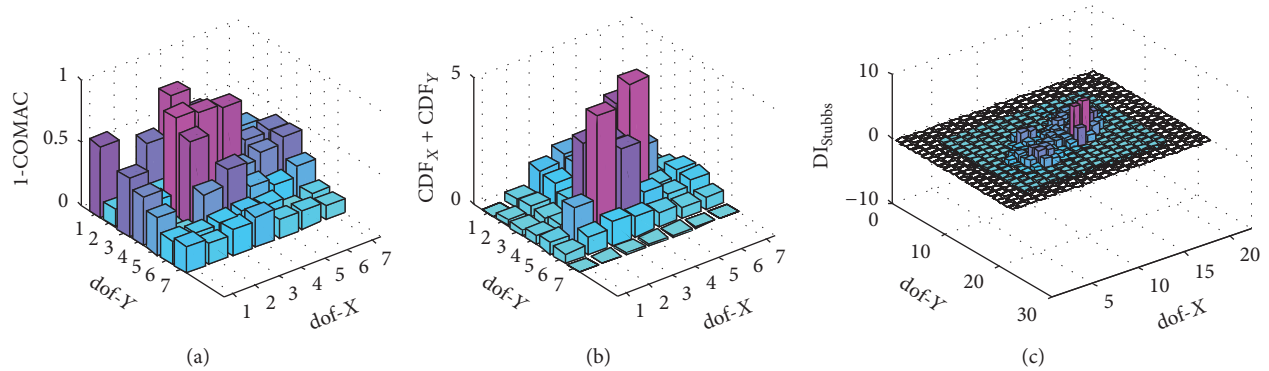


FIGURE 7: Damage indicators calculated for DS3 versus DS0 for a 49-dof model. (a) COMAC, (b) CDF, and (c) DI_{Stubbs} .

In summary, vibration-based damage detection can be satisfactorily performed using frequency variations and MAC. The identification of the damage spatial distribution using vibration-based methods in URM structures is still difficult. However, the results show that CDF performs better than COMAC and DI_{Stubbs} . Consequently, in the physical test, only frequency differences, MAC, and CDF were considered to identify damage.

4. Physical Test

4.1. Experimental Procedure. For the physical experiments, an unreinforced masonry panel was constructed using

industrially manufactured clay masonry units ($230 \text{ mm} \times 110 \text{ mm} \times 75 \text{ mm}$) in combination with a lime based mortar, with a cement:lime:sand ratio of 1:1:6. The masonry array followed a common bond pattern (header course of bricks after every three stretcher courses). The dimensions of the two-leaf panel were 1150 mm long, 1150 mm high, and 230 mm thick. The masonry panel was embedded at the base in a reinforced concrete foundation ($400 \text{ mm} \times 640 \text{ mm} \times 2050 \text{ mm}$) to replicate a fully fixed support condition. The masses of the specimen and the concrete base were estimated as 520 kg and 1300 kg, respectively. The properties of the materials used in these experiments were determined according to standardized material tests [29–31] giving as

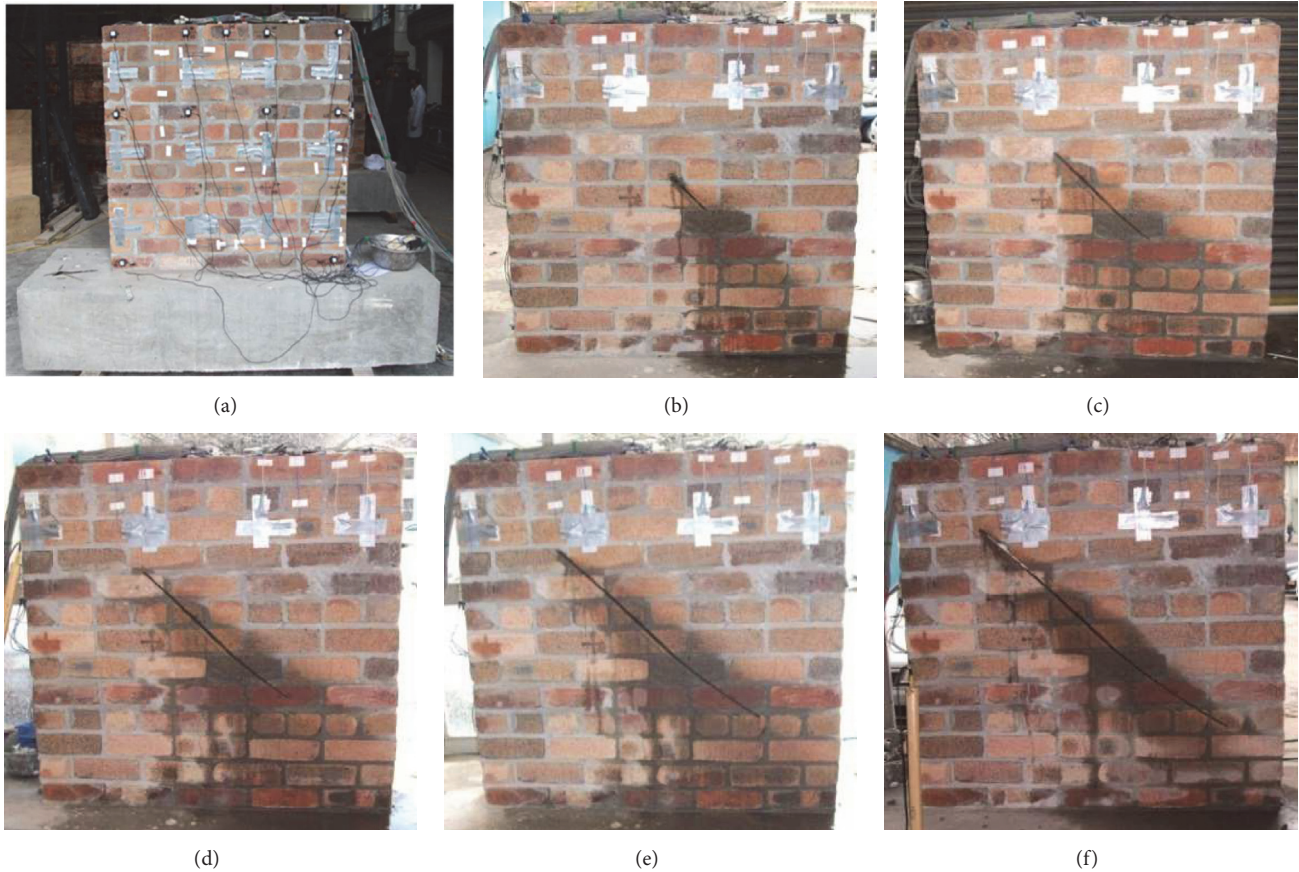


FIGURE 8: Specimen at different damage states. (a) DS0, (b) DS1, (c) DS2, (d) DS3, (e) DS4, and (f) DS5.

results a masonry compressive strength of 15 MPa and a masonry Young's modulus of 5 MPa.

A diagonal crack was generated in the panel by cutting through the masonry with a chainsaw. The cut was initiated at the center of the panel and progressively extended towards the corners of the specimen. The advantage of this artificial damage was that the alteration produced in the system was clear and easily quantifiable. Six states of damage were generated, the same as those generated in the numerical model and defined in Table 1. The physical specimen constructed for this experiment and the cut generated at each damage state is shown in Figure 8.

This specimen was instrumented with accelerometers (Crossbow CXL02LF1Z and Crossbow CXL10LF1Z) that recorded the vibration in the direction normal to the plane of the panel. A grid of 14 measurement points was selected to measure the specimen's response (Figure 9) similar to the grid considered for the 16-dof model described in the first part of this work (Figure 3(a)). As only 10 accelerometers were available for the test, the data was recorded in two sequences using different instrument setups (Table 3).

For each set-up, the panels were excited by impacts with a calibrated hammer (Dytran model 5803A) at the 16 grid points defined for recording the response, but on the panel face opposite to that on which the accelerometers were mounted. This procedure was repeated two times for each

TABLE 3: Instrumental set-up for modal tests.

	Instrumented grid points
Set-up 1	G01, G02, G03, G04, G05, G06, G07, G08, G13, and G16
Set-up 2	G01, G02, G03, G04, G09, G10, G11, G12, G13, and G16

instrumental set-up. Hence, 64 impacts were applied to the panel.

The data acquisition system was composed of a 48-channel signal conditioning box that amplifies the sensor signals to the range of ± 10 V. This equipment was connected to a 16-bit Analog to Digital Converter manufactured by National Instruments (NI9205 analog input module). The system was controlled by a Labview-based code. The data was collected at a rate of 500 samples per second. Each response record was cleaned using a 5th-order Butterworth low-pass filter at 200 Hz and a notch filter to remove the 50 Hz frequency characteristic of the power supply network in New Zealand.

The response of the panel due to the impact excitation was employed to determine the specimen's modal frequencies and mode shapes. These modal parameters were extracted from the recorded response by applying two operational modal analysis procedures: the Stochastic Subspace Identification [32] and Frequency Domain Decomposition [33, 34]. These

TABLE 4: Modal frequencies detected by applying SSI method.

	Freq. 1		Freq. 2		Freq. 3		Freq. 4		Freq. 5			
	Average (CoV)		Average (CoV)		Average (CoV)		Average (CoV)		Average (CoV)			
DS0	8.940 (8%)		18.226 (6%)		—		49.723 (3%)		63.816 (1%)			
DS1	9.083 (2%)	N	17.198 (2%)	Y	42.933 (2%)		—		59.576 (2%)		Y	
DS2	10.185 (2%)	Y	—		41.655 (3%)	N	47.672 (2%)	N	53.368 (2%)	N	56.857 (3%)	Y
DS3	10.572 (3%)	Y	20.535 (2%)	Y	40.940 (5%)	N	48.084 (3%)	N	54.107 (5%)	N	60.164 (2%)	Y
DS4	10.571 (3%)	Y	20.946 (4%)	Y	41.410 (3%)	N	50.370 (2%)	N	54.171 (1%)	Y	60.947 (1%)	Y
DS5	10.633 (4%)	Y	20.899 (3%)	Y	42.733 (3%)	N	—		53.285 (1%)	Y	61.564 (1%)	Y

TABLE 5: Modal frequencies detected by applying FDD method.

	Freq. 1		Freq. 2		Freq. 3		Freq. 4		Freq. 5			
	Average (CoV)		Average (CoV)		Average (CoV)		Average (CoV)		Average (CoV)			
DS0	8.838 (11%)		17.822 (8%)		—		48.384 (4%)		64.014 (1%)			
DS1	9.155 (5%)	N	16.927 (3%)	N	41.016 (0%)		49.316 (2%)	N	58.431 (2%)		Y	
DS2	10.376 (5%)	Y	—		—		45.703 (3%)	N	53.955 (2%)	Y	59.896 (4%)	Y
DS3	10.742 (3%)	Y	—		41.406 (5%)	N	46.875 (2%)	N	54.688 (2%)	Y	58.919 (2%)	Y
DS4	10.620 (3%)	Y	—		41.193 (6%)	N	47.852 (2%)	N	52.083 (3%)	Y	—	
DS5	10.864 (6%)	Y	21.680 (4%)	Y	42.236 (6%)	N	47.363 (1%)	N	54.688 (3%)	N	—	

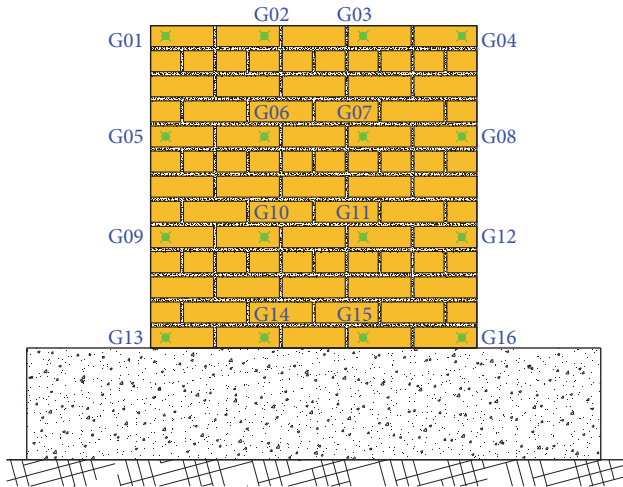


FIGURE 9: Excitation/measurement grid.

system identification methods have been successfully applied for extracting modal properties of structures excited by impacts and other kind of broadband excitation [8, 11, 35–37].

A time series and power spectrum of one hammer impact recorded along with the response power spectrum recorded by the accelerometer are presented in Figure 10 as an illustrative example.

4.2. Experimental Results. The records of responses due to each impact with the hammer (64 in total) were processed independently to identify the modal properties. The average values and coefficient of variation (CoV) of the modal frequencies identified from this set of 64 records are shown in Tables 4 and 5. These tables contain the results obtained for each DS using the SSI and FDD methods.

The frequencies detected at different damage states (DS) were paired, based on frequency similitude and visual comparison of the corresponding mode shapes, in an attempt to follow the evolution of modal response due to the damage. Not all the modes were detected in every DS and in some cases the modes “split” in two closely spaced frequencies (Freq. 5).

4.2.1. Variation in Modal Frequencies. A “two-sample *t*-test for equal means distributions” was conducted to determine which frequency had a statistically significant variation relative to the initial condition. A 95% confidence level was considered. The results of this analysis are presented in Tables 4 and 5. Label “Y” indicates that the frequency difference relative to the precedent DS is statistically significant, while label “N” indicates the opposite.

In general, it is usual that damage generates decay in modal frequencies due to stiffness degradation. With that in consideration, an apparently anomalous frequency increase with the progression of damage was detected for the first modal frequency (Freq. 1). However, a deeper analysis of these results led to the conclusion that this mode was related to a rigid-body rocking behavior of the entire panel-base system [27]. The detected frequency coincided with the theoretical values expected for rocking behavior [38]. Apparently, the hypothesis that the concrete base-block would provide fully fixed base conditions was not perfectly satisfied and a slight rocking of the entire panel-base system occurred because the surface underneath the foundation block was not perfectly even.

Rigid-body rocking behavior only depends on the mass, geometry, and conditions applied to initiate the oscillation of the structure (in the considered experiment it was the hammer impact), and it is independent of the internal stiffness of the body. Hence, the rocking frequency depended

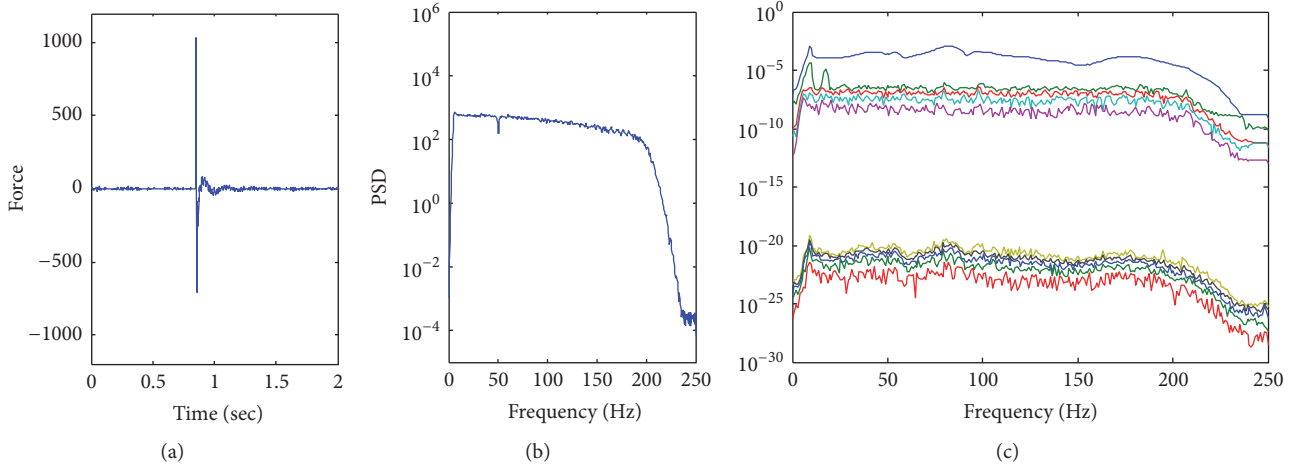


FIGURE 10: (a) Time series and (b) power spectrum of one impact recorded by the hammer and (c) response power spectrum recorded by the accelerometer.

only on the magnitude of the hammer impact. An increase of the first frequency was plausible, and it would depend on the magnitude of the impact. It can be inferred that the frequency variations associated with this mode cannot be used as a damage indicator, because it was affected not only by the crack generated but also by the initial conditions of rocking movement.

Rocking might be avoided by applying a better connection of the surface underneath the base-block or by fixing the base-block to the floor. In addition, sensors might be attached to the base-block to identify its rigid-body like rocking response.

Regarding the second modal frequency (Freq. 2), it was only detected in a sufficient number of damage states (DS0, DS1, DS3, DS4, and DS5) by the SSI method (Table 4). In the case of FDD method (Table 5), Freq. 2 was detected only in three damage states (DS0, DS1, and DS5). In one of them (DS1), the frequency change was statistically nonsignificant. Therefore, the analysis was conducted based only on observations made on SSI results.

A statistically significant decay between DS0 and DS1 was observed for Freq. 2. This decay was interpreted as the consequence of the initial degradation of the system stiffness. Freq. 2 was not detected in DS2, but, in the succeeding states of damage (DS3 and DS4), a frequency increment was observed. Even though this state might be considered anomalous because this frequency was not related to a rocking mode, it is necessary to note that the stiffness degradation is not the only reflection of structural damage. Damage may also alter the boundary/connectivity conditions and mass distribution within the specimen. These kinds of system changes would be reflected differently in the modal response and not necessarily as frequency drops. At this level of damage, the diagonal cut virtually divided the panel into two triangular sections with completely different support/connectivity conditions and kinematic response. The bending mode around a horizontal axis originally identified at DS0 mutated into a bending mode around an oblique axis. This behavior was also detected by the numerical model of

DS3 and onwards as it is shown in Figure 11. Then, for DS5 the frequency drops again, because of the further extension of the diagonal cut that reduced the stiffness of the healthy segments of panel that connect both triangular sections.

The third and fourth modal frequencies determined from the panel test (Freq. 3 and Freq. 4) revealed no statistically significant variations and, therefore, no conclusive observation could be stated.

The fifth frequency (Freq. 5) displayed a clear and statistically significant decrement, but not totally consistent with the damage progression. As mentioned before, Freq. 5 “split” in two closely spaced frequencies. This phenomenon was explained by the alterations in the connectivity conditions generated by the permanent separation of part of the panel due to the cut and, therefore, it might produce geometrical nonlinearity.

4.2.2. Modal Assurance Criteria. In this study MAC values smaller than 80% were associated with significant differences between a pair of mode shape vectors, and consequently it might be considered evidence of damage. MAC was calculated using the mode shape vectors detected in each damage state, and the average MAC of each damage state is presented in Figure 12. Based on this criterion, it was demonstrated that MAC was an effective damage detector, no matter which of the system identification techniques were used to extract the modal properties. The results show that MAC decayed significantly and progressively with the development of damage. The only anomaly was observed when DS2 is compared to DS0 (Figure 12(a)). In that case, MAC magnitude dropped that broke the expected tendency. This is explained by the nondetection of Freq. 2 (around 18 Hz) at DS2 using the SSI method. This mode usually exhibited the highest MAC. It was the main contributor to the average MAC calculated for the damage state.

4.2.3. Curvature Damage Factor. CDF was able to roughly identify the damage spatial distribution of DS3 and onwards when the modal properties were extracted using the SSI

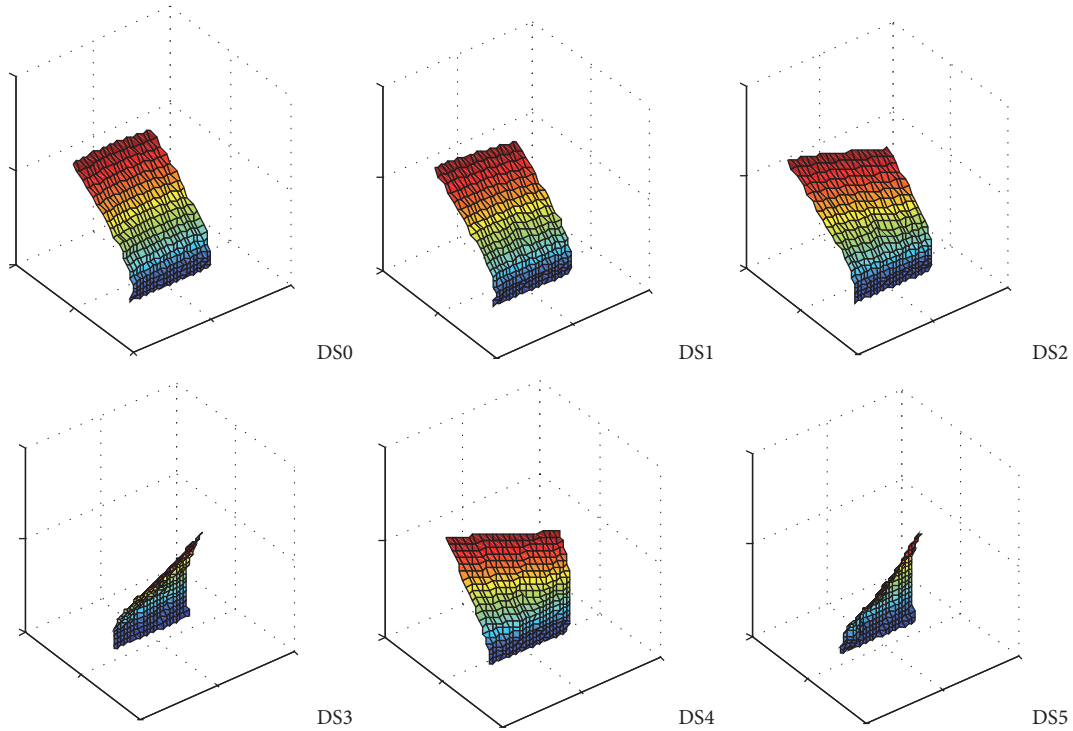


FIGURE 11: Modal displacements for Freq. 2 at different levels of damage.

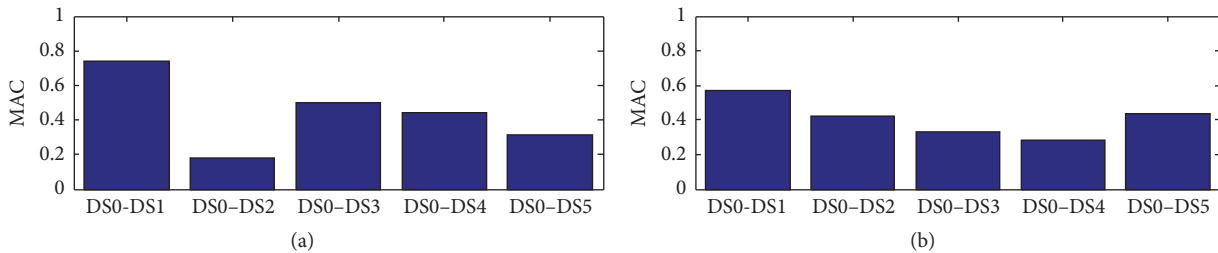


FIGURE 12: Average MAC experimentally determined. (a) SSI method and (b) FDD method.

method (Figure 13) and the damage of DS2 and onwards in the case of FDD method (Figure 14). The most prominent peaks of this indicator were recorded at the center of the specimen. The peak distribution and magnitude gradually expanded to one of the upper corners coinciding with the observed damage progression. The performance of CDF would be improved by incrementing the number of sensors placed on the specimen, to obtain a more accurate representation of the mode shapes. However, the instrumental density required to obtain an acceptable resolution may be impractical for a real application to URM structures. It is also important to remember that CDF is a damage indicator which performance is especially sensitive to noise contamination.

5. Results Discussion

Numerical simulations were used to evaluate the performance of a set of five vibration-based damage indicators in describing the damage distribution in an URM panel.

Damage was simulated by a diagonal “clean cut” of the panel whose length was progressively extended from the center to the corners.

The results of these numerical simulations demonstrated that significant variations in modal frequencies were generated in the structure due to damage. A clear correlation was noted between the progressive frequency decay and the damage severity. MAC was able to detect damage and especially effective in representing progression of damage severity.

In terms of the identification of the spatial distribution of damage, the damage indicator based on mode shapes (COMAC) performed poorly. This indicator proved to be sensitive to noise measured. It required a large number of recording points (high instrumental density in physical experiments) to achieve an acceptable resolution in identifying damage distribution. Damage indicators based on modal curvature (CDF and $DI_{Stubbbs}$) proved to be more effective. CDF was less sensitive to noise content than $DI_{Stubbbs}$. The performance of both indicators can be improved by

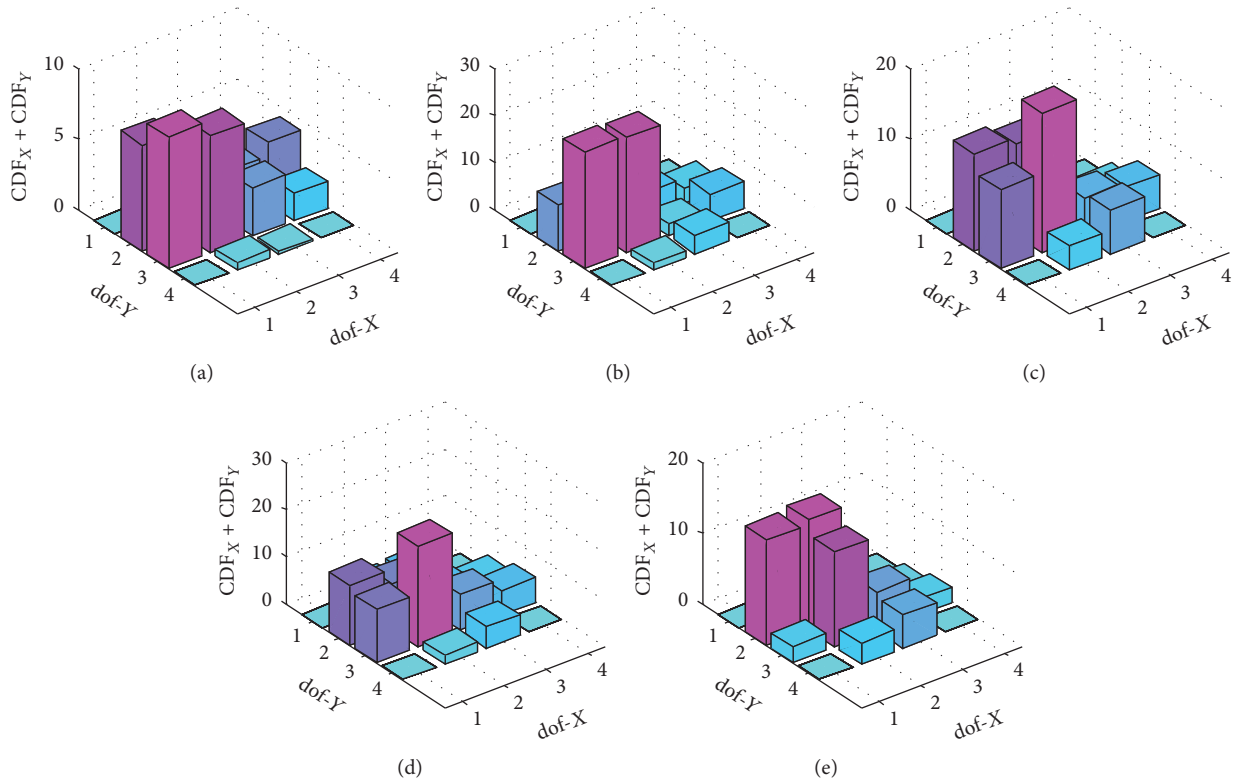


FIGURE 13: CDF calculated the modal data obtained from SSI Method. (a) DS0 versus DS1, (b) DS0 versus DS2, (c) DS0 versus DS3, (d) DS0 versus DS4, and (e) DS0 versus DS5.

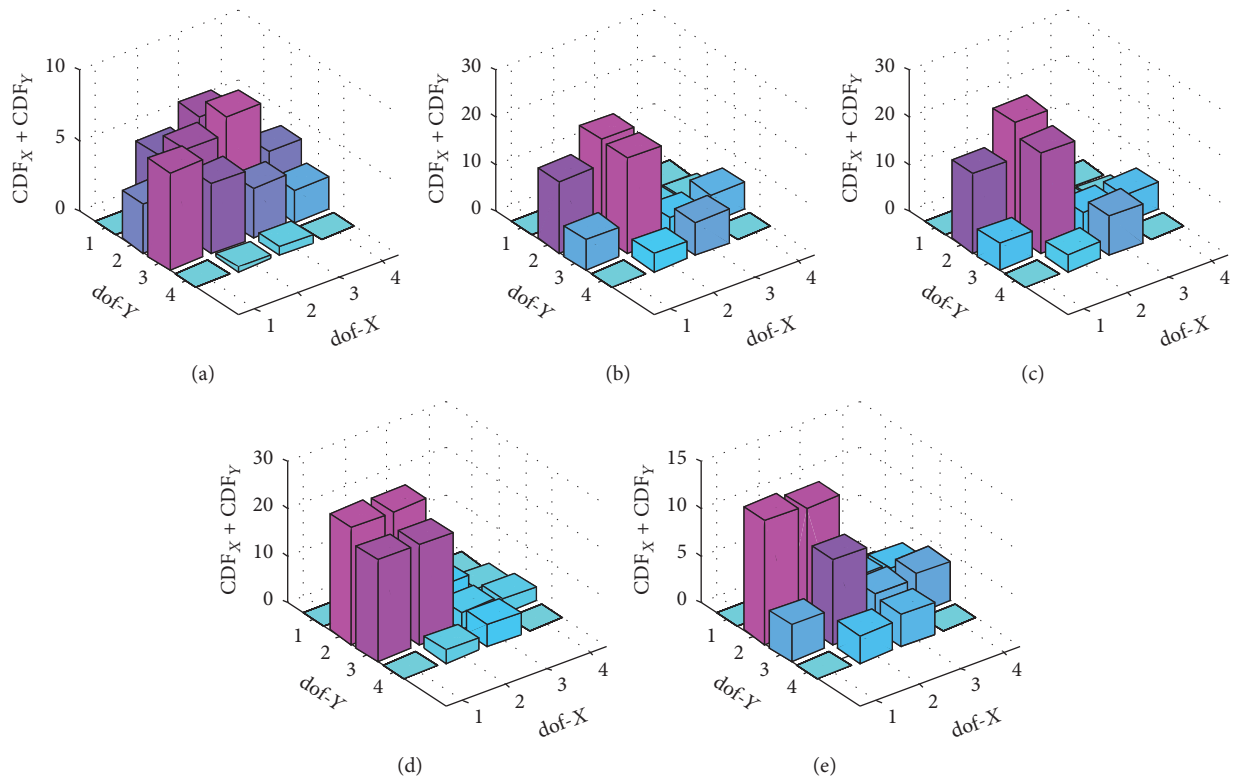


FIGURE 14: CDF calculated the modal data obtained from FDD Method. (a) DS0 versus DS1, (b) DS0 versus DS2, (c) DS0 versus DS3, (d) DS0 versus DS4, and (e) DS0 versus DS5.

incrementing the number of degrees of freedom to determine the mode shapes and mode shapes curvatures. The artificial expansion of degrees of freedom (interpolation by adjusting an analytical function) implemented to calculate DI_{Stubbs} frequently leads to an incorrect identification of damage.

In the physical experiments, six different damage configurations and the modal response extracted for each state of damage was used to identify damage.

The results of the vibration-based methods demonstrated that statistically significant variations in modal frequencies may be used to detect damage. Nevertheless, it was difficult to identify a clear trend between frequency shifts and damage progression. The damage not only degraded stiffness but also altered the internal boundary/connectivity condition of the specimen. These alterations affected the kinematic behavior of the system and the results interpretation based only on modal frequencies became complex. In contrast, MAC was effective in detecting damage and in representing progression of damage severity.

CDF was only able to roughly identify the spatial distribution of damage. This kind of indicators requires high instrumental densities to obtain acceptable resolution in the identification of damage distribution. COMAC and DI_{Stubbs} were not applied to the results of physical test because of their poor performance in numerical simulations.

6. Conclusions

Vibration-based damage detection can be satisfactorily applied in URM structures using frequency variations and MAC. The identification of the damage spatial distribution using vibration-based methods is still difficult, and a dense grid of measurement points is needed to obtain an adequate resolution. Such a dense instrumental grid becomes impractical in real applications. Instead, it is recommended to generate a database of the modal properties whose size is large enough to perform a statistical analysis of the variations observed in the measured modal properties and the associated damage indicators. For this purpose, a dense grid of measurement points is not required.

When damage identification procedures are applied to URM structures, it would be recommended to perform vibration-based damage identification to initially and roughly detect the damage distribution (identifying which part of the structure is affected) and then other kinds of nondestructive techniques (e.g., ultrasonic or X-ray explorations) can be applied to assess the severity of damage and determine the local spatial distribution.

For future experiments, it is recommended to prepare in advance the surface where the specimen will be placed using a rubber or grout layer underneath the foundation block. If it is possible, the base-block should be mechanically fixed to the floor to avoid rocking response. Also, it is suggested to attach a control accelerometer to the base-block. The information obtained from this control accelerometer can be used to identify rigid-body rocking response.

Conflicts of Interest

The authors declare that there are no conflicts of interest regarding the publication of this paper.

Acknowledgments

The authors acknowledge the support of the New Zealand Foundation for Research, Science and Technology (Project UOAX0411) for this experimental program and the support the Universidad Católica de la Santísima Concepción in Chile that partially supported the final stage of this study through the Research and Innovation Direction (Proyecto DIN 06/2013).

References

- [1] C. R. Farrar and K. Worden, "An introduction to structural health monitoring," *Philosophical Transactions of the Royal Society A: Mathematical, Physical & Engineering Sciences*, vol. 365, no. 1851, pp. 303–315, 2007.
- [2] J. M. W. Brownjohn, "Structural health monitoring of civil infrastructure," *Philosophical Transactions of the Royal Society A: Mathematical, Physical & Engineering Sciences*, vol. 365, no. 1851, pp. 589–622, 2007.
- [3] A. Rytter, *Vibration based inspection of civil engineering structures [Ph.D. thesis]*, Department of Building Technology and Structural Engineering, University of Aalborg, Denmark, 1993.
- [4] K. Worden and J. M. Dulieu-Barton, "An overview of intelligent fault detection in systems and structures," *Structural Health and Monitoring*, vol. 3, no. 1, pp. 85–98, 2004.
- [5] E. Durukal, S. Cimilli, and M. Erdik, "Dynamic response of two historical monuments in Istanbul deduced from the recordings of Kocaeli and Düzce earthquakes," *Bulletin of the Seismological Society of America*, vol. 93, no. 2, pp. 694–712, 2003.
- [6] C. Gentile and A. Saisi, "Ambient vibration testing of historic masonry towers for structural identification and damage assessment," *Construction and Building Materials*, vol. 21, no. 6, pp. 1311–1321, 2007.
- [7] K. Beyen, "Structural identification for post-earthquake safety analysis of the Fatih mosque after the 17 August 1999 Kocaeli earthquake," *Engineering Structures*, vol. 30, no. 8, pp. 2165–2184, 2008.
- [8] L. F. Ramos, G. De Roeck, P. B. Lourenço, and A. Campos-Costa, "Damage identification on arched masonry structures using ambient and random impact vibrations," *Engineering Structures*, vol. 32, no. 1, pp. 146–162, 2010.
- [9] L. F. Ramos, L. Marques, P. B. Lourenço, G. De Roeck, A. Campos-Costa, and J. Roque, "Monitoring historical masonry structures with operational modal analysis: Two case studies," *Mechanical Systems and Signal Processing*, vol. 24, no. 5, pp. 1291–1305, 2010.
- [10] F. Ceroni, S. Sica, M. Rosaria Pecce, and A. Garofano, "Evaluation of the natural vibration frequencies of a historical masonry building accounting for SSI," *Soil Dynamics and Earthquake Engineering*, vol. 64, pp. 95–101, 2014.
- [11] G. Osmancikli, Ş. Uaçk, F. N. Turan, T. Türker, and A. Bayraktar, "Investigation of restoration effects on the dynamic characteristics of the Hagia Sophia bell-tower by ambient vibration test," *Construction and Building Materials*, vol. 29, pp. 564–572, 2012.

- [12] C. Oyarzo-Vera, J. Ingham, and N. Chouw, "Vibration-based damage identification of an unreinforced masonry house model," *Advances in Structural Engineering*, vol. 20, no. 3, pp. 331–351, 2016.
- [13] V. Gattulli, M. Lepidi, and F. Potenza, "Dynamic testing and health monitoring of historic and modern civil structures in Italy," *Structural Monitoring and Maintenance*, vol. 3, no. 1, pp. 71–90, 2016.
- [14] R. Ceravolo, G. Pistone, L. Z. Fragonara, S. Massetto, and G. Abbiati, "Vibration-based monitoring and diagnosis of cultural heritage: A methodological discussion in three examples," *International Journal of Architectural Heritage*, vol. 10, no. 4, pp. 375–395, 2016.
- [15] C. Gentile, A. Saisi, and A. Cabboi, "Structural identification of a masonry tower based on operational modal analysis," *International Journal of Architectural Heritage*, vol. 9, no. 2, pp. 98–110, 2015.
- [16] C. Oyarzo-Vera and N. Chouw, "Vibration based damage identification of an unreinforced masonry panel," in *Proceedings of the 5th International Operational Modal Analysis Conference (IOMAC '13)*, pp. 1–10, Guimarães, Portugal, May 2013.
- [17] L. F. Ramos, *Damage identification on masonry structures based on vibration signatures [Ph.D. in Civil Engineering]*, Escola de Engenharia, Universidade do Minho, Braga, Portugal, 2007.
- [18] O. S. Salawu, "Detection of structural damage through changes in frequency: a review," *Engineering Structures*, vol. 19, no. 9, pp. 718–723, 1997.
- [19] G. W. Snedecor and W. G. Cochran, *Statistical Methods*, Iowa State University Press, 8th edition, 1989.
- [20] S. W. Doebling, C. R. Farrar, M. B. Prime, and D. W. Shevitz, "Damage identification and health monitoring of structural and mechanical systems from changes in their vibration characteristics: a literature review," Tech. Rep., Los Alamos National Laboratory, Los Alamos, NM, USA, 1996.
- [21] W. Heylen, S. Lammens, and P. Sas, *Modal analysis theory and testing*, Katholieke Universiteit Leuven, Leuven, Belgium, 2nd edition, 1997.
- [22] A. K. Pandey, M. Biswas, and M. M. Samman, "Damage detection from changes in curvature mode shapes," *Journal of Sound and Vibration*, vol. 145, no. 2, pp. 321–332, 1991.
- [23] M. M. Abdel Wahab and G. de Roeck, "Damage detection in bridges using modal curvatures: application to a real damage scenario," *Journal of Sound and Vibration*, vol. 226, no. 2, pp. 217–235, 1999.
- [24] N. Stubbs, J.-T. Kim, and K. Topole, "An efficient and robust algorithm for damage localization in offshore platforms," in *Proceedings of the 10th ASCE Structures Conference*, 1992.
- [25] P. Cornwell, S. W. Doebling, and C. R. Farrar, "Application of the strain energy damage detection method to plate-like structures," *Journal of Sound and Vibration*, vol. 224, no. 2, pp. 359–374, 1999.
- [26] DDS, *FEMTools Model Updating—Theoretical Manual*, Dynamic Design Solutions NV, Leuven, Belgium, 2008.
- [27] C. Oyarzo Vera, *Damage identification of unreinforced masonry structures based on vibration response [Ph.D. in Civil Engineering]*, Department of Civil and Environmental Engineering, University of Auckland, Auckland, New Zealand, 2012.
- [28] H. Derakhshan, M. C. Griffith, and J. M. Ingham, "Airbag testing of multi-leaf unreinforced masonry walls subjected to one-way bending," *Engineering Structures*, vol. 57, pp. 512–522, 2013.
- [29] ASTM C67, *Standard Test Methods for Sampling and Testing Brick and Structural Clay Tile*, Officials Standard, ASTM International, West Conshohocken, Pa, USA, 2009.
- [30] ASTM C109, *Standard Test Method for Compressive Strength of Hydraulic Cement Mortars (Using 2-in. or [50-mm] Cube Specimens)*, Officials Standard, ASTM International, West Conshohocken, Pa, USA, 2008.
- [31] ASTM C1314, *Standard Test Method for Compressive Strength of Masonry Prisms*, Officials Standard, ASTM International, West Conshohocken, Pa, USA, 2010.
- [32] P. van Overschee and B. de Moor, *Subspace Identification for Linear Systems: Theory Implementation Applications*, Kluwer Academic Publishers, Boston, Mass, USA, 1996.
- [33] R. Brincker, P. Andersen, and L. Zhang, "Modal identification from ambient responses using frequency domain decomposition," in *Proceedings of the 18th International Modal Analysis Conference (IMAC '00)*, San Antonio, Tex, USA, 2000.
- [34] R. Brincker, C. E. Ventura, and P. Andersen, "Damping estimation by frequency domain decomposition," in *Proceedings of the 19th International Modal Analysis Conference (IMAC '01)*, Kissimmee, Fla, USA, 2001.
- [35] A. C. Altunişik, A. Bayraktar, and B. Sevim, "Operational modal analysis of a scaled bridge model using EFDD and SSI methods," *Indian Journal of Engineering & Materials Sciences*, vol. 19, no. 5, pp. 320–330, 2012.
- [36] E. Reynders, D. Degrauwe, G. De Roeck, F. Magalhães, and E. Caetano, "Combined experimental-operational modal testing of footbridges," *Journal of Engineering Mechanics*, vol. 136, no. 6, pp. 687–696, 2010.
- [37] E. Reynders and G. D. Roeck, "Reference-based combined deterministic-stochastic subspace identification for experimental and operational modal analysis," *Mechanical Systems and Signal Processing*, vol. 22, no. 3, pp. 617–637, 2008.
- [38] G. W. Housner, "The behavior of inverted pendulum structures during earthquakes," *Bulletin of the Seismological Society of America*, vol. 53, no. 2, pp. 403–417, 1963.

Research Article

The Monitoring of Palazzo Lombardia in Milan

**Marta Berardengo,¹ Giorgio Busca,² Simone Grossi,²
Stefano Manzoni,² and Marcello Vanali¹**

¹*Dipartimento di Ingegneria e Architettura, Università di Parma, Parma, Italy*

²*Dipartimento di Meccanica, Politecnico di Milano, Milano, Italy*

Correspondence should be addressed to Marcello Vanali; marcello.vanali@unipr.it

Received 27 June 2017; Revised 19 September 2017; Accepted 28 September 2017; Published 24 October 2017

Academic Editor: Michele Palermo

Copyright © 2017 Marta Berardengo et al. This is an open access article distributed under the Creative Commons Attribution License, which permits unrestricted use, distribution, and reproduction in any medium, provided the original work is properly cited.

This paper discusses the monitoring of Palazzo Lombardia, one of the tallest high-rise buildings in Italy. First, the layout of the monitoring system is addressed for a general description of the sensors used. The paper provides details about how data coming from transducers are used. Special focus is put on the use of signals acquired by means of accelerometers, which are employed for the estimation of modal parameters through operational modal analysis. The procedure used for choosing the modal analysis algorithm and fixing the values of its main parameters is discussed in detail. The modal identification results on the first eight months of monitoring are discussed in the second part of the manuscript, together with a statistical analysis. This allows for a first model of the relationships between eigenfrequencies and environmental variables aiming at a general structural health monitoring procedure based on the evolution of the building's modal parameters.

1. Introduction

Structural health monitoring (SHM) is the discipline aiming at finding reliable strategies to assess the healthy condition of civil and mechanical structures [1]. For the last two decades, this research field has attracted the attention of many researchers because of the significant outcomes in case of success of this new approach to maintenance. The main advantage of using these techniques is the possibility to switch from a time-based maintenance to a condition-based method [2]. If maintenance was based on measurements collected from the structure, it would be possible to repair structural elements only when really needed. The main advantage is economic, but the consequence on safety of structures is also significant. These techniques allow establishing continuous monitoring systems on important structures such as flyovers, dams, and power stations to enhance their reliability during normal operational life and after extraordinary events such as earthquakes.

Damage identification could be performed at five different levels of detail: simply detecting the presence of damage and its localization, evaluating the type of damage, quantifying its entity, and finally estimating the residual life [3].

The general process to achieve these aims is based on the acquisition of data from several sensors fixed to the structure and the elaboration of this information in order to estimate one or more features sensitive to damage. Since damage could be seen as a stiffness reduction or the inception of nonlinear behaviour, for instance, due to a crack, a common strategy is to measure vibrations and extract damage features from the dynamic response of the structure in operational conditions [4]. Depending on the method used to evaluate the presence of damage, strategies for SHM can be roughly divided into two groups: model-based and data-driven [3]. The former detects damage by evaluating the difference between features extracted from the real structure and those coming from a physical model that should be as much accurate as possible. The latter usually identifies damage through a statistical comparison between features coming from an unknown scenario of the monitored structure and those coming from its healthy condition.

For civil structures, both approaches can be used, though methods based on physical models are usually more popular because they can achieve all the five levels of damage identification and because of the strong experience of civil engineers in building reliable models. Among model-based strategies,

linear methods are well-established techniques that are based on simple assumptions: damage is a stiffness reduction which modifies the structural dynamic parameters such as vibration frequencies [5–7], mode shapes and their curvatures [8–11], flexibility matrix [12–14], and modal strain energy [15–17]. However, the accuracy of these methods in finding damage, especially at their first stage of inception, depends on the uncertainty of modal parameter identification and the variation of structural properties due to the environmental conditions [18–22].

Normally, in the context of SHM, dynamic parameters such as natural frequencies and mode shapes are identified from the dynamic response of the structure in operational conditions [23, 24]. This requirement comes from the necessity to keep the structure accessible to the public but having a continuous control of its health condition at the same time. Operational modal analysis (OMA) is an only-output technique that can estimate modal parameters without using any actuator [25–27]. This property is advantageous because usually actuators are bulky machineries that require closing the structure to the public. However, the quality of the identification strongly depends on the noise affecting the signals and the frequency resolution of the data used for the analysis. Generally, incipient damage produces a slight change of modal parameters; then it is fundamental to keep the estimation uncertainty under control to detect a small anomaly in modal parameters.

Beyond the uncertainty of modal identification process, another issue that can nullify damage detection is the effect of environmental conditions. Modal parameters, especially eigenfrequencies, might strongly change because of a variation of the environmental conditions such as temperature, humidity, and wind speed. If these variables cannot be filtered out from the damage identification process, two scenarios could happen: the variation of the modal parameters generated by the environment could be recognised as damage without any reason or the variation due to the environmental conditions could cover damage which is actually present in the structure.

In this context, this paper offers a study based on the data collected from the new skyscraper of the Lombardia Regional Government. This building is made up of 42 floors and it is equipped with a continuous monitoring system collecting data from several accelerometers and inclinometers. Since the monitored floors are just 5 (see Section 2), it is not convenient to use mode shapes for SHM purposes. Indeed, the aim of this work is to explore the use of frequencies as damage features focusing on the qualification of the modal identification uncertainty and the effects of the environmental conditions. However, also mode shapes are taken into account because the number of sensors could be increased in the near future with the consequent possible use of mode shapes for SHM purposes as well.

The paper is structured as follows. Section 2 describes the structure and the layout of the monitoring system. Section 3 discusses the identification algorithms considered and the characterisation of their accuracy. Section 4 presents the results of the modal parameter identification carried out on the first eight months of the operation of the monitoring

system. Finally, Section 5 presents a first-attempt empirical model to link the eigenfrequency behaviour to environmental factors.

2. Layout of the Monitoring System

The Palazzo Lombardia building is the first in a series of high-rise buildings that have been built in Milano in the last years. It is the current seat for the Regional Government and therefore is considered of strategic relevance. The complex is made up of five lower buildings (about 40 m high, called Cores 2, 3, 4, 5, and 6), surrounding the high-rise tower (Core 1), which scored, at the time of construction, the new height record in Italy (161 m). The monitoring system is targeted to control Core 1 tower and is capable of handling both dynamic vibration signals and static variables, as well as the wind conditions. Figure 1 shows a schematic representation of the system layout, while a full description of the installed sensor network and its performances can be found in [28].

Five floors are instrumented with inclinometers and accelerometers according to the general layout given in Figure 1. The setup was designed in accordance with the dynamic testing results [29] in order to be able to identify at least the first three vibration modes and to assess wind comfort issues.

In order to be able to monitor vibration comfort levels against wind serviceability and perform continuous operational modal analysis identifications, very high sensitivity low noise accelerometers had to be employed. Moreover, the building's first natural frequency is around 0.3 Hz, thus posing problems on both the sensor choice and the data acquisition hardware. Since a cabled solution has been chosen (synchronized wireless measurements were not considered affordable on such a high building), the sensor types were chosen in order to minimize the needed cabling.

On the other hand, the selected tilt sensors had to provide long-term stability and a certified temperature sensitivity in order to guarantee reliability to the static measurements.

According to all the above stated needs, the following sensors were chosen:

- (i) Accelerometers: PCB 393B31 piezoelectric units, which have been proven to have a very low noise floor level and guarantee good frequency response down to 0.1 Hz, having a 4.9 m/s^2 full scale value
- (ii) Inclinometers: $\pm 5^\circ$ Singer TS servo-inclinometers with extended temperature calibration. They are high reliability sensors with a frequency response up to 3 Hz, which is enough to cover the building's first frequencies
- (iii) Wind speed/direction: anemometer NESA ANS-VV1-A + ANS-DVE-A (potentiometric wind direction), with a 50 m/s full scale value

Data acquisition is performed 24 h per day with a final sampling frequency of 250 Hz on all the channels. This is enough to assess wind comfort and vibration disturbances and provide data to modal analysis purposes [25, 30–32]. The data acquisition device is Field-Programmable Gate

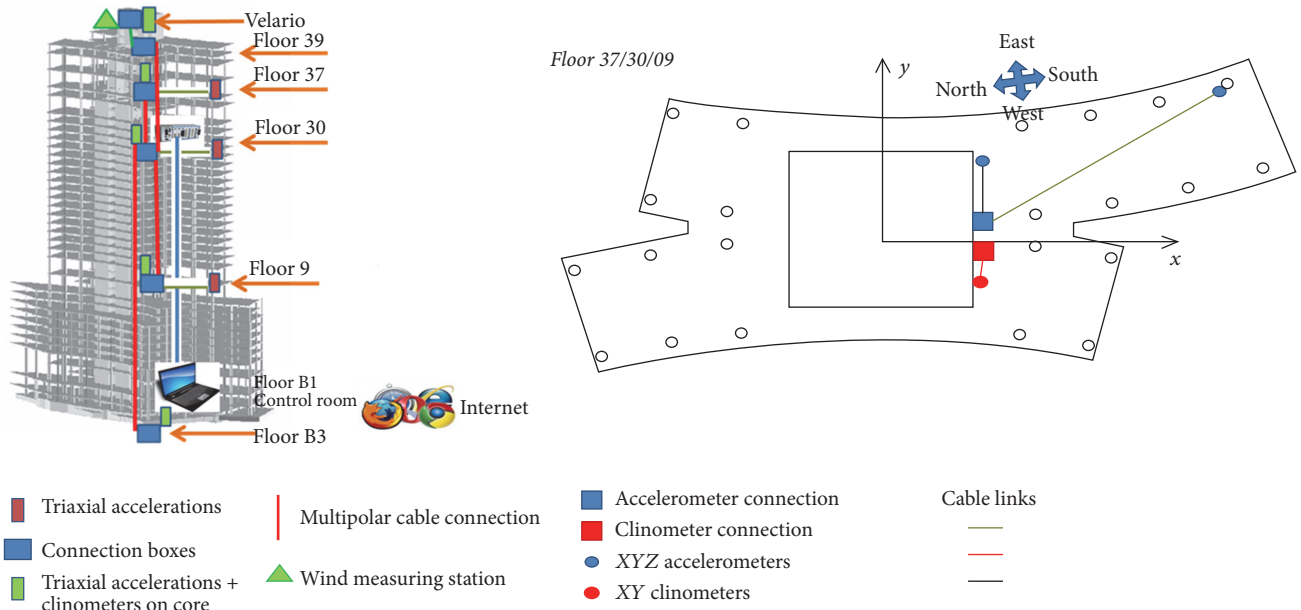


FIGURE 1: Layout of the monitoring system. Floor B3 and Velario differ from floors 37/30/09 because of the lack of the external accelerometers. In each accelerometer location, there are three accelerometers measuring in x , y , and z (out of the figure) directions. In inclinometer location, there are two inclinometers measuring around the x and y axes.

Array (FPGA) based, using 24-bit converters and built-in antialiasing filters.

A total of 24 high sensitivity piezoelectric accelerometers and 10 inclinometers are installed along the whole building together with the wind measurement station on top of it. A new data file is generated every 10 minutes ready to be analysed. This monitoring system is also integrated with some temperature and radiation power sensors previously installed in the building.

3. Identification of Modal Parameters

As described in the previous section, the monitoring system is made from inclinometers, accelerometers, and transducers for environmental variables (e.g., temperature, wind strength, and direction). One of the approaches used for monitoring the building is the continuous modal parameter identification using the accelerometer signals, coupled to the analysis of the data collected by means of the inclinometers. The modal data are employed to investigate the dynamic behaviour of the structure, while the signals provided by the inclinometers are used to describe its static behaviour.

The modal extraction is performed by means of OMA. This is a very attractive approach when monitoring huge structures because it allows considering the unmeasured environmental excitation as the source to force the system (e.g., [33–40]). This section focuses on the choice of the algorithm used to carry out modal extraction. Two different algorithms were tested: the polyreference least-squares complex-frequency (pLSCF) domain method and a method based on the frequency domain decomposition (FDD), which relies on the singular value decomposition (SVD). The two methods are compared in terms of dispersion and bias effects

on the estimated modal parameters using the Markov Chain Monte Carlo (MCMC) method. This analysis also allowed finding the optimal values for the parameters used in the analysis of the real data.

3.1. OMA Algorithms. The two algorithms that were taken into account are the pLSCF and the FDD, as already mentioned. They are briefly discussed here to provide the most relevant information. More details can be found in the referenced works.

With regard to pLSCF, one of its main properties is that it provides clean and easy-to-interpret stabilization diagrams and this reduces the amount of complexity for its use as well as difficulties for getting reliable results. This has caused the pLSCF to become the industrial standard for modal analysis at the present time [25, 26]. pLSCF is a least-squares approach in frequency and can be used in OMA. In this case, the inputs to the method are the positive power spectra of the system responses [25].

The second algorithm taken into consideration is the FDD. As mentioned, it is based on SVD. SVD [41] is a linear algebra technique that can achieve factorization of a complex matrix. FDD identification method works by decomposing the power spectral density (PSD) matrix in its principal components at each spectral line. More details can be found in the wide referenced literature (e.g., [25, 27]).

There are two parameters which must be considered as inputs when using the two mentioned OMA identification approaches: the frequency resolution R of the power spectra and the number of averages N used to calculate them [42]. It is known in the literature that a narrow frequency resolution allows improving the accuracy of the modal identification. It is also easy to understand that the higher the number of

TABLE 1: Reference parameters for the Monte Carlo simulations.

First eigenfrequency	First mode shape	Second eigenfrequency	Second mode shape	Third eigenfrequency	Third mode shape
0.32 Hz	Bending (east-west direction)	0.40 Hz	Bending (north-south direction)	0.63 Hz	Torsion

averages is, the cleaner the power spectra will be and the more reliable the modal identification will thus be. This would suggest increasing the time length of the acceleration signals used to calculate the power spectra. Indeed, if T_t is the total time of the acceleration time histories used for the modal extraction and if the whole time records are divided into N subrecords of time length t_t (with no overlap), it results that

$$R = \frac{1}{t_t} = \frac{N}{T_t} \implies T_t = \frac{N}{R}. \quad (1)$$

Therefore, T_t must be increased in order to both increase N and decrease R .

However, T_t cannot be increased indefinitely because the structure changes its behaviour in time: for example, the modal parameters of a structure change between day and night due to thermal shifts. Hence, a high value of T_t would lead to results of OMA which would be a sort of averaged result, preventing the description of the time trends of the identified modal parameters. Therefore, it is important to choose T_t not too high for describing the modal behaviour of the structure in time; at the same time, T_t must be not too low because this would cause a poor accuracy on the identified modal parameters. According to these points, a maximum possible value for T_t was fixed equal to 10800 s (i.e., 3 hours), which is a time span over which an initial data check did not evidence any significant effect of the environmental conditions. Once this threshold was fixed, the effects of different values of R and N were studied by means of MCMC simulations. These simulations and their results are described in Section 3.2.

3.2. Markov Chain Monte Carlo Simulations. The comparison of pLSCF and FDD was carried out by means of the MCMC method. Time histories of accelerations were generated numerically with the goal to make them as close as possible to those collected by the accelerometers placed in the building. Then these numerical time records were provided as inputs to the two algorithms.

These simulated signals were generated by means of a modal model of the structure, considering the first three modes. The data used to build such a model came from a former modal analysis carried out just after the building construction (see Table 1) [29]. The PSDs of the generated signals were made as close as possible to the PSDs of the actual signals collected by the accelerometers. The reference actual PSDs were chosen from a day with very low wind in order to test the case with the poorest signal-to-noise ratio.

The effect of the electrical noise due to the transducers, cables, and so forth was taken into account as well. Indeed, random noise was added to the generated signals and this

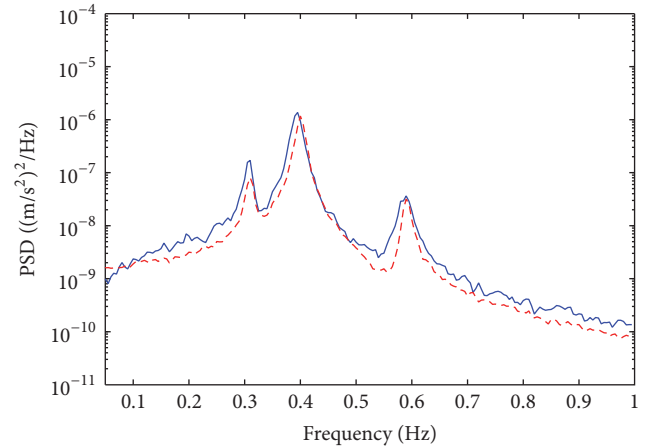


FIGURE 2: Experimental (solid curve) and numerical (dashed curve) PSD for an accelerometer on floor 30 in case of low wind.

allowed testing the modal extraction in situations close to the real application. The PSD of the added random noise was obtained from the accelerometer and acquisition board data sheets.

Figure 2 shows a comparison between a PSD of a simulated signal and a real one. The agreement is satisfactory. Obviously, since the signals are of random nature, Hanning window was always used [43, 44] to process the time signals before passing in the frequency domain. This figure also shows that the value of the numerical PSD curve far from the resonances is close to the experimental one. This proves that the amount of random noise added to the numerical signals was correct.

The signal generation for each configuration tested (i.e., fixed values of N and R) was repeated 300 times. Then, modal identification was carried out for each iteration. The focus of the analysis was on the estimation of eigenfrequencies and mode shape components. Since the mode shape vectors are made from many numbers (i.e., many eigenvector components), the results related to mode shapes were described by a synthetic index: the modal assurance criterion (MAC) [41] between the identified mode shapes and the reference ones used in the modal model.

This procedure allowed us to build statistical populations for the following indexes:

- (i) Errors between estimated and reference eigenfrequency values: these errors account for bias on the estimations by computing the population mean values μ and for the dispersion of the estimation by employing the standard deviation σ

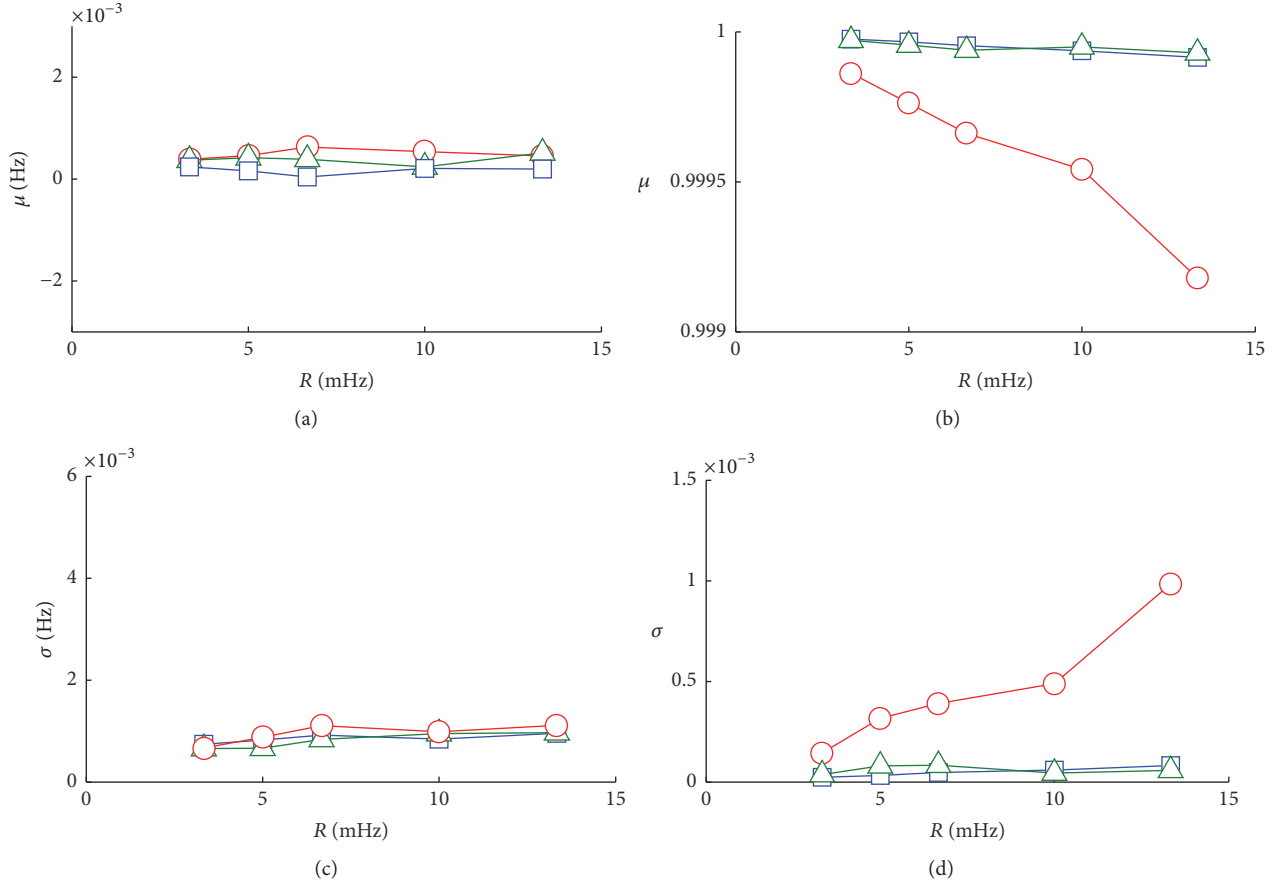


FIGURE 3: Results of the MCMC simulations for pLSCF as function of R ($N = 36$): mean value of the error for the eigenfrequency estimation (a), mean value of the MAC (b), σ of the error for the eigenfrequency estimation (c), and σ for the MAC (d). Curves with squares (\square) for the first mode, with circles (\circ) for the second mode, and with triangles (\triangle) for the third mode.

- (ii) MAC value: the mean MAC value μ accounts for bias, while again dispersion is related to the standard deviation σ of the MAC populations

The trends of these mean and standard deviation values were investigated as function of two input variables: the number of averages N and the frequency resolution R employed to calculate the power spectra provided as inputs to the modal identification algorithms. The populations of the errors on the eigenfrequencies and each eigenvector component were almost Gaussian. It is important to remark that the MAC results obviously show nonsymmetric populations. This means that the value of σ associated with the MAC populations cannot be directly related to any confidence interval of the estimates (an identification of the type of distribution would be required). However, the value of σ for the MAC is shown here for the sake of conciseness to provide an indication about the dispersion of the results in place of showing the standard deviation related to each eigenmode component (which would be correct under a metrological point of view).

Table 2 shows the limit values of R and N tested in the MCMC simulations. Each of the selected R - N pairs was such that the limit on the total time history, 10800 s, was satisfied;

TABLE 2: Values of T_t , R , and N tested in the Monte Carlo simulations.

Tested values of T_t [s]	Tested values of N	Tested values of R [mHz]
From 1000 to 10800	From 13 to 72	From 3.3 to 13

therefore, the pairs leading to T_t higher than 10800 s were discarded (an exception was made for few pairs considered for checking the results). It is noticed that in this case overlap between two subsequent subrecords was not used to increase N for a given value of R . The value of the overlap V was thus always equal to 0% [43].

Figures 3–6 show the results in terms of μ and σ for the first three modes of the building as function of the frequency resolution and the number of averages. Particularly, Figures 3 and 4 show the results for pLSCF, while Figures 5 and 6 show the results for FDD.

The analysis of these figures suggests the use of pLSCF for estimating the eigenfrequencies. Conversely, the FDD is more accurate for identifying mode shapes. With regard to eigenfrequencies, the values of μ of the differences between

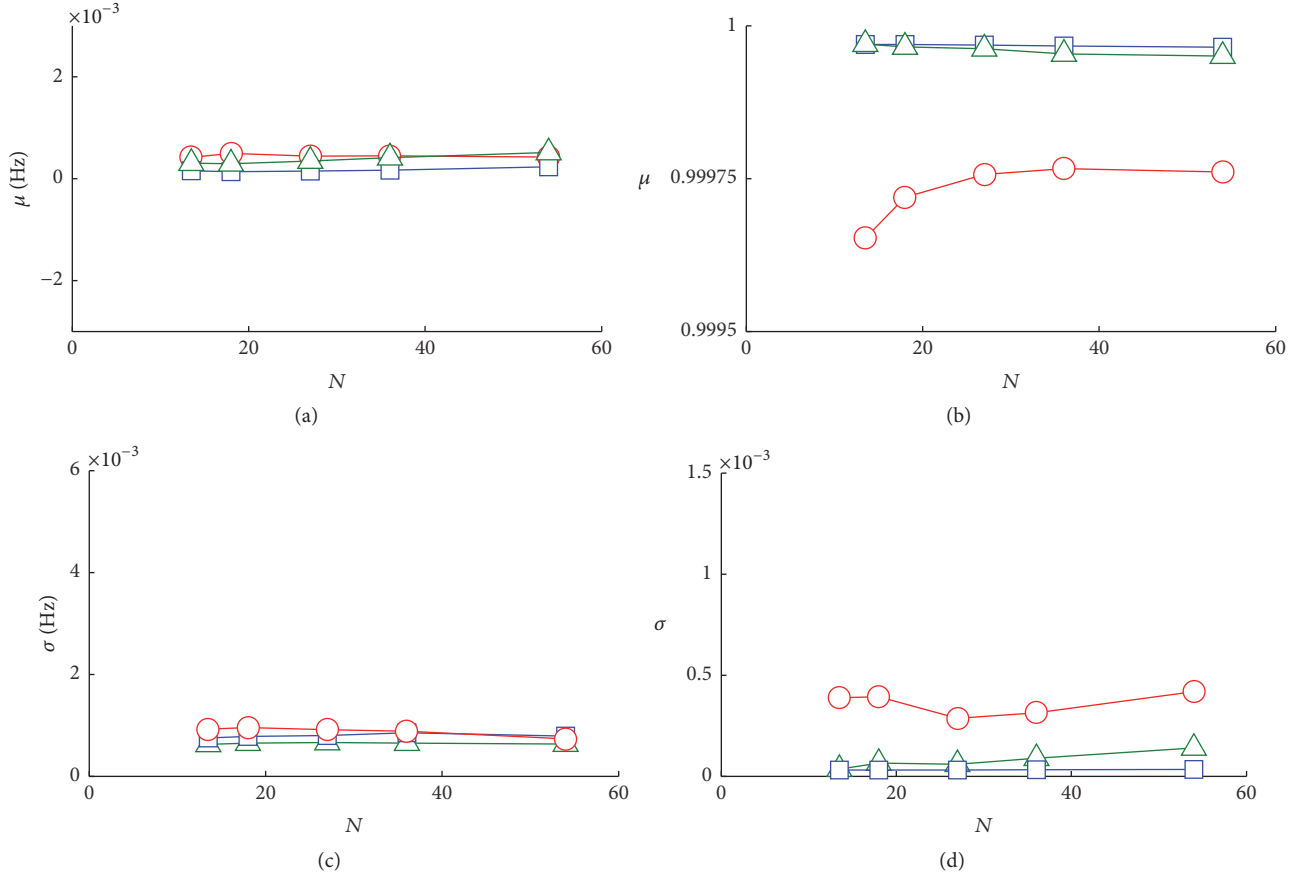


FIGURE 4: Results of the MCMC simulations for pLSCF as function of N ($R = 5$ mHz): mean value of the error for the eigenfrequency estimation (a), mean value of the MAC (b), σ of the error for the eigenfrequency estimation (c), and σ for the MAC (d). Curves with squares (\square) for the first mode, with circles (\circ) for the second mode, and with triangles (\triangle) for the third mode.

estimated and reference values are similar for the two algorithms (and negligible). Conversely, the dispersion of the error is much lower in the case of the pLSCF (see Figures 3(a), 3(c), 4(a), 4(c), 5(a), 5(c), 6(a), and 6(c)). As for the MAC, the FDD provides better results for the second mode (see Figures 3(b), 3(d), 4(b), 4(d), 5(b), 5(d), 6(b), and 6(d)). Therefore, a mixed approach was used when analysing real data: the use of pLSCF for identifying poles (and thus eigenfrequencies) and then FDD for the mode shape components.

Therefore, choosing a mixed approach allows improving the accuracy associated with the estimated modal quantities. The MCMC simulation also allowed finding reliable data about the effect of frequency resolution and number of averages of the power spectra and thus choosing properly their values (see Table 3). The bias values associated with the identified eigenfrequencies are very low, as evidenced by Figures 3(a) and 4(a). Instead, the expected values of the dispersion associated with the identified eigenfrequencies are gathered in Table 4 and can be used as an estimation of the uncertainty of the identification method [45].

It is remarked that, for the configuration of values of Table 3, the MCMC test was repeated with a higher number of simulations (using an adaptive version of the MCMC [46])

TABLE 3: Chosen values of T_t , R , and N to be used in OMA with real signals.

Chosen value of T_t [s]	Chosen value of N	Chosen value of R [mHz]
7200	36	5

TABLE 4: Expected values of σ on the eigenfrequency estimations.

σ on the first eigenfrequency	σ on the second eigenfrequency	σ on the third eigenfrequency
0.8 mHz	0.8 mHz	0.6 mHz

to assess statistical reliability. The results obtained are almost the same as those already shown with 300 simulations.

4. Trend of the Identified Modal Parameters for the High-Rise Building

The values of R and N chosen with the MCMC simulations, as well as the use of the mixed approach pLSCF/FDD, allowed developing an automatic OMA identification system. To do

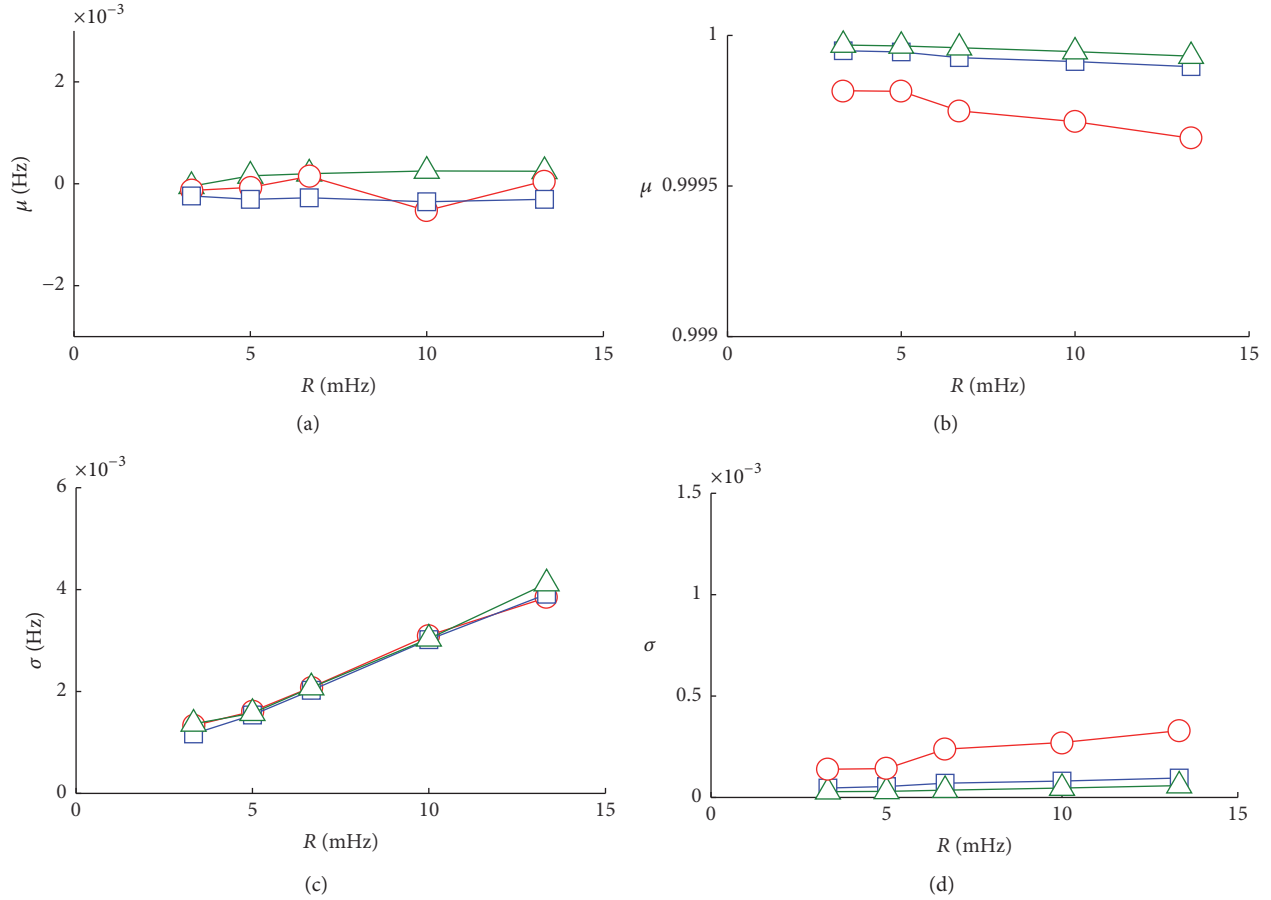


FIGURE 5: Results of the MCMC simulations for FDD as function of R : mean value of the error for the eigenfrequency estimation ($N = 48$) (a), mean value of the MAC ($N = 36$) (b), σ of the error for the eigenfrequency estimation ($N = 48$) (c), and σ for the MAC ($N = 36$) (d). Curves with squares (\square) for the first mode, with circles (\circ) for the second mode, and with triangles (\triangle) for the third mode.

this, an automated data check procedure was also developed. Relying on the use of the Skewness coefficient and peak-peak values of the signals, corrupted time records (e.g., due to saturation, lightning, and transducer damage) are automatically discarded before modal identification.

The automated extraction was applied to eight months of vibration data coming from the installed monitoring system. Figures 7–9 show the trend of the first three eigenfrequencies of the structure. Instead, Figure 10 shows the MAC trend for the first mode. The changes of the eigenfrequencies are always lower than 5%. Furthermore, the uncertainty interval equal to $\pm 2\sigma$ (see Table 4) around the identified eigenfrequency value for the first mode is shown in Figure 11. This $\pm 2\sigma$ interval expresses a level of confidence of about 95% [45]. The width of the uncertainty intervals is clearly overestimated (indeed the cycles due to daily variability are clearly visible), which is probably due the fact that the value of σ was estimated through MCMC considering a day with very low wind (see previously in the paper). Therefore, when the wind increases (even slightly) the signal-to-noise ratio of the accelerometer signals and the accuracy of the estimations of the modal parameters improve as well. The consequence is that σ appears to be overestimated in this case.

The wind speed is proven to be able to change the eigenfrequency values significantly. Indeed, the spikes towards zero in Figures 7–9 are always related to the presence of an increased value of the root mean square (RMS) of the acceleration signals (the RMS is calculated on the frequency band of the considered mode). This RMS is strongly correlated with the wind speed (Figure 12 shows that peaks of the RMS of vibration correspond to peaks of the wind speed sensor).

It is also remarked that the eigenfrequency trends show a daily cycle due to temperature and sun exposure trends, as evidenced in Figure 13.

As for the MACs, slight decreases in time are evident. However, more data are needed (at least one year of data for a whole seasonal cycle) for a consistent analysis of such a trend. Moreover, the MAC changes are within the dispersion found with the MCMC simulations (see previously in the paper).

5. Empirical Model of the Eigenfrequencies

An empirical model to describe the behaviour of the eigenfrequencies as function of environmental factors was developed. Something similar will be performed for the mode shapes. The aim of the empirical model is to have a reliable tool

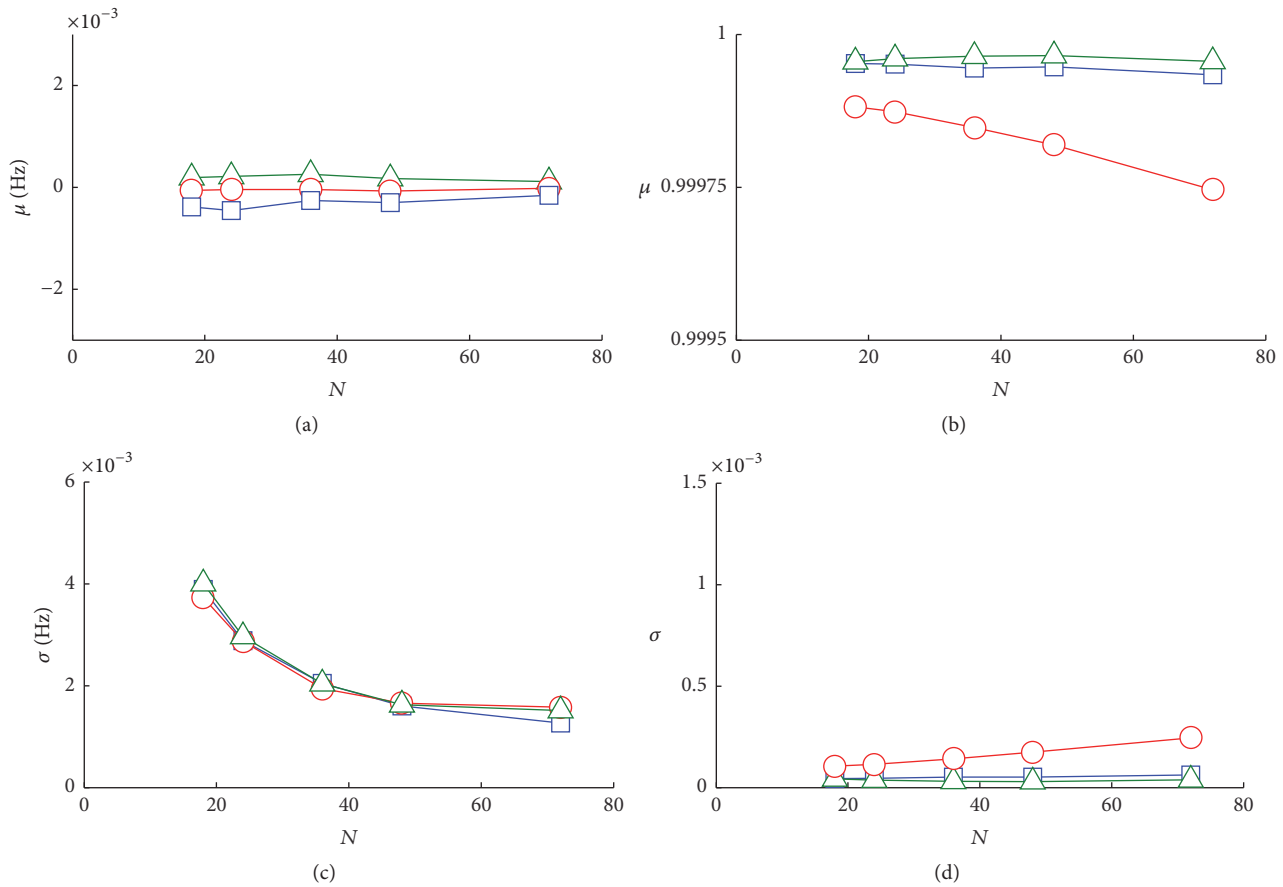


FIGURE 6: Results of the MCMC simulations for FDD as function of N ($R = 5$ mHz): mean value of the error for the eigenfrequency estimation (a), mean value of the MAC (b), σ of the error for the eigenfrequency estimation (c), and σ for the MAC (d). Curves with squares (\square) for the first mode, with circles (\circ) for the second mode, and with triangles (\triangle) for the third mode.

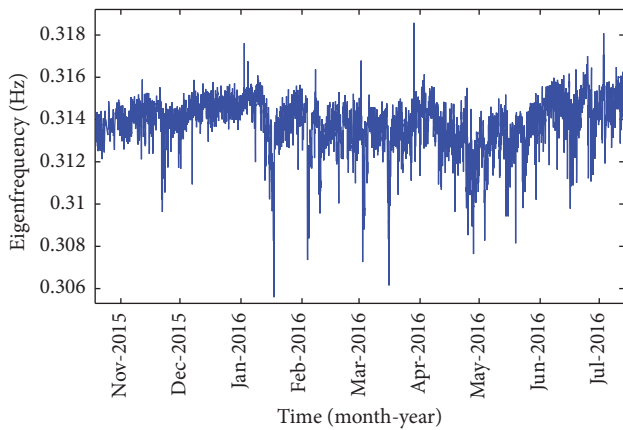


FIGURE 7: Time trend of the first eigenfrequency.

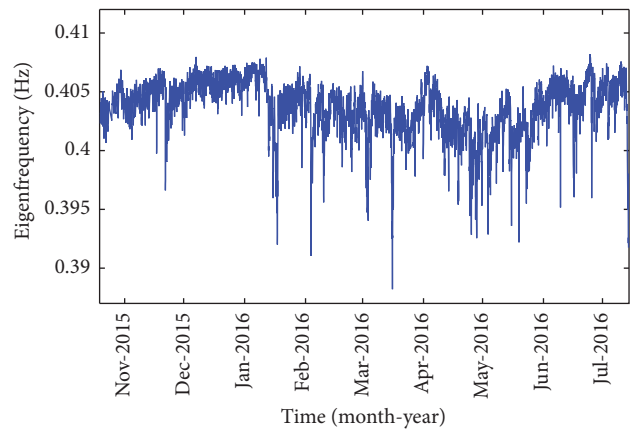


FIGURE 8: Time trend of the second eigenfrequency.

to describe the evolution of natural frequencies due to environmental factors. If the model is accurate enough, discrepancies between experimental data and model results could be employed to assess the presence of a change in the structure not due to environmental factors and thus possibly due to damage. Indeed, if a change of the eigenfrequencies

could not be described by the model, a check of the building would be required.

Many correlation studies were carried out before developing the statistical model in order to understand which variables should have been used as inputs to the model: for

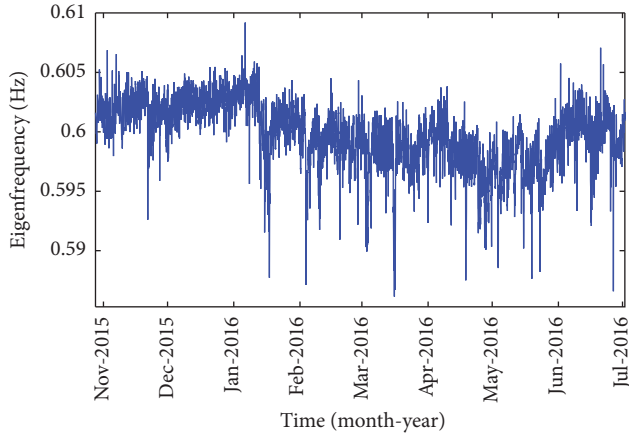


FIGURE 9: Time trend of the third eigenfrequency.

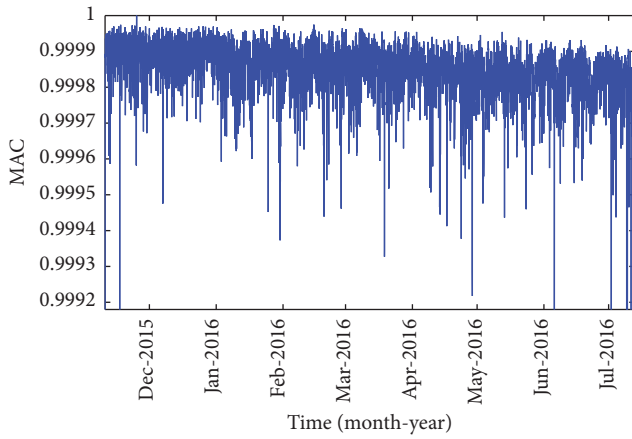
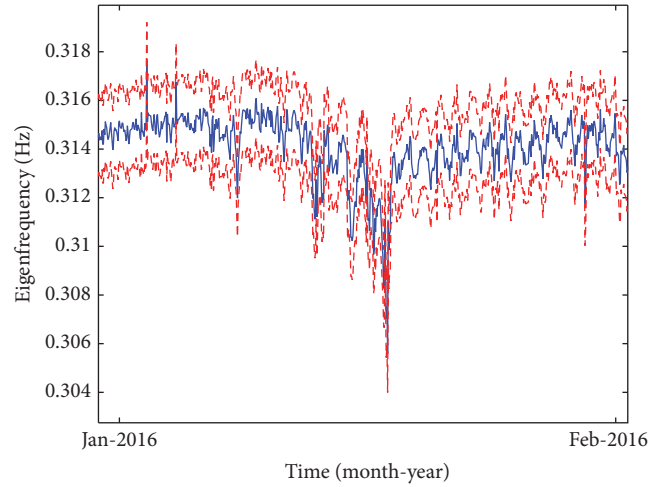


FIGURE 10: Time trend of the MAC of the first mode.

example, sun exposure, temperature, level of the aquifer, and wind speed and direction.

A first analysis showed that many environmental factors affect the building behaviour. Particularly, as already mentioned, the first natural frequencies can undergo shifts due to sun exposure, temperature, adjustments of the foundations, wind speed and direction, and so forth. The problem is quite complex and it is difficult to understand which parameters should be included in the empirical model for several reasons: firstly, only general information is available; for example, the authors do not have any temperature or radiation map but just a punctual value, while the acceleration sensors are distributed along the whole building. Secondly, it is important to understand which variables are correlated in order not to include them in the model and to avoid redundancy in the information. Finally, it has to be underlined that the available data do not come from a planned test but are related to the actual environmental conditions during the observation period. All these aspects make the problem difficult to approach; for this reason, the authors decided to try to reduce its complexity by considering few synthetic variables able to take into account the effect of most of the environmental parameters. To this purpose, the authors

FIGURE 11: Trend of the first eigenfrequency (solid blue curve) and $\pm 2\sigma$ interval (dashed red curves).

selected two quantities: the acceleration RMS and the value of the building inclination. Many correlation studies were carried out, showing the correlation between these synthetic parameters and the environmental factors. Finally, the authors chose as inputs of the empirical model the following three physical quantities which demonstrated no (or negligible) correlation:

- (i) The RMS A_{RMS} of the signal of the accelerometer placed in correspondence of the instrumented degree of freedom of the building with the highest mode shape component associated with the eigenfrequency considered. This allows automatically taking into account wind speed and direction. Obviously, the RMS is calculated on the frequency range of the mode considered
- (ii) Inclination at the 3rd floor underground of the building I_{-3} in east-west direction (about x -axis, see Figure 1) (see Figure 14(a)). This accounts for the possible foundation adjustments
- (iii) Inclination at the 30th floor of the building I_{30} in east-west direction (about x -axis, see Figure 1) (see Figure 14(b)). This accounts for sun exposure and temperature effects.

Linear regression was performed between each of the three eigenfrequencies and the three mentioned inputs. After the checks for the significance of the regression (e.g., check of the residues [47]), the model was further refined. Particularly the RMS of the accelerometer was replaced by its logarithm. Indeed, this allowed increasing significantly the correlation between the statistical model and the modal parameter values identified experimentally. Different indexes were used to quantify this correlation (e.g., PRESS [47]). Finally, the model used was

$$f_i = B_i I_{30} + C_i I_{-3} + D_i \log A_{\text{RMS}}, \quad (2)$$

where f_i is the i th eigenfrequency (with $i = 1, 2, 3$), while B_i , C_i , and D_i are the constants to be determined.

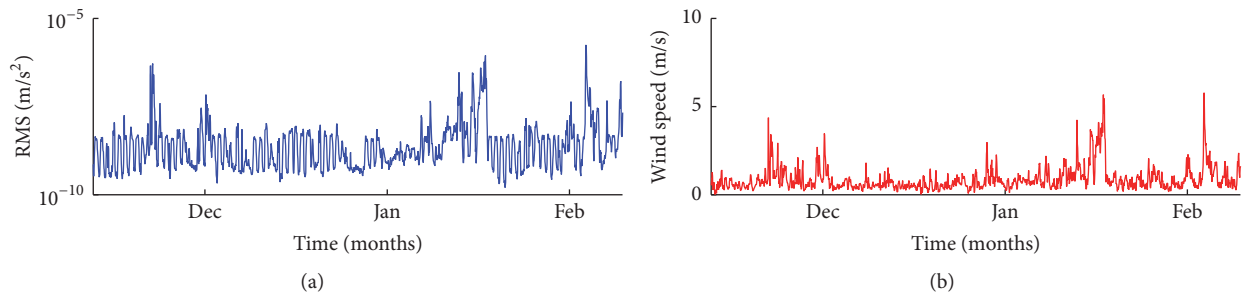


FIGURE 12: Trend of the vibration RMS (at floor 37 in x direction, see Figure 1) (a) and the corresponding wind speed (b).

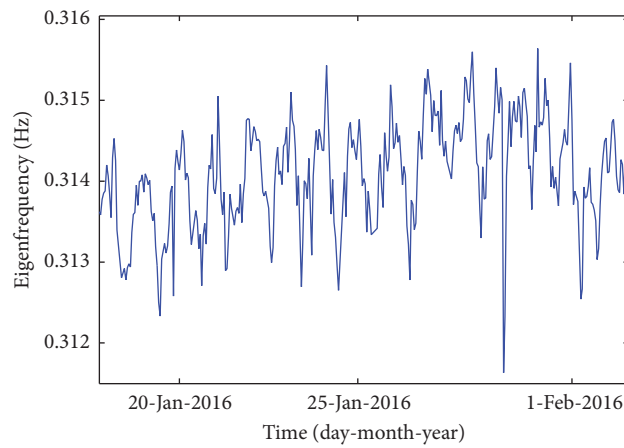


FIGURE 13: Trend of the first eigenfrequency where the daily changes are evident.

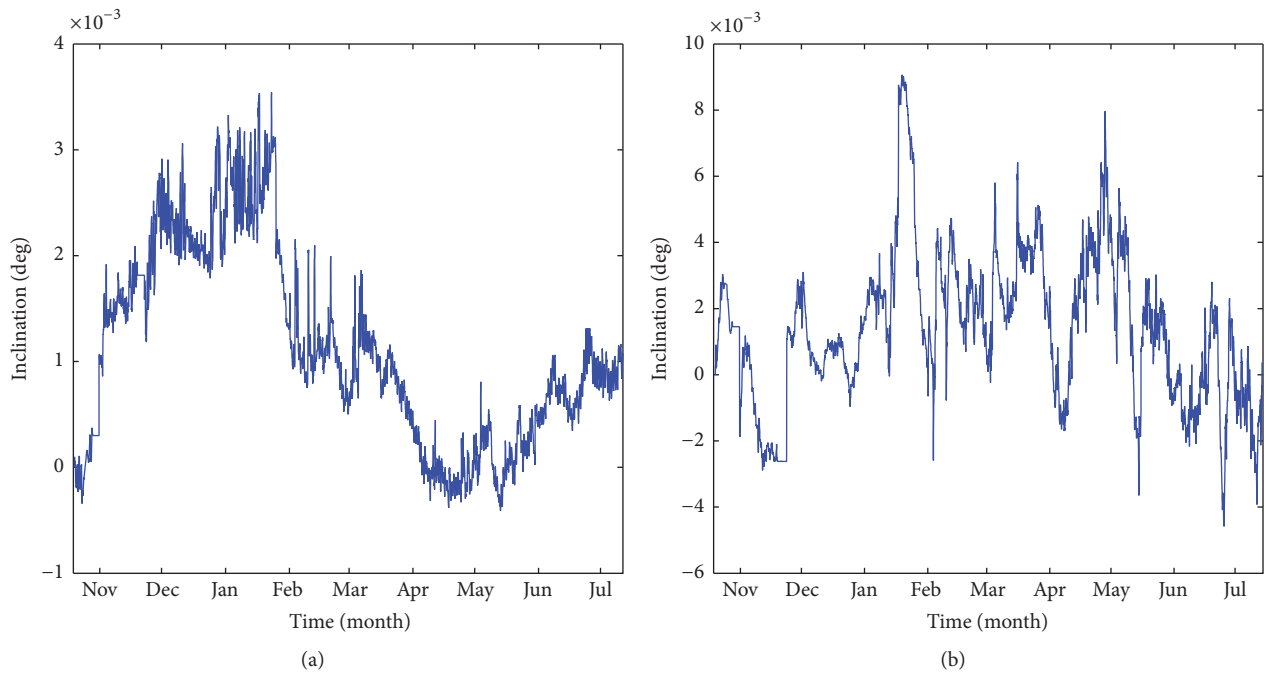


FIGURE 14: Trend of inclination (from a given reference value) between 2015 and 2016: inclinometer at the 3rd floor underground of the building in east-west direction (a) and at the 30th floor of the building in east-west direction (b).

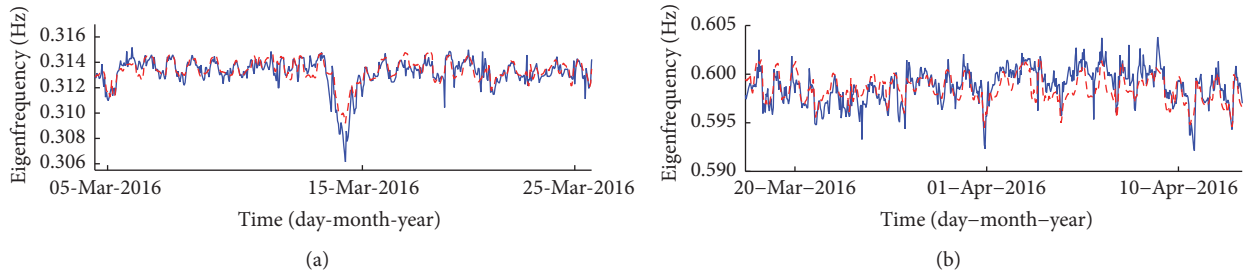


FIGURE 15: Trend of experimental (blue solid curves) and reconstructed (red dashed curves) eigenfrequencies: first eigenfrequency (a) and third eigenfrequency (b).

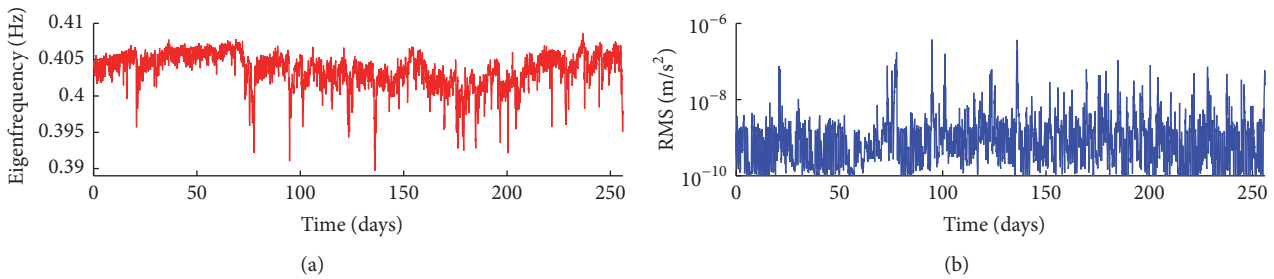


FIGURE 16: Experimental trend of the second eigenfrequency (a) and the vibration RMS at floor 37 in x direction (see Figure 1) calculated on the frequency range of the second eigenfrequency (b).

However, the correlation level must be further increased (and confidence intervals must be estimated [47]). To do this, more data are needed to find out all the possible input parameters that must be considered in the model as well as possible transformations (e.g., application of logarithm).

Nevertheless, the current version of the model shows a moderately satisfactory behaviour (see Figure 15). The sudden changes of the eigenfrequency value are shown to be mainly due to the acceleration RMS value (as already mentioned and as also evidenced by Figure 16, where the peaks of the vibration RMS correspond to sudden decreases of the eigenfrequency considered), while the values of inclination are able to properly describe the long-time trends (from daily trends to seasonal trends), as expected.

When more data coming from the system will be available, they will be used to further improve the model presented herein.

6. Conclusion

The paper has described the monitoring system installed and a proposed data analysis strategy for Palazzo Lombardia, one of the tallest buildings in Milano. The layout of the system is presented, highlighting the measured variables and therefore the data available for a health monitoring strategy.

An approach based on automatic and continuous modal parameter extraction has then been presented. The main features of the automatic modal analysis software used for modal identification are then provided, explaining how Markov Chain Monte Carlo simulations were used to optimise it.

This automatic identification system allowed producing the first plots of the trends of the modal parameters of the

building along eight months of monitoring. These modal parameters allowed the authors to develop a first-attempt empirical model to describe the relationship between the first three eigenfrequencies of the building and a number of input variables representative of the environmental conditions. The statistical model proved to be able to estimate the predicted values for the identified frequencies as a function of environmental conditions and therefore could be used (after its improvement) to detect anomalous trends indicating a change in the structure.

Conflicts of Interest

The authors declare that there are no conflicts of interest regarding the publication of this paper.

Acknowledgments

The authors wish to acknowledge the Lombardia Government authority and the people at CarboThermo group (facility manager) for the support given.

References

- [1] E. Mesquita, P. Antunes, F. Coelho, P. André, A. Arède, and H. Varum, "Global overview on advances in structural health monitoring platforms," *Journal of Civil Structural Health Monitoring*, vol. 6, no. 3, pp. 461–475, 2016.
- [2] D. Duarte, B. Marado, J. Nogueira, B. Serrano, V. Infante, and F. Moleiro, "An overview on how failure analysis contributes to flight safety in the Portuguese Air Force," *Engineering Failure Analysis*, vol. 65, pp. 86–101, 2016.

- [3] C. R. Farrar and K. Worden, *Structural Health Monitoring: A Machine Learning Perspective*, Wiley, 2012.
- [4] S. Da Silva, M. Todd, J. S. Sakellariou, and M. Ghandchi-Tehrani, "The use of vibration signals for structural health monitoring, system identification, test planning/optimization, and dynamic model validation/updates," *Shock and Vibration*, vol. 2016, Article ID 9581650, 2 pages, 2016.
- [5] O. S. Salawu, "Detection of structural damage through changes in frequency: a review," *Engineering Structures*, vol. 19, no. 9, pp. 718–723, 1997.
- [6] D. P. Patil and S. K. Maiti, "Detection of multiple cracks using frequency measurements," *Engineering Fracture Mechanics*, vol. 70, no. 12, pp. 1553–1572, 2003.
- [7] Z. Yang and Le Wang, "Structural damage detection by changes in natural frequencies," *Journal of Intelligent Material Systems and Structures*, vol. 21, no. 3, pp. 309–319, 2010.
- [8] A. K. Pandey, M. Biswas, and M. M. Samman, "Damage detection from changes in curvature mode shapes," *Journal of Sound and Vibration*, vol. 145, no. 2, pp. 321–332, 1991.
- [9] C. P. Ratcliffe, "A frequency and curvature based experimental method for locating damage in structures," *Journal of Vibration and Acoustics*, vol. 122, no. 3, pp. 324–329, 2000.
- [10] C. S. Hamey, W. Lestari, P. Qiao, and G. Song, "Experimental damage identification of carbon/epoxy composite beams using curvature mode shapes," *Structural Health and Monitoring*, vol. 3, no. 4, pp. 333–353, 2004.
- [11] M.-K. Yoon, D. Heider, J. W. Gillespie Jr., C. P. Ratcliffe, and R. M. Crane, "Local damage detection with the global fitting method using mode shape data in notched beams," *Journal of Nondestructive Evaluation*, vol. 28, no. 2, pp. 63–74, 2009.
- [12] G. Li, K. Hao, Y. Lu, and S. Chen, "A flexibility approach for damage identification of cantilever-type structures with bending and shear deformation," *Computers & Structures*, vol. 73, no. 6, pp. 565–572, 1999.
- [13] Z. G. Zhou, L. D. Wegner, and B. F. Sparling, "Vibration-based detection of small-scale damage on a bridge deck," *Journal of Structural Engineering—ASCE*, vol. 133, no. 9, pp. 1257–1267, 2007.
- [14] J. Li, B. Wu, Q. C. Zeng, and C. W. Lim, "A generalized flexibility matrix based approach for structural damage detection," *Journal of Sound and Vibration*, vol. 329, no. 22, pp. 4583–4587, 2010.
- [15] Z. Y. Shi, S. S. Law, and L. M. Zhang, "Structural damage localization from modal strain energy change," *Journal of Sound and Vibration*, vol. 218, no. 5, pp. 825–844, 1998.
- [16] N. Stubbs and J.-T. Kim, "Improved damage identification method based on modal information," *Journal of Sound and Vibration*, vol. 252, no. 2, pp. 223–238, 2002.
- [17] S. Choi, S. Park, N.-H. Park, and N. Stubbs, "Improved fault quantification for a plate structure," *Journal of Sound and Vibration*, vol. 297, no. 3-5, pp. 865–879, 2006.
- [18] G. Tondreau and A. Deraemaeker, "Numerical and experimental analysis of uncertainty on modal parameters estimated with the stochastic subspace method," *Journal of Sound and Vibration*, vol. 333, no. 18, pp. 4376–4401, 2014.
- [19] M. Ralbovsky, M. Kwapisz, and A. Vorwagner, "Uncertainty of bridge vibration properties and its consequence for damage identification," in *Proceedings of the 5th ECCOMAS Thematic Conference on Computational Methods in Structural Dynamics and Earthquake Engineering, COMPDYN 2015*, pp. 2545–2557, May 2015.
- [20] J. Kullaa, "Structural health monitoring under nonlinear environmental or operational influences," *Shock and Vibration*, vol. 2014, Article ID 863494, 9 pages, 2014.
- [21] G. Comanducci, F. Ubertini, and A. L. Materazzi, "Structural health monitoring of suspension bridges with features affected by changing wind speed," *Journal of Wind Engineering & Industrial Aerodynamics*, vol. 141, pp. 12–26, 2015.
- [22] N. Dervilis, H. Shi, K. Worden, and E. J. Cross, "Exploring environmental and operational variations in SHM data using heteroscedastic Gaussian processes," in *Proceedings of the 34th IMAC, Conference and Exposition on Structural Dynamics, 2016*, vol. 2, pp. 145–152, January 2016.
- [23] C. Devriendt, F. Preseznik, G. De Sitter et al., "Structural health monitoring in changing operational conditions using transmissibility measurements," *Shock and Vibration*, vol. 17, no. 4-5, pp. 651–675, 2010.
- [24] X. Zhu and H. Hao, "Development of an integrated structural health monitoring system for bridge structures in operational conditions," *Frontiers of Structural and Civil Engineering*, vol. 6, no. 3, pp. 321–333, 2012.
- [25] C. Rainieri and G. Fabbrocino, *Operational Modal Analysis of Civil Engineering Structures*, Springer, New York, NY, USA, 2014.
- [26] B. Peeters, H. Van Der Auweraer, P. Guillaume, and J. Leuridan, "The PolyMAX frequency-domain method: a new standard for modal parameter estimation?" *Shock and Vibration*, vol. 11, no. 3-4, pp. 395–409, 2004.
- [27] R. Brincker, L. Zhang, and P. Andersen, "Modal identification of output-only systems using frequency domain decomposition," *Smart Materials and Structures*, vol. 10, no. 3, pp. 441–445, 2001.
- [28] M. Berardengo, A. Cigada, S. Manzoni, and M. Vanali, "design and installation of a permanent monitoring system for Palazzo Lombardia in Milano, Italy," in *Proceedings of the VII European Congress on Computational Methods in Applied Sciences and Engineering - ECCOMAS Congress 2016*, pp. 3640–3651, Crete Island, Greece, June 2016.
- [29] A. Cigada, E. Mola, F. Mola, G. Stella, and M. Vanali, "Dynamic behavior of the palazzo lombardia tower: Comparison of numerical models and experimental results," *Journal of Performance of Constructed Facilities*, vol. 28, no. 3, pp. 491–501, 2014.
- [30] ISO2631-1, *Mechanical vibration and shock - Evaluation of Human Exposure to Whole-Body Vibration - Part 1: General Requirements*, 1997.
- [31] L. G. Griffis, "Serviceability limit states under wind load," *Engineering Journal*, vol. 30, no. 1, pp. 1–16, 1993.
- [32] P. Mendis, T. Ngo, N. Haritos, A. Hira, B. Samali, and J. Cheung, "Wind loading on tall buildings," *Electronic Journal of Structural Engineering Special Issue: Loading on Structures*, vol. 3, pp. 41–54, 2007.
- [33] G. Busca, A. Cigada, E. Mola, F. Mola, and M. Vanali, "Dynamic testing of a helicopter landing pad: Comparison between operational and experimental approach," *Journal of Civil Structural Health Monitoring*, vol. 4, no. 2, pp. 133–147, 2014.
- [34] S. Campagnari, F. di Matteo, S. Manzoni, M. Scaccabarozzi, and M. Vanali, "Estimation of axial load in tie-rods using experimental and operational modal analysis," *Journal of Vibration and Acoustics*, vol. 139, no. 4, article 041005, 2017.
- [35] G. James III, T. Carne, and J. Lauffer, "The natural excitation technique (next) for modal parameter extraction from operating structures," *The International Journal of Analytical and Experimental Modal Analysis*, vol. 10, no. 4, pp. 260–277, 1995.

- [36] F. Ubertini, C. Gentile, and A. L. Materazzi, "Automated modal identification in operational conditions and its application to bridges," *Engineering Structures*, vol. 46, pp. 264–278, 2013.
- [37] T. Wang, O. Celik, F. N. Catbas, and L. M. Zhang, "A frequency and spatial domain decomposition method for operational strain modal analysis and its application," *Engineering Structures*, vol. 114, pp. 104–112, 2016.
- [38] C. Devriendt and P. Guillaume, "Identification of modal parameters from transmissibility measurements," *Journal of Sound and Vibration*, vol. 314, no. 1-2, pp. 343–356, 2008.
- [39] A. Brandt, M. Berardengo, S. Manzoni, and A. Cigada, "Harmonic scaling of mode shapes for operational modal analysis," in *Proceedings of the ISMA 2016 - International Conference on Noise and Vibration Engineering and USD2016 - International Conference on Uncertainty in Structural Dynamics*, pp. 2809–2818, Leuven, Belgium, September 2016.
- [40] C. Rainieri and G. Fabbrocino, "Development and validation of an automated operational modal analysis algorithm for vibration-based monitoring and tensile load estimation," *Mechanical Systems and Signal Processing*, vol. 60, pp. 512–534, 2015.
- [41] D. J. Ewins, *Modal testing: Theory, Practice and Application*, Baldock: Research Studies Press Ltd., 2nd edition, 2000.
- [42] J. S. Bendat and A. G. Piersol, *Engineering Applications of Correlation and Spectral Analysis*, Wiley-Interscience, New York, NY, USA, 1993.
- [43] A. Brandt, *Noise and Vibration Analysis—Signal Analysis and Experimental Procedures*, John Wiley & Sons, Chichester, UK, 2011.
- [44] G. D'Antona and A. Ferrero, *Digital Signal Processing for Measurement Systems: theory and Applications (Information Technology: Transmission, Processing and Storage)*, Springer, New York, NY, USA, 2006.
- [45] JCGM 100:2008, *Evaluation of Measurement Data—Guide to the Expression of Uncertainty in Measurement*, 2008.
- [46] JCGM101:2008, *Evaluation of Measurement Data—Supplement 1 to the Guide to the Expression of Uncertainty in Measurement—Propagation of Distributions Using a Monte Carlo Method*, 2008.
- [47] D. C. Montgomery, *Design and Analysis of Experiments*, John Wiley & Sons, 7th edition, 2009.

Research Article

Damage Identification of a Derrick Steel Structure Based on the HHT Marginal Spectrum Amplitude Curvature Difference

Dongying Han,¹ Shimin Wei,¹ Peiming Shi,² Ying Zhang,³ Kai Gao,¹ and Nengyuan Tian¹

¹School of Vehicles and Energy, Yanshan University, Qinhuangdao 066004, China

²School of Electrical Engineering, Yanshan University, Qinhuangdao 066004, China

³School of Electrical and Computer Engineering, Georgia Institute of Technology, Atlanta, GA 30332, USA

Correspondence should be addressed to Dongying Han; dongying.han@163.com

Received 25 April 2017; Revised 18 July 2017; Accepted 7 August 2017; Published 17 September 2017

Academic Editor: Giada Gasparini

Copyright © 2017 Dongying Han et al. This is an open access article distributed under the Creative Commons Attribution License, which permits unrestricted use, distribution, and reproduction in any medium, provided the original work is properly cited.

For the damage identification of derrick steel structures, traditional methods often require high-order vibration information of structures to identify damage accurately. However, the high-order vibration information of structures is difficult to acquire. Based on the technology of signal feature extraction, only using the low-order vibration information, taking the right front leg as an example, we analyzed the selection of HHT marginal spectrum amplitude and the calculation process of its curvature in practical application, designed the damage conditions of a derrick steel structure, used the index and intrinsic mode function (IMF) instantaneous energy curvature method to perform the damage simulation calculation and comparison, and verified the effect of identifying the damage location in a noisy environment. The results show that the index can accurately determine the location of the damage element and weak damage element and can be used to qualitatively analyze the damage degree of the element; under the impact load, the noise hardly affects the identification of the damage location. Finally, this method was applied to the ZJ70 derrick steel structure laboratory model and compared with the IMF instantaneous energy curvature method. We verified the feasibility of this method in the damage location simulation experiment.

1. Introduction

Derrick steel structures play an important role in the oil and gas exploration and development [1, 2]. During long-term service, because of various factors such as disassembly and corrosion, damage inevitably occurs, which gradually reduces the safety performance and carrying capacity of the derrick steel structures and forms security risks [3–5]. In recent years, the damage detection method based on structural signal feature extraction [6, 7] has attracted the attention of many scholars; this method mainly uses the vibration signal from the vibration sensors to collect structural damage. Using signal-processing methods, the appropriate damage-sensitive indicators are analyzed, and further structural-damage identification or health monitoring is realized [8].

Huang et al. proposed Hilbert-Huang transform (HHT) method, which is a new, self-adaptive frequency analysis method [9], and included the empirical mode decomposition (EMD) and Hilbert transform (HT); the core is the

EMD. Chen et al. used the instantaneous frequency of IMFs (intrinsic mode functions) as the component damage index of structure damage detection [10–12]. Pines and Salvino combined the EMD with Hilbert transform to obtain the phase of the component signals and used the phase information of different degrees of freedom to identify the structure damage [13]. Li et al. [14] used the method of wavelet analysis to analyze the maximum energy of the intrinsic mode functions (IMFs) component, which includes the wavelet coefficients for damage identification. Cheraghi and Taheri [15] analyzed the energy of the IMF component signal, selected the effective characteristic information as the damage sensitivity index, and applied it to identify the pipeline structure damage. Rezaei and Taheri [16, 17] used the energy of the first-order IMF component after the decomposition of the signal EMD as a damage sensitivity index to diagnose the damage of the pipeline structure. Chen et al. proposed to show the status of damage material wing box of the material of the feature vector-relative variation of the instantaneous frequency [18].

Cao et al. [19] proposed a structural-damage early-warning method based on the EMD, where the structure before and after damage in the component of the IMF's energy distribution changes as the damage-sensitive index, and applied the method to model Health Monitoring Benchmark structure damage identification. Ren et al. [20] applied the improved HHT method to the damage identification of engineering structures and proposed the method to identify the damage location of the structure using the structural before and after the damage in the first-order response to a first-order IMF feature energy ratio. Wang et al. applied the method to the bridge structure. The HHT theory has not been used in complex structures, such as derrick steel structures, but it has been used in simple structures in the literature [21]. Li et al. applied the method to the crack identification of the rotor [22]. This paper realized the damage identification of the derrick steel structure based on the HHT marginal spectrum amplitude curvature difference and only used a low-level vibration information structure. The simulation calculated the damage identification of the derrick and compared it with the IMF instantaneous energy curvature difference. Finally, the feasibility of the method was verified with derrick damage location simulation experiments.

2. HHT Marginal Spectrum Amplitude Curvature

2.1. HHT Theory. The HHT method consists of two parts: EMD and HT. The original signal $x(t)$ is decomposed into a series of IMFs and a residual function by EMD:

$$x(t) = \sum_{i=1}^n c_i + r_n. \quad (1)$$

Hilbert transformation of the IMF component:

$$\hat{c}_i = \frac{1}{\pi} \int_{-\infty}^{+\infty} \frac{c_i(\tau)}{t - \tau} d\tau. \quad (2)$$

Based on this function, the analytic signal is established, and the instantaneous amplitude and phase function are obtained:

$$\begin{aligned} z_i &= c_i + j\hat{c}_i = a_i e^{j\varphi_i}, \\ a_i &= \sqrt{c_i^2 + \hat{c}_i^2}, \\ \varphi_i &= \arctan \frac{\hat{c}_i}{c_i}. \end{aligned} \quad (3)$$

The instantaneous frequency is defined as the derivative of the instantaneous phase:

$$\omega_i = \frac{d\varphi_i}{dt}. \quad (4)$$

Signal $x(t)$ can be expressed as

$$x(t) = \text{RE} \sum_{i=1}^n a_i e^{j\varphi_i} = \text{RE} \sum_{i=1}^n a_i e^{j \int \omega_i dt}. \quad (5)$$

Here, we ignore the residual component of the original signal r_n ; RE denotes the real part. We call the above formula on the right part of the equal sign the Hilbert spectrum:

$$H(\omega, t) = \text{RE} \sum_{i=1}^n a_i(t) e^{j \int \omega_i(t) dt}. \quad (6)$$

Hilbert marginal spectrum is obtained by integrating the above formula with time:

$$h(\omega) = \int_0^T H(\omega, t) dt. \quad (7)$$

2.2. HHT Marginal Spectrum Amplitude Curvature. After the structure is applied to the vibrational excitation, the vibration response signal of different parts of the structure is extracted. After the signal is decomposed by the EMD, a series of IMF components is obtained, the main IMF component is selected, and the marginal spectrum amplitude is calculated. Then, the relative HHT marginal spectrum amplitude at different parts of the structure is

$$R_i = \frac{F_i}{F_0}, \quad (8)$$

where F_i is the HHT marginal spectrum of different parts of the structure and F_0 is the HHT marginal spectrum of the structure reference position.

The HHT marginal spectrum amplitude curvature of different parts of structures is approximately calculated by the central difference method:

$$\Phi_i = \frac{R_{i+1} - 2R_i + R_{i-1}}{l^2}, \quad (9)$$

where R_i is calculated at the site of the relative HHT marginal spectrum amplitude, R_{i+1} and R_{i-1} are calculated at the sites adjacent to the relative HHT marginal spectrum amplitude, and l is the distance between adjacent parts.

The difference in HHT marginal spectrum amplitude curvature is

$$\Delta\Phi_i = \Phi_{ui} - \Phi_{di}, \quad (10)$$

where Φ_{ui} is the HHT marginal spectrum amplitude curvature before structural damage.

3. Extracting the Signal Characteristics of the Derrick Steel Structure

3.1. Establishment of the Simulation Model of the Derrick Steel Structure. The model of the derrick steel structure is 2.951 m high, and the maximum hook load is 13.9 kN. Its material is Q235 steel. The structure was divided into 274 elements and 142 nodes, and its finite-element model is shown in Figure 1. The right front pillar nodes of the derrick steel structure were numbered 1–20 from the bottom. There was one element between every two nodes, and the elements were numbered 1–19 from the bottom to the top.

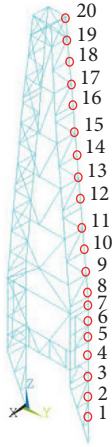


FIGURE 1: Finite-element model of the derrick steel structure.

3.2. Derrick Steel Structure Model Analysis. The modal analysis of the model shows that the first three orders of the frequency were 17.53, 18.0, and 38.71 Hz. The first-order vibration mode was mainly the left-and-right first-order bending overall vibration; the second-order vibration mode was mainly the front-and-back first-order bending overall vibration; the third-order vibration mode was mainly torsional vibration.

We used a random-noise acceleration load in the vibration model of the derrick steel structure; the sampling frequency of the random-noise acceleration loads was 1000 Hz; the amplitude was 1.2 m/s^2 ; and the load acted on node 20 along the direction of y -axis for 2 s. We used the complete method to solve the transient dynamics, and the acceleration response of nodes 1–20 of the right front pillar of the derrick steel structure in the y direction was extracted.

3.3. Extracting the HHT Marginal Spectrum Amplitude Curvature. Our example structure has 15 nodes. The acceleration response of the Fourier spectral analysis in Figure 2 shows that random loads can stimulate the first- and third-order frequencies (17.53 Hz and 38.71 Hz) in the derrick steel structure, and the first-order vibration is prioritized.

Considering the complexity of the derrick steel structure, the nodes in the lower part of the derrick steel structure cannot stimulate the third-order frequency under a random load. Therefore, we used the bandpass filter and HHT combination of methods to extract the first-order vibration information of the derrick steel structure and determine the cut-off frequency of 17 Hz and 18 Hz. We filtered the other frequency components using the EMD decomposition, as shown in Figure 3.

Figure 3 shows that the main characteristic information of the signal is concentrated in the first-order IMF component; therefore, we only extracted the marginal spectrum amplitude of the first-order IMF component. The marginal spectrum of the first-order IMF component of node 15 is shown in Figure 4. We could extract the marginal spectrum amplitude of the derrick steel structure from its vibration in

TABLE 1: Damage condition of the derrick steel structure.

Condition	Damage degree	Damage type	Damage position
1	5%		16
2	20%	Single damage	10
3	30%		5
4	5%		8, 14
5	10%	Double damage	5, 13
6	5%, 10%		5, 13

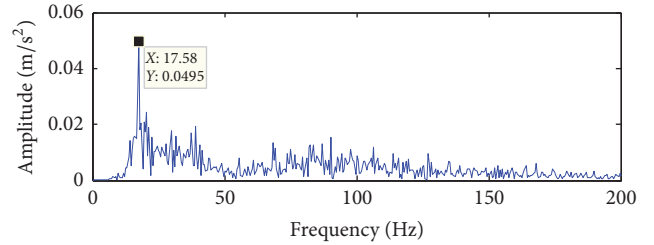


FIGURE 2: Spectral analysis of the acceleration response of node 15 in the derrick steel structure.

the first-order frequency. In the derrick, we selected node 1 as the reference point and calculated the HHT marginal spectrum amplitude curvature of nodes 1–20.

4. Simulation Analysis

4.1. Damage Condition Design. In the practical condition of the derrick steel structure, damage most likely occurs in the front pillar, so we selected the right front pillar of the derrick steel structure for the study. Damage was set up in two cases: single damage and double damage. Damage can be achieved by reducing the stiffness of the element, and the specific damage conditions are shown in Table 1.

4.2. Identifying Damage Location. The nonstationary signal can be decomposed into an intrinsic mode function (IMF) and a residual function by empirical modal decomposition. Each component of the IMF contains the local characteristics of different time scales in the original signal. The IMF instantaneous energy reflects the change over time of each component. To verify the effectiveness of this method, we used the HHT marginal spectrum amplitude curvature difference and IMF instantaneous energy curvature difference to identify the damage location under six damage conditions. We calculated the derrick steel structure in good conditions and six damage conditions of the HHT marginal spectrum amplitude curvature and IMF instantaneous energy curvature of nodes 1–20. Then, we compared our results with the corresponding node of curvature difference before and after the derrick steel structure was damaged. The sensor is disturbed by external noise in practical conditions, so we verified the effect of identifying the damage location in a noisy environment.

The above analysis is shown in Figure 5. Figures 5(a)–5(d) show the single-damage conditions, where elements 16, 10,

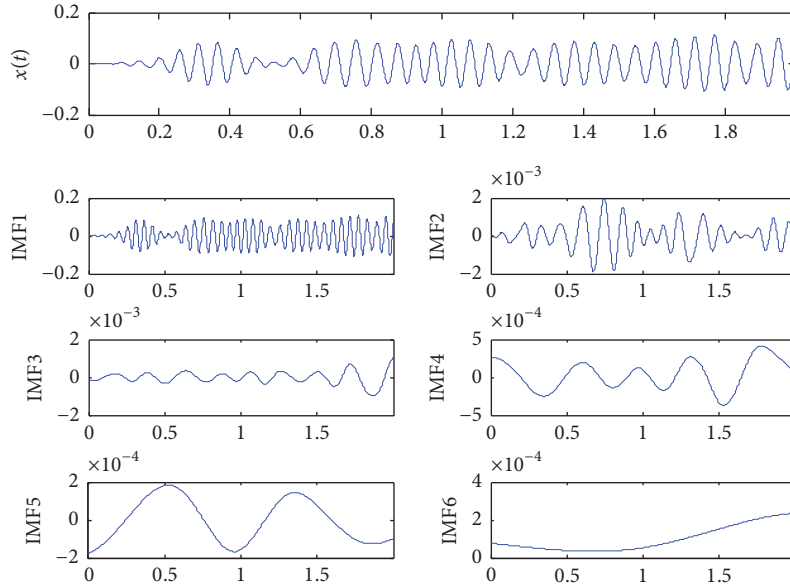


FIGURE 3: First-order vibration response of node 15 in the derrick steel structure and EMD.

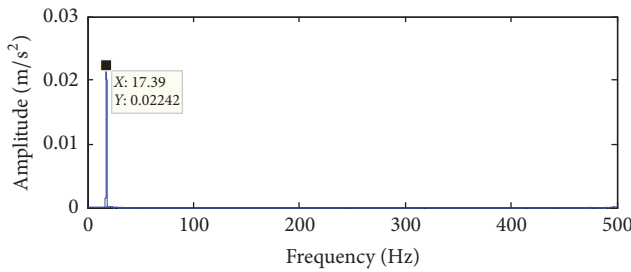


FIGURE 4: First-order IMF component marginal spectrum of node 15 in the derrick steel structure.

and 5 were clearly damaged. Figures 5(a) and 5(d) show the 5% damage condition of element 16. Figure 5(e) is the relation curve between the HHT marginal spectrum curvature difference and the node in 10% random noise of damaged element 5; Figures 5(f)–5(i) show the double-damage conditions. We can clearly identify the position of the upper and lower parts of the damaged element in the pillar. Figures 5(g) and 5(h) compare the same damage location with different degrees of damage, and the upper part of the damage element in the pillar of Figure 5(h) is easier to identify than that in Figure 5(g). Figure 5(j) is the relation curve between the HHT marginal spectrum curvature difference and the node in 10% random noise of damaged elements 5 and 13. The comparison shows that the noise under the impact load hardly affected the damage location identification of the derrick steel structure. Therefore, both methods can identify the damage location of the derrick, and the rule based on the HHT method is as follows. The HHT marginal spectrum amplitude curvature difference of the damaged element at two ends of the node mutates, and neighboring nodes have opposite signs. The absolute value of one curvature difference of the node is the maximum of nearby nodes, which can

make the HHT marginal spectrum curvature difference of adjacent nodes increase. For the double-damaged places, the HHT marginal spectrum amplitude curvature difference is sensitive to the lower part of the damaged element of the pillar identification. When the damaged position is identical, with the increase in damage degree, it is easier to identify the position of the upper damaged element, and the position of the weakly damaged element can be correctly identified.

4.3. Damage Degree Identification. Supposing that the stiffness of element 13 of the right front pillar of the derrick steel structure successively was reduced by 5%, 10%, 15%, 20%, 25%, 30%, 35%, 40%, 45%, and 50%, we calculated the HHT marginal spectrum amplitude curvature difference of node 13 of element 13 at the corresponding damage degree. Figure 6 shows the histogram of the relationship between the absolute value of the HHT marginal spectrum amplitude curvature difference and the damage degree.

Figure 6 shows that the absolute value of the HHT marginal spectrum amplitude curvature difference of node 13 increases with the increase in damage degree. Therefore, we can qualitatively analyze the damage degree of a derrick steel structure based on the HHT marginal spectrum amplitude curvature difference.

5. Experimental Analysis

5.1. Damage Location Simulation and Sensor Layout. The ZJ70-type derrick steel structure laboratory model was made according to the prototype equipment of a 7000 m drilling rig with a proportion of 1:18. The model is a front-opening model with beam pillars and is divided into four segments. The upper part is the overall structure of the closed segment; the other three segments have a front-opening shape of “ \cap .” The components of the main body are connected with pins, and its physical model is shown in Figure 7.

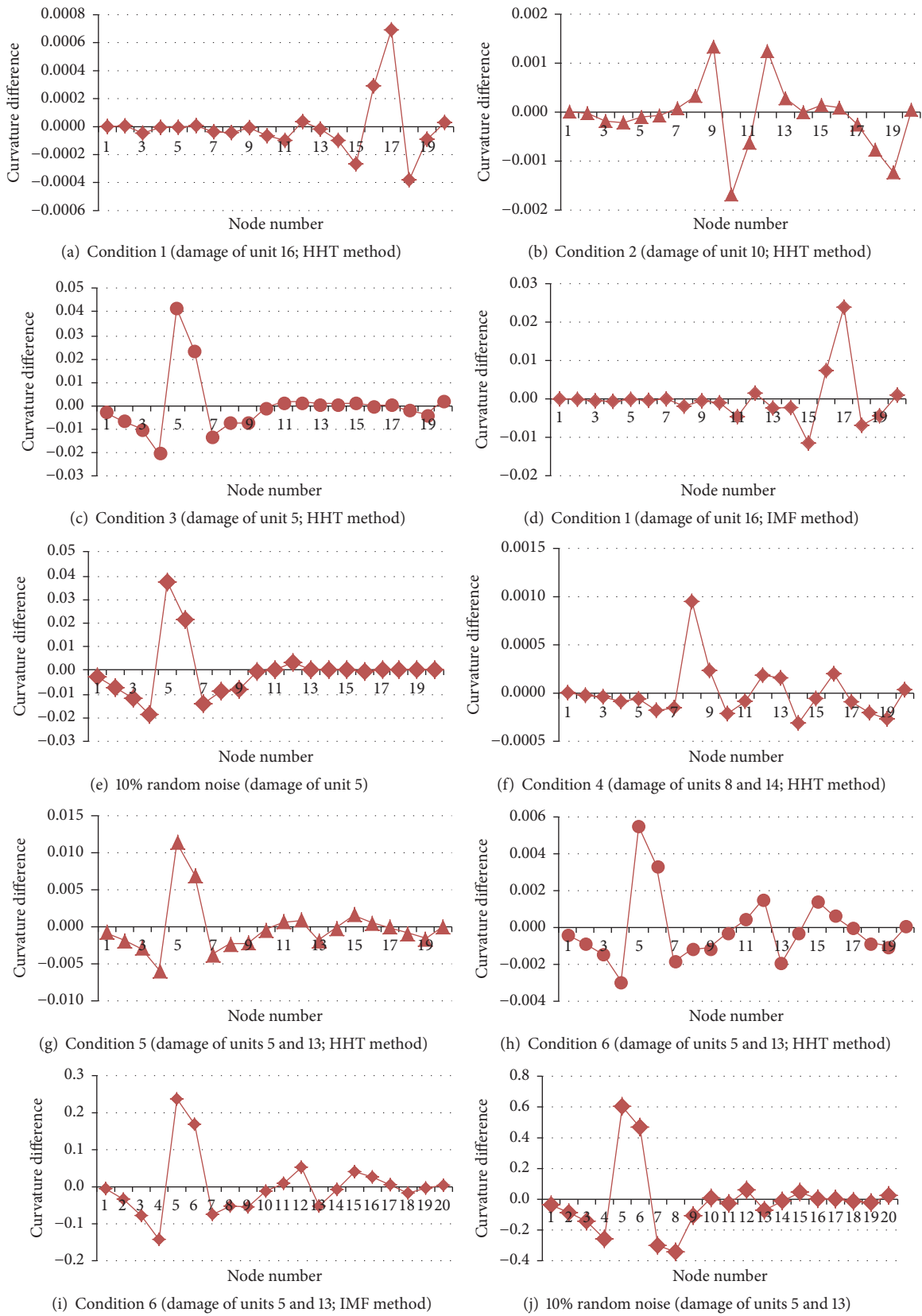


FIGURE 5: Relationship between the difference of the HHT marginal spectrum curvature and the nodes.

TABLE 2: Damage experimental conditions of the derrick steel structure.

Condition	Damage form	Damage type	Damage position
1	Pin loose	Single damage	The place between second segment and third segment
2		Single damage	The place between third segment and forth segment
3		Double damage	Integrating the first two kinds of damage location

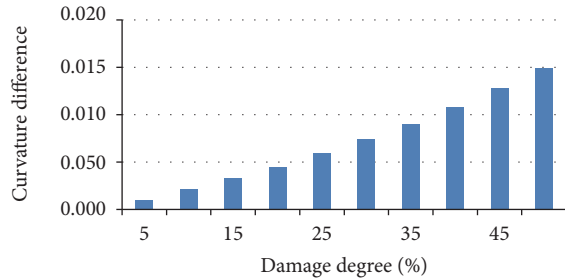


FIGURE 6: Relationship between the difference of the HHT marginal spectrum curvature and the damage degree.



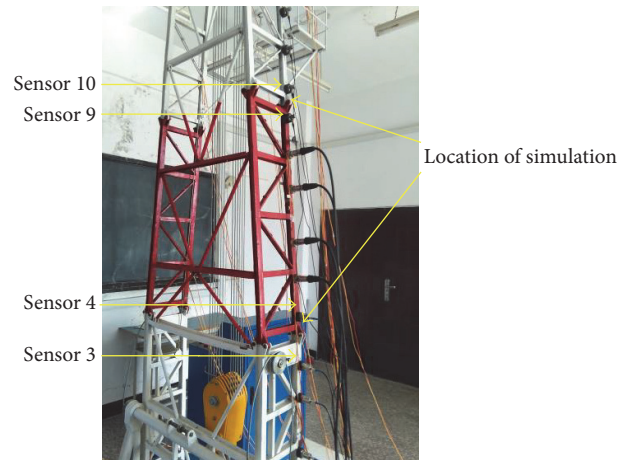
FIGURE 7: Laboratory model of the ZJ70-type derrick steel structure.

We numbered the segments of the derrick steel structure number as 1–4 from top to bottom. Because of the limited conditions, the experiment of the derrick steel structure was based on one of the two front-opening pillars as the object of study, and the damage forms are simulated by loosening the pin between two segments. We simulated 3 damage conditions. The specific damage conditions are shown in Table 2.

In the experiment, 12 acceleration sensors were used to collect the vibration signals of different parts of the derrick steel structure. The sensors were numbered 1–12 from top to bottom. Conditions 1 and 2 simulated the damage between sensors 6 and 7; Condition 3 simulates the damage between sensors 3 and 4 and the damage between sensors 9 and 10. Figure 8 shows the measured distance between adjacent acceleration sensors under three damage conditions. When we calculated the HHT marginal spectrum amplitude curvature, we selected sensor 1 as the reference point.



(a) Single damage



(b) Double damage

FIGURE 8: Damage location simulation and sensor layout.

5.2. Experimental Signal Acquisition. The vibration excitation mode in the experiments was marked to ensure that the vibration position was identical before and after the simulation of the derrick steel structure. The 12 sensors simultaneously collected the vibration signal of the derrick steel structure; the interface shows the time-domain signal window in real time and 12 channels. To easily observe the signal collected by each sensor, Figure 9 is based on Condition 1 as an example, and we intercepted the time-domain signal of sensors 1–12 of the derrick steel structure before it became damaged.

5.3. Analysis of Experimental Results. We calculated the HHT marginal spectrum amplitude curvature difference and IMF instantaneous energy curvature difference of the derrick steel

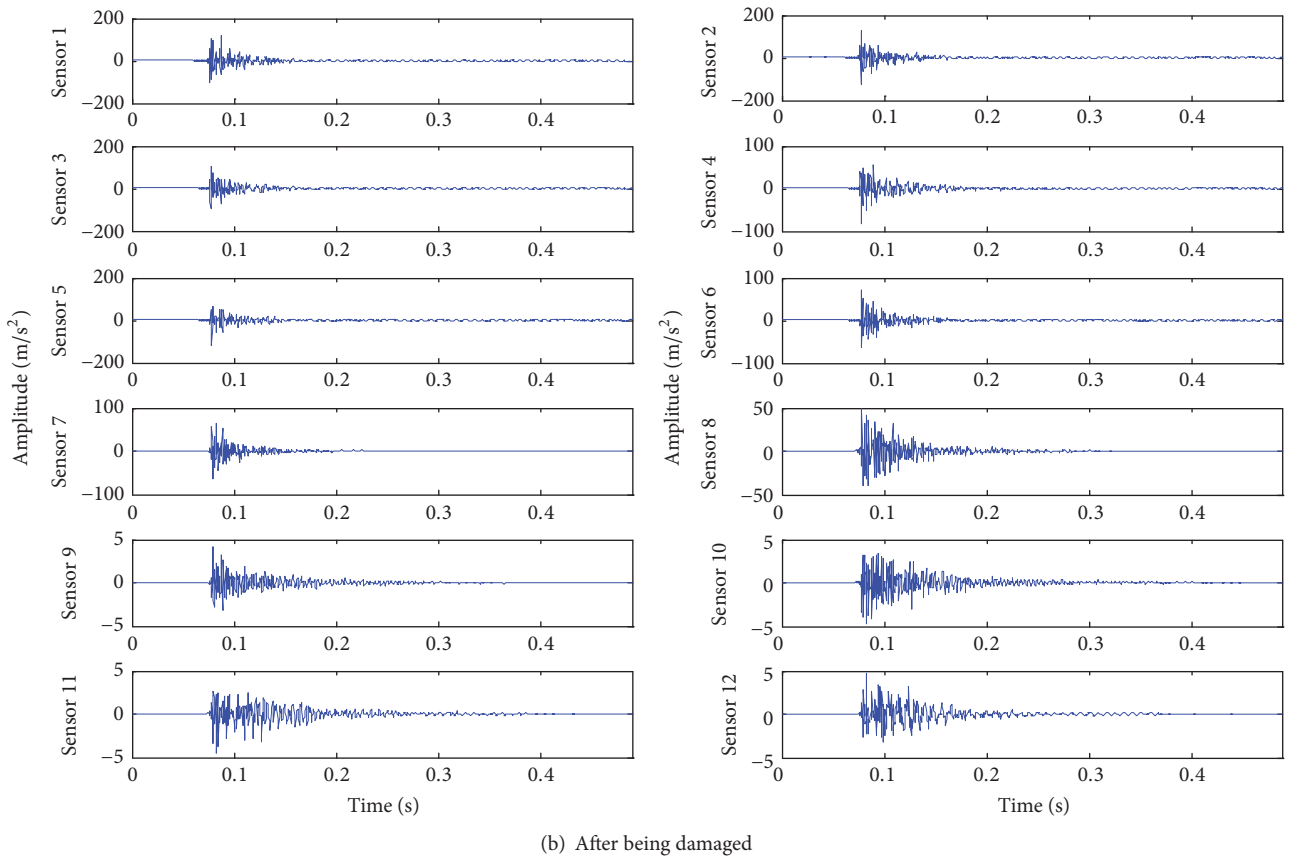
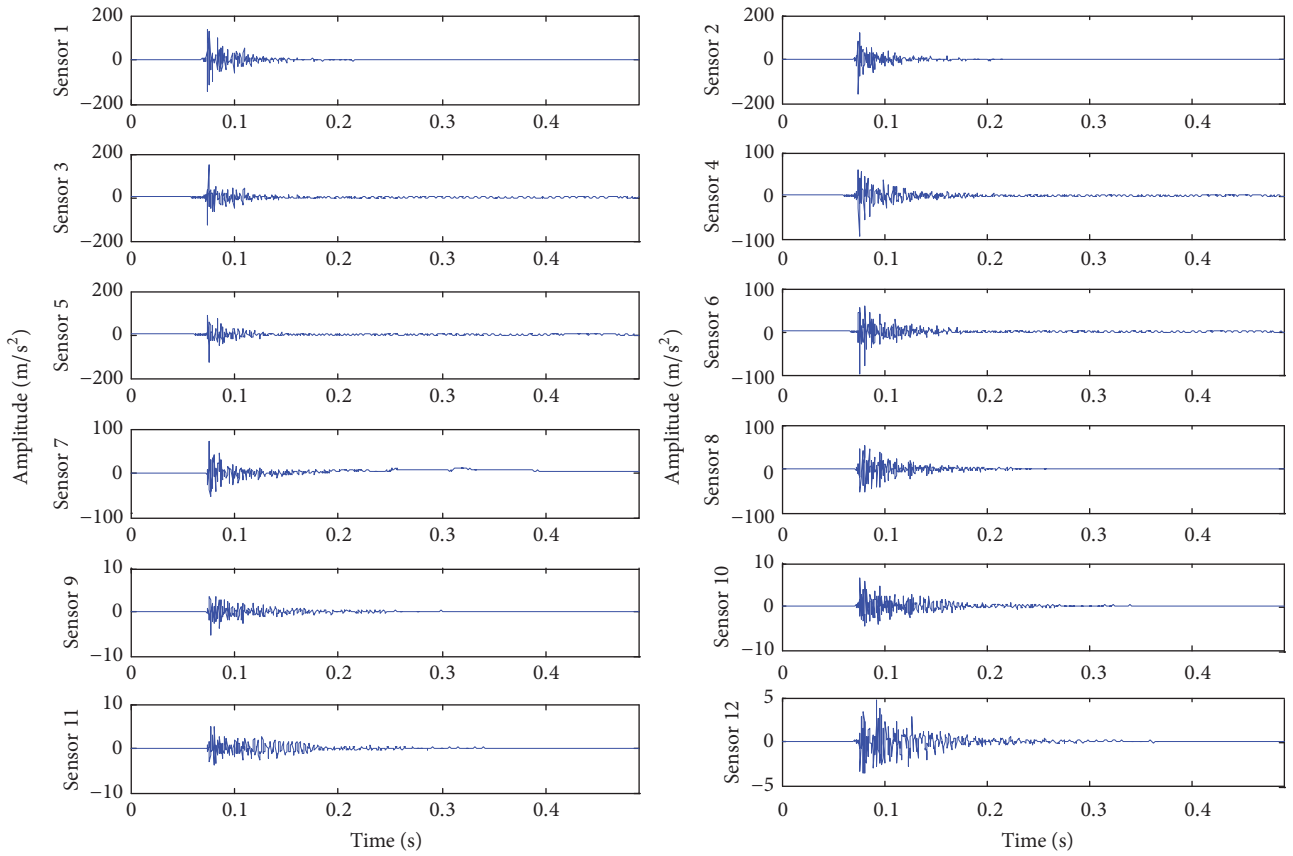


FIGURE 9: Time-domain signal of sensors 1–12 before and after the damage of the derrick steel structure under Condition 1.

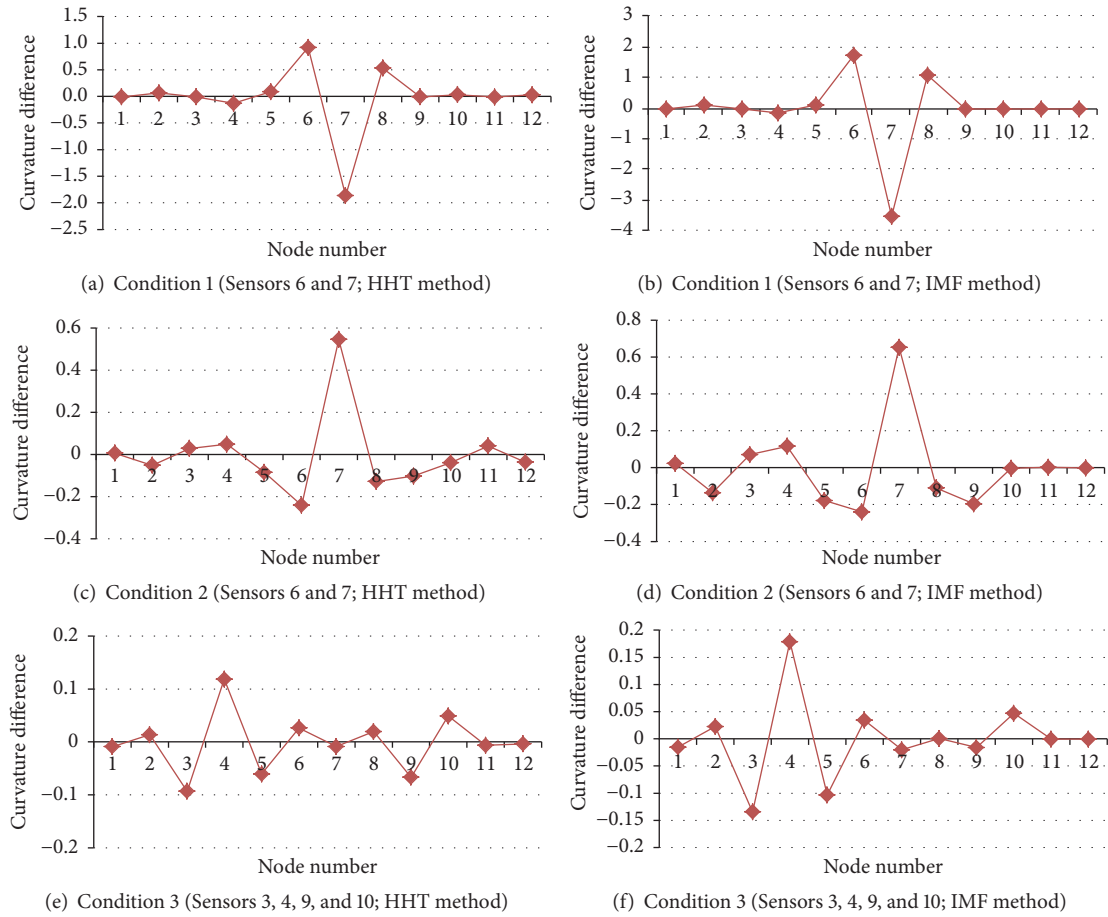


FIGURE 10: Relationship between the HHT marginal spectrum curvature difference or IMF instantaneous energy curvature difference and the sensors.

structure in three conditions and show its relationship with sensors 1–12 in Figure 10.

In conditions 1 and 2, the derrick steel structure was simulated with single damage. Figures 10(a) and 10(b) show the significant mutations of the damage sensitivity index of sensors 6 and 7, which is consistent with the presupposition of damage position. Therefore, the single damage of the derrick steel structure can be accurately identified based on the HHT marginal spectrum amplitude curvature difference and IMF instantaneous energy curvature difference. Condition 3 simulates the double damage of the derrick steel structure. Figure 10(c) clearly shows that the damage-sensitive index of sensors 3 and 4 mutated and significantly changed. Sensors 9 and 10 had the largest amplitude of variation of the damage-sensitive index with the adjacent value, which is also consistent with the preset double-damage position. Therefore, the double-damage position of the derrick steel structure can also be identified by the damage sensitivity index.

6. Conclusions

Vibration sensors have been widely studied and applied to collect vibration signals to detect the structural state of damage in health-monitoring technology. We only used the

low-level vibration information of the derrick steel structure to propose a damage identification method for derrick steel structures based on the HHT marginal spectrum amplitude curvature difference.

(1) The HHT marginal spectrum amplitude curvature difference is related to the position of damaged elements. From the comparison with IMF instantaneous energy curvature difference, the position of damaged elements and the weak damage of the derrick steel structure can be accurately identified based on the HHT marginal spectrum amplitude curvature difference.

(2) The HHT marginal spectrum amplitude curvature difference can qualitatively analyze the damage degree of the elements, and the larger absolute value of the HHT marginal spectrum amplitude curvature difference between two ends of the damaged element increases with the increase in damage degree of the element.

(3) The simulation experiment of the damage location of the derrick steel structure shows that the damage identification method for derrick steel structures based on the HHT marginal spectrum amplitude curvature difference and IMF instantaneous energy curvature difference can extract the low-level vibration information. Thus, we can correctly identify the location of damaged elements and easily obtain

the low-level vibration information of derrick steel structures in practice, which indicates that the method is reliable and easy to operate.

Conflicts of Interest

The authors declare that there are no conflicts of interest regarding the publication of this paper.

Acknowledgments

This work was supported by Hebei Provincial Natural Science Foundation of China (no. E2015203190) and Key Project of Natural Science Research in Colleges and Universities of Hebei Province (Grant no. ZD2015050).

References

- [1] D. Han, Z. Li, and G. Zhou, "Simulation model for ultimate bearing capacity of in-service oil drilling derrick," *Shiyou Xuebao/Acta Petrolei Sinica*, vol. 28, no. 2, pp. 120–128, 2007.
- [2] J. Liu, G. Zhou, and G. Han, "Simulation model for in-service rig derrick based on finite dynamic model," *Shiyou Xuebao/Acta Petrolei Sinica*, vol. 30, no. 5, pp. 788–792, 2009.
- [3] D. D. Bueno, C. R. Marqui, V. Lopes Jr., M. J. Brennan, and D. J. Inman, "Structural damage identification and location using grammian matrices," *Shock and Vibration*, vol. 19, no. 3, pp. 287–299, 2012.
- [4] D.-Y. Han and P.-M. Shi, "Damage identification of derrick steel structures based on frequency and equivalent damage coefficient," *Gongcheng Lixue/Engineering Mechanics*, vol. 28, no. 9, pp. 109–114, 2011.
- [5] H. Dongying and S. Peiming, "Identification of derrick steel structures damage based on frequency and bp neural network," *China Safety Science Journal*, vol. 18, no. 10, pp. 118–123, 2008.
- [6] Z. Qu, S. Jin, H. Feng, Z. Zeng, Y. Zhou, and J. Li, "Multi-scale chaotic characteristic analysis of detection signals in pipeline pre-warning system based on empirical mode decomposition," *Shiyou Xuebao/Acta Petrolei Sinica*, vol. 29, no. 2, pp. 313–316, 2008.
- [7] Y. Zhang, S. Jin, J. He, S. Chen, and J. Li, "Extraction method for pipeline leakage feature based on dynamic pressure signal," *Shiyou Xuebao/Acta Petrolei Sinica*, vol. 31, no. 2, pp. 338–342, 2010.
- [8] J. Sun, S. Jin, and J. Sun, "Monitoring and pre-warning system for security of pipelines based on data fusion of multi-seismic sensors," *Shiyou Xuebao/Acta Petrolei Sinica*, vol. 30, no. 3, pp. 465–468, 2009.
- [9] N. E. Huang, Z. Shen, S. R. Long et al., "The empirical mode decomposition and the Hilbert spectrum for nonlinear and non-stationary time series analysis," *The Royal Society of London. Proceedings. Series A. Mathematical, Physical and Engineering Sciences*, vol. 454, no. 1971, pp. 903–995, 1998.
- [10] H. G. Chen, Y. J. Yan, and J. S. Jiang, "Vibration-based damage detection in composite wingbox structures by HHT," *Mechanical Systems and Signal Processing*, vol. 21, no. 1, pp. 307–321, 2007.
- [11] H. Chen, Y. Yan, J. Jiang, and Q. Liu, "Application of Hilbert-Huang transform to damage detection for wing box section," *Zhendong yu Chongji/Journal of Vibration and Shock*, vol. 25, no. 3, pp. 81–98, 2006.
- [12] H. G. Chen, Y. J. Yan, W. H. Chen, J. S. Jiang, L. Yu, and Z. Y. Wu, "Early damage detection in composite wingbox structures using hilbert-huang transform and genetic algorithm," *Structural Health Monitoring*, vol. 6, no. 4, pp. 281–297, 2007.
- [13] D. Pines and L. Salvino, "Structural health monitoring using empirical mode decomposition and the Hilbert phase," *Journal of Sound and Vibration*, vol. 294, no. 1-2, pp. 97–124, 2006.
- [14] H. Li, X. Deng, and H. Dai, "Structural damage detection using the combination method of EMD and wavelet analysis," *Mechanical Systems and Signal Processing*, vol. 21, no. 1, pp. 298–306, 2007.
- [15] N. Cheraghi and F. Taheri, "A damage index for structural health monitoring based on the empirical mode decomposition," *Journal of Mechanics of Materials and Structures*, vol. 2, no. 1, pp. 43–62, 2007.
- [16] D. Rezaei and F. Taheri, "Experimental validation of a novel structural damage detection method based on empirical mode decomposition," *Smart Materials and Structures*, vol. 18, no. 4, Article ID 045004, 2009.
- [17] D. Rezaei and F. Taheri, "Damage identification in beams using empirical mode decomposition," *Structural Health Monitoring*, vol. 10, no. 3, pp. 261–274, 2011.
- [18] H. Chen, L. Zhang, J. Li, and W. Chen, "Improved EMD-based structural damage feature extraction," *Zhendong Ceshi Yu Zhenduan/Journal of Vibration, Measurement and Diagnosis*, vol. 32, no. 4, pp. 645–648, 2012.
- [19] L. Cao, A. Li, Y. Deng, and Y. Ding, "Structural damage alarming based on empirical mode decomposition," *Zhendong Ceshi Yu Zhenduan/Journal of Vibration, Measurement and Diagnosis*, vol. 32, no. 3, pp. 392–396, 2012.
- [20] Y.-C. Ren and P. Weng, "Structural damage detection based on improved Hilbert-Huang transform," *Zhendong yu Chongji/Journal of Vibration and Shock*, vol. 34, no. 18, pp. 195–199, 2015.
- [21] X.-M. Wang, F.-L. Huang, G. Ma, and J.-J. Liu, "An HHT-based method to eliminate short-time strong disturbance from measured signals of bridge," *Journal of Central South University of Technology (English Edition)*, vol. 14, no. 6, pp. 848–852, 2007.
- [22] B. Li, C. Zhang, and Z. He, "HHT-based crack identification method for start-up rotor," *Frontiers of Mechanical Engineering*, vol. 7, no. 3, pp. 300–304, 2012.

Research Article

A Signal Decomposition Method for Ultrasonic Guided Wave Generated from Debonding Combining Smoothed Pseudo Wigner-Ville Distribution and Vold–Kalman Filter Order Tracking

Junhua Wu, Xinglin Chen, and Zheshu Ma

School of Automotive and Traffic Engineering, Nanjing Forestry University, Nanjing, Jiangsu 210037, China

Correspondence should be addressed to Junhua Wu; bjtime13@126.com

Received 15 May 2017; Accepted 3 August 2017; Published 14 September 2017

Academic Editor: Michele Palermo

Copyright © 2017 Junhua Wu et al. This is an open access article distributed under the Creative Commons Attribution License, which permits unrestricted use, distribution, and reproduction in any medium, provided the original work is properly cited.

Carbon fibre composites have a promising application future of the vehicle, due to its excellent physical properties. Debonding is a major defect of the material. Analyses of wave packets are critical for identification of the defect on ultrasonic nondestructive evaluation and testing. In order to isolate different components of ultrasonic guided waves (GWs), a signal decomposition algorithm combining Smoothed Pseudo Wigner-Ville distribution and Vold–Kalman filter order tracking is presented. In the algorithm, the time-frequency distribution of GW is first obtained by using Smoothed Pseudo Wigner-Ville distribution. The frequencies of different modes are computed based on summation of the time-frequency coefficients in the frequency direction. On the basis of these frequencies, isolation of different modes is done by Vold–Kalman filter order tracking. The results of the simulation signal and the experimental signal reveal that the presented algorithm succeeds in decomposing the multicomponent signal into monocomponents. Even though components overlap in corresponding Fourier spectrum, they can be isolated by using the presented algorithm. So the frequency resolution of the presented method is promising. Based on this, we can do research about defect identification, calculation of the defect size, and locating the position of the defect.

1. Introduction

Carbon fibre composite is widely used in modern industry, such as aerospace domain and military products, because of its high strength and light weight. At present, such a material has been generalized to automotive industry, obviously reducing the weight of automobile. Debonding defect is a major defect of the carbon fibre composites. A great number of investigations of the nondestructive evaluation and testing (NDE/NDT) have done research for this type of defect [1–5].

Currently, ultrasonic guided wave (GW) testing has emerged as a popular NDE/NDT technique. The method can estimate the location, severity, and type of defects. Successful applications of defect identification of carbon fibre composites have been done [3, 6, 7]. However, dispersion effects and noise make ultrasonic testing waves as multicomponent signals, which results in that it is difficult to do NDE/NDT with

raw testing waves. Therefore, isolating different components of GW and obtaining the corresponding time-frequency distributions (TFD) are vital for the inspection of the defect.

A number of scholars have done investigations about signal processing methods of GWs. Kerckel et al. [8] used Bayesian parameter estimates to isolate multiple modes in GW signals collected from laser ultrasonic testing on a manufacturing assembly line. Cai et al. [9] provided a time-distance domain transform (TDDT) method to interpret the dispersion of Lamb waves, which can result in high spatial resolution images of damage areas. Rizzo and di Scalea utilized Discrete Wavelet Transform (DWT) to extract wavelet domain features for enhanced defect characterization in multiwire strand structures [10]. Gangadharan et al. presented a time reversal technique using GWs to detect damage in an aluminum plate, and good results were achieved [11]. The wavelet analysis is widely used [12–17] in domains; many

successful applications of wavelet transform (WT) for GW signals have been done. Li et al. [14] proposed a combined method employing empirical mode decomposition (EMD) and wavelet analysis to attain good time resolution of the response signals. Paget et al. [15] proposed a new damage-detection technique based on WT with a new basis. Yu et al. [16] used the techniques of statistical averaging to reduce global noise and discrete wavelet denoising using a Daubechies wavelet to remove local high-frequency disturbances. Y. Y. Kim and E.-H. Kim [17] evaluated the effectiveness of WT analysis for studying the wave dispersion.

EMD, which can isolate adaptively different components, was proposed by Huang in 1998 [18]. At present, many investigations of theory and application have been done [19–24]. Li et al. [14], Osegueda et al. [20], and Salvino et al. [22] used EMD to process GW signals in plate structures. However, the frequency resolution of EMD is a limitation. Reference [25] reveals that when the ratio between a relatively low frequency and a relatively high frequency is greater than 0.75, two components of a signal cannot be separated.

In 1993, Vold and Leuridan [26] proposed Vold–Kalman filter order tracking (VKF_OT) for the estimation of a single order component. In 1997, they [27] derived a scheme to simultaneously estimate multiple components. Instantaneous frequency of the isolated component is a necessary prior knowledge for VKF_OT. Therefore, we introduce Smoothed Pseudo Wigner-Ville distribution (SPWVD), which can remove the cross-term in frequency direction and time direction of the time-frequency panel, to get instantaneous frequencies of isolated components. We present a signal decomposition method for ultrasonic GWs combining VKF_OT and SPWVD in this paper.

The rest of this paper is organized as follows. Section 2 presents the theories of Smoothed pseudo Wigner-Ville distribution and Vold–Kalman filter order tracking. The principle of algorithm is illustrated in Section 3. Section 4 provides an illustration of the presented method. The details of the experiment are described in Section 5. Section 6 shows the application of the presented algorithm to the experimental signals. Finally, Section 7 concludes.

2. Smoothed Pseudo Wigner-Ville Distribution and Vold–Kalman Filter Order Tracking

2.1. Smoothed Pseudo Wigner-Ville Distribution. Wigner-Ville distribution has a fine time-frequency resolution and can reach the low boundary of Heisenberg uncertainty principle. It is defined as [28]

$$\text{WVD}_s(t, f) = \int_{-\infty}^{\infty} s\left(t + \frac{\tau}{2}\right) s\left(t - \frac{\tau}{2}\right) e^{-j2\pi f\tau} d\tau. \quad (1)$$

However, for multicomponent signals, it suffers from inevitable interference of cross-terms. SPWVD can remove

it in frequency direction and time direction of the time-frequency panel. And the formula of SPWVD is as follows [28]:

$$\text{SPW}_s(n, \Theta) = \sum_{k=-L+1}^{L-1} |h(k)| \cdot \sum_{l=M+1}^{M-1} g(l) s(n+l+k) s^*(n+l-k) e^{-j2k\Theta}, \quad (2)$$

where $g(l)$ and $h(k)$ are smoothing window functions in time direction and frequency direction, respectively. s is an analyzed signal, and n and Θ are time variable and frequency variables, respectively. The time resolution and frequency resolution of SPWVD are promising. Moreover, no interference is in the representation.

2.2. Vold–Kalman Filter Order Tracking. Isolation of different modes is important for defect identification by ultrasonic guided waves. On this basic, we can locate the defect and evaluate the defect size. Therefore, VKF_OT is employed to separate wave packages.

In this paper, the angular-displacement VKF_OT techniques are adapted. The method is used to obtain the tracked components by minimizing the energy of errors for both the structural and data equations by mean of one of the least squares approaches [29].

The k th order component can be defined as

$$f_k(t) = a_k(t) \theta_k(t) + a_{-k}(t) \theta_{-k}(t), \quad (3)$$

where $a_k(t)$ is the complex envelope and $a_{-k}(t)$ is the complex conjugate of $a_k(t)$ to make $f_k(t)$ a real waveform. It is noted that $\theta_k(t)$ is a carrier wave and defined as

$$\theta_k(t) = \exp\left(ki \int_0^t \omega(u) du\right), \quad (4)$$

where du is the speed of the reference axle and $\int_0^t \omega(u) du$ is the elapsed angular displacement. The discrete form of (4) can then be written as

$$\theta_k(n) = \exp\left(ki \sum_{m=0}^n \omega(m) \Delta T\right). \quad (5)$$

2.2.1. The Structural Equation. As the tracked component $f_k(t)$ can be written as (3), where the envelope $a_k(t)$ needs to be computed. Generally, $a_k(t)$ fulfills [29]

$$\frac{d^s a_k(t)}{dt^s} = \psi_k(t), \quad (6)$$

where $\psi_k(t)$ is a higher-degree term in $a_k(t)$. The corresponding discrete forms can be expressed,

$$\nabla^s a_k(n) = \psi_k(n), \quad (7)$$

where ∇ is the difference operator, the index s is the differentiation order, and $\psi_k(n)$ physically is a combination of other spectral components and additional measurement noise.

2.2.2. *The Data Equation.* A measured signal $y(n)$ can be taken as a combination of several components, $f_k(t)$, and measurement noise,

$$y(n) = \sum_{k \in j} a_k(n) \theta_k(n) + \xi(n), \quad (8)$$

where the integral number $j (= \pm 1, \pm 2, \pm 3, \dots, \text{and/or } \pm K)$ is the order of spectral components to be tracked and $\xi(n)$ is unwanted spectral components and measurement errors. Each component $a_k(n)$ of interest modulates with a carrier wave $\theta_k(n)$.

2.2.3. *Calculation of the Tracked Component f .* Let $s = 2$ and let data length be N ; then the calculation matrix form can be expressed as [29]

$$\begin{bmatrix} -2 & 1 & 0 & 0 & 0 & \cdots & 0 & 0 \\ 1 & -2 & 1 & 0 & 0 & \cdots & 0 & 0 \\ 0 & 1 & -2 & 1 & 0 & \cdots & 0 & 0 \\ \vdots & \vdots \\ 0 & 0 & 0 & 0 & 0 & \cdots & -2 & 1 \end{bmatrix} \begin{bmatrix} a_k(1) \\ a_k(2) \\ a_k(3) \\ \vdots \\ a_k(N) \end{bmatrix} = \begin{bmatrix} \psi_k(1) \\ \psi_k(2) \\ \psi_k(3) \\ \vdots \\ \psi_k(N) \end{bmatrix}. \quad (9)$$

To simultaneously track multiple orders and spectral components such as resonance, it can be extended to all order components of interest as well. Let

$$\begin{aligned} \overleftarrow{M} &= \begin{bmatrix} -2 & 1 & 0 & 0 & 0 & \cdots & 0 & 0 \\ 1 & -2 & 1 & 0 & 0 & \cdots & 0 & 0 \\ 0 & 1 & -2 & 1 & 0 & \cdots & 0 & 0 \\ \vdots & \vdots \\ 0 & 0 & 0 & 0 & 0 & \cdots & -2 & 1 \end{bmatrix}, \\ \overleftarrow{A} &= \begin{bmatrix} a_k(1) \\ a_k(2) \\ a_k(3) \\ \vdots \\ a_k(N) \end{bmatrix}, \\ \overleftarrow{Z} &= \begin{bmatrix} \tilde{\psi}_k(1) \\ \tilde{\psi}_k(2) \\ \tilde{\psi}_k(3) \\ \vdots \\ \tilde{\psi}_k(N) \end{bmatrix}, \end{aligned} \quad (10)$$

and then (9) becomes

$$\begin{bmatrix} \overleftarrow{M} & 0 & 0 & 0 & \cdots & 0 & 0 \\ 0 & \overleftarrow{M} & 0 & 0 & \cdots & 0 & 0 \\ 0 & 0 & \overleftarrow{M} & 0 & \cdots & 0 & 0 \\ \vdots & \vdots & \vdots & \vdots & \vdots & \vdots & \vdots \\ 0 & 0 & 0 & 0 & \cdots & 0 & \overleftarrow{M} \end{bmatrix} \overleftarrow{A} = \overleftarrow{Z}, \quad (11)$$

where elements \tilde{a}_k in the matrix \overleftarrow{A} are column vectors with a length N , which is the k th order component; $\tilde{\psi}_k$ are error vectors with a dimension $N \times 1$; and M is a matrix with a dimension $N \times N$.

The terms with negative indexes in (8) assure $f_k(t)$ to be a real waveform. \tilde{y} is the measured signal with a length of N , ξ an error vector with dimension $N \times 1$, and \overleftarrow{B}_k consists of carrier signals, as

$$\overleftarrow{B}_k = \begin{bmatrix} \theta_k(1) & 0 & 0 & \cdots & 0 \\ 0 & \theta_k(2) & 0 & \cdots & 0 \\ 0 & 0 & \theta_k(3) & \cdots & 0 \\ \vdots & \vdots & \vdots & \vdots & \vdots \\ 0 & 0 & 0 & \cdots & \theta_k(N) \end{bmatrix} \overleftarrow{A} = \overleftarrow{Z}. \quad (12)$$

Thus, (8) can be rewritten as

$$\tilde{y} - [\overleftarrow{B}_1 \ \overleftarrow{B}_2 \ \overleftarrow{B}_3 \ \cdots \ \overleftarrow{B}_k] \begin{bmatrix} \tilde{a}_1 \\ \tilde{a}_2 \\ \tilde{a}_3 \\ \vdots \\ \tilde{a}_K \end{bmatrix} = \tilde{\xi}. \quad (13)$$

As the angular-velocity VKF_OT scheme, we introduce a weighting factor and combine (9) and (13), and then

$$\begin{bmatrix} 0 \\ 0 \\ 0 \\ \vdots \\ 0 \\ \tilde{y} \end{bmatrix} - \begin{bmatrix} r\overleftarrow{M} & 0 & 0 & \cdots & 0 & 0 \\ 0 & r\overleftarrow{M} & 0 & \cdots & 0 & 0 \\ 0 & 0 & r\overleftarrow{M} & \cdots & 0 & 0 \\ \vdots & \vdots & \vdots & \vdots & \vdots & \vdots \\ 0 & 0 & 0 & \cdots & 0 & r\overleftarrow{M} \\ \overleftarrow{B}_1 & \overleftarrow{B}_2 & \overleftarrow{B}_3 & \cdots & \overleftarrow{B}_{k-1} & \overleftarrow{B}_k \end{bmatrix} \begin{bmatrix} \tilde{a}_1 \\ \tilde{a}_2 \\ \tilde{a}_3 \\ \vdots \\ \tilde{a}_{K-1} \\ \tilde{a}_K \end{bmatrix} = \begin{bmatrix} r\overleftarrow{Z} \\ \xi \end{bmatrix}. \quad (14)$$

Equation (14) can be symbolized as

$$\overleftrightarrow{Y} - \overleftrightarrow{P} \overleftrightarrow{A} = \overleftrightarrow{E}. \quad (15)$$

The evaluation of tracked order components is exactly to find a vector \overleftrightarrow{A} fulfilling

$$\min_{\overleftrightarrow{A}} \left(\|\overleftrightarrow{E}\|^2 \right) = \min_{\overleftrightarrow{A}} \left(\overleftrightarrow{E}^H \overleftrightarrow{E} \right) = \min_{\overleftrightarrow{A}} (J); \quad (16)$$

that is, $\partial J / \partial \overleftrightarrow{A} = 0$. The vector \overleftrightarrow{A} can be written as

$$\overleftrightarrow{P}^H \overleftrightarrow{P} \overleftrightarrow{A} = \overleftrightarrow{P}^H \overleftrightarrow{Y}. \quad (17)$$

The matrix $\overleftrightarrow{P}^H \overleftrightarrow{P}$ is written as

$$\overleftrightarrow{P}^H \overleftrightarrow{P} = \begin{bmatrix} \overleftrightarrow{S} & \overleftrightarrow{B}_{1,2} & \overleftrightarrow{B}_{1,3} & \cdots & \overleftrightarrow{B}_{1,K} \\ \overleftrightarrow{B}_{2,1} & \overleftrightarrow{S} & \overleftrightarrow{B}_{2,3} & \cdots & \overleftrightarrow{B}_{2,K} \\ \overleftrightarrow{B}_{3,1} & \overleftrightarrow{B}_{1,2} & \overleftrightarrow{S} & \cdots & \overleftrightarrow{B}_{3,K} \\ \vdots & \vdots & \vdots & \ddots & \vdots \\ \overleftrightarrow{B}_{K,1} & \overleftrightarrow{B}_{K,2} & \overleftrightarrow{B}_{K,3} & \cdots & \overleftrightarrow{S} \end{bmatrix}, \quad (18)$$

where $\overleftrightarrow{S} = r^2 \overleftrightarrow{M}^T \overleftrightarrow{M} + \overleftrightarrow{I}$ and $\overleftrightarrow{B}_{u,v} = B_u^H B_v$. Moreover, \overleftrightarrow{P}^H is written as

$$\overleftrightarrow{P}^H = \left[\overleftrightarrow{B}_1 \quad \overleftrightarrow{B}_2 \quad \overleftrightarrow{B}_3 \quad \cdots \quad \overleftrightarrow{B}_K \right]^T, \quad (19)$$

where \overleftrightarrow{B}_K is the complex conjugate of \overleftrightarrow{B}_K .

3. Principle of the Presented Algorithm

As mentioned above, SPWVD has a promising time-frequency resolution. Therefore, we obtain frequencies and durations of modes from SPWVD distributions of testing guided waves. Furthermore, VKF_OT is adapted to realize isolation of different wave packages with obtained mode frequencies. Finally, the final mode waveforms are cut out from the wave packages of modes by durations of modes. The processing steps of the extension algorithm are shown in Figure 1 and are as follows.

(1) *Smoothed Pseudo Wigner-Ville Distribution.* SPWVD is used for processing testing signal to get corresponding time-frequency distribution. And the promising time-frequency resolution of the method can lead to a high calculation accuracy of frequencies and durations of modes.

(2) *Extracting and Separating Valuable Areas of the Time-Frequency Panel.* To extract and separate different modes,

we do the following. (1) sum coefficients of each frequency-indexed group, and the calculation formula is

$$E(\Theta) = \sum_{n=1}^N \text{SPW}_s(r, \Theta), \quad (20)$$

where N denotes the number of the time variables of the time-frequency panel. (2) Calculate minimal values and maximum values of summations. Lines of the minimal values in the time-frequency panel can separate the valuable areas. And the maximum value evaluates whether the energy of a mode is strong enough to be kept. (3) Conduct threshold processing for the maximum values. And the equation is defined as

$$E(\Theta)_{\max} = \begin{cases} \text{keep} & E(\Theta)_{\max} > T_0 \\ \text{discard} & E(\Theta)_{\max} \leq T_0, \end{cases} \quad (21)$$

where $E(\Theta)_{\max}$ means the maximum of $E(\Theta)$. T_0 denotes the threshold for sift valuable modes. A mode with a strong energy is more valuable for detecting the debonding defect, so a threshold process is introduced to improve calculation efficiency. Moreover, the noise can also be removed by this operation. After this step, the areas of the time-frequency panel corresponding to the significant modes can be extracted and separated. Moreover, corresponding frequencies at the maximum values are taken as the mode frequencies.

(3) *Vold-Kalman Filter Order Tracking.* The mode frequencies have been calculated in Step (2). So we employ VKF_OT to filter the specific mode waveform with these frequencies. The different modes f_{0i} ($i = 1, 2, \dots, M$) can be preliminarily isolated, and M is number of the maximum values obtained in Step (2).

(4) *Peak-Track Algorithm.* Conduct the peak-track algorithm for the significant areas of SPWVD to obtain the primary IA of different modes. The principle of the peak-track algorithm can be found in [30]. And then, the IAs of significant modes can be obtained.

(5) *Constructing Filters in Time Domain.* To remove calculation error of the mode waveform from result obtained in Step (3), we construct a corresponding filter in time domain based on the primary IAs of different modes obtained in Step (4). And the equation is as follows:

$$A_i = \begin{cases} 1 & A_{0i} > T_A \\ 0 & A_{0i} \leq T_A, \end{cases} \quad (22)$$

where A_i is the value of the i th filter in time domain and A_{0i} denote the primary IAs of the i th modes. T_A is a threshold to remove calculation error of the mode waveform.

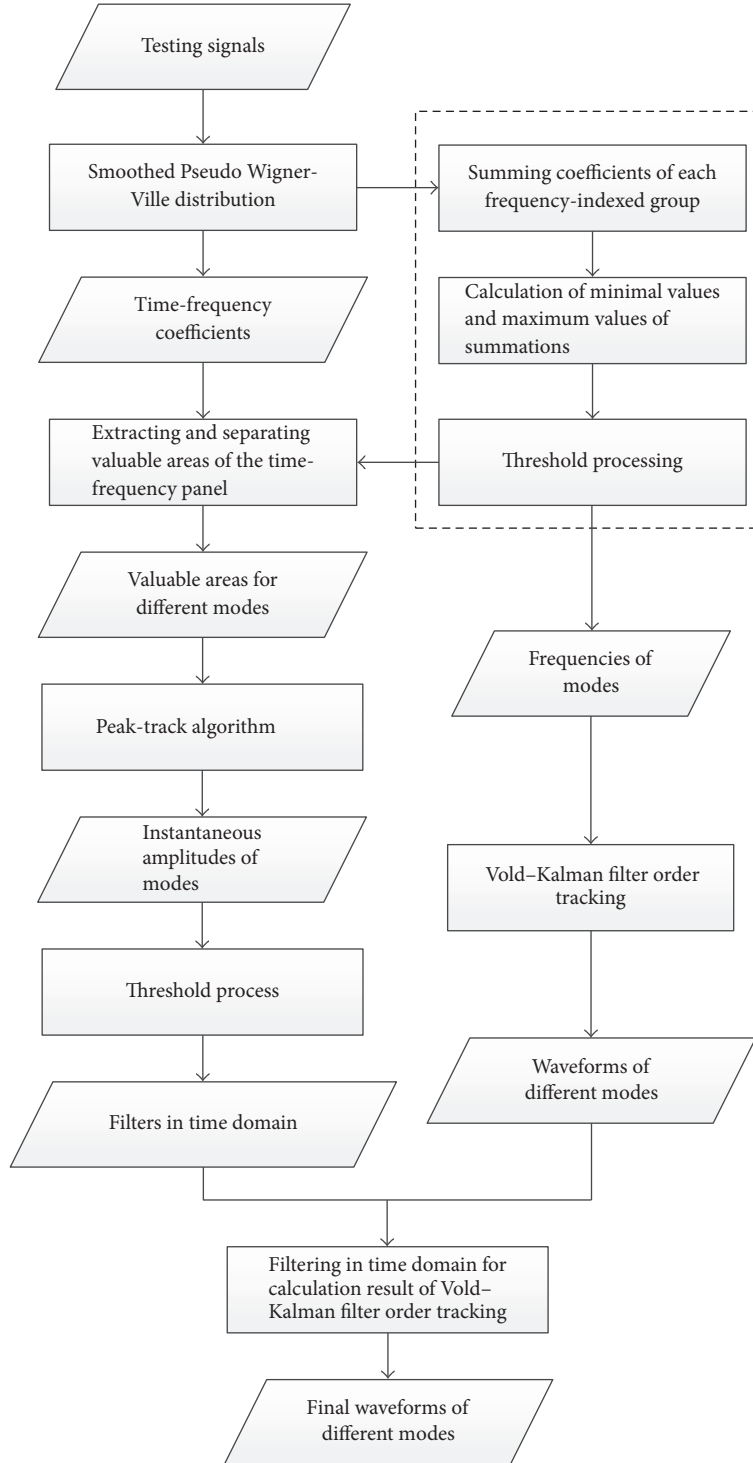


FIGURE 1: The different steps of the algorithm presented in the paper.

(6) *Filtering in Time Domain for Calculation Result of Vold-Kalman Filter Order Tracking.* Calculate the inner product between the mode waveforms obtained in Step (3) and the filter in time domain from Step (5). And then the final calculation result is obtained. The equation is

$$f_i = A_i * f_{0i}. \quad (23)$$

In Section 4, the details of the present algorithm will be illustrated with a sample signal.

4. Illustration of the Presented Algorithm

We construct a sample signal to illustrate the presented algorithm,

$$s(t) = s_1(t) + s_2(t) + s_3(t),$$

$$s_1(t) = \begin{cases} 0 & 0 \leq t \leq 0.00005 \\ 4000(t - 0.00005) \sin(300000 \times 2\pi t) & 0.00005 < t \leq 0.0003 \\ -4000(t - 0.00055) \sin(300000 \times 2\pi t) & 0.0003 < t \leq 0.00055 \\ 0, & 0.00055 < t \leq 0.001 \end{cases}$$

$$s_2(t) = \begin{cases} 0 & 0 \leq t \leq 0.00025 \\ 4000(t - 0.00025) \sin(55000 \times 2\pi t) & 0.00025 < t \leq 0.0005 \\ -4000(t - 0.00075) \sin(55000 \times 2\pi t) & 0.0005 < t \leq 0.00075 \\ 0, & 0.00075 < t \leq 0.001 \end{cases} \quad (24)$$

$$s_3(t) = \begin{cases} 0 & 0 \leq t \leq 0.00045 \\ 4000(t - 0.00045) \sin(50000 \times 2\pi t) & 0.00045 < t \leq 0.0007 \\ -4000(t - 0.00075) \sin(50000 \times 2\pi t) & 0.0007 < t \leq 0.00095 \\ 0, & 0.00095 < t \leq 0.001. \end{cases}$$

The sampling frequency is 2 MHz. The sample signal consists of three modes at frequencies of 50, 55, and 300 kHz. The curve of the sample signal in time domain is shown in Figure 2.

Firstly, we employ SPWVD for the sample signal to obtain the corresponding time-frequency panel, which is shown in Figure 3. As can be seen in Figure 3, the time resolution and frequency resolution of the time-frequency are promising. Besides, no interference is in the representation. However, the difference between the component at 50 kHz and the component at 55 kHz is so little that the two components cannot be separated in the SPWVD distribution of the sample signal, so is in Fourier spectrum, as shown in Figure 4.

After that, (20) is used on the SPWVD distribution. As shown in Figure 5, three maximum values at 50, 55, and 300 kHz are kept. So VKF_OT is employed on the sample signal with 50, 55, and 300 kHz to get the corresponding filtering results.

And then, the primary IAs of different modes are obtained by the peak-track algorithm. The filters in time domain of different modes are obtained by employing (22) on the primary IAs, as shown in Figure 6. We can adjust the threshold in (22) to get filters in time domain of different modes with a high accuracy in time resolution.

Finally, we conduct time-domain filter for the result of VKF_OT, and the results are shown in Figure 7. As presented in Figure 7, the decomposition results almost overlap with the corresponding original modes. To further validate the effectiveness of the presented algorithm, we calculate the error of the decomposition result, as shown in Figure 8. The absolute error is less than 0.1 for the modes at 50 and 55 kHz and is less than 0.02 for the mode at 300 kHz, which reveals

that the calculation accuracy of the presented algorithm is promising.

To compare with EEMD, the sample signal is also processed by this decomposition method. Figure 9 shows the coefficients of correlation between different IMFs and the sample signal. We can learn that IMFs 1–4 are vital components of the signal, as the coefficients of correlation are relatively greater. So these IMFs are shown in Figure 10. It is visible that the mode mixing occurs in EEMD for modes at 50 and 55 kHz, as shown in Figure 10(b). Because the ratio between modes at 50 and 55 kHz is greater than 0.75, they cannot be separated, as revealed in [25]. Therefore, the poor frequency resolution is a limitation of EEMD for its application.

5. Details of the Experimental

The material of the specimen is a specific composite material. The size is 400 mm × 300 mm × 3 mm and contains 15 layers. The corresponding size diagram is presented in Figure 11. Two debonding defects are in the specimen. The side length of the defects is, respectively, 20 mm and 30 mm.

Figure 12 is the diagram of the testing principle. In testing process, the exciting probe sends an exciting wave, and then the receiving probe will receive excited lamb waves. The excitation wave is a sine wave with a frequency of 100 kHz. The sampling frequency is 20 MHz. Three sets of signal are collected in the experiment, responding to three situations, that is, no defect, 20 mm defect, and 30 mm defect, respectively. The corresponding GWs collected in the experiment are presented in Figure 13.

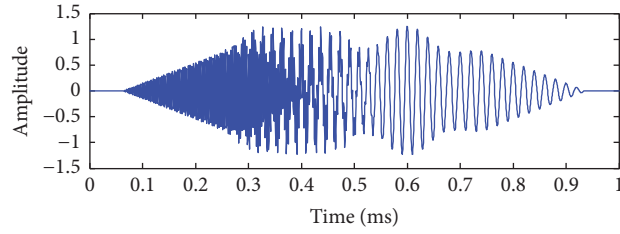


FIGURE 2: The curve of the sample signal in time domain.

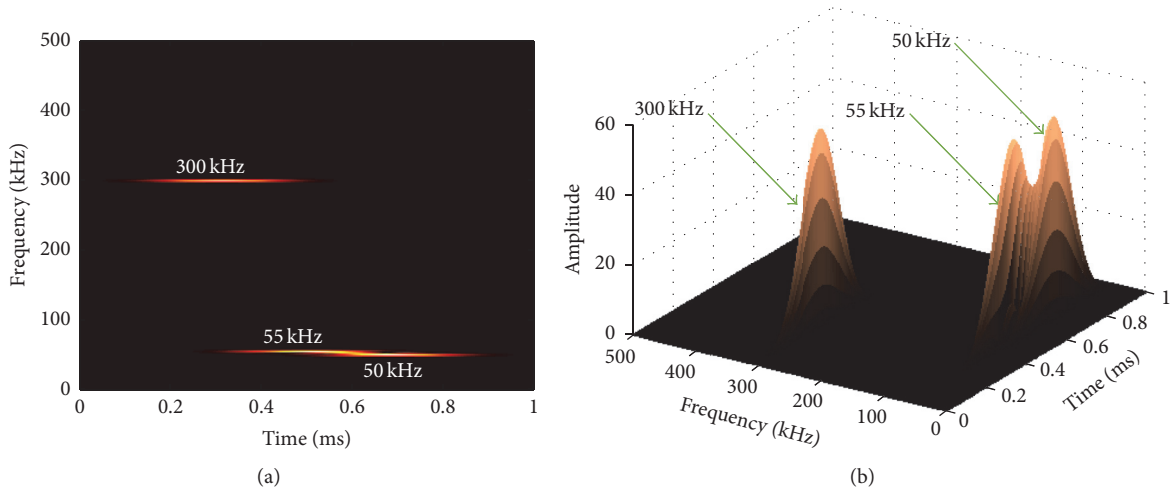


FIGURE 3: The representation of the sample signal by using SPWVD.

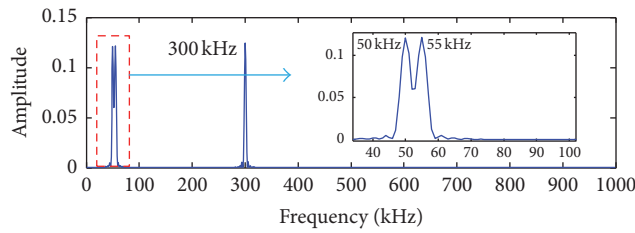


FIGURE 4: The Fourier spectrum of the sample signal.

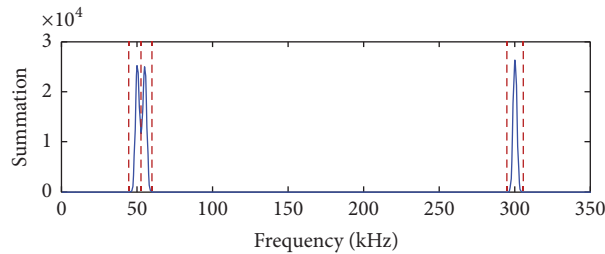


FIGURE 5: The different frequency-group summations of the time-frequency panel of the sample signal.

6. Result and Discussion

Figure 15 presents the decomposition result of experimental signals by using the presented algorithm. As shown in Figures 14 and 15, two modes exist in the experimental signal of no

defect and are at 50.3 kHz and 34.5 kHz. The signal of 20 mm defect consists of modes at 49.2 kHz, 41.2 kHz, and 34.1 kHz. And the signal of 30 mm defect consists of modes at 49.8 kHz, 44.8 kHz, and 33.9 kHz. Figure 16 shows these modes are decomposed by the presented algorithm. This indicates the

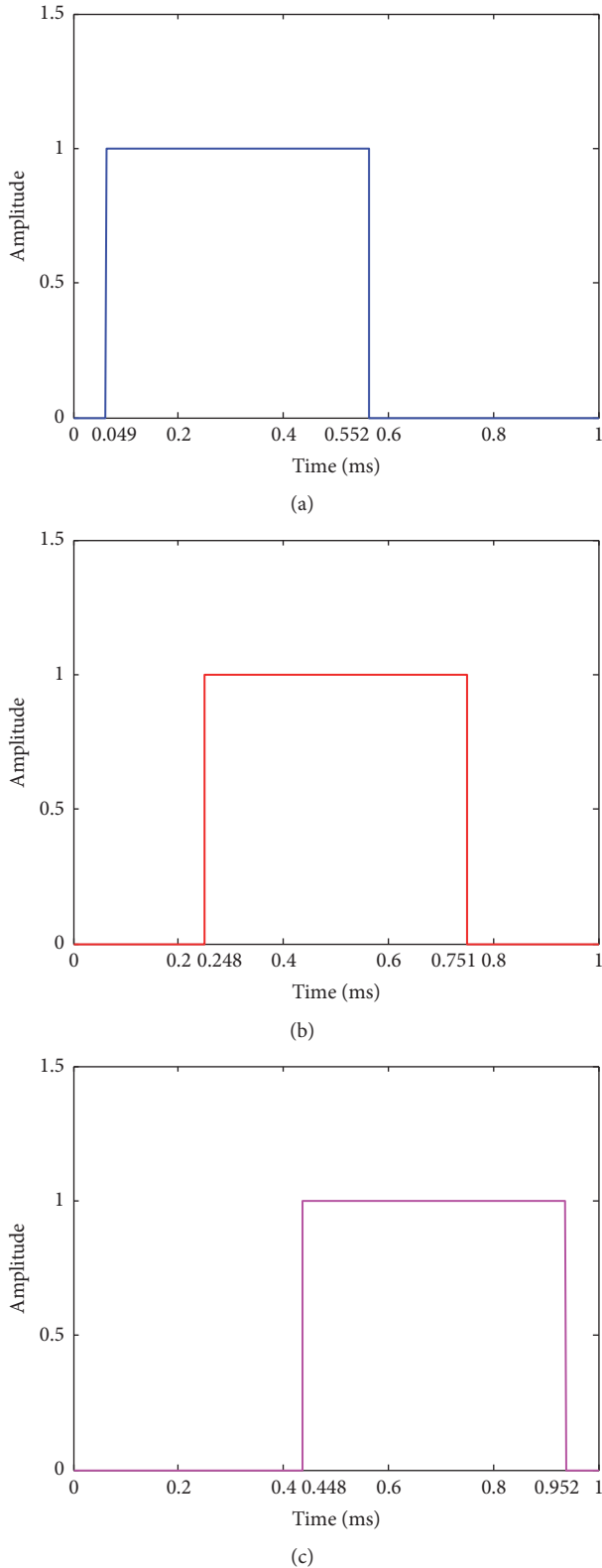


FIGURE 6: The filters in time domain of different modes: (a) mode at 300 kHz, (b) mode at 55 kHz, and (c) mode at 50 kHz.

method is effective in isolating different modes. Besides, considering that 50.3 kHz, 49.2 kHz, and 49.8 kHz pose little

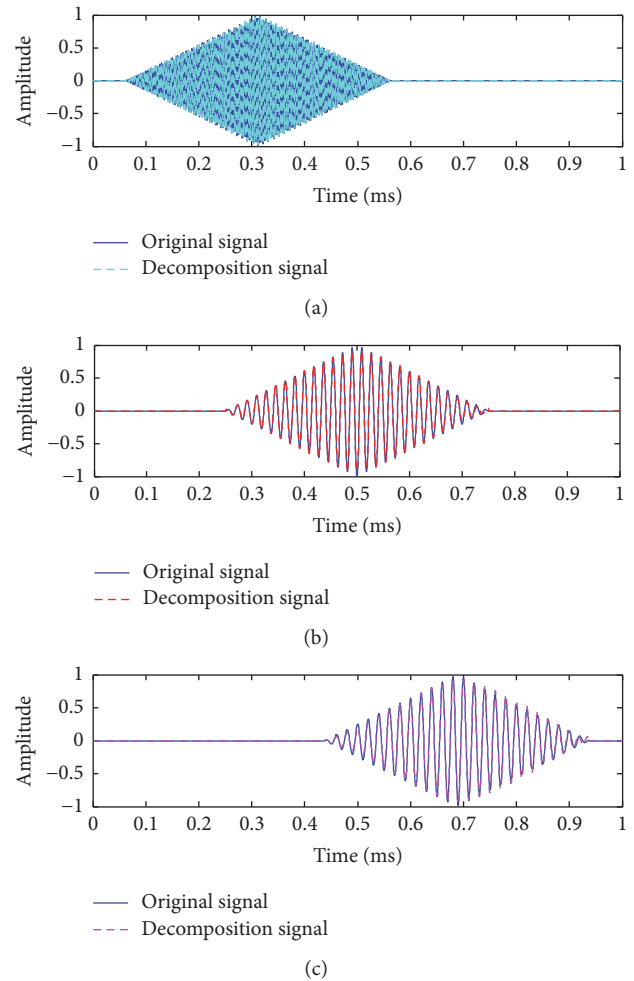


FIGURE 7: The decomposition result and the original modes of the sample signal x by the presented algorithm: (a) mode at 300 kHz, (b) mode at 55 kHz, and (c) mode at 50 kHz.

differences and this phenomenon is similar to 34.5 kHz, 34.1 kHz, and 33.9 kHz, it seems that defects stimulate new modes and 41.2 kHz for 20 mm defect and 44.8 kHz for 30 mm defect. On the basis of this phenomenon, we can try to detect the defect. Moreover, the frequency of the new mode becomes greater along with the defect size (41.2 kHz for 20 mm and 44.8 kHz for 30 mm). Maybe we can try to evaluate the size of the defect, according to this relationship. Finally, as we have isolated different wave packets, the location of defect can be obtained by the decomposition results.

7. Conclusion

This paper presents a decomposition algorithm aiming to analyze the characteristics of ultrasonic GWs generated in a NDT for the debonding in a type of composite material by combining SPWVD and VKF_OT. The presented method succeeds in isolating different GW modes. On the basis of

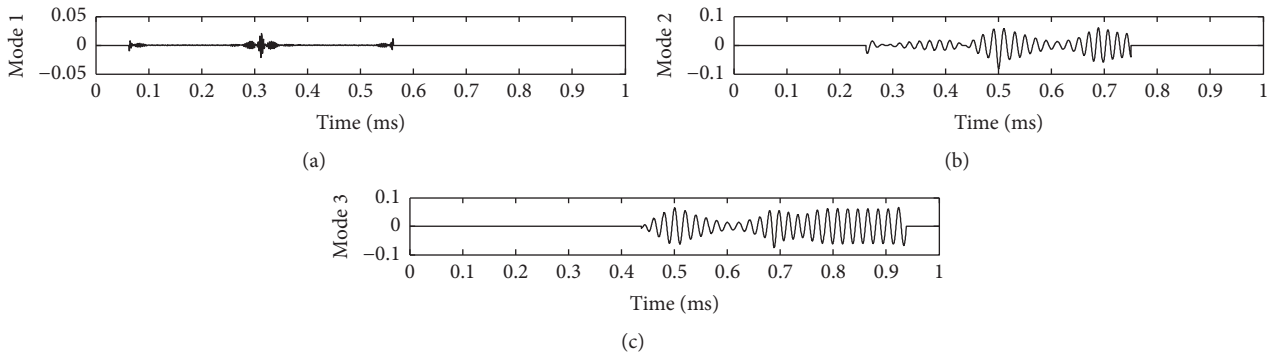


FIGURE 8: The errors of decomposition result of the sample signal x by the presented algorithm: (a) mode at 300 kHz, (b) mode at 55 kHz, and (c) mode at 50 kHz.

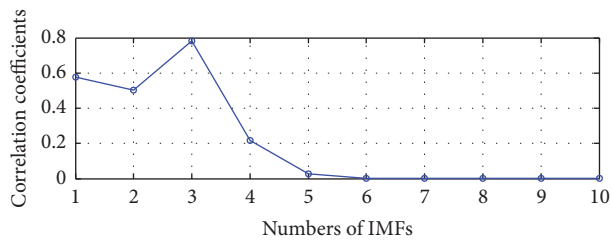


FIGURE 9: Correlation coefficients between IMFs and the original signal.

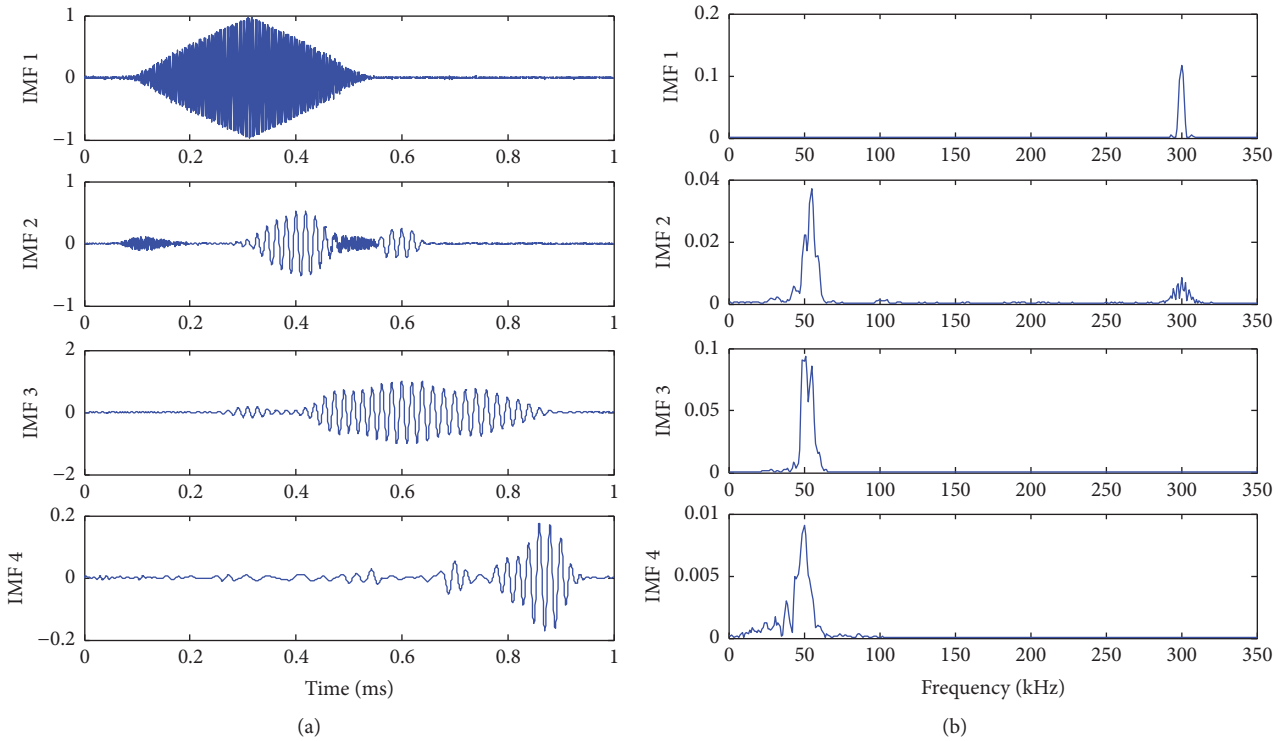


FIGURE 10: The IMFs 1–4 in the EEMD of the sample signal and the corresponding Fourier spectrums: (a) the IMFs and (b) the corresponding Fourier spectrums.

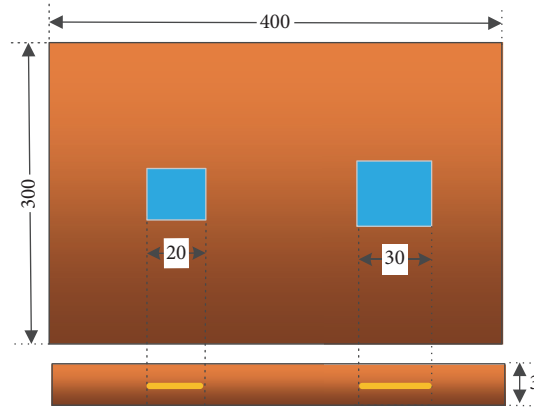


FIGURE 11: The size diagram of the specimen.

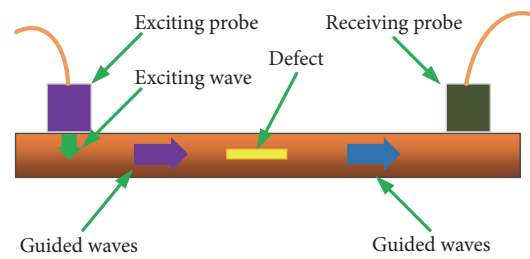


FIGURE 12: The diagram of the testing principle.

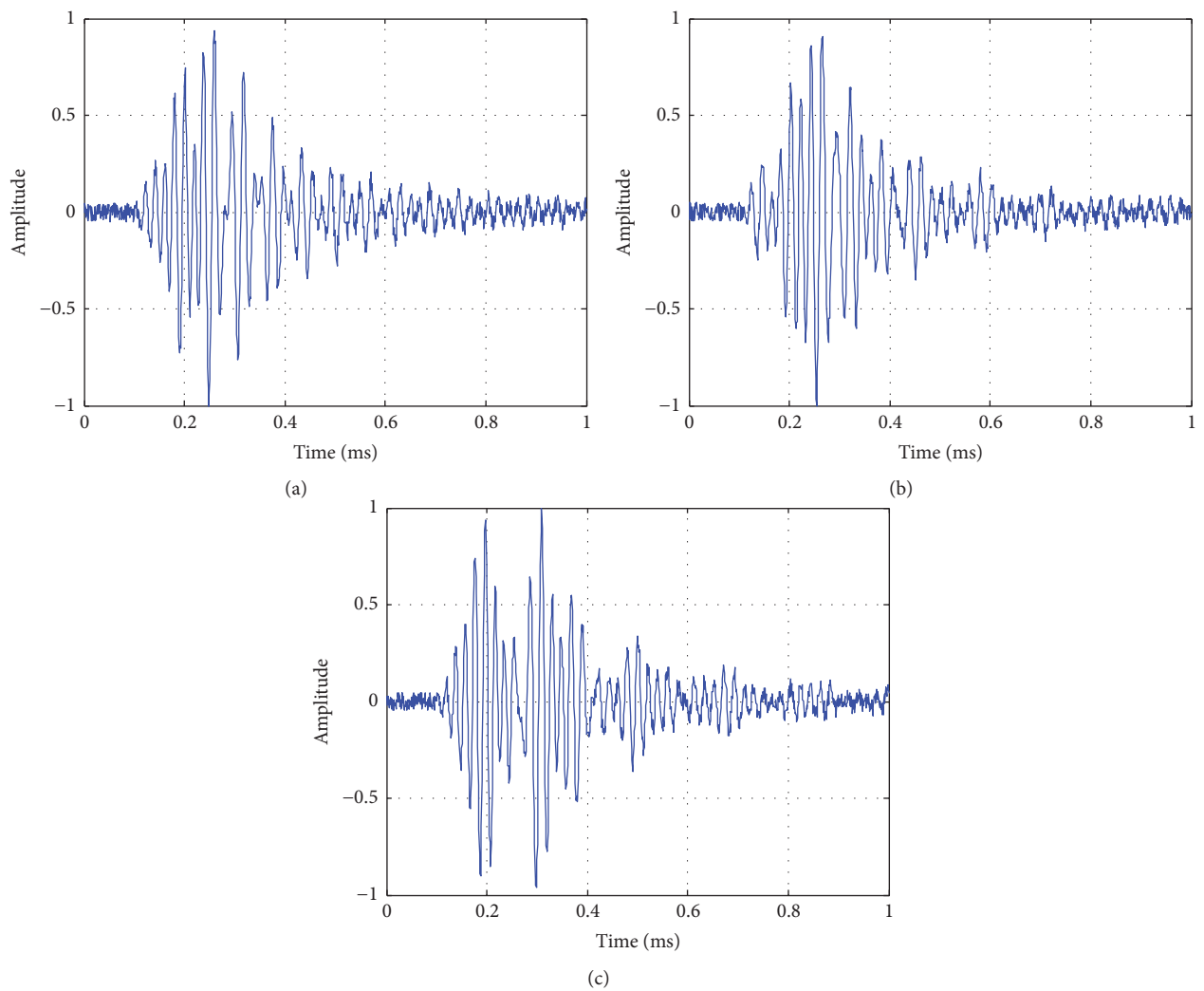
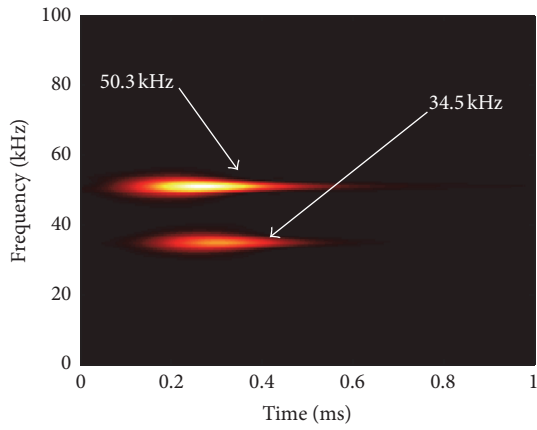
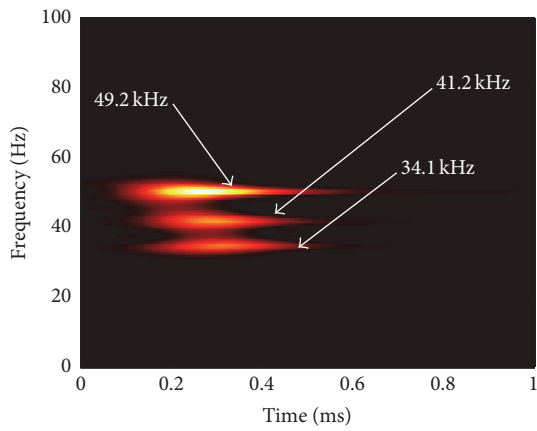


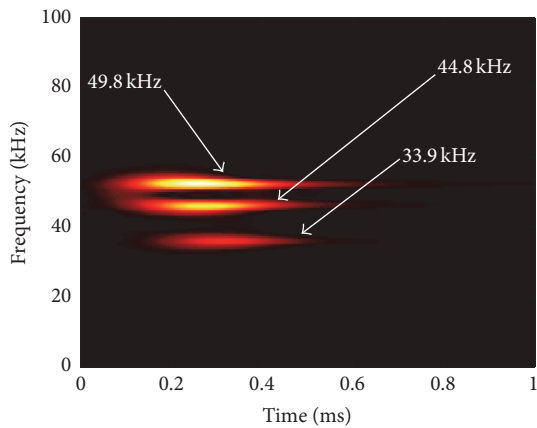
FIGURE 13: The GWs collected in the experiment: (a) no defect, (b) 20 mm, and (c) 30 mm.



(a)



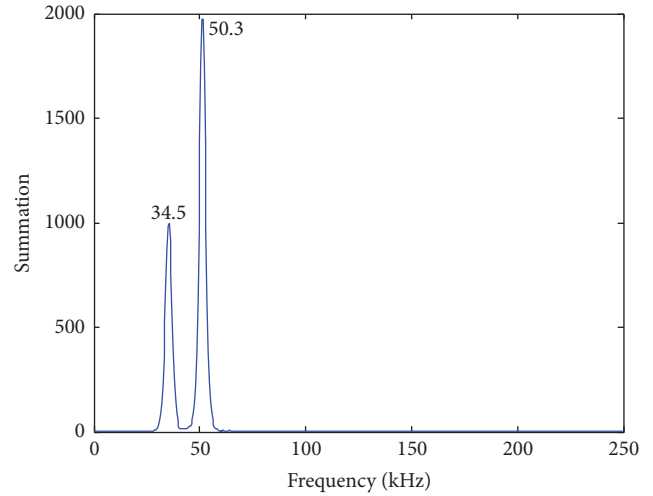
(b)



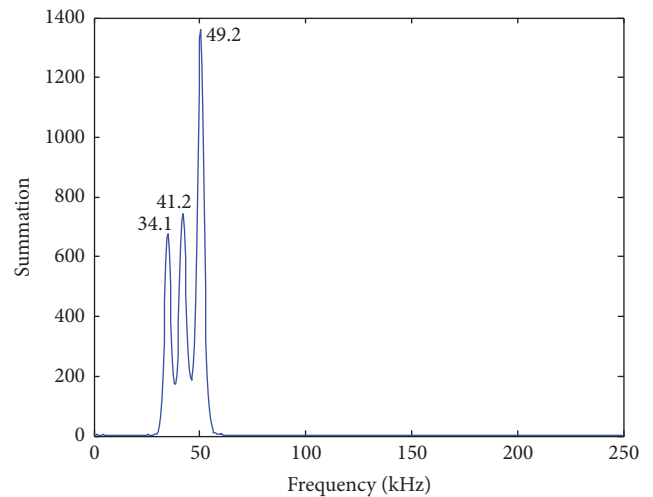
(c)

FIGURE 14: The SPWVD representations of the GWs in the experiment: (a) no defect, (b) 20 mm, and (c) 30 mm.

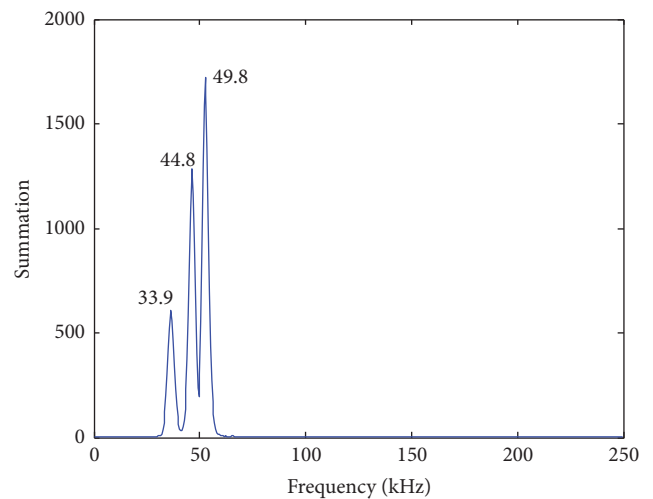
the presented algorithm, the characteristics of the experimental signals were investigated. Some conclusions, which are valuable for identification of defect, calculation of defect size, and locating defect, are obtained. The technique also can be applied in analogue NDTs and NDEs on the basis of the ultrasonic GWs. Further research will be done to validate the feasibility for locating defects by the algorithm.



(a)



(b)



(c)

FIGURE 15: The different frequency-group summations of the time-frequency panel of the experimental signals: (a) no defect, (b) 20 mm, and (c) 30 mm.

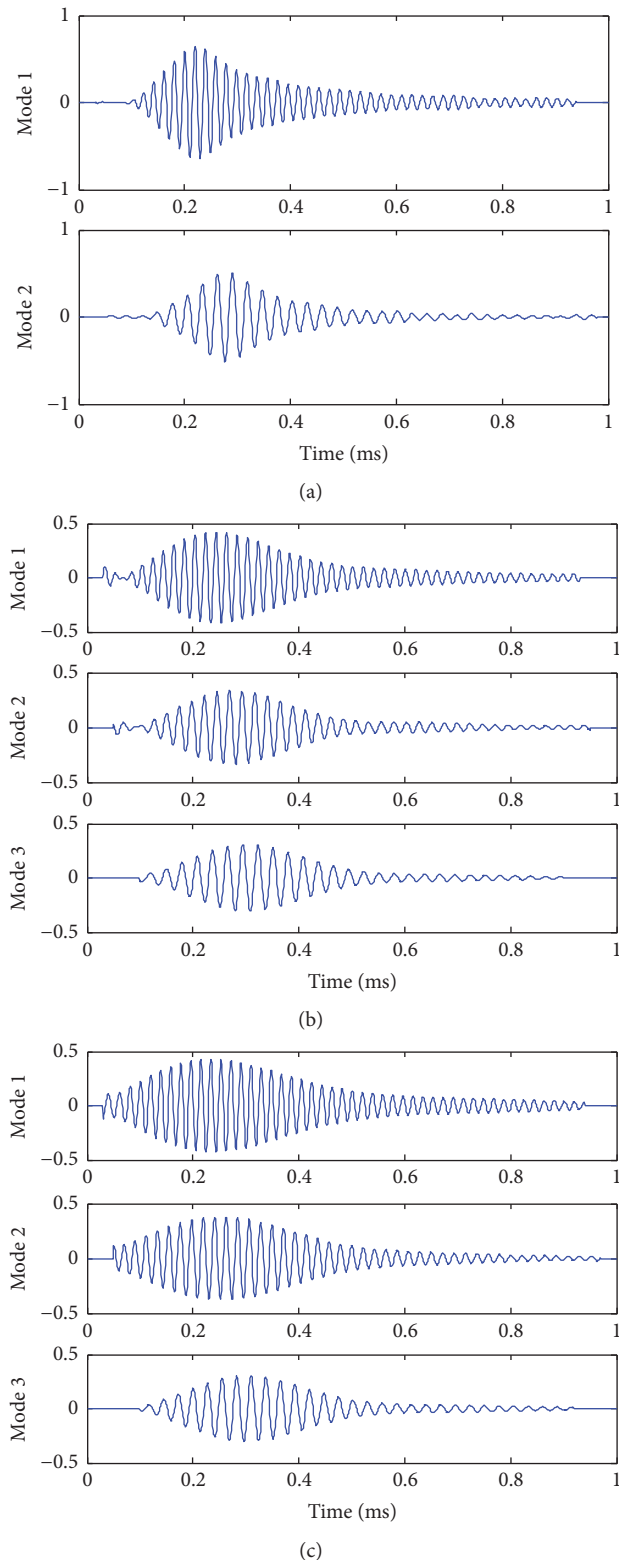


FIGURE 16: The decomposition result of experimental signals by using the presented algorithm: (a) no defect, (b) 20 mm, and (c) 30 mm.

Conflicts of Interest

The authors declare that they have no conflicts of interest.

References

- [1] R. Zhou, Z. Li, and J. Sun, "Crack deflection and interface debonding in composite materials elucidated by the configuration force theory," *Composites Part B: Engineering*, vol. 42, no. 7, pp. 1999–2003, 2011.
- [2] T. Liu, W. Zhang, and S. Yan, "A novel image enhancement algorithm based on stationary wavelet transform for infrared thermography to the de-bonding defect in solid rocket motors," *Mechanical Systems and Signal Processing*, vol. 62, no. 10, pp. 366–380, 2015.
- [3] J. Li, Y. Lu, R. Guan, and W. Qu, "Guided waves for debonding identification in CFRP-reinforced concrete beams," *Construction and Building Materials*, vol. 131, pp. 388–399, 2017.
- [4] J. Wu, Z. Ma, and Y. Zhang, "A Time-Frequency Research for Ultrasonic Guided Wave Generated from the Debonding Based on a Novel Time-Frequency Analysis Technique," *Shock and Vibration*, vol. 2017, Article ID 5686984, 2017.
- [5] L. Longbiao, "Modeling the Effect of Interface Wear on Fatigue Hysteresis Behavior of Carbon Fiber-Reinforced Ceramic-Matrix Composites," *Applied Composite Materials*, vol. 22, no. 6, pp. 887–920, 2015.
- [6] S. Khare, M. Razdan, P. Munshi, B. V. S. Sekhar, and K. Balasubramanian, "Defect detection in carbon-fiber composites using lamb-wave tomographic methods," *Research in Nondestructive Evaluation*, vol. 18, no. 2, pp. 101–119, 2007.
- [7] K. S. Tan, N. Guo, B. S. Wong, and C. G. Tui, "Experimental evaluation of delaminations in composite plates by the use of Lamb waves," *Composites Science and Technology*, vol. 53, no. 1, pp. 77–84, 1995.
- [8] S. W. Kerckel, M. B. Klein, and B. Pouet, "Bayesian separation of Lamb wave signatures in laser ultrasonics," in *Proceedings of the Applications and Science of Computational Intelligence III*, vol. 4055 of *Proceedings of SPIE*, pp. 350–361, April 2000.
- [9] J. Cai, L. Shi, and X. P. Qing, "A time-distance domain transform method for Lamb wave dispersion compensation considering signal waveform correction," *Smart Materials and Structures*, vol. 22, no. 10, Article ID 105024, 2013.
- [10] P. Rizzo and F. L. di Scalea, "Feature extraction for defect detection in strands by guided ultrasonic waves," *Structural Health Monitoring*, vol. 5, no. 3, pp. 297–308, 2006.
- [11] R. Gangadharan, C. R. L. Murthy, S. Gopalakrishnan, and M. R. Bhat, "Time reversal technique for health monitoring of metallic structure using Lamb waves," *Ultrasonics*, vol. 49, no. 8, pp. 696–705, 2009.
- [12] T. Liu, S. Yan, and W. Zhang, "Time-frequency analysis of nonstationary vibration signals for deployable structures by using the constant-Q nonstationary gabor transform," *Mechanical Systems and Signal Processing*, vol. 75, pp. 228–244, 2016.
- [13] W. Wu, G. Jiang, S. Huang, and C. J. Leo, "Vertical dynamic response of pile embedded in layered transversely isotropic soil," *Mathematical Problems in Engineering*, Article ID 126916, 12 pages, 2014.
- [14] H. Li, X. Deng, and H. Dai, "Structural damage detection using the combination method of EMD and wavelet analysis," *Mechanical Systems and Signal Processing*, vol. 21, no. 1, pp. 298–306, 2007.
- [15] C. A. Paget, S. Grondel, and K. Levin, "Damage assessment in composites by Lamb waves and wavelet coefficients," *Smart Materials and Structures*, vol. 12, no. 3, pp. 393–412, 2003.
- [16] L. Yu, J. Bao, and V. Giurgiutiu, "Signal processing techniques for damage detection with piezoelectric wafer active sensors

- and embedded ultrasonic structural radar,” in *Proceedings of the Smart Structures and Materials 2004 - Sensors and Smart Structures Technologies for Civil, Mechanical, and Aerospace Systems*, pp. 492–503, USA, March 2004.
- [17] Y. Y. Kim and E.-H. Kim, “Effectiveness of the continuous wavelet transform in the analysis of some dispersive elastic waves,” *The Journal of the Acoustical Society of America*, vol. 110, no. 1, pp. 86–94, 2001.
- [18] D. Yu, J. Cheng, and Y. Yang, “Application of EMD method and Hilbert spectrum to the fault diagnosis of roller bearings,” *Mechanical Systems and Signal Processing*, vol. 19, no. 2, pp. 259–270, 2005.
- [19] L. Yu, S. Wang, and K. K. Lai, “Forecasting crude oil price with an EMD-based neural network ensemble learning paradigm,” *Energy Economics*, vol. 30, no. 5, pp. 2623–2635, 2008.
- [20] R. Osegueda, V. Kreinovich, S. Nazarian, and E. Roldan, “Detection of cracks at rivet holes in thin plates using Lamb-wave scanning,” in *Proceedings of the International Society for Optical Engineering: Smart Nondestructive Evaluation and Health Monitoring of Structural and Biological Systems II*, pp. 55–66, USA, March 2003.
- [21] Y. Yu and C. Junsheng, “A roller bearing fault diagnosis method based on EMD energy entropy and ANN,” *Journal of Sound and Vibration*, vol. 294, no. 1-2, pp. 269–277, 2006.
- [22] L. Salvino, A. Purekar, and D. J. Pines, “Health monitoring of 2-D plates using EMD and hilbert phase,” in *Proceedings of the 4th International Workshop on Structural Health Monitoring*, Stanford University, Calif, USA, 2005.
- [23] Z. H. Guo, W. G. Zhao, H. Y. Lu, and J. Wang, “Multi-step forecasting for wind speed using a modified EMD-based artificial neural network model,” *Renewable Energy*, vol. 37, no. 1, pp. 241–249, 2012.
- [24] A. Y. Fu, W. Liu, and X. Deng, “Detecting phishing web pages with visual similarity assessment based on Earth Mover’s Distance (EMD),” *IEEE Transactions on Dependable and Secure Computing*, vol. 3, no. 4, pp. 301–311, 2006.
- [25] G. Rilling and P. Flandrin, “One or two frequencies? The empirical mode decomposition answers,” *IEEE Transactions on Signal Processing*, vol. 56, no. 1, pp. 85–95, 2008.
- [26] H. Vold and J. Leuridan, “High resolution order tracking at extreme slew rates, using kalman tracking filters,” *SAE Technical Papers*, 1993.
- [27] H. Vold, H. Herlufsen, M. Mains, and D. Corwin-Renner, “Multi axle order tracking with the Vold-Kalman tracking filter,” *S V Sound and Vibration*, vol. 31, no. 5, pp. 30–34, 1997.
- [28] P. Flandrin and B. Escudié, “An interpretation of the Pseudo-Wigner-Ville distribution,” *Signal Processing*, vol. 6, no. 1, pp. 27–36, 1984.
- [29] M.-C. Pan, W.-C. Chu, and D.-D. Le, “Adaptive angular-velocity Vold-Kalman filter order tracking-Theoretical basis, numerical implementation and parameter investigation,” *Mechanical Systems and Signal Processing*, vol. 81, pp. 148–161, 2016.
- [30] Z. Chen and R. C. Maher, “Semi-automatic classification of bird vocalizations using spectral peak tracks,” *The Journal of the Acoustical Society of America*, vol. 120, no. 5, pp. 2974–2984, 2006.

Research Article

Optimization Method of the Car Seat Rail Abnormal Noise Problem Based on the Finite Element Method

Huijie Yu, Xinkan Zhang, and Chen Zhang

School of Mechanical Engineering, University of Shanghai for Science and Technology, Shanghai, China

Correspondence should be addressed to Huijie Yu; yuhj2000@163.com

Received 1 April 2017; Revised 31 May 2017; Accepted 18 July 2017; Published 7 September 2017

Academic Editor: Michele Palermo

Copyright © 2017 Huijie Yu et al. This is an open access article distributed under the Creative Commons Attribution License, which permits unrestricted use, distribution, and reproduction in any medium, provided the original work is properly cited.

The finite element model of the seat rail is established with a spring-damping element to simulate the ball in the rail joint part. The stiffness and damping parameters of the joint part are determined by the combination of finite element method and experiment. Firstly, the natural frequencies and modes of the guide rail are obtained by modal experiment. The stiffness of the spring-damping element is optimized in the finite element software to make the natural frequencies and modes of the system consistent with the experimental ones. Secondly, the dynamic response curve of the key nodes is obtained through sweeping experiment, and the damping of the spring-damping element is optimized in the finite element software to make the nodal response of the system output consistent with the experiment. Then, the gap of the joint part of the car seat rail is studied considering the factors of load and structure randomness. The influence factors of the gap are selected by Hammersley experimental design method. The results show that the gap is normally distributed, and therefore the confidence interval of the gap is obtained. Finally, the joint probability distribution of the gap is obtained under the condition that the load and the structure are all random, which provides the theoretical guidance for determining the reasonable gap of the joint.

1. Introduction

With the progress of the times and the improvement of living standards, private cars have been rapidly entering thousands of households. The users' requirements for private cars have also changed from a simple trip to a comfortable ride. Some of the advanced foreign car manufacturers in the early 1980s began to pay attention to body structure vibration and rough road bumps producing noise problems. In the 1990s, Volkswagen, GM, Ford, Toyota, and other well-known car companies set up research centers to deal with the noise problems from vehicle structural vibration, noise, and rough road surface roughness [1]. Nowadays, the rising awareness on environment issues keeps stimulating higher demand for vehicles' qualities. Therefore, the international automotive industry has put forward a new standard, namely, Noise, Vibration, and Harshness standard, referred to by NVH standard [2]. In general, all tactile and auditory perceptions of the occupants in the car belong to the NVH problem. The more serious the car's vibration and noise problems are, the more irritable and uneasy the occupant will become.

From the NVH point of view, a vehicle is a system consisting of an exciter (engine), an actuator (suspension, etc.), and a vibration noise generator (body). Today, NVH problem is one of the major problems that car manufacturers have been most concerned about, from large system-level vehicle NVH standard analysis process to small NVH component-level problems. According to statistics, most of the major car manufacturers have put more than 20% of the R&D funding to solve the vehicle NVH problem [3].

The guide rail of car seat is the connection between the car seat and the car floor. Its role is to adjust the seat position back and forth and to protect the occupants' safety. Seat rail quality determines the user experience. A good rail should not only be safe and reliable in the locked state, but also be smooth in the adjustment of seat position forth and back. However, when the vehicle is moving, the car seat rails will produce abnormal sound, which is usually solved by workers with their own experience when they encounter the problems. Their temporary solutions are inadequate to solve the seat rail abnormal sound completely. However, the increasing complaint and discontent of the users have

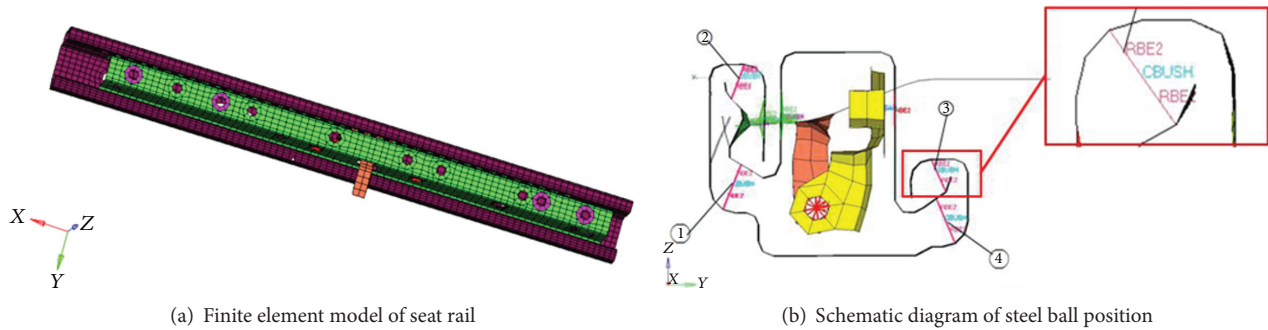


FIGURE 1

caught seat manufacturers' attention. The manufacturers have been putting great efforts to conduct experimental research to explore the causes of this problem. After long trials and exploration, engineers attribute the abnormal sound of rails to the uneven internal force of the balls. There are 4 slides between the inner rail and the outer rail, and 4 to 6 balls inside each slide. When the guide rail receives the random road excitation from the vehicle body, balls are subjected to uneven force. Some of them show the state of compression, and some of them show the state of separation. When the rail is subjected to the load of driving direction, noise is generated when the inner and outer rails are misaligned. Of course, the field engineer also gives the solution to this problem, which is to preload the rail before mounting. For example, if the nominal diameter of the steel ball is 6 mm, the actual spacing between the inner and outer rails is preloaded to 5.8 mm during installation so that the ball is actually in a preload state after the installation is complete. This solution is effective in the actual operation process. If the preload value is reasonable, the problem of abnormal sound in rails will be improved significantly. Therefore, the preload value for guidance is the key to solve the problem. If the preload is too little, noise will not be reduced effectively. On the other hand, if the preload is too large, serious slip will lock in the rail. Thus, the preload value, which is set to be the maximum value of the gap, may suppress the occurrence of the gap effectively, and it will be a reasonable preload value.

With the development of finite element method, it is an effective tool to solve the vibration and noise problem of vehicle seat by using finite element technology to simulate the dynamic characteristics of various parts of seat. To solve these problems, the dynamic finite element software can be used to analyze the dynamics of the steel ball. The gap between the steel ball and the inner and outer rails is analyzed by statistic method to observe the distribution of the gap and give the reasonable preloading value for guidance. However, many of the problems encountered will be the key to the successful solution. First of all, the interface between the steel ball and the inner and outer rail is actually a linear roller guide model. How can we establish the finite element model of the ball, so that the combination can be simulated exactly? It is also necessary to find a definite amount that can characterize the compacted and segregated state that occurs between the joint part. Secondly, this gap is affected by a number of uncertain

factors, like random excitation of road, manufacturing error of balls, elastic modulus, and so on. However, deterministic finite element dynamic analysis will not show the influence factors other than external excitation, which cannot meet the actual demand of this issue. The stochastic finite element theory can treat the load, the strength of materials, and parts of the geometry as random variables to solve the problem. It is the numerical analysis theory based on the traditional finite element theory, and it is the combination of random field theory and finite element method [4].

In this paper, a finite element modeling method is studied for a vehicle seat rail. The spring-damping modeling method for the joint part of linear roller is studied emphatically, and a complete method is proposed to optimize the stiffness and damping parameters of the joint using a combination of experiment and finite element analysis. Then, a series of dynamic analyses are carried out on the new dynamic model, and the distribution of the joint gap under the dynamic excitation is statistically analyzed. Finally, the distribution of the joint gap is investigated by using DOE and stochastic study considering the external excitation and the uncertainty of the structure itself.

2. FEA Model Set-Up

As the thicknesses of the inner and outer guide rails are all 1.4 mm, the rails can be regarded as thin-walled parts. We adopt the method of extracting the middle layer. Using the CAE software, thin-walled parts are mathematically discretized by shell element, and a detailed finite element model is established. In this model, the outer rail is 450 mm long and the inner rail is 402 mm. The CQUAD4 unit with the basic dimension of 5 mm × 5 mm is used. There are 7913 nodes and 7406 units in total. The isotropic material is used to establish the material model. Its elastic modulus E is 210 GPa. Poisson's ratio is 0.3. Density is 7900 Kg/m³. The finite element model is shown in Figure 1.

The handling of the internal steel ball is the key to this modeling. There are twenty guide balls in the rail, eight of which are $\Phi 6$, and twelve of which are $\Phi 8$. According to their position in the guide rail structure, the steel balls are divided into four groups, as shown in Figure 1.

Figure 1 shows the finite element model of the guide rail and the position diagram of the inner ball. In the modeling

process, steel balls are represented by CBUSH spring elements overlapped with each other in the position of the steel ball. The PBUSH attribute of the spring element can give the stiffness in 6 directions (three axial degrees of freedom, three rotational degrees of freedom). Due to the positional symmetry of the steel balls, the same stiffness coefficient is assigned to each group of springs, so that the four sets of springs have 24 degrees of freedom.

It is important to note that the CBUSH element needs to specify the local coordinate system, that is, the above six DOF directions are for the local coordinate system in which the CBUSH element is located. As the CBUSH element requires stiffness and damping parameters to represent the contact relationship, how to get the kinetic parameters of the junction becomes the key technology of the modeling method. The follow-up content will elaborate the method of combining the finite element method and the experiment to combine the dynamic parameter identification method.

3. Experiments

3.1. Modal Experiment of Car Seat Rail. The purpose of this modal experiment is to obtain the information of modal natural frequency, vibration mode, and damping ratio, which can provide reference for the revision of finite element calculation model by experimentally testing and analyzing a certain type of vehicle seat rails. It is necessary to determine the support mode, the excitation mode, the excitation point, and the response point in the modal experiment. The DH5927 dynamic testing and analysis equipment, three-way acceleration sensor, and impact hammer were used in modal experiment. The excitation adopts the hammering method. The excitation signal produced by the hammer has the advantage that the bandwidth of the signal can be controlled by different materials of the hammer. The higher the material stiffness, the wider the pulse signal spectrum will be. The adequate bandwidth can get more modes in one time. The hammering method is fixing the response point and moving the thumping point to compensate for the shortage of the number of acceleration sensors. For the excitation points and response points, the selected response points can reflect the basic outline of the specimen, while the nodes of main vibration modes should be avoided, and the test point which may have more local modes should be encrypted. In this modal experiment, four acceleration sensors are arranged. The transfer function is tested by moving the excitation point and fixing the response point.

According to vibration mechanics, the vibration of the structure is mainly due to the low-order natural frequency and its vibration mode. Due to the influence of the damping in the actual structure, the vibration modes of the higher-order frequencies will decay rapidly. In addition, when the sensitive frequency of the guide is less than 40 Hz, the first and second natural frequency and vibration mode can be found and used as the optimization target in stiffness optimization.

Table 1 shows the natural frequency of the experimental mode. Figure 2 shows the steady-state experiment of a certain

TABLE 1: Natural frequency and damping coefficient.

Order	Frequency (Hz)	Damping ratio (%)	Mode of vibration
1	7.22	3.74	Torsion of outer rail
2	12.65	2.57	Swing of Internal rail

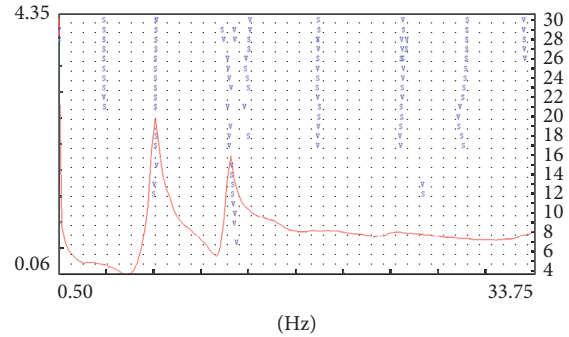


FIGURE 2: The stable diagram of the mode experiment for a certain point of force hammer.

point hammer excitation mode experiment. Figure 3 is the first and second modes of the experimental mode.

3.2. Frequency Sweep Experiment of Car Seat Rail. The purpose of this experiment is to obtain the time-acceleration curve of the excitation point and the time-acceleration response curve of the characteristic node by sweeping a certain type car seat rail, which provides the basis for the optimization of contact damping in finite element calculation. The DH5927 dynamic test and analysis system, three-way acceleration sensor, and HEV-20 exciter were used in modal experiment. There are 5 experimental output points, of which three time-acceleration curves will be used to fit the results of the finite element analysis output, and the remaining two points are used to validate the fitted parameters. The selection and installation of the sensor have a significant impact on the measurement results. The sensor should be installed in the condition of sufficient rigidity and without increasing the structural quality and then measure the true direction of the vibration signal. The excitation source of the sweep experiment needs to meet the following conditions: the amplitude level should satisfy certain conditions and the component being excited should have anti-interference ability when the exciter has tiny nonlinear behavior. In engineering fields, the sinusoidal signal is often chosen as the excited signal. The excited point selects the bolt installation hole at the bottom of the guide rail, which is consistent with the excited point in the practical working condition of the guide rail. The rails are suspended using a flexible rope during the entire excitation to simulate the unrestrained state.

The frequency sweep experiment uses the exciter as a frequency generator. As the exciter and the track are composed of open-loop system, it can be seen that the collected excitation and response signals have a significant signal amplification at the resonance, as shown in Figure 4,

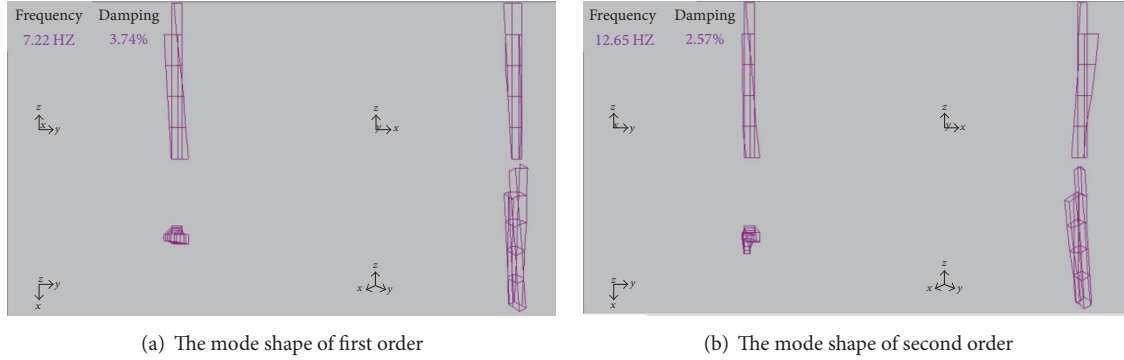


FIGURE 3

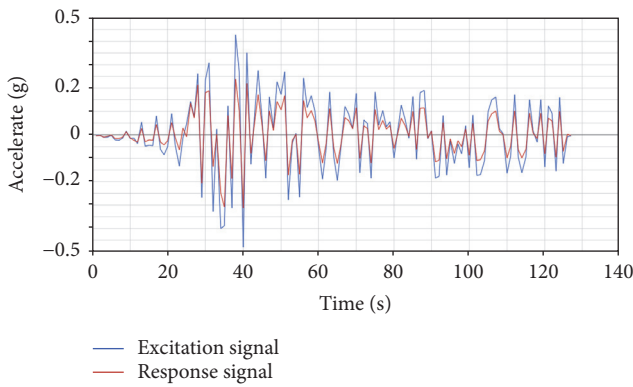


FIGURE 4: Excitation/response signal collected by frequency sweep experiment. The abscissa is for the sweep time (s), and the vertical axis is for the excitation amplitude (g).

in which the red signal is the response signal and the blue one is the excitation signal.

4. Research on Modeling of Car Seat Rail Joint

Based on the above two experiments, the stiffness and damping of the spring-damper element embedded in the joint part are optimized using OptiStruct and HyperStudy of FEM software. The equivalent contact stiffness and damping obtained from optimization characterize the contact properties in the joint part and thus allow us to establish a more accurate dynamic model of vehicle seat guide.

4.1. Least Squares Method and Curve Fitting. The least squares method is a kind of technique of mathematical optimization, minimizing the sum of squares of errors to find the best function of the data match [5]. Unknown data can be easily obtained using the least squares method, and the sum of the squares of the errors between the obtained data and the actual data can be minimized. The least squares method can also be used for curve fitting, and some other optimization problems can also be expressed by least squares by minimizing energy or maximizing entropy.

The specific approach to data fitting is as follows: for the given data (x_i, y_i) ($i = 0, 1, \dots, m$), finding $p(x) \in \Phi$ in the

function class Φ , minimizing the sum of square the error $r_i = p(x_i) - y_i$ ($i = 0, 1, \dots, m$),

$$\sum_{i=0}^m r_i^2 = \sum_{i=0}^m [p(x_i) - y_i]^2. \quad (1)$$

In the geometric sense, it means searching for the curve $y = p(x)$, which of the square sum of the distance from the given point (x_i, y_i) ($i = 0, 1, \dots, m$) is minimum (see Figure 5).

The function $p(x)$ is called the fitting function or the least squares solution. The method of finding the fitting function $p(x)$ is called the least squares method of curve fitting.

Polynomial Fitting. Given the data point (x_i, y_i) ($i = 0, 1, \dots, m$), Φ is a function class consisting of polynomials whose number does not exceed n ($n \leq m$).

Solve formula

$$p_n(x) = \sum_{k=0}^n a_k x^k \in \Phi \quad (2)$$

to make

$$I = \sum_{i=0}^m [p_n(x_i) - y_i]^2 = \sum_{i=0}^m \left(\sum_{k=0}^n a_k x_i^k - y_i \right)^2 = \min. \quad (3)$$

The general method of polynomial fitting can be summarized as follows:

- (1) Use the known data to draw a rough graphic of functions—Scatter plot—to determine the number of times of fitting polynomials.
- (2) Calculate

$$\sum_{i=0}^m x_i^j \quad (j = 0, 1, \dots, 2n) \quad (4)$$

$$\sum_{i=0}^m x_i^j y_i \quad (j = 0, 1, \dots, 2n).$$

- (3) Write a formal equation and find a_0, a_1, \dots, a_n .

TABLE 2: The natural frequency of the rail model after optimization.

Order	Experimental values (Hz)	Optimization value (Hz)	Vibration mode
1	7.22	7.220026	Torsion of outer rail
2	12.65	12.65000	Swing of Internal rail

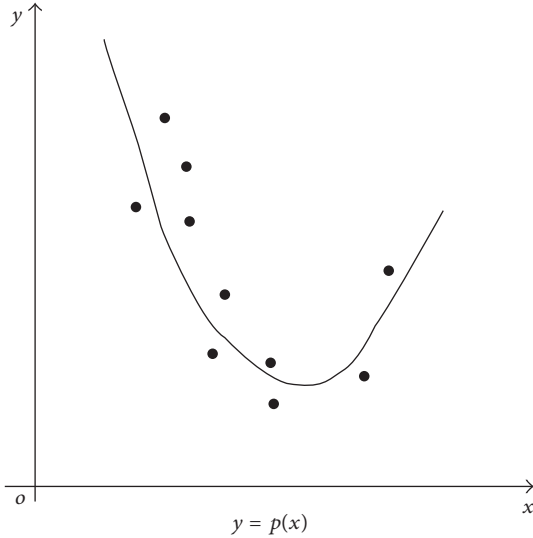


FIGURE 5

(4) Write the fitting polynomial:

$$p_n(x) = \sum_{k=0}^n a_k x^k. \quad (5)$$

4.2. Stiffness Optimization of Car Seat Rail Joint. Under the OptiStruct in HyperWorks, the Lanczos method is used to extract the real eigenvalues of free modal for guide rail model by mass matrix normalization. In the initial analysis, a set of initial stiffness values are given for the spring, in which the rail calculation mode is in the same order of magnitude as the experimental mode natural frequency. The modal results are found to be not sensitive to the four sets of rotation angles, freedom, and stiffness, so only the stiffness of four axial displacements of these springs is considered. When the 12 rigidities are specified as 500 N/m, the first and second mode natural frequency of the guide rail system is given in Table 1 in the previous chapter.

In the OptiStruct module, the stiffness of the spring element is taken as the design variable and the least squares method is used to optimize the stiffness.

(1) *Design Variable.* The design variables are the stiffness of the joint to be optimized, that is, \vec{K}_x , \vec{K}_y , and \vec{K}_z of the four springs, with 12 design variables. According to engineering experience, the design range of the stiffness is set to 1 N/m to 1000 N/m, and the initial stiffness value is 500 N/m.

TABLE 3: Contact stiffness parameter after optimization (N/m).

Number of Spring group	X direction	Y direction	Z direction
1	205.5	155.2	158.3
2	223.3	151.9	154.7
3	201.3	152.1	152.9
4	205.0	155.7	155.9

(2) *Design Objective.* Using the least squares method to minimize the objective function:

$$\min f(f_1, f_2, \dots, f_n) = \sqrt{\sum_{i=1}^n (F_i - f_i)^2}, \quad (6)$$

where F_i is the natural frequency of the experimental mode and f_i is the natural frequency of the modal.

(3) *Analysis of Optimization Results.* After optimization, the least squares deviation of the objective function is $2.59e^{-5}$. The optimized natural frequency is shown in Table 2, and the spring stiffness is shown in Table 3.

After comparison, the optimized vibration mode of the guide rail system coincides with the corresponding vibration mode of the experimental mode, so we believe that the optimized spring stiffness is the equivalent contact stiffness of the joint to be obtained.

4.3. Damping Optimization of Car Seat Rail Joint. The time-domain signal of the excitation and response of the sweep test is obtained in the previous section, as shown in Figure 4. In order to be able to compare with the experimental results, the excitation signal in Figure 4 is used as the excitation signal in the finite element software, and the transient analysis is carried out using the OptiStruct solver. The selection of the excitation point and the response point corresponds to their position in the actual sweep test. In the first calculation, the initial value of the structural damping is specified as 0.2 and the initial value of the contact damping is set to 2. As shown in Figure 6, the results of finite element calculation are output under the excitation signal excitation given in Figure 4.

The red curve is the time-acceleration response signal getting from software before optimization, and the blue curve is the experimental response signal after sparse processing in Figure 4.

It can be seen that the peaks of these two curves are close to each other. The finite element calculation curves are well consonant with the test data. On the other hand, the previous optimization of the binding site of the stiffness value is consistent with the actual rail.

TABLE 4: The data sheet of design variable (Ns/m).

Design variable	Notes	Lower limit	Initial value	Upper limit
G	Structural damping	0.1	0.2	0.3
C11	x directions of first set	0.2	2	20
C12	y directions of first set	0.2	2	20
C13	z directions of first set	0.2	2	20
C21	x directions of second set	0.2	2	20
C22	y directions of second set	0.2	2	20
C23	z directions of second set	0.2	2	20
C31	x directions of third set	0.2	2	20
C32	y directions of third set	0.2 </tr		

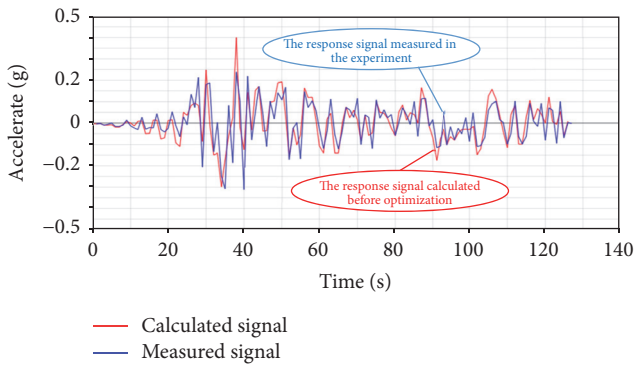


FIGURE 6: The output of the finite element calculation and experiment.

Then, we further fit the FE output to the experimental output curve to obtain a set of optimized damping coefficients, which is exactly the joint contact damping we are looking for. In HyperStudy curve fitting, we must explicitly design variables, objective function, design goals, and other objects.

(1) *Design Variables.* There are structure damping coefficient and damping coefficient of three directions in four sets of spring, which have 13 design variables. The initial damping value of a given structure is 0.2, and the variation range is 0.1 to 0.3. The spring-damping coefficient is set to 2 and the range of variation is 0.2 to 20. Table 4 lists the specific values.

Four sets of spring have been defined in the model as shown in Figure 1(b). In Table 4, “G” is the structural damping, and “C” is the damping of the three directions (x , y , z) in four sets of spring.

(2) *Objective Function.* Using the least square method as the objective function:

$$\text{OBJ} = \frac{\sum_{i=1}^{127} (y_i/\eta_i)^2}{127}, \quad (7)$$

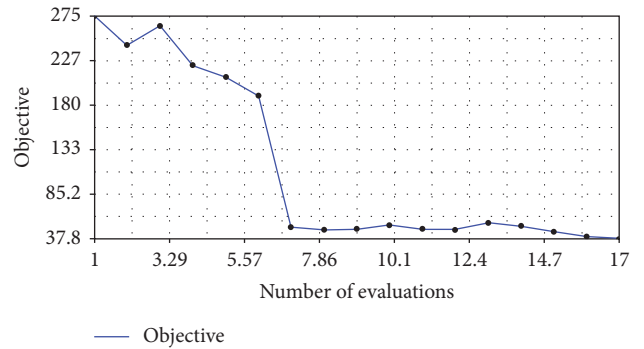


FIGURE 7: The convergent curve of the objective function.

where y_i is the displacement response of the corresponding points on the response curve of the finite element result.

η_i is the displacement response of each point after sparse processing.

$i = 1, 2, \dots, 127$ (there are 127 points in the curve).

(3) *Design Objective.* Minimize the objective function: $\min(\text{OBJ})$.

According to the objective function, the target value OBJ before optimization is 274.64. After HyperStudy optimization, the target OBJ reduces to 37.81. The number of iterations is 17 as shown in Figure 7. The finite element calculation response curve is further approximated to the experimental output curve as shown in Figure 8.

The blue curve is the experimental response signal after sparse processing in Figure 4. The green curve is the time-acceleration response signal getting from software after optimization.

After optimization is completed, the optimal solution of a set of contact damping is shown in Table 5.

So far, the contact stiffness and contact damping of the joint of the rail model are all optimized, and the finite element model is reestablished based on the optimized contact damping and contact stiffness. The relative displacement between the two ends of the spring element can be output by the

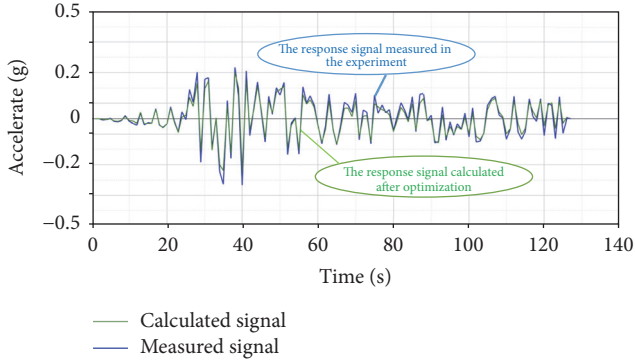


FIGURE 8: The optimized output and experimental output of the finite element software.

TABLE 5: Results of damping optimization (Ns/m).

Number of spring group	X direction	Y direction	Z direction
1	14.2	3.4	4.7
2	17.3	13.7	1.8
3	2.7	9.5	1.3
4	6.1	19.1	5.3

appropriate excitation signal to the guide rail model, which is between the steel ball and the inner/outer rail.

5. Discussion

5.1. Gap Evaluation of Car Seat Rail Joint under Uncertain Excitation. Under uncertain external loads which depend on time-domain or frequency domain, the spring-damper element embedded in the joint part will behave irregularly, resulting in a gap. In order to statistically analyze the confidence interval of the gap, the transient analysis can be carried out on the dynamic model of the guide rail, and the gap of the guide joint is studied using statistical method. The frequency response analysis is used to verify the results. Finally, the interval confidence intervals of the joints are calculated under dynamic excitation. Seat mass is converted to forces which are applied to both ends of the rail and the excitation location, as shown in Figure 9.

Gap calculation formula:

$$\text{gap} = \sum_{i=1}^{20} \frac{\vec{v}_{i-A} - \vec{v}_{i-B}}{20}, \quad (8)$$

where \vec{v}_{i-A} and \vec{v}_{i-B} represent the time domain or frequency response of displacement of two terminal points of CBUSH unit, respectively, and 20 is the number of CBUSH units, that is, the number of the replaced steel balls.

Figure 9(a) shows that the seat quality is converted into force to be applied to the position where the guide rail is connected with the seat. The whole chair weighs 12 KG and is evenly distributed on both side rails; then one side rail is subjected to 60 N vertical force. Both ends are connected. Figure 9(b): Because the signal phase difference has little influence on the vibration amplitude, the same excitation

TABLE 6: Interval confidence table.

Confidence	Gap value
90%	0.116 mm
95%	0.137 mm
99%	0.180 mm

signal is adopted in the three mounting points, and the phase error of the excitation signal is not considered.

5.1.1. Evaluation Method of Seat Joint Gap Using Transient Analysis. As the amplitude of actual road conditions is random, the results of the road spectrum will reflect the actual rail gap situation more accurately. Therefore, the road spectrum of the rail-body-connection point is collected when the car is driving on the road, and the data is used as the excitation signal of the rails, as shown in Figure 10.

The z direction excitation signal is applied to the connecting position of the guide rail and the vehicle body. As the excitation of the road profile, the 20 pairs of spring ends inserted in the inner joint of the guide rail are inevitably dislocated, and the relative displacement between the two ends of the 20 sets of springs can be obtained, as shown in Figure 11. Point A is a node that connects directly to the inner rail, while point B is a node that connects the outer rail.

It is shown that the maximum value of the gap is 0.23 mm in the time-history curve with the time span of 100 seconds. In order to further determine the confidence interval of the seat guide gap, the relative displacement between the two ends of 20 springs in Figure 6 is calculated. Each curve outputs 400 points evenly, and 8000 points of the 20 curves constitute our statistical sample space. In Figure 12, the ordinate values of 8000 points are illustrated.

Figure 12(a) is the relative displacement of the two ends of the spring distribution histogram. According to the mathematical statistics, the data of this group obey $N(0.00027, 0.0701)$; we can see that the gap we are concerned with is only limited to the right half of the normal distribution. Figure 12(b): The left part of the ball is actually pressed by the situation.

Since Figure 12(b) is half of the normal distribution, the mean value of this part can be obtained easily, which is 0.028 mm. Therefore, the mean value of the gap is 0.028 mm. From the mathematical statistics it can be seen that the probability density function of the branch is twice the normal distribution probability density function, but the range of x is 0 to $+\infty$.

According to the normal distribution table, 90% of the grasp of the gap does not exceed 0.116 mm; 95% of the grasp of the gap does not exceed 0.137 mm; 99% of the grasp of the gap does not exceed 0.180 mm, as shown in Table 6.

5.1.2. Evaluation Method of Seat Joint Gap Using Frequency Response Analysis. The conversion from the time domain to

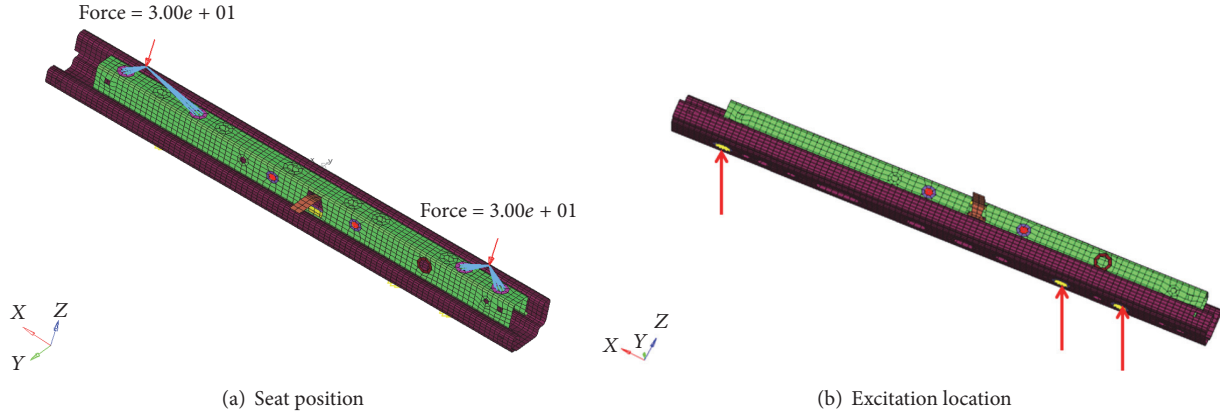


FIGURE 9

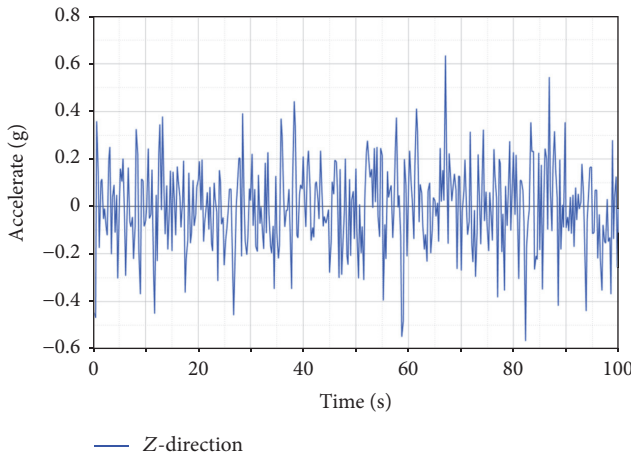
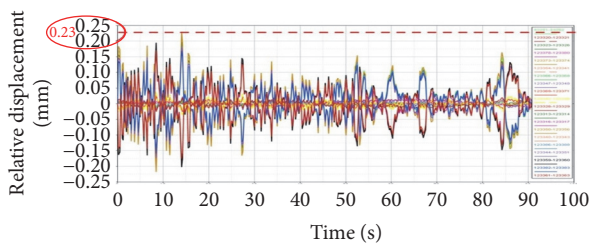
FIGURE 10: The z direction spectrum collected when the vehicle speed is 60 km/h.

FIGURE 11: The relative displacement-time curve of the two ends of the spring under the excitation of 60 km/h.

the frequency domain signal requires a Fourier transform. The ideal Fourier transform is defined as follows:

$$\begin{aligned} X(\omega) &= \int_{-\infty}^{\infty} x(t) e^{-j\omega t} dt \\ &= \sum_{n=-\infty}^{\infty} x(n\Delta t) e^{-j2\pi k \Delta f n \Delta t} \Delta t. \end{aligned} \quad (9)$$

Since the idealized Fourier transform is not windowed, the time is considered to be from negative infinity to positive

infinity, which leads to an increase in the magnitude of the frequency domain by N times the number of time-domain signal samples. In addition, the Fourier transform is a bilateral spectrum, but, in reality, we only take part of the frequency greater than zero. In order to compensate for the loss of energy, the amplitude of the unilateral spectrum needs to be doubled. The sampling time-domain signal ranges from 0 to the end of time T , which is the ideal signal plus a rectangular window. The definition formula is

$$X(\omega) = \int_0^T x(t) e^{-j\omega t} dt = \int_{-\infty}^{\infty} w_R(t) x(t) e^{-j\omega t} dt, \quad (10)$$

where w_R is the window function and the rectangular window can be defined as

$$w_R(t) = \begin{cases} 1, & t \in [0, T] \\ 0, & t \notin [0, T] \end{cases}. \quad (11)$$

The relationship between the Fourier transform and the ideal Fourier transform, which have practical engineering significance, is

$$\text{Engineering_FFT}_{\text{mag}} = \frac{|\text{FFT}|}{N} \times 2. \quad (12)$$

Figure 13(a) is the frequency domain signal after the engineering Fourier transform for the excitation signal shown in Figure 10; Figure 13(b) is the frequency-acceleration curve of the low frequency band. The maximum amplitude of the Fourier transform of the excitation signal is 0.0134 g, or 0.134 m/s².

According to Figure 13, since the response of the frequency excitation will only amplify significantly at the resonant point, statistical methods such as transient response analysis will be meaningless. In addition, vibration mechanics is based on the assumption of linear small deformation, so you can use the amplitude of 1 unit sinusoidal excitation A on the track for frequency response analysis; then you can extract the peak value of the gap δ_A between the two ends of the spring. The peak of the gap is

$$\delta_B \leq \delta_A \cdot \max[B(\omega)] \quad (13)$$

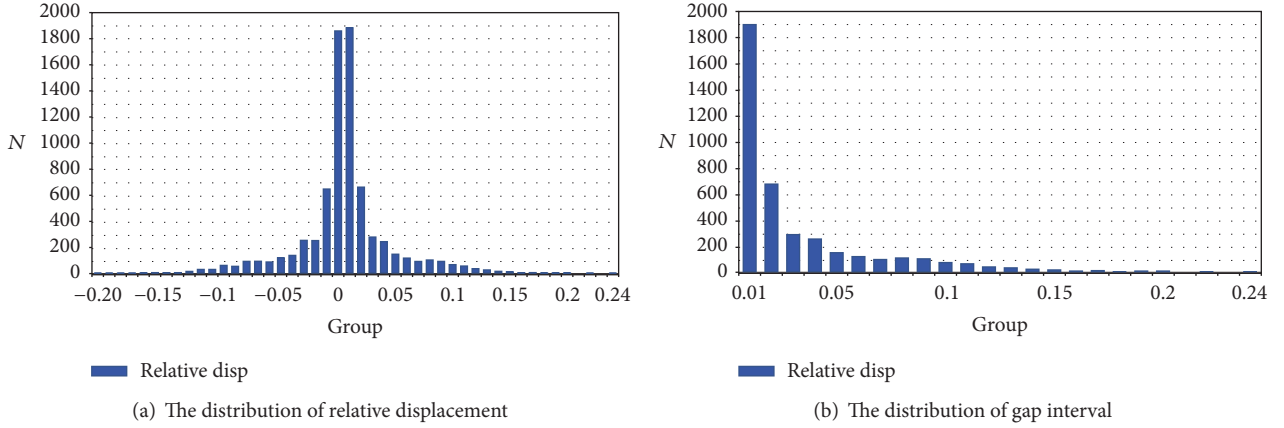


FIGURE 12

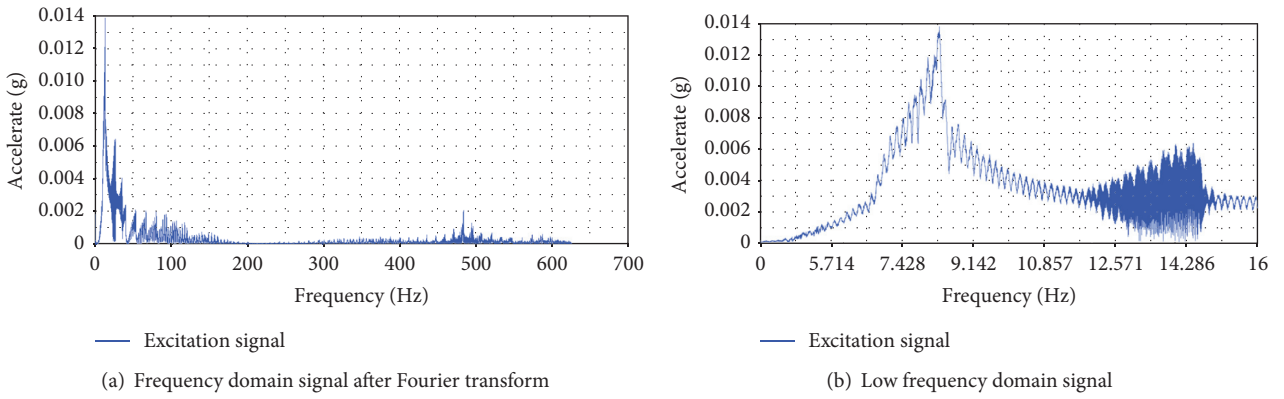


FIGURE 13

According to formula (13), frequency response excitation is carried out in the same excitation position with a unit sinusoidal excitation (amplitude of 1 mm/s^2), and sweep frequency range is $4 \sim 36 \text{ Hz}$. The curve of relative displacement between the two ends of the spring with frequency is shown in Figure 14.

It can be seen that the maximum relative displacement of the two ends of the spring is $A = 0.000176 \text{ mm}$ under the unit sinusoidal excitation with amplitude of 1 mm/s^2 .

Substituting formula (13):

$$\begin{aligned} \delta_B &\leq \delta_A \cdot \max [B(\omega)] = 0.000176 \times 134 \\ &= 0.0236 \text{ mm}. \end{aligned} \quad (14)$$

Thus, the peak value of the time-domain signal shown in Figure 11 is 0.76 g . After the Fourier transform, the excitation peak at the resonant point is 0.0134 g , and the resulting gap does not exceed 0.0236 mm . When the frequency excitation peak is 1 m/s^2 :

$$\begin{aligned} \delta_B &\leq \delta_A \cdot \max [B(\omega)] = 0.000176 \times 1000 \\ &= 0.176 \text{ mm}. \end{aligned} \quad (15)$$

The results show that when the frequency excitation amplitude is 1 m/s^2 , the gap will not exceed 0.176 mm .

5.2. Gap Evaluation of Car Seat Rail Joint under Uncertain Structure

5.2.1. Screening Influence Factors of Gap in Seat Rail Joint.

In order to study the influence of eight factors on the gap of the joint, experiments need to be designed to screen out the factors that have an important impact to focus on inspection. The first-round selection is determined by using the Hammersley design method, which is uniform and robust in multidimensional problems. The values of each factor are interval uncertain values, which belong to an infinite number of theoretical levels. The optimization problem is defined in HyperStudy, including defining eight factors as design variables and assigning the initial value and the upper and lower limits, as shown in Table 7.

As can be seen from Figure 13, the random excitations in the time domain are applied. In a transient analysis, the relative displacement of the balls assumes a normal distribution. For a normal distribution, the confidence can be predicted from the mean and the equation. In a similar way, when considering a random structure, four responses, as shown in Table 7, which correspond to 90%, 95%, 99%, and 100% confidence in the case of random loads, can be defined as the relative displacement. In a transient analysis, all four responses are deterministic, but after a set of randomized

TABLE 7: Valve table of experimental design variable.

Factor	Notes	Lower limit	Initial value	Upper limit
t_{up}	Internal rail thickness (mm)	1.30	1.40	1.50
t_{down}	Outer rail thickness (mm)	1.30	1.40	1.50
E	Elastic modulus of guide material (Mpa)	200000	210000	220000
ν	Poisson's ratio of guide material	0.27	0.3	0.33
ρ	Guide material density (T/mm ³)	$7.70e-9$	$7.80e-9$	$7.90e-9$
r_{up}	Ridge radius of inner rail (mm)	-1	0	1
r_{down}	Ridge radius of outer rail (mm)	-1	0	1
d	Manufacturing error of ball diameter (mm)	-1	0	1

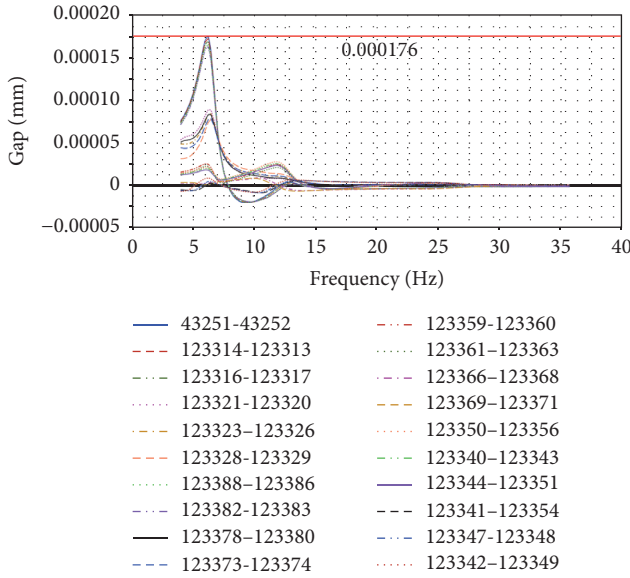


FIGURE 14: The relative displacement-frequency curve of the two ends of the spring.

studies based on the response surface, these four responses show some distribution.

In Table 8, \vec{v}_i-A and \vec{v}_i-B represent the displacement response of the spring-damper element to the inner and outer rail joints, respectively, expressed in a one-dimensional vector. t_{up}' and t_{down}' are the inner and outer rail thickness after deformation. N represents the total number of points in the time course; sum and sqrt are the one-dimensional vector summation and the root function, respectively. In addition, gap represents the maximum gap, meaning the maximum value of the gap in one transient analysis. The other three are 99%, 95%, and 90% of the gap, and the confidence value is 99%. For example, in a transient analysis, the gap in the time domain is 99% may not exceed this value. The other three responses can be studied in the same way.

After the design variables and response definitions are complete, the main effect is calculated using the DOE method of the Hammersley sampling design, and several factors that have the greatest effect on the response are selected as shown in Figure 14. Table 9 lists the main effects of the Hammersley sampling design (Figure 15).

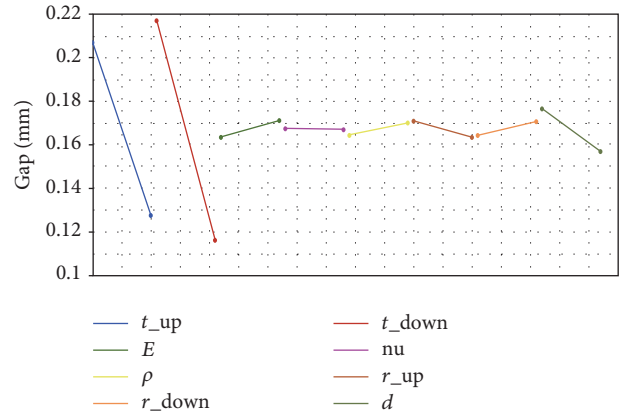


FIGURE 15: The schematic diagram of the main effect of the design of the Hammersley sampling.

It can be determined that the inner rail thickness (t_{up}), the outer rail thickness (t_{down}), and the ball diameter manufacturing error (d) have an important effect on the response (gap_{max}).

5.2.2. *The Random Structure Distribution under Different Excitation Confidences.* The internal rail thickness (t_{up}), outer rail thickness (t_{down}), and ball diameter manufacturing error (d) as design variables, to meet the normal distribution, are shown in Table 10.

According to the distribution of the parameters in Table 10, the Hammersley samples were used to generate a set of 1000 combinations of design variables to extract the response values, and four confidence intervals were obtained.

Under a transient load, the clearance corresponding to the outside confidence is defined as shown in the definition in Table 8. In a set of randomness studies based on the response surface, the gap will exhibit some distribution. The random distribution of gaps and the confidence table are shown in Figure 16.

Figure 16 shows the stochastic distribution of 90, 95%, 99%, and 100% confidence intervals of random load. Combining the above studies, considering the joint distribution of load and structure random, the joint confidence interval joint table can be obtained, as shown in Table 11.

It can be seen that with the increase of the load confidence and the structural confidence, the joint gap tends to increase,

TABLE 8: Gap responses of different confidences.

Response	Confidence	Definitions
$\text{gap}_{\mu+1.65\sigma}$	90%	$\text{gap}_{\mu+1.65\sigma} = \frac{\sum(\vec{v}_{i_A} - \vec{v}_{i_B})}{N} + 1.65 * \left(\frac{\text{sqrt}\left(\frac{\sum\left(\left(\vec{v}_{i_A} - \vec{v}_{i_B}\right) - \sum\left(\vec{v}_{i_A} - \vec{v}_{i_B}\right)/N\right)^2}{N}\right)}{N} \right)$
$\text{gap}_{\mu+1.96\sigma}$	95%	$\text{gap}_{\mu+1.96\sigma} = \frac{\sum(\vec{v}_{i_A} - \vec{v}_{i_B})}{N} + 1.96 * \left(\frac{\text{sqrt}\left(\frac{\sum\left(\left(\vec{v}_{i_A} - \vec{v}_{i_B}\right) - \sum\left(\vec{v}_{i_A} - \vec{v}_{i_B}\right)/N\right)^2}{N}\right)}{N} \right)$
$\text{gap}_{\mu+2.58\sigma}$	99%	$\text{gap}_{\mu+2.58\sigma} = \frac{\sum(\vec{v}_{i_A} - \vec{v}_{i_B})}{N} + 2.58 * \left(\frac{\text{sqrt}\left(\frac{\sum\left(\left(\vec{v}_{i_A} - \vec{v}_{i_B}\right) - \sum\left(\vec{v}_{i_A} - \vec{v}_{i_B}\right)/N\right)^2}{N}\right)}{N} \right)$
gap_{\max}	100%	$\text{gap}_{\max} = \max(\vec{v}_{i-A} - \vec{v}_{i-B}) - \left(\frac{t_{\text{up}}'}{2} + \frac{t_{\text{down}}'}{2} - 1.4 \right)$

TABLE 9: The sampling design and the main effect of the value of Hammersley.

Variable name	Main effect
t_{up}	-0.08
t_{down}	-0.101
E	0.007
ν	0.001
ρ	0.005
r_{up}	-0.007
r_{down}	-0.006
d	-0.02

and the effect of the load uncertainty is greater than the structural uncertainty.

Based on the above conclusions, consider the gap value of 0.1968 mm as the recommended installation preload value, using 90% of the structure confidence external and 99% of the load confidence. The specific basis is as follows.

The impact of load uncertainty is higher than the degree of structural uncertainty, which can be key consideration.

In reality, structural uncertainty cannot be measured directly. It is difficult to accurately control.

In engineering fields, seat manufacturers preload the rail to the value of 0.2 mm when they solve the problem of abnormal noise, which also shows that the research work done in this paper accurately predicts the rail preload value, providing theoretical basis to solve this problem.

6. Conclusions

With passengers' increasing requirements of comfort, noise, vibration, and harshness (NVH) have become one of the major concerns of car manufacturers. In this paper, the study of the gap between the car seat rail joints is a component-level NVH problem. By studying the finite element dynamic model of the car seat rail joint, the problem of the gap

distribution of the joint is analyzed according to a series of dynamic responses under the uncertainty of the external load. Furthermore, in the case that the structural parameters of the guide rail itself are uncertain, the randomness of the gap was also studied in this paper. The significance of this paper is predicting the distribution of gap in the joint of car seat guide rail by finite element simulation and providing the guiding value of installation preloading, which provides not only a solution but also the theoretical basis for field engineer to solve the problem of track abnormal sound.

The research results completed in this paper are listed as follows:

(1) Based on a certain model of car seat rail, the modal experiment and sweep experiment are carried out. Through these two experiments, the dynamic performance of the car seat guide is further studied.

(2) The finite element dynamic model of automobile seat rail is established in HyperMesh. The coupling part is embedded in a spring-damping unit, and the contact behavior of the joint is characterized by stiffness and damping. The stiffness and damping are optimized by the combination of experiment and finite element optimization software, so as to ensure the modeling accuracy of the finite element dynamic model.

(3) Under the condition that the external load of the seat rail is uncertain, a series of dynamic analyses of the guide rail is carried out. The joint gap is studied by the dynamic response of the spring-damping unit embedded in the joint. Then the reliable prediction of the gap is analyzed statistically, which is found to be 0.180 mm. In other words, when considering the random load, it is recommended to preload 0.180 mm when the rail is installed.

(4) The dynamic behavior of the spring-damper element is studied under the consideration of the structural uncertainties of the guide rail itself. The authors use the DOE to screen out the important influence own uncertainty factors and then carry on the randomness research. The results show that the distribution of influencing factors has little effect on the final distribution of interfacial gap.

TABLE 10: Random distribution table of design variables.

Factor	Random distribution	Parameter a (mm)	Parameter b (mm ²)
t_{up}	Normal distribution (μ, σ^2)	1.40	0.0015
t_{down}	Normal distribution (μ, σ^2)	1.40	0.0015
d	Normal distribution (μ, σ^2)	0	0.1

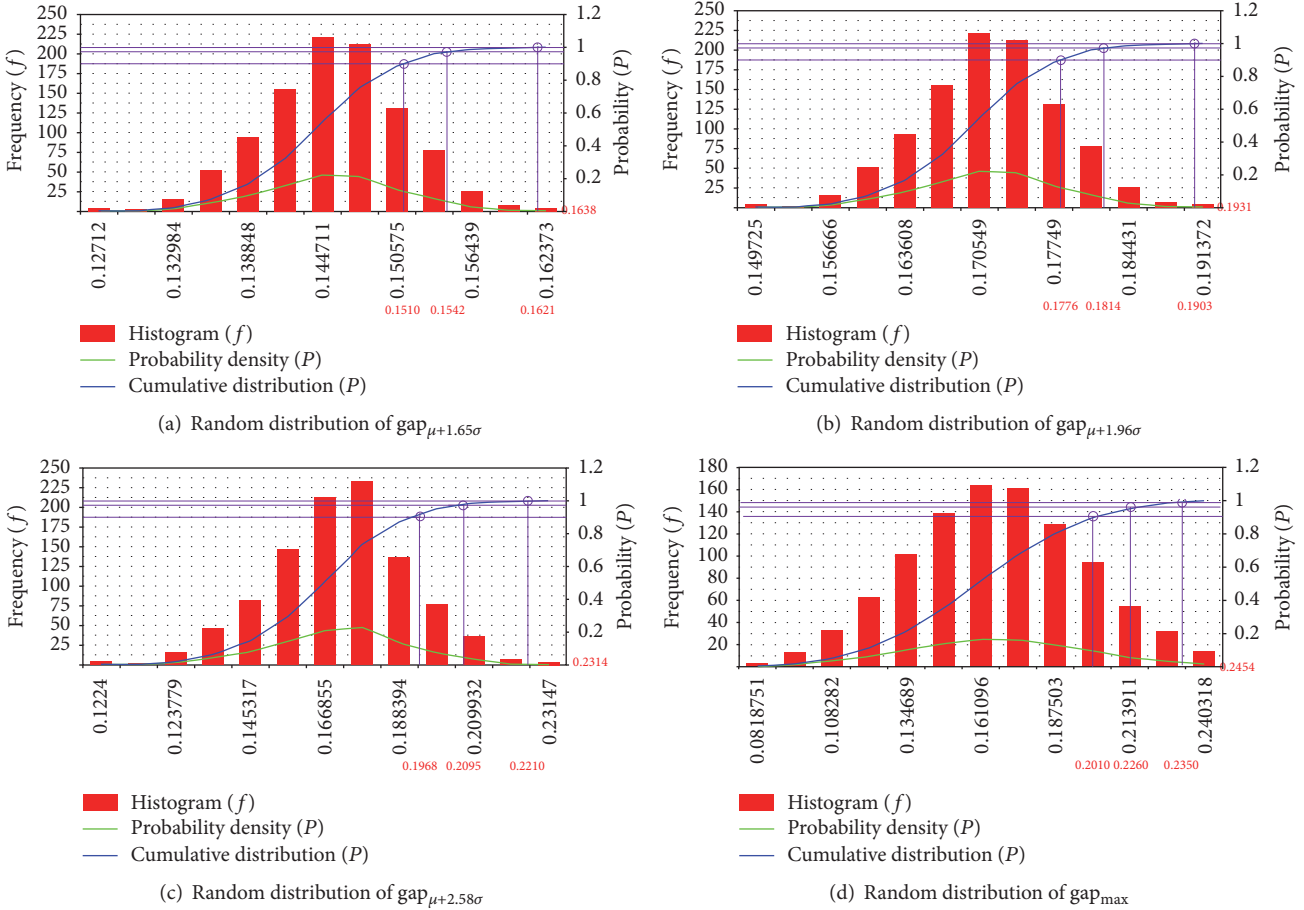


FIGURE 16

TABLE 11: Confidences of junction gap (mm).

Load confidence	Structural confidence External			
	90%	95%	99%	100%
90%	0.1510	0.1542	0.1621	0.1638
95%	0.1776	0.1814	0.1903	0.1931
99%	0.1968	0.2095	0.2210	0.2314
100%	0.2010	0.2260	0.2350	0.2454

(5) Based on the randomness study, the joint confidences are given under the influence of two kinds of uncertainties of load and structure. The reliable gap prediction value is 0.197 mm. In other words, in considering the load and structural random factors, it is recommended to preload 0.197 mm when the rail is installed.

Conflicts of Interest

There are no conflicts of interest regarding the publication of this paper.

Acknowledgments

Thanks are due to the support of the Civil-Military Integration Project of Shanghai, no. 201643.

References

- [1] L.-I. Zhang, "Analysis and Enlightenment of Global Automobile Industry Value Chain - Taking GM, Ford, Volkswagen and Toyota as examples," *Value Engineering*, vol. 3, pp. 47–49, 2006.
- [2] J. He, G. Shen, and W. Tie-gang, "Visuality of NVH in Vehicle [J]," *Bus Technology and Research*, vol. 5, pp. 15–17, 2007.

- [3] J. Zhang, *Optimization Design and Research of Powertrain Mounting System for Light Buses*, Wuhan University of Science and Technology, Wuhan, China, 2013.
- [4] W. Jian-Jun, Y. Chang-Bo, and L. Qi-Han, "Stochastic Finite Element Method in Engineering [J]," *Acta Mechanica Sinica*, vol. 26, no. 2, pp. 297–303, 2009.
- [5] M. Kamiński, "The Stochastic Perturbation Method for Computational Mechanics," *The Stochastic Perturbation Method for Computational Mechanics*, 2013.

Research Article

Vibration Analysis for Monitoring of Ancient Tie-Rods

L. Collini, R. Garziera, and K. Riabova

Department of Engineering and Architecture, University of Parma, Viale Delle Scienze 181/A, 43124 Parma, Italy

Correspondence should be addressed to K. Riabova; ksenia.riabova@gmail.com

Received 26 April 2017; Accepted 20 June 2017; Published 20 August 2017

Academic Editor: Pedro Galvín

Copyright © 2017 L. Collini et al. This is an open access article distributed under the Creative Commons Attribution License, which permits unrestricted use, distribution, and reproduction in any medium, provided the original work is properly cited.

This paper presents an application of vibration analysis to the monitoring of tie-rods. An algorithm for the axial load estimation based on experimentally measured natural frequencies is introduced and its application to a case study is reported. The proposed model of a tie-rod incorporates elastic bed-type boundary conditions that represent the contact between stonework and the tie-rod. The weighed differences between experimentally and numerically determined frequencies are minimized with respect to the parameters of the model, the main being the axial load and the stiffness at the tie-rod/wall interface. Thus, the multidimensional optimization problem is solved. Results are analysed in comparison to a model with simple fixed-end boundary conditions. In addition, the analytical formulation of the problem is delivered.

1. Introduction

The present paper reviews the applications of vibration analysis to the monitoring of the so-called “*tie-rods*.” Tie-rods are metal beams used in a wide range of civil constructions. The main purpose of these structural elements is to provide support for masonry arches and vaults in ancient buildings, like churches, cathedrals, and castles, which are known to lurch and founder in course of time. Tie-rods are subjected to axial tension and, thus, help the building resist lateral loads exerted by walls and facades. Figure 1 pictures a typical layout of tie-rods supporting arches of the first floor terrace in the medieval *Castello di Torrechiara* (Castle of Torrechiara) in the province of Parma, Italy.

Over the years, deformations of masonry walls and eventual displacements in the building may cause significant changes in the axial loads of tie-rods. In the extremes, this can lead to either of two scenarios: failure in structural integrity of tie-rods (damages and cracks) or loss of loads and subsequent performance decline, a phenomenon referred to as the “laziness” of tie-rods. Both of the scenarios are dangerous for the safety and integrity of buildings and can lead to irretrievable harm to the precious historical heritage of the human race. For this reason regular monitoring of tie-rods’ condition is of a great importance.

Health monitoring of tie-rods includes two major steps. The first one is identification of axial load and the second

one is damage identification. As for the first one, multiple methods have been developed to accomplish this task and the details on the state of art are provided in the next section. Such experimental techniques should be as less invasive as possible and at the same time provide sufficient data on the beam condition. Generally this type of testing is referred to as “nondestructive.”

In particular, nondestructive testing (NDT) is the process of investigating structures and elements for characteristics, discontinuities, changes in properties, and so forth without harming the continuity and usability of the part under testing. One of the relatively cheap, easily executable, and reliable NDT techniques is vibration analysis (VA). This way of health monitoring of the structures can be applied to testing whole buildings as well as its smallest parts depending on the scope and approach used. VA is based on investigation of dynamics of a structure under a certain excitation: it can be an impact hammer or a shaker. The response to the excitation is registered via sensors: accelerometers, optic sensors, laser, and so forth. Vibrational response contains information about the main structural characteristics of the system: mass and stiffness. Based on the knowledge of modal parameters, conclusions are drawn on the loading and structural integrity of the elements.

A reliable experimental technique helps to validate analytical and numerical models used for prediction of cracked beam dynamics. The purpose of this research is to develop a



FIGURE 1: Tie-rods in the Castle of Torrechiara in Langhirano, Parma, Italy.

VA procedure based on quantitative and qualitative analysis of frequency response functions.

The further sections describe a method for axial load identification in tie-rods developed by the Department of Industrial Engineering of the University of Parma. This approach combines in situ dynamic tests and computations that make use of a beam model with complex boundary conditions. The method was tested and improved throughout some years since it was applied for multiple case studies of monitoring such famous Italian historic buildings as *Duomo di Parma* (Cathedral of Parma), *Basilica della Madonna dell'Umiltà* in Pistoia (Church of Our Lady of Humility), *Rocca Sanvitale di Fontanellato* (Sanvitale Fortress of Fontanellato), and *Casa Romei* (Romei House) in Ferrara, as reported by the authors Collini et al. in [1–7].

2. State of the Art in Axial Load Identification in Tie-Rods

The structural characterization of tie-rods is crucial for the safety assessment of historical buildings. The main parameters that characterize the behaviour of tie-rods are the tensile force, the modulus of elasticity of the material, and the rotational stiffness at both restraints. In the last decades several techniques for an indirect nondestructive evaluation of such parameters have been proposed. The nondestructive procedures currently available for the structural characterization of tie-rods can be grouped in static, static-dynamic, and pure dynamic approaches. Pioneering static methods presented, for instance, in works of Pozzati [8] and in [9, 10], in spite of minor differences, are based on measures of displacement and/or strain at few cross-sections of the tie-rod due to applied static loads. Bati and Tonietti introduced a static approach for force identification that consisted of measuring three vertical displacements and strains variations at three sections of the tie-rod under a concentrated load [10]. Even if the data postprocessing is quite straightforward, these methods are extremely sensitive to the experimental error in the measures of displacement. In addition, since tie-rods

are usually positioned at considerable heights, the need of measuring vertical deflections with respect to a reference fixed base makes static methods difficult in practice.

Mixed approaches try to identify the unknown parameters by combining static and dynamic measures. Blasi and Sorace [11–13] modelled tie-rods as simply supported Euler beams with rotational springs of similar stiffness added on each edge. The stiffness of the spring and the force were the two unknowns obtained from the system of equations, built with a static equation for deflection and a dynamic equation for natural frequencies. Thus, this method required data from two separate experiments, that is, in situ measurements of the central deflection under static load and of the fundamental natural frequency, which can be obtained by hammer impact testing and Fourier transforming the recorded accelerations. Testing of this method in laboratory conditions showed good results; however, measurement errors can cause significant deviation in results for the two unknowns. Even though static-dynamic methods can exploit additional dynamic information for the characterization, they are still affected by the shortcomings related to deflection measurements.

Such drawbacks are avoided in pure dynamic procedures [14–28], where, in general, the difference between the experimental and the calculated natural frequencies of vibration is minimized in order to identify the unknown parameters.

Lagomarsino and Calderini [14] developed an algorithm to identify the axial tensile force in ancient tie-rods by using the first three natural frequencies. The tie-rod was modelled as an Euler beam of uniform cross-section, neglecting the shear deformation and rotary inertia, and was assumed to be simply supported at the ends with additional rotational springs.

Recently Maes et al. introduced a method that enables definition of axial loads in slender beams with unknown boundary conditions, taking into account effects of rotational inertia of the beam and masses of sensors [15]. However, it requires data from five or more sensors along the length of the beam to determine all the introduced unknowns of the inverted problem. A similar technique of the axial force identification was developed by Li et al. [16], focusing on studies of Euler–Bernoulli beams and takes into account bending stiffness effects.

Rebecchi et al. established an analytical method of processing experimental data from five instrumented sections of a prismatic slender beam, which showed excellent results in estimation of the axial load in tie-rods [17]. The method does not require any exact value of effective length of the beam but neglects both rotary inertia and shear deformations effects in the solution for beam vibrations. For cases of similar beams their colleagues Tullini et al. proposed a static method of axial force identification [18–20]. The analytical algorithm makes use of any set of experimental data represented by flexural displacements or curvatures measured at five cross-sections of the beam subjected to an additional concentrated lateral load. Gentilini et al. developed in [21] a procedure that combines dynamical testing with FEM simulations using added masses. The method was tested out for tie-rods of various lengths and load intensity, showing reliable results.

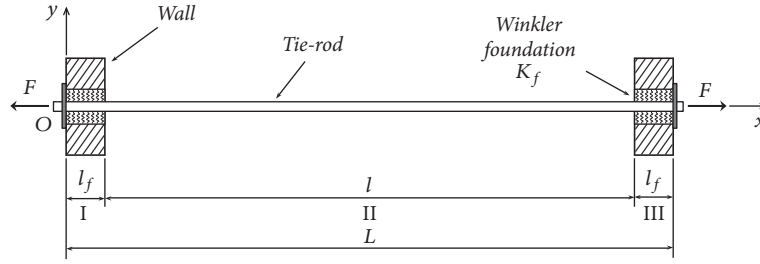


FIGURE 2: Tie-rod with elastic bed-type boundaries.

Livingston et al. identified the tensile force in prismatic beams of uniform section by using modal data and assuming rotational and vertical springs at each end of the beam [22]. Shear deformation and rotary inertia were neglected (according to the Euler beam model).

Another fully dynamic procedure has been proposed by Kim and Park [23]. It allows identifying the tension force and flexural and axial stiffness of the cable from measured natural frequencies. Anyway this technique is not immediately applicable to tie-rods since they cannot be modelled as cables and present uncertain constraints due to the portion of the rod inserted into the masonry wall or column.

Amabili et al. [1–6] developed a two-step method consisting of in situ measurements of tie-rods' natural frequencies and further elaboration of the data via an optimization algorithm based on the Rayleigh–Ritz method [7]. Varying certain parameters, the main of which was the sought axial load, this algorithm matched estimated sets of frequencies with those determined from experiments. The considered numerical models allowed analysis of ancient tie-rods affected by non-perfect constraints, added masses, discontinuities, irregular cross-sections, and complex boundary conditions. Different importance of the natural frequencies can be as well taken into account. The technique is of simple execution and allows minimizing the measurement error. Its functionality and reliability have been proved as it has been applied with success to many case studies.

3. Dynamic Method for Load Identification

The first step of the method is the in situ experimental identification of natural frequencies of the tie-rods by measuring the frequency response functions (FRFs) via instrumented hammer excitation. Precisely the testing technique used for the investigation of tie-rods in Casa Romei located in the city of Ferrara, Emilia-Romagna, Italy, was described in [1–3]. The first four to six natural frequencies, which can be extracted with high precision, were in the focus. Subsequently, an axially loaded tie-rod was modelled in finite element method (FEM) software Abaqus 6.13 as a general case of a Timoshenko beam, using three-dimensional beam elements retaining shear deformation and rotational inertia. The parametric model enabled considering nonuniform cross-sections of rods, since this is often the case for hand-made tie-rods in old buildings.

The interface tie-rod/wall was assumed to be a continuous elastic bed; that is, extremities of tie-rods inserted inside

masonry walls were modelled as resting on Winkler-type foundation. This type of boundary has been used in dynamics of particular cases, for example, for beams or rails subjected to travelling loads, as reported by Farghaly and Zeid [29], Ruge and Birk [30], and Koroma et al. [31]. In our case we discretized the elastic bed into separate springs equispaced along the length of the bed l_f , each of a stiffness k_f (see Figure 2).

Clearly, the foundation may have a nonuniformly distributed stiffness, which would result in different k_f assigned to each spring. The advantage of the Winkler bed compared to other types of boundaries generally used for tie-rods is that a number of springs placed closely exhibit more complex behaviour than linear and/or rotational springs attached to a single node. Hence, it is a reliable way of modelling a real wall-rod contact condition. The optimization parameters in this case were the unknown axial load, the stiffness of the foundation, and the length of the rod inside the wall. In real cases the lengths of the extremities inserted into the masonry and the stiffness of the foundation most likely differ for each end of the tie-rod. This complication has been avoided in the reported case study; however, the method proposed hereby is capable of taking into account other desired parameters of the model.

3.1. Analytical Formulation of the Problem. As shown in Figure 2, tie-rod was divided into three sections of length l_f , section I; l , section II; and again l_f , section III, where l_f identifies the portion inserted into the wall and l is the measured “free” length. At the tips of the rod free-end boundary conditions were applied and between the sections, correspondingly, the conditions of congruence.

Assuming the hypotheses of Bernoulli–Euler beam theory for the analytical formulation, we chose to neglect the shear deformation and rotational inertia, because the subject of this study was a slender rod, for which the ratio of linear dimensions of cross-sections to length is a very small number.

The energy approach was used to obtain the equations of motion via Lagrangian of the system [1]. Thus, the energy functionals were given by (1)–(4) as follows.

Kinetic energy is

$$T = \frac{1}{2} \int_0^L \left[\rho A \left(\frac{\partial w}{\partial t} \right)^2 + \rho I \left(\frac{\partial^2 w}{\partial x \partial t} \right)^2 \right] dx. \quad (1)$$

Potential energy of elastic strain is

$$U = \frac{1}{2} \int_0^L \left[EI \left(\frac{\partial^2 w}{\partial x^2} \right)^2 \right] dx. \quad (2)$$

Potential energy associated with the axial load is

$$V_F = \frac{1}{2} \int_0^L \left[F \left(\frac{\partial w}{\partial x} \right)^2 \right] dx. \quad (3)$$

Potential energy associated with the elastic foundation is

$$V_w = \frac{1}{2} \int_0^L K_f w^2 \left[H(l_f - x) + H(x - L + l_f) \right] dx. \quad (4)$$

Total potential energy is

$$\Pi = U + V_F + V_w. \quad (5)$$

The Heaviside function $H(x)$ in (4) allows us to write down a single expression for the whole tie-rod, taking into account different conditions for its parts.

We proceeded defining the Lagrangian of the system, which is equal to the difference between the overall kinetic and potential energy:

$$L \left(w, \frac{\partial w}{\partial x}, \frac{\partial w}{\partial t}, \frac{\partial^2 w}{\partial x^2}, \frac{\partial^2 w}{\partial x \partial t} \right) = T - \Pi. \quad (6)$$

Applying Hamilton's principle, we obtained the system of Lagrange equations of motion (7), where q_k indicated every generalized coordinate (degree of freedom) and the number of differential equations was equal to the number of dofs. In our case the degree of freedom was represented by the function $w(x, t)$.

$$\frac{\partial}{\partial t} \left(\frac{\partial L}{\partial \dot{q}_k} \right) - \frac{\partial L}{\partial q_k} = 0. \quad (7)$$

Sequentially substituting (1)–(5) into (6) and then differentiating the Lagrangian as shown in (7), we obtained the equation of natural vibrations of the rod:

$$EI \frac{\partial^4 w}{\partial x^4} + \rho A \frac{\partial^2 w}{\partial t^2} - F \frac{\partial^2 w}{\partial x^2} + K_f w \left[H(l_f - x) + H(x - L + l_f) \right] = 0. \quad (8)$$

As stated above, the ends of tie-rods (where $x = 0$ and $x = L$) were considered free and between parts I-II and II-III

eight conditions of continuity emerged; this provides twelve conditions that were expressed in form of the following:

$$\begin{aligned} x = 0 : & \begin{cases} Q_I = 0 \\ M_I = 0, \end{cases} \\ x = L : & \begin{cases} Q_{III} = 0 \\ M_{III} = 0, \end{cases} \\ x = l_f : & \begin{cases} w_I = w_{II} \\ \frac{\partial w_I}{\partial x} = -\frac{\partial w_{II}}{\partial x} \\ Q_I = Q_{II} \\ M_I = M_{II}, \end{cases} \\ x = L - l_f : & \begin{cases} w_{II} = w_{III} \\ \frac{\partial w_{II}}{\partial x} = -\frac{\partial w_{III}}{\partial x} \\ Q_{II} = Q_{III} \\ M_{II} = M_{III}. \end{cases} \end{aligned} \quad (9)$$

The shearing force Q and the bending moment M were defined by

$$Q = EI \frac{\partial^3 w}{\partial x^3} - F \frac{\partial w}{\partial x}, \quad (10)$$

$$M = EI \frac{\partial^2 w}{\partial x^2}.$$

For each section of the tie-rod (see Figure 2 for the reference system), a separate function w was introduced: $w_I(x, t)$, $w_{II}(x, t)$, $w_{III}(x, t)$. The differential equation of motion (8) was solved by means of the Fourier method (11), where $W_i(x)$ is the form function, $\tau_i(t)$ is the time function, and i takes on a value from 1 to 3 according to each section of the rod.

$$w_i(x, t) = W_i(x) \tau_i(t). \quad (11)$$

It is evident that the parts vibrate with the same time frequency; thus, we could get rid of the index i in $\tau_i(t)$. For the time function we obtained (12) for all three sections of the rod, with ω being a natural frequency in rad/s and B_1 and B_2 being coefficients defining the phase.

$$\tau(t) = B_1 \cos \omega t + B_2 \sin \omega t. \quad (12)$$

After the substitution of (12) and (11) into (8), the form of (13) for parts I, III, and II was delivered.

$$\begin{aligned} \frac{d^4 W_{II}}{dx^4} - \frac{F}{\rho A c^2} \frac{d^2 W_{II}}{dx^2} - \frac{\omega^2}{c^2} W_{II} &= 0, \\ \frac{d^4 W_{I,III}}{dx^4} - \frac{F}{\rho A c^2} \frac{d^2 W_{I,III}}{dx^2} + \left(\frac{K_f}{\rho A c^2} - \frac{\omega^2}{c^2} \right) W_{I,III} &= 0. \end{aligned} \quad (13)$$

Ordinary differential equations (13) were solved using the general solution given as

$$W_{I,II,III}(x) = Ce^{sx}. \quad (14)$$

Further, the algebraic equations (15) in coefficients s were obtained throughout substitution of the general solution (14) into the differential equations (13).

$$s_{II}^4 - \frac{F}{\rho Ac^2} s_{II}^2 - \frac{\omega^2}{c^2} = 0, \quad (15)$$

$$s_{I,III}^4 - \frac{F}{\rho Ac^2} s_{I,III}^2 + \left(\frac{K_f}{\rho Ac^2} - \frac{\omega^2}{c^2} \right) = 0.$$

Each of equations in (15) provided correspondingly four solutions for s : two complex $s_3 = \pm ik_3$ and two real roots $s_4 = \pm k_4$ for the first equation and four complex roots $s_{1,2} = \pm k_1 \pm ik_2$ for the second one. All of the parameters s in a certain form contain ω , F , and K_f . Still, to keep our expressions

simplified, we used parameters s in the form functions for the natural modes of the tie-rod:

$$W_I(x) = C_1 e^{s_1 x} + C_2 e^{-s_1 x} + C_3 e^{s_2 x} + C_4 e^{-s_2 x},$$

$$W_{II}(x) = C_5 e^{s_3 x} + C_6 e^{-s_3 x} + C_7 e^{s_4 x} + C_8 e^{-s_4 x}, \quad (16)$$

$$W_{III}(x) = C_9 e^{s_1 x} + C_{10} e^{-s_1 x} + C_{11} e^{s_2 x} + C_{12} e^{-s_2 x}.$$

Substituting the forms (16) into twelve conditions (9), we hence obtained a homogeneous system of twelve equations containing twelve unknowns $C_1 \dots C_{12}$, which in a matrix form is expressed as

$$[M] \{C\} = \{0\}. \quad (17)$$

In order to provide a nontrivial solution the determinant of the matrix M in (17) was supposed to be equal to zero (18), which resulted in a characteristic equation of the eigenvalue problem.

$$\det \begin{bmatrix} s_1^2 & s_1^2 & s_2^2 & s_2^2 & 0 & 0 & 0 & 0 & 0 & 0 & 0 & 0 \\ s_1^3 & -s_1^3 & s_2^3 & -s_2^3 & 0 & 0 & 0 & 0 & 0 & 0 & 0 & 0 \\ e^{s_1 l_f} & e^{-s_1 l_f} & e^{s_2 l_f} & e^{-s_2 l_f} & -e^{s_3 l_f} & -e^{-s_3 l_f} & -e^{s_4 l_f} & -e^{-s_4 l_f} & 0 & 0 & 0 & 0 \\ s_1 e^{s_1 l_f} & -s_1 e^{-s_1 l_f} & s_2 e^{s_2 l_f} & -s_2 e^{-s_2 l_f} & -s_3 e^{s_3 l_f} & s_3 e^{-s_3 l_f} & -s_4 e^{s_4 l_f} & s_4 e^{-s_4 l_f} & 0 & 0 & 0 & 0 \\ s_1^2 e^{s_1 l_f} & s_1^2 e^{-s_1 l_f} & s_2^2 e^{s_2 l_f} & s_2^2 e^{-s_2 l_f} & -s_3^2 e^{s_3 l_f} & -s_3^2 e^{-s_3 l_f} & -s_4^2 e^{s_4 l_f} & -s_4^2 e^{-s_4 l_f} & 0 & 0 & 0 & 0 \\ s_1^3 e^{s_1 l_f} & -s_1^3 e^{-s_1 l_f} & s_2^3 e^{s_2 l_f} & -s_2^3 e^{-s_2 l_f} & -s_3^3 e^{s_3 l_f} & s_3^3 e^{-s_3 l_f} & -s_4^3 e^{s_4 l_f} & s_4^3 e^{-s_4 l_f} & 0 & 0 & 0 & 0 \\ 0 & 0 & 0 & 0 & e^{s_3(L-l_f)} & e^{-s_3(L-l_f)} & e^{s_4(L-l_f)} & e^{-s_4(L-l_f)} & -e^{s_1(L-l_f)} & -e^{-s_1(L-l_f)} & -e^{s_2(L-l_f)} & -e^{-s_2(L-l_f)} \\ 0 & 0 & 0 & 0 & s_3 e^{s_3(L-l_f)} & -s_3 e^{-s_3(L-l_f)} & s_4 e^{s_4(L-l_f)} & -s_4 e^{-s_4(L-l_f)} & -s_1 e^{s_1(L-l_f)} & s_1 e^{-s_1(L-l_f)} & -s_2 e^{s_2(L-l_f)} & s_2 e^{-s_2(L-l_f)} \\ 0 & 0 & 0 & 0 & s_3^2 e^{s_3(L-l_f)} & s_3^2 e^{-s_3(L-l_f)} & s_4^2 e^{s_4(L-l_f)} & s_4^2 e^{-s_4(L-l_f)} & -s_1^2 e^{s_1(L-l_f)} & -s_1^2 e^{-s_1(L-l_f)} & -s_2^2 e^{s_2(L-l_f)} & -s_2^2 e^{-s_2(L-l_f)} \\ 0 & 0 & 0 & 0 & s_3^3 e^{s_3(L-l_f)} & -s_3^3 e^{-s_3(L-l_f)} & s_4^3 e^{s_4(L-l_f)} & -s_4^3 e^{-s_4(L-l_f)} & -s_1^3 e^{s_1(L-l_f)} & s_1^3 e^{-s_1(L-l_f)} & -s_2^3 e^{s_2(L-l_f)} & s_2^3 e^{-s_2(L-l_f)} \\ 0 & 0 & 0 & 0 & 0 & 0 & 0 & 0 & s_1^2 e^{s_1 L} & s_1^2 e^{-s_1 L} & s_2^2 e^{s_2 L} & s_2^2 e^{-s_2 L} \\ 0 & 0 & 0 & 0 & 0 & 0 & 0 & 0 & s_1^3 e^{s_1 L} & -s_1^3 e^{-s_1 L} & s_2^3 e^{s_2 L} & -s_2^3 e^{-s_2 L} \end{bmatrix}. \quad (18)$$

Equation (18) is to be solved for the natural frequencies ω by means of, for instance, the Newton-Raphson method. Furthermore, the dispersion between analytically and experimentally determined frequencies can be minimized with respect to parameters F and K_f , following the optimization procedure described in the next sections. This approach in a closed form delivers solution for the sought axial load in tie-rod.

3.2. Numerical Model and Optimization Procedure. Tie-rods were modelled in FEM software using beam elements. In this case the beam is represented with a one-dimension body, that is, a wire (line, curve, polyline), and cross-section shapes and dimensions are assigned to this body as one of the properties, which allowed taking into account irregular cross-sections, added masses, elastic supports, and so forth. The beam model shows good results for analyses of long slender beams. For beam elements there is an option of modelling the axial tensile load as a bolt pretension load. Tie-rods were modelled

using 50–60 B31 2-node linear beam elements in 3D space implying Timoshenko's beam theory.

The FEM simulation was divided into two steps: as a first step a pretension load F was applied to the beam and as a second step the modal analysis was performed. The FEM model was parametric, since the tensile load and elastic foundation parameters were unknown. The idea here was to "tune" these parameters in order to match results of physical tests and FEM simulations. Optimization criterion given by (19) represented a residual error between n natural frequencies defined via experimental modal analysis $\{f_1^{\text{exp}}, \dots, f_n^{\text{exp}}\}$ and numerically $\{f_1^{\text{FEM}}, \dots, f_n^{\text{FEM}}\}$. The error function contained weight coefficients p_k arbitrary assigned to each natural mode. Hence, the minimum of the multiparameter function R delivered the optimal solution.

$$R = \sqrt{\sum_{k=1}^n p_k^2 (f_k^{\text{exp}} - f_k^{\text{FEM}})^2}. \quad (19)$$



FIGURE 3: Inner yard of Casa Romei and zoom of the ground floor tie-rods.

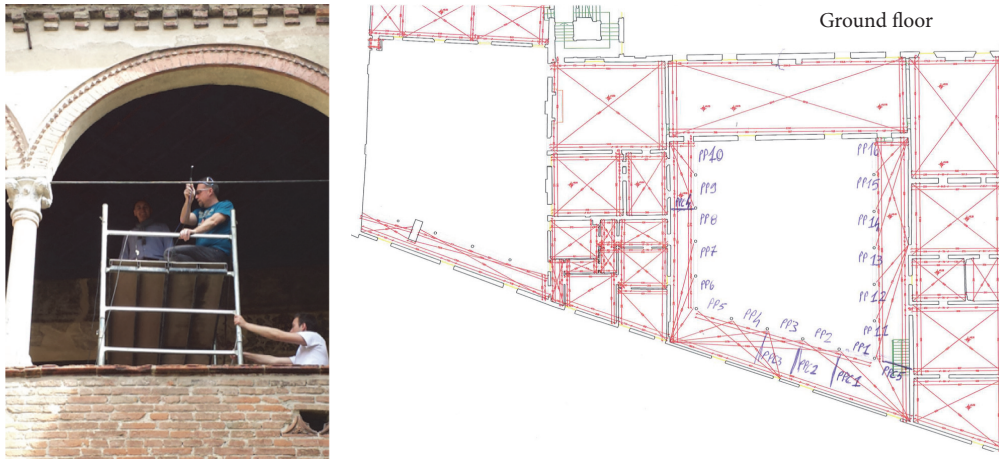


FIGURE 4: Our team during hammer excitation of a tie-rod; map of ground floor.

By using a parametric FEM model the representation of a tie-rod became flexible and first 6 natural frequencies were matched with overall accuracy up to 1%. Parameterisation of the FEM model was achieved by direct coding of the analysis input file, since parametric analysis is not enabled inside the graphical interface of Abaqus. Afterwards the script was executed automatically inside the optimization program coded in C. The latter program automatically extracted the required results from the text files with analysis outputs created by Abaqus.

As a first iteration we analytically investigated the function R (19) for a tie-rod with fixed and/or simply supported conditions, with length L and axial load F being optimization parameters. On a reasonable range of optimization parameters the residual error (19) had only a forced minimum at the minimal value of the length parameter. The found absolute minimum was lying, however, below the measured length of a tie-rod. This behaviour proved the necessity of modelling more complex boundary conditions. However, this first iteration provided a rough idea of the sought axial load and we could set the range for F around this value.

Subsequently we modelled the elastic bed boundaries, representing a general condition of translational and rotational stiffness acting for the length l_f , as in the sketch displayed in Figure 2. Elastic bed consists of equispaced linear

elastic springs each of stiffness k_f . Further the optimization has been done with respect to the sought axial load and the parameters of elastic foundation. We needed to provide sets of experimentally obtained frequencies, ranges, and step sizes of optimization parameters and sets of weight coefficients p_k to the code in C that

- (i) forms a matrix of parameters;
- (ii) launches the FEM analysis for each nod of the grid, extracts and filters natural frequencies from the output;
- (iii) calculates the value of residual error (19) for each step;
- (iv) finds the local minimum of the function (19) and the corresponding combination of parameters including the sought tensile load;
- (v) refines the grid of parameters and repeats the procedure again.

3.3. Application to a Case Study. The method described hereby was applied to investigation of tie-rods installed in “Casa Romei” located in Ferrara, Italy (see Figures 3 and 4). Romei House is a perfect example of a 15th century palace, in which you can see rich gothic decoration of the Late Middle

TABLE 1: Experimental acquisitions.

Tie-rod number	Cross-section A [mm ²]	Length l [mm]	Natural frequencies [Hz]					
			I	II	III	IV	V	VI
PT1	52×9	3178	15.30	—	49.00	—	92.30	—
PT2	51×9	3233	16.80	—	53.80	—	98.80	—
PT3	52×10	3228	16.30	—	53.80	—	103.00	—
PT4	51×10	3218	16.00	33.50	51.30	71.80	95.00	121.80
PT5	53×10	3188	5.50	—	28.30	—	65.50	91.00
PT6	50×20	2748	21.75	49.00	85.25	131.20	188.50	255.20
PT7	50×20	2768	20.00	45.50	80.00	123.80	179.20	242.20
PT8	50×20	3358	14.75	32.75	55.75	85.25	121.20	176.50
PT9	50×20	3248	15.50	34.25	58.75	90.00	128.00	173.00
PT10	50×20	3388	17.75	38.00	63.25	94.75	133.00	177.50
PT11	50×12	3440	13.25	29.75	51.25	78.25	111.50	150.80
PT12	50×12	3298	14.50	30.25	48.25	69.25	94.00	122.20
PT13	50×12	3140	13.75	—	47.25	—	95.75	—
PT14	50×12	2510	19.25	46.50	—	84.00	—	134.50

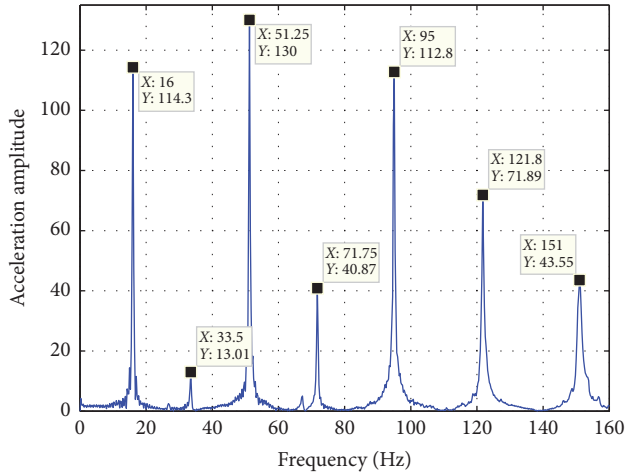


FIGURE 5: FRF plot (acceleration amplitude versus frequency).

Ages combine with elements of the Early Renaissance. Tie-rods have been placed in this building in different times along its existence, differing in dimensions and cross-section shapes.

First, measurements of geometrical characteristics and of natural frequencies were performed for each tie-rod. Then experimental acquisition was carried out to determine the natural frequencies from the analysis of response to dynamical excitation applied to tie-rods in horizontal plane; as an example, a frequency response function (FRF) for a ground floor tie-rod is shown in Figure 5.

For further analysis, first four to six natural frequencies were identified for each tie-rod. Six eigenmodes were considered sufficient, since identification of higher modes might appear inaccurate due to larger possible measurement errors.

Having performed multiple experimental studies of tie-rods, the authors concluded that the variation of the material was less significant than in the boundary conditions. Thus,

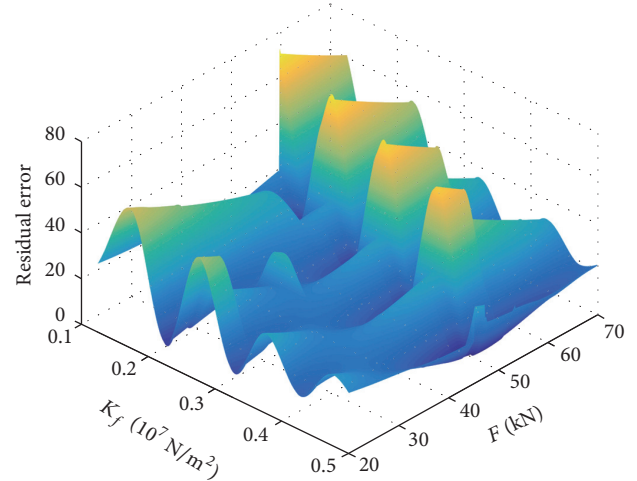


FIGURE 6: Residual error function as function of elastic bed stiffness and axial load.

the material properties were kept constant in this case study: material was assumed to be general iron with characteristics: $E = 210$ GPa, $\nu = 0.3$, $\rho = 7850$ kg/m³.

3.4. Load Identification Results. Table 1 summarizes the data on cross-section A , free length l , and natural frequencies of the ground floor tie-rods (see Figure 4 for layout). Some of the frequencies in Table 1 are missing, due to the eventual position of the accelerometer over a modal node; in these cases higher frequencies were considered in the optimization process.

A typical graphic scenario of the optimization process is depicted in Figure 6. Here several values of the function R (19) were plotted versus axial load F and distributed stiffness of the elastic bed K_f , for the tie-rod PT2. The length of elastic bed l_f (see Figure 2) was kept constant. It is notable that many minima are present in correspondence to certain F - K_f couples and one of them is a local minimum. The grid

TABLE 2: Summary of results.

Tie-rod number	Axial load F [kN]	Stress [MPa]	Bed stiffness K_f [10^7 MN/m 2]	Residual error
PT1	29.40	62.82	50.00	0.31
PT2	46.90	102.18	0.48	6.04
PT3	37.50	72.12	253.00	3.95
PT4	38.70	75.88	3.75	0.77
PT5	1.00	1.89	26.75	1.17
PT6	66.50	66.50	113.00	0.48
PT7	54.50	54.50	57.50	1.43
PT8	46.30	46.30	60.00	6.60
PT9	44.50	44.50	62.50	7.33
PT10	79.90	79.90	76.00	2.22
PT11	30.10	50.17	99.50	6.53
PT12	37.20	62.00	4.25	0.48
PT13	28.20	47.00	5.50	0.27
PT14	38.00	63.33	2.13	5.58

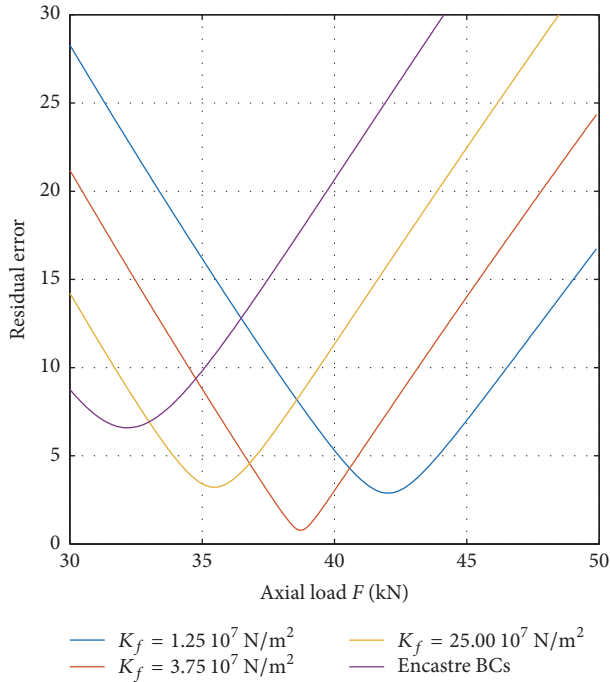


FIGURE 7: Influence of the elastic bed on the axial load determination.

of parameters F and K_f was then reduced around it, in order to refine the search of the optimal values.

Naturally, the so-defined minima of the residual error (19) were not independent; nevertheless, once the main parameter (axial load F) was optimized, the influence of stiffness of constraints on the first parameter was nearly negligible.

The model with elastic foundation boundaries delivered improvement of results as illustrated in Figure 7. The plot shows residual error curves for the tie-rod PT4 at different values of stiffness K_f compared to the clamped boundaries. It indicates that the minimum of the error (19) decreases from 6.59 (encastré BCs) to 0.77 for the optimal stiffness $K_f =$

3.75×10^7 N/m 2 . The corresponding optimal value of the axial load in this tie-rod increases by 20% from 32.20 kN (encastré BCs) to 38.70 kN (elastic bed). We presume that a model with simple clamped boundaries underestimated the axial load; thus, the proposed method reveals to be conservative for the load estimation.

Table 2 summarizes the results of the computation process of the reported case study.

3.5. Analysis of the Results. Tensile loads cause normal stresses that need to be estimated for evaluation of reliability and integrity of tie-rods. This safety assessment can be carried out based on the values of average axial stress $\bar{\sigma}_{k,N}$, to which each tie-rod is subjected. The stress was calculated with respect to the optimal axial load $F_{k,opt}$ and the minimum cross-section area $A_{k,min}$:

$$\bar{\sigma}_{k,N} = \frac{F_{k,opt}}{A_{k,min}}. \quad (20)$$

This stress (20) is average since it assumes a uniform section without taking into consideration such local effects as screws, fillets, holes, joints, and so forth that tie-rods might incorporate. However, these stress concentrators should be considered, if present, for correct local strength verification, eventually via FEM analysis.

In Figure 8 the stresses in rods PT1–PT14 are plotted. Apart from PT5, all tie-rods worked properly and below the allowable stress of 120 MPa for ancient iron. Rod PT5 was evidently unloaded, which indicated that there was either some damage or malfunction at the anchorages; the issue has been stated in the appropriate technical report of the case study. For comparison, Figure 8 reports also average stresses calculated for the case of encastré boundary conditions: safety improvement was definitely confirmed.

In Section 3.2 we introduced the residual error (19) to compute “distance” between experimental and numerical frequencies. In the formula the difference (in Hz) between each couple of frequencies is multiplied by a weight coefficient

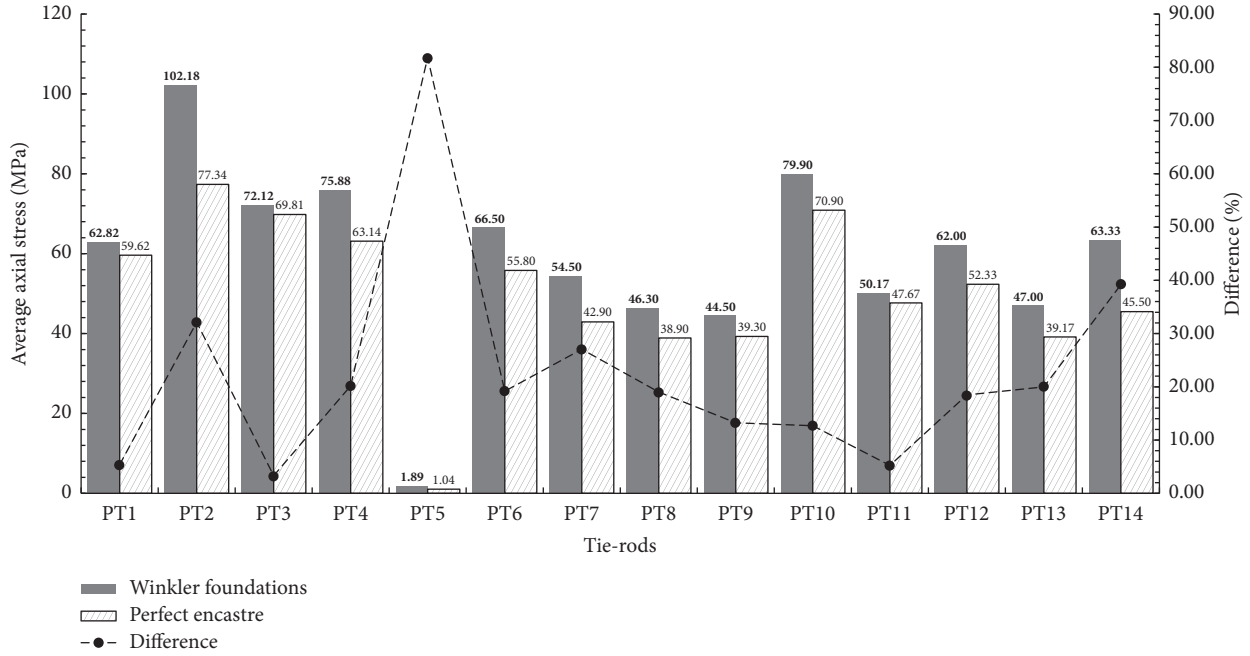


FIGURE 8: Average stress state in tie-rods: comparison between encasté and elastic foundation boundaries.

TABLE 3: Results of computation with three sets of weights for the tie-rod PT4.

Sets of weight coefficients	Axial load F [kN]	Bed stiffness K_f [10^7 MN/m 2]	Natural frequencies [Hz]					
			I	II	III	IV	V	VI
$W_1 = \{1, 1, 1, 1, 1, 1\}$	39.00	3.50	16.03	32.91	51.37	72.03	95.32	121.53
$W_3 = \{4, 1, 0.5, 0.25, 0.1, 0.05\}$	38.60	4.50	16.04	32.95	51.48	72.25	95.69	122.13
$W_2 = \{10, 1, 1, 1, 1, 1\}$ optimal values	38.70	3.75	16.00	32.85	51.31	71.97	95.28	121.55
W_2 , encasté BCs	32.20	∞	15.68	32.47	51.33	72.97	97.91	126.50
Experimentally defined frequencies			16.00	33.50	51.30	71.80	95.00	121.80

p_k in order to attribute higher or lower importance to some frequencies rather than others. The set of weight coefficients was arbitrary chosen, but generally higher importance has been given to the first frequencies.

A sensitivity analysis has been conducted to evaluate the influence of weight coefficients on our results. The plot in Figure 9 shows three residual error functions for the tie-rod PT4 corresponding to three different sets of weight coefficients. The sets taken into consideration were $W_1 = \{1, 1, 1, 1, 1, 1\}$, $W_2 = \{10, 1, 1, 1, 1, 1\}$, and $W_3 = \{4, 1, 0.5, 0.25, 0.1, 0.05\}$. We see that each set generated a different interpolated surface; however, the error reached minimum around the same value of the sought axial load, as reported in Table 3. Many other reasonable sets of weight coefficients have been tested, confirming their low influence on the resulting axial load, which proved the stability of our model with respect to these arbitrary assigned parameters.

4. Conclusions

In this paper a procedure for axial load identification in structural tie-rods was demonstrated and approved via an experimental study of an ancient mansion. The method is

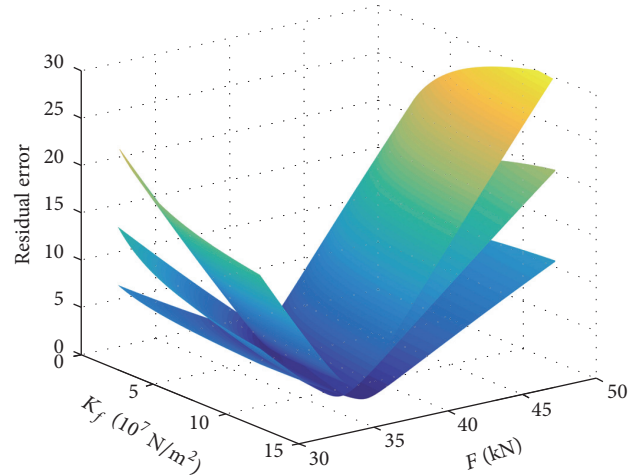


FIGURE 9: Residual error functions for sets of weight coefficients W_1 , W_2 , W_3 .

based on a tie-rod model represented by a beam with ends supported by an elastic Winkler-type foundation. The elastic bed was used to simulate the contact condition between a

tie-rod and a masonry wall. The proposed method consisted of an experimental and a computational stage. The experimental part was a relatively simple vibrational test for natural frequencies identification. The computational part was an optimization procedure for axial load estimation based on finite element modelling. The optimization has been done with respect to two parameters: the sought axial load and the distributed stiffness of the elastic bed at the boundaries. The technique provided a solution for uncertain boundary conditions and is capable of identifying axial load with high accuracy.

Investigation of the behaviour of natural frequencies depending on the parameters showed that axial load tends to shift the set of frequencies (the higher the load the higher the frequencies), while the elastic foundation stiffness changes the “distance” between natural frequencies.

As a result, consideration of elasticity at anchorages exhibited increase in axial load by up to 40%. This means that assumption of simple boundary conditions is not sufficient for modelling a tie-rod dynamic response. The sensitivity analysis has proved that the optimization result was stable to variation of weight coefficients and was converging to the same axial load. Thus, the method has been approved in practice and is suitable for in situ identification of axial load in ancient tie-rods.

Nomenclature

A :	Cross-section area of the tie-rod
B_1, B_2 :	Coefficients in the time function of the solution for tie-rod deflection
C :	Coefficient of the general solution for the form function
C_1, \dots, C_{12} :	Coefficients of the solution for tie-rod deflection that satisfy the specific boundary conditions
C :	Constant equal to the ratio $\sqrt{EI/\rho A}$
E :	Elastic modulus of the tie-rod material
F :	Axial load acting on the tie-rod
f_k^{exp} :	Natural frequency number k determined experimentally
f_k^{FEM} :	Natural frequency number k determined from FEM
$H(x)$:	Heaviside function
I :	Moment of inertia of the cross-section about z -axis
K_f :	Distributed stiffness of the elastic bed
k_f :	Stiffness of the separate springs that discretize the elastic bed
k_1, \dots, k_4 :	Real constants used in the expressions for s
L :	Total length of the tie-rod
l_f :	Lengths of the tie-rod portion inserted into the wall, sections I and III
L :	“Free” length of the tie-rod, section II
M :	Matrix of the system of linear algebraic equations for the unknowns C_1, \dots, C_{12}
N :	Poisson’s ratio

Π :	Total potential energy
p_k :	Weight coefficient of a frequency number k
R :	Residual error between two sets of n natural frequencies
P :	Density of the tie-rod material
$s, s_{\text{I,II,III}}, s_1, \dots, s_4$:	Coefficients in the exponent of the solution for tie-rod deflection
T :	Kinetic energy
$\tau_i(t), \tau(t)$:	Time function in the Fourier solution for tie-rod deflection
U :	Potential energy of elastic strain
V_F :	Potential energy associated with the axial load
V_w :	Potential energy associated with the elastic foundation
Ω :	Natural frequency in rad/s
$w(x, t)$:	Tie-rod deflection in xOy plane
$w_{\text{I,II,III}}(x, t)$:	Deflection for each section of the tie-rod
$W(x)$:	Form function of the tie-rod deflection
$W_{\text{I,II,III}}(x)$:	Form functions for each section of the tie-rod.

Conflicts of Interest

The authors declare that there are no conflicts of interest regarding the publication of this paper.

References

- [1] M. Amabili, S. Carra, L. Collini, R. Garziera, and A. Panno, “Estimation of tensile force in tie-rods using a frequency-based identification method,” *Journal of Sound and Vibration*, vol. 329, no. 11, pp. 2057–2067, 2010.
- [2] R. Garziera, M. Amabili, and L. Collini, “A hybrid method for the nondestructive evaluation of the axial load in structural tie-rods,” *Nondestructive Testing and Evaluation*, vol. 26, no. 2, pp. 197–208, 2011.
- [3] L. Collini, R. Fagiani, R. Garziera, K. Riabova, and M. Vanali, “Load and effectiveness of the tie-rods of an ancient dome: technical and historical aspects,” *Journal of Cultural Heritage*, vol. 16, no. 4, pp. 597–601, 2015.
- [4] L. Collini and R. Garziera, “Measurement of the tensile force in the hoop tie-rods of an historical dome,” in *Proceedings of PROHITECH14 - 2nd International Conference on Protection of Historical Constructions*, SYKORA, Antalya, Turkey, 2014.
- [5] K. Riabova, L. Collini, and R. Garziera, “Numerical method for the estimation of tensile load in tie-rods,” in *Proceedings of the 14th Youth Symposium on Experimental Solid Mechanics*, vol. 3, Traunkirchen Monastery, Austria, 2015.
- [6] L. Collini, R. Garziera, and K. Riabova, “Experimental and numerical determination of the axial load in structural tie-rods with complex boundary conditions,” in *Proceedings of the XXXVI Iberian Latin American Congress on Computational Methods in Engineering*, SWGE Sistemas, Rio de Janeiro, Brazil, November 2015.
- [7] M. Amabili and R. Garziera, “A technique for the systematic choice of admissible functions in the Rayleigh-Ritz method,” *Journal of Sound and Vibration*, vol. 224, no. 3, pp. 519–539, 1999.

- [8] P. Pozzati, *Teoria e Tecnica delle Strutture (Theory and Technique of Structures)*, UTET, Turin, Italy, 1977.
- [9] M. L. Beconcini, "Un metodo pratico per la determinazione del tiro nelle catene (a practical method for the determination of tensile load in tie-rods)," *Costruire in Laterizio* 54/96, pp. 299–301, 1996.
- [10] S. B. Bati and U. Tonietti, "Experimental methods for estimating in situ tensile force in tie-rods," *Journal of Engineering Mechanics*, vol. 127, no. 12, pp. 1275–1283, 2001.
- [11] C. Blasi and S. Sorace, *Sulla determinazione del "tiro" nelle catene mediante prove statiche e dinamiche*, Atti III Congresso Nazionale ASS.I.R.CO, Catania, Italy, November 1988.
- [12] C. Blasi and S. Sorace, "Determining the axial force in metallic rods," *Structural Engineering International (IABSE)*, vol. 4, no. 4, pp. 241–246, 1994.
- [13] S. Sorace, "Parameter models for estimating in-situ tensile force in tie-rods," *Journal of Engineering Mechanics*, vol. 122, no. 9, pp. 818–825, 1996.
- [14] S. Lagomarsino and C. Calderini, "The dynamical identification of the tensile force in ancient tie-rods," *Engineering Structures*, vol. 27, no. 6, pp. 846–856, 2005.
- [15] K. Maes, J. Peeters, E. Reynders, G. Lombaert, and G. De Roeck, "Identification of axial forces in beam members by local vibration measurements," *Journal of Sound and Vibration*, vol. 332, no. 21, pp. 5417–5432, 2013.
- [16] S. Li, E. Reynders, K. Maes, and G. De Roeck, "Vibration-based estimation of axial force for a beam member with uncertain boundary conditions," *Journal of Sound and Vibration*, vol. 332, no. 4, pp. 795–806, 2013.
- [17] G. Rebecchi, N. Tullini, and F. Laudiero, "Estimate of the axial force in slender beams with unknown boundary conditions using one flexural mode shape," *Journal of Sound and Vibration*, vol. 332, no. 18, pp. 4122–4135, 2013.
- [18] N. Tullini, "Bending tests to estimate the axial force in slender beams with unknown boundary conditions," *Mechanics Research Communications*, vol. 53, pp. 15–23, 2013.
- [19] N. Tullini, G. Rebecchi, and F. Laudiero, "Bending tests to estimate the axial force in tie-rods," *Mechanics Research Communications*, vol. 44, pp. 57–64, 2012.
- [20] N. Tullini and F. Laudiero, "Dynamic identification of beam axial loads using one flexural mode shape," *Journal of Sound and Vibration*, vol. 318, no. 1-2, pp. 131–147, 2008.
- [21] C. Gentilini, A. Marzani, and M. Mazzotti, "Nondestructive characterization of tie-rods by means of dynamic testing, added masses and genetic algorithms," *Journal of Sound and Vibration*, vol. 332, no. 1, pp. 76–101, 2013.
- [22] T. Livingston, J. G. Béliveau, and D. R. Huston, "Estimation of axial load in prismatic members using flexural vibrations," *Journal of Sound and Vibration*, vol. 179, no. 5, pp. 899–908, 1995.
- [23] B. H. Kim and T. Park, "Estimation of cable tension force using the frequency-based system identification method," *Journal of Sound and Vibration*, vol. 304, no. 3–5, pp. 660–676, 2007.
- [24] C. Urbano, "Sulla determinazione del tiro nelle catene degli archi: considerazioni teoriche ed applicazioni sperimentali (on the determination of tensile load in tie-rods of arcs: theoretical considerations and experimental applications)," *Costruzioni Metalliche*, vol. 5, pp. 315–323, 1967.
- [25] M. Arduini, R. Carli, and P. Cesari, "Tecniche di identificazione dello sforzo e del grado di vincolo nei tiranti strutturali con metodi dinamici (identification techniques of stress and the degree of constraint in the structural tie-rods with dynamic methods)," *Ingegneri Architetti Costruttori (INARCOS)*, vol. 563, pp. 493–496, 1995.
- [26] E. Viola, M. Dilena, and E. Artioli, "Identification of metallic rods by frequency estimation on the historical church tower in S.Vito al Tagliamento (PN)-Italy," in *Proceedings of the International Conference on Restoration, Recycling and Rejuvenation Technology for Engineering and Architecture Application*, pp. 173–179, Cesena, Italy, June 2004.
- [27] W.-X. Ren, G. Chen, and W.-H. Hu, "Empirical formulas to estimate cable tension by cable fundamental frequency," *Structural Engineering and Mechanics*, vol. 20, no. 3, pp. 363–380, 2005.
- [28] S. Park, S. Choi, S.-T. Oh, N. Stubbs, and H.-C. Song, "Identification of the tensile force in high-tension bars using modal sensitivities," *International Journal of Solids and Structures*, vol. 43, no. 10, pp. 3185–3196, 2006.
- [29] S. H. Farghaly and K. M. Zeid, "An exact frequency equation for an axially loaded beam-mass-spring system resting on a Winkler elastic foundation," *Journal of Sound and Vibration*, vol. 185, no. 2, pp. 357–363, 1995.
- [30] P. Ruge and C. Birk, "A comparison of infinite Timoshenko and Euler-Bernoulli beam models on Winkler foundation in the frequency- and time-domain," *Journal of Sound and Vibration*, vol. 304, no. 3-5, pp. 932–947, 2007.
- [31] S. G. Koroma, M. F. M. Hussein, and J. S. Owen, "Vibration of a beam on continuous elastic foundation with nonhomogeneous stiffness and damping under a harmonically excited mass," *Journal of Sound and Vibration*, vol. 333, no. 9, pp. 2571–2587, 2014.

Research Article

Experimental Research on Seismic Performance of a New-Type of R/C Beam-Column Joints with End Plates

Shufeng Li, Qingning Li, Haotian Jiang, Hao Zhang, and Lizhong Zhang

School of Civil Engineering, Xi'an University of Architecture and Technology, Xi'an 710055, China

Correspondence should be addressed to Shufeng Li; 1371757493@qq.com

Received 17 March 2017; Accepted 12 April 2017; Published 4 May 2017

Academic Editor: Michele Palermo

Copyright © 2017 Shufeng Li et al. This is an open access article distributed under the Creative Commons Attribution License, which permits unrestricted use, distribution, and reproduction in any medium, provided the original work is properly cited.

This paper presents a new-type of fabricated beam-column connections with end plates. The joint details are as follows: the concrete beams are connected to column by end plates and six high strength long bolts passing through the core area. In addition, in order to increase the stiffness and shear strength, stirrups are replaced by the steel plate hoop in the core zone. To examine the fail behavior of the fabricated beam-column connection specimens, a quasi-static test is conducted for nine full-scale models to obtain the hysteresis curves, skeleton curves, ductility, energy dissipation capacity, and other seismic indicators. The experimental results show that all specimens failed in bending in a malleable way with a beam plastic hinge and the hysteresis curves are excellently plump for the end plate connections. From the seismic indexes, the fabricated connection specimens exhibit better seismic performance, which can provide reference for the application of prefabricated frame structure in the earthquake area.

1. Introduction

The advantages of prefabricated frame structure include simple construction, flexible arrangement, and green environmental protection, which fully reflects the industrial character of modern architecture. In the frame structure, the node plays the role of load transmission, which is the key part of the seismic of structure. The postearthquake investigation found that, in most cases, the collapse of the frame structure is caused by the failure of the node, which shows that the node connection performance reliability of the prefabricated structure is poorer, so their application has been limited in earthquake area. In order to improve the overall seismic performance of the assembly structure, we need to carry on deeper theoretical and experimental research on the assembly node. In recent years, a lot of researches were conducted and achieved notable results. Mao et al. [1] put forward a new combination of bolt end plate connection steel beam-reinforced concrete column node and conduct simulated seismic loading test; the results showed that the steel beam-reinforced concrete column composite joint with high strength bolted end plate was used as a new-type of joint, which has excellent seismic performance and excellent

construction performance. A novel type of composite joint was presented by Wang and Zhang [2]; some quasi-static tests were performed on flush and extended end plate joints. These blind bolted end plate composite joints to concrete-filled thin-walled steel tubular (CFTST) columns exhibited favorable seismic behavior and energy dissipation capacity. Wu et al. [3] proposed a new design of bolted beam-to-column connections for concrete-filled steel tubes (CFT) and conducted a series of cyclic loading experiments. Experimental results showed that the bolted connections had superior seismic resistance in stiffness, strength, ductility, and energy dissipation mechanisms. From the domestic and foreign researches [4–12], it can be found that the end plate bolt connection applied in steel structure and composite structure has better seismic performance. At present, the researches on the application of end plate bolt connection in concrete structure are less, so the research of seismic performance for such node has practical significance. Besides, prestressed concrete has been widely used in the assembly structure because of its advantages. Some research on unbonded prestressed concrete is conducted by domestic and foreign scholars. The United States early launched a PRESS research program; the experimental study of unbonded prestressed

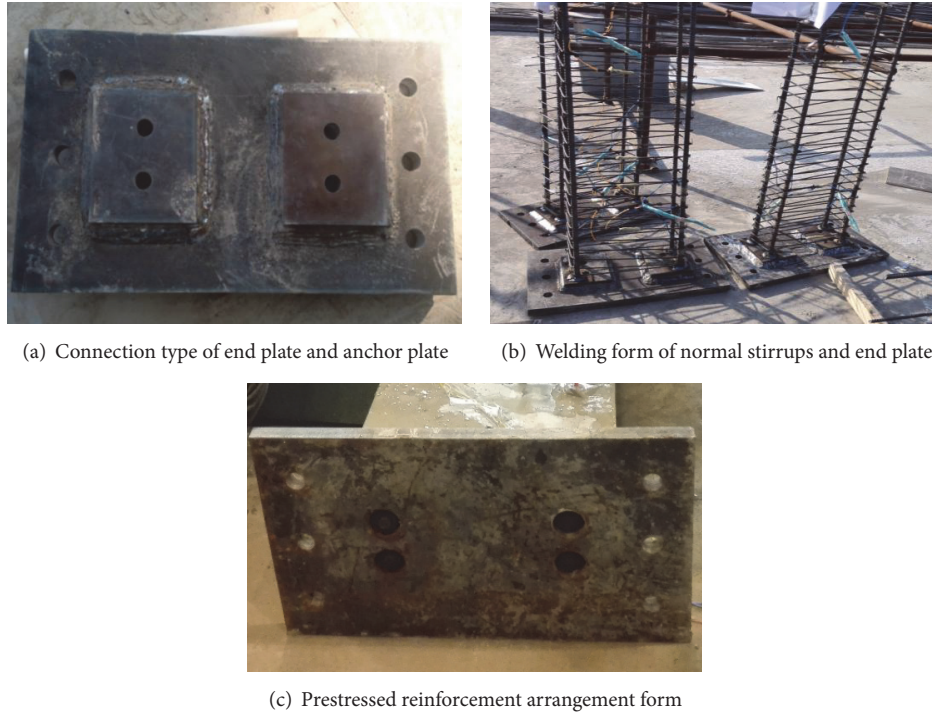


FIGURE 1: Concrete structure of beam.

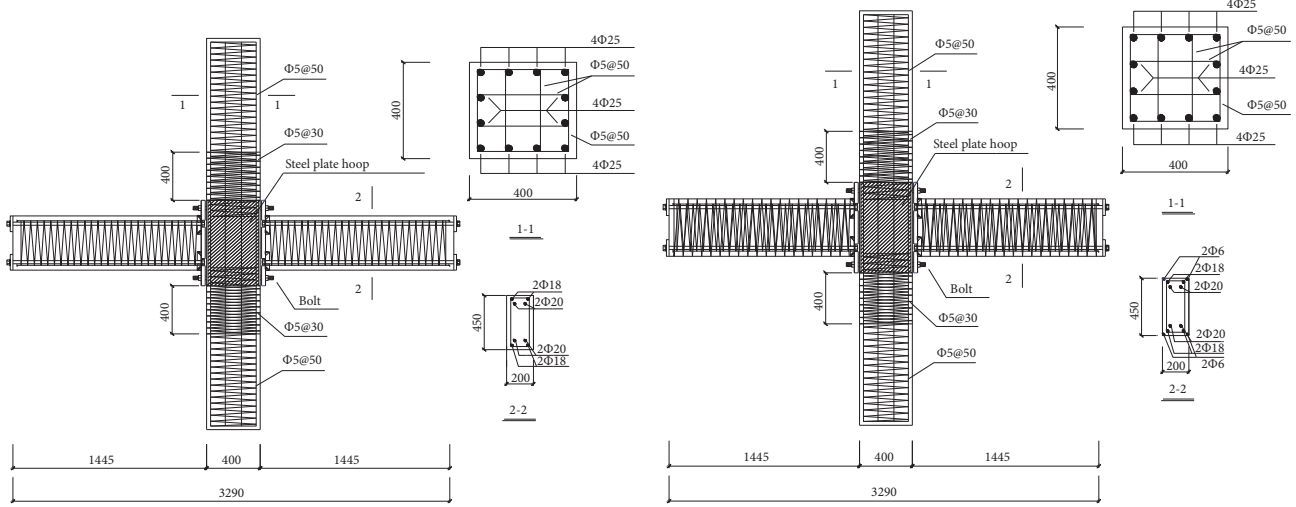
frame joints was carried out [13]. The experimental results showed that the unbonded prestressed tendons can significantly reduce the damage degree of the core area in the case of large lateral displacement. The mechanical properties of unbonded prestressed concrete frame joints under low cyclic loading tests were studied by Dong et al. [14]; the results indicated that the unbonded prestressed concrete frame joints have good seismic performance, and the ductility and deformation recovery ability are better than the cast-in-place frame node. Experiments on two concrete joints and two prestressed concrete frame joints were conducted under low frequency cyclic loading by Fu et al. [15]; the results demonstrated that the residual deformation of prestressed concrete assembly frame joints is less than that of cast in situ concrete joints, and the cracking resisting capacity, stiffness, and deformation recovering capacity of the core joint regions of the assembled specimens are better. From the experimental research, the unbonded prestressed concrete structure has the advantages of strong deformation recovering capacity, better cracking resisting capacity, high stiffness, and ductility. At present, it has been adopted in multistorey and high-rise structures, such as Paramount Building, Guangdong International Building, New Century Building, and Nanjing TV Tower. Based on the research results of scholars from different countries and the concept of restricted concrete, a new-type of fabricated beam-column connections with end plates is proposed in this paper. The normal stirrups in the beam and column are replaced by high strength spiral hoop. The partially prestressed concrete beams are adopted in all specimens. For the convenience of construction, the end plate and anchor plate are welded together by groove welding;

ordinary reinforcements used in the beam are vertically welded on the end plate by the pier head and prestressed reinforcements passing through anchor plate are anchored inside the end plate by nuts, which can be seen in Figure 1.

2. Experimental Program

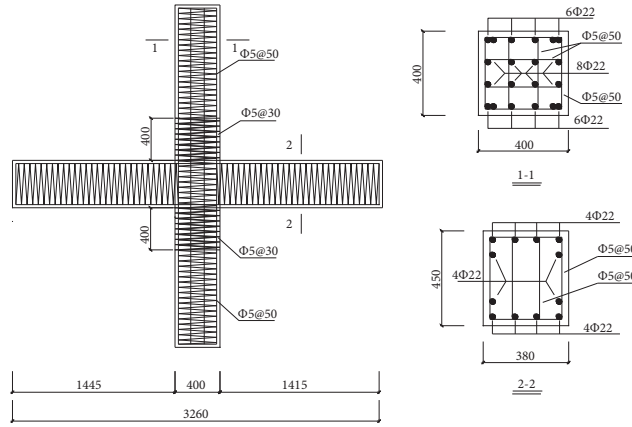
2.1. Specimens. A total of nine full-scale fabricated beam-column connection specimens are selected for the test investigation, where RC-01 is cast-in-place concrete joint. All specimens are expected to exhibit strong-column-weak-beam behavior [16]. Compared with specimens #PAN-05 and #PAN-06, double stirrup confined concrete beams are used in the specimens #PAN-07 and #PAN-08, and four longitudinal reinforcements with the diameter of 6 mm are arranged at the four corners of stirrup to fasten the outer stirrup framework, as shown in Figure 3. The diameter of Grade HTH1100 spiral stirrup used in the specimens is 5 mm. The size of end plate is 400 mm × 30 mm × 710 mm. Grade HTH1080 bolts with 27 mm diameter are used for all connections. Besides, stirrups are replaced by 4 mm thick steel plate hoop in the core zone. The size and details of all specimens are shown in Figure 2 and listed in Table 1, respectively.

2.2. Material Properties. According to the standard for test method of mechanical properties on ordinary concrete [17], material tests of concrete and high-performance grouting material are performed. Test results indicate that the concrete compressive cube strengths of beam and column are 28 Mpa and 41.9 Mpa, respectively. The flexural strength of G-1 high strength grouting material is 3.02 Mpa and the compressive



(a) Size and reinforcement of #PAN-01~06 specimens

(b) Size and reinforcement of #PAN-07~08 specimens



(c) Size and reinforcement of RC-01 specimens

FIGURE 2: Size and reinforcement of specimens (unit: mm).



FIGURE 3: Double stirrup arrangement form.



FIGURE 4: Pier head material test.

strength is 41 Mpa. Besides, the mechanical properties of longitudinal reinforcement and spiral stirrup are also tested. The test values are listed in Table 2. In addition, the tensile test

is conducted for the pier head. The results demonstrate that damage cannot occur at the welded pier head of the ordinary reinforcement, as shown in Figure 4.

TABLE 1: Arrangement of reinforcement of specimen.

Specimen	Strength of concrete	Section type	Section size (mm)	Longitudinal reinforcement	Stirrup spacing (mm)	Stirrup encryption area (mm)
Column	C60	Rectangle	400 × 400	16Φ22HRB600	50	30
RC-01	C60	Rectangle	450 × 380	12Φ22HRB600	50	30
#PAN-01	C35	Rectangle	450 × 200	4Φ20HTH1080 4Φ18HRB400	110	90
#PAN-02	C35				50	40
#PAN-03	C35				60	50
#PAN-04	C35				70	60
#PAN-05	C35				90	70
#PAN-06	C35				100	80
#PAN-07	C35				90 (double stirrup)	70 (double stirrup)
#PAN-08	C35				100 (double stirrup)	80 (double stirrup)

TABLE 2: Indexes of reinforcement mechanical performance.

Material property	Diameter					
	5	6	10	18	20	27
Yield strength/Mpa	1111.01	540.64	376.62	447.85	1160	1120
Ultimate strength/Mpa	1336.7	681.98	560.17	630.72	1230	1180
Strength-yield ratio	1.20	1.26	1.49	1.41	1.06	1.05
Percentage elongation after fracture	1.2	8.24	10.36	12.47	12	14

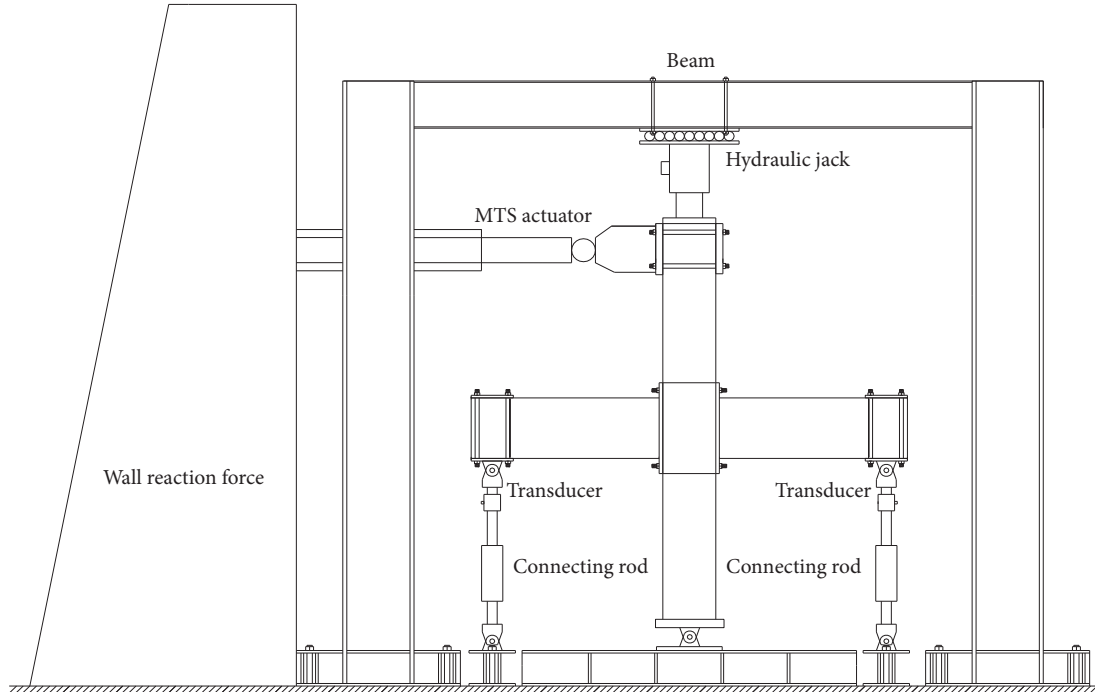


FIGURE 5: Schematic view of the loading device.

3. Test Loading Device and History

In this test, pseudo static cyclic loading is used and loading method of column end is adopted. The schematic diagram of loading device is shown in Figure 5. The test setup consists of

a 100 T horizontal actuator applied at the column end and a 500 kN capacity hydraulic jack positioned vertically at the top of column. All specimens are subjected to a constant axial load of 800 kN at the top of the column through the hydraulic jack placed on the column top. Based on the Specification



FIGURE 6: Internal damage state of node core area.

of Test Methods for Earthquake Resistant Building [18], the mixed load method of load and displacement is used in this test. The load-control is adopted and repeated once at each control point before the specimens yielded. The displacement control is used and repeated three times after the specimens yielded.

4. Analysis on Test Results

4.1. Test Process. Under the action of low frequency cyclic loading, the shear failure occurs in the core area of the RC-01 because of the fault of the design, and the bending failure of beam end occurs to the #PAN series test specimen of monolayer stirrup with the similar destruction process. When the cracking load is reached, the vertical bending cracks appear in the beam region close to the core area, the crack width is about 0.05 mm, and it is completely closed after unloading. As the load increases, there are more cracks, whose length and width increase constantly with the oblique trend, and the distribution range gradually spreads away from the core zone. When reaching the yield load, the width of maximum crack is about 0.2 mm. In the stage of displacement control, the concrete protective layer falls off, but the concrete internal damage is not serious, which shows that the specimens have good deformation performance. When the horizontal displacement reaches about 150 mm, the bearing capacity of the joint decreases to 85% of the peak load, and the specimens have a visible plastic hinge destruction zone, and the test is stopped. The failure modes of double-layer stirrup specimens #PAN-07 and #PAN-08 and monolayer stirrup specimens are basically identical. The cracking load and ultimate load of the double ring specimen are relatively high; double ring specimens have small damage region at the same time; the main reason is that outer stirrup can better restrain concrete cover, which indicates that double-layer stirrups have a remarkable impact on concrete core. During the whole process of the test, there is no sign of separation between the end plate and the column and no buckling occurring to the end plate. The node core zone is in the state of three-dimensional stress under the restraint of steel plate hoop and there is no shear failure as well as slippage happening. After the test, it is found that the concrete cover of the joint core area is shed, but there are no obvious cracks inside the concrete, which can be seen in Figure 6. No fracture and sealing off occur at the pier head between nonprestressed reinforcement and end plate. In addition, for specimen #PAN-02, slippage occurs to the pedestal during

the loading because of the equipment problems, positive displacement, and negative displacement are asymmetric. Later, equipment is set again and reinforcing specimen is loaded again. For #PAN-06 and #PAN-07, in the load process, the prestressed tendons are separated from the nuts at $1\Delta_y$ and $4\Delta_y$, respectively, where Δ_y is the yield displacement, for which the main reason is the fact that the length of the thread between prestressed reinforcement and nut is not enough. Compared with other test specimens, the specimens are suggested keeping at least three threads. Figure 7 shows the final damage state of different test specimens.

4.2. Hysteresis Curve. The recorded force-displacement hysteresis curves for all specimens are shown in Figure 8. The hysteresis curve of the RC-01 shows a certain pinch phenomenon because the shear failure occurs in the core area. However, the specimen has a certain bearing capacity after falling off of concrete cover and there is no phenomenon of mutation of bearing capacity, which indicates that high strength spiral stirrups can provide a better constraint effect for concrete core. For the fabricated node specimens, during the initial loading, the hysteretic curves are in the elastic stage and there are hardly residual deformations after unloading. With the cyclic increasing, the vertical bending cracks appear in the beam end; however because of the influence of the prestressed reinforcement, residual deformations are very small corresponding to unloading. After the nonprestressed reinforcement yielded, the following hysteresis curve is carried out under displacement control; there is no obvious bearing capacity drop in the cycles of the same displacement and the hysteresis loop is plump and stable, so the specimens have good energy dissipation capacity. When the specimens are close to failure, the bearing capacity has no obvious decrease after reaching the peak point; the main reason is that, under the constraint of the high strength spiral stirrup, the internal core concrete on the beam end can still bear a certain load. From the cyclic curves of #PAN-07 and #PAN-08, the force-displacement hysteresis curves are plump; the specimens exhibit higher bearing capacity and better seismic performance.

4.3. Skeleton Curve. The skeleton curve derived from the hysteresis curve is a valuable tool for quantifying seismic performance index. Figure 9 shows the backbone curves of all test specimens. As can be seen from Figure 9, the skeleton curves of all fabricated node specimens show the same tendency. The backbone curves increase linearly before



(a) #PAN-01 ultimate failure diagram



(b) #PAN-02 ultimate failure diagram



(c) #PAN-03 ultimate failure diagram



(d) #PAN-04 ultimate failure diagram



(e) #PAN-05 ultimate failure diagram



(f) #PAN-06 ultimate failure diagram



(g) #PAN-07 ultimate failure diagram



(h) #PAN-08 ultimate failure diagram

FIGURE 7: Continued.



(i) RC-01 ultimate failure diagram

FIGURE 7: Specimens ultimate failure modes.

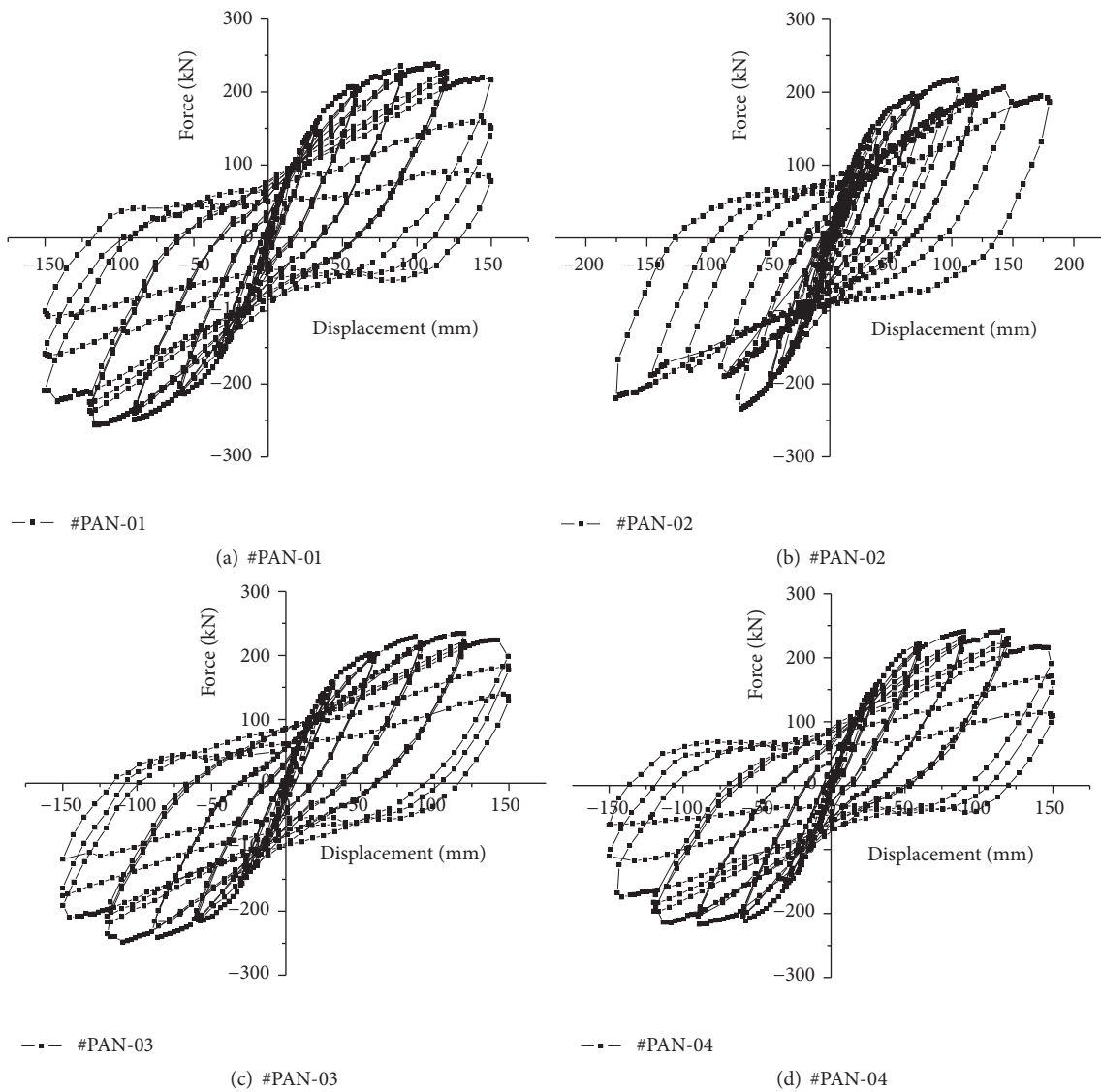


FIGURE 8: Continued.

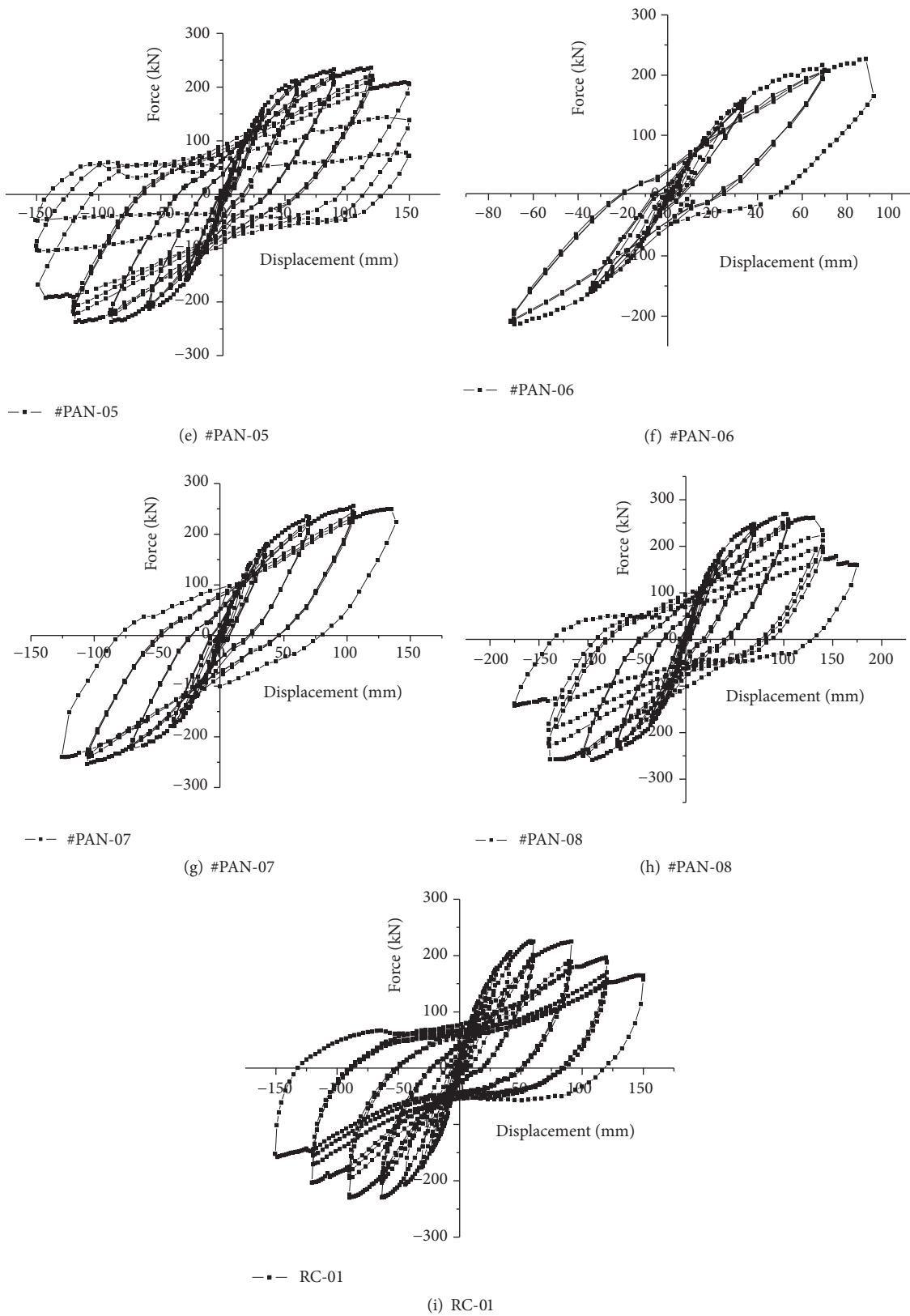


FIGURE 8: $P - \Delta$ curve of specimens.

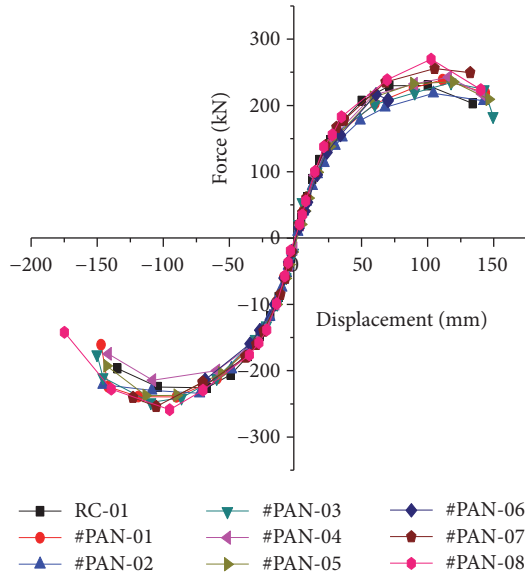


FIGURE 9: Skeleton curve of specimens.

the specimens yielded. Under the control of large displacement, there is no obvious bearing capacity degeneration and the limit displacement point is far away from the yield displacement point, which shows that the assembly joint has good deformation performance [19]. There is no big difference among the limit bearing capacity of the specimens; the main reason is that the final failure modes of all fabricated specimens are beam end bending failure instead of shear failure, which shows that the high strength spiral stirrup can better confine concrete and greatly improve the shear bearing capacity of the cross section. Conclusion can be made from skeleton curves of #PAN-07 and #PAN-08 that double-layer spiral stirrups used in the beam have remarkable influences on the bearing capacity.

4.4. Stiffness Degeneration. Stiffness degeneration refers to the phenomenon that the horizontal lateral resistant force decreases as the number of cycle goes up while maintaining the same peak displacement. The beam-column node is the key of the structural force transmission, whose degree of stiffness degeneration has a great influence on the overall structure seismic performance. The stiffness degeneration of the structural member can be obtained by the coefficient of bearing capacity decrease, which can be seen in (1), where P_j^i is the load value under the i th cycle when the relative lateral displacement Δ/Δ_y is j ; P_j^1 is the maximum load when Δ/Δ_y is j .

$$\lambda_i = \frac{P_j^i}{P_j^1}. \quad (1)$$

Figure 10 presents the stiffness degeneration of prefabricated joints, where Δ_y is the displacement corresponding to the yield load; it can be seen that the prefabricated nodes have a longer horizontal branch after the test specimens

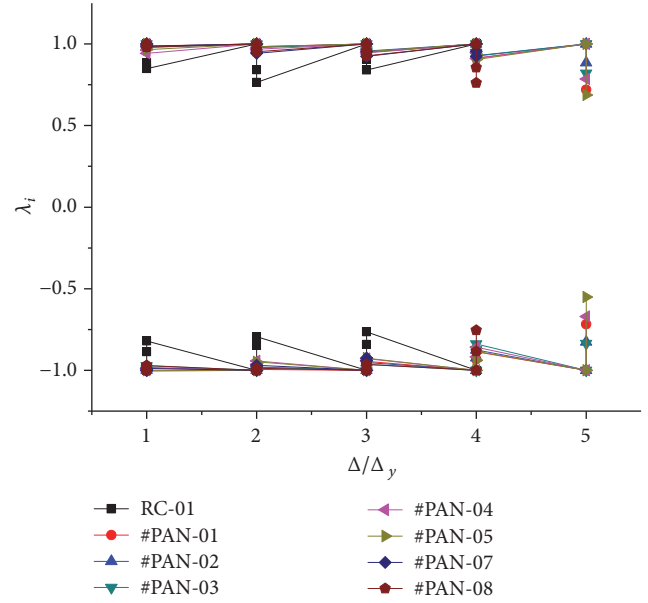


FIGURE 10: Strength degradation curve of specimens.

yielded. When approaching damage, the cracks of the beam end plastic hinge region develop fully, the concrete protective layer falls off, and the strength decreases greatly. However, the stiffness degeneration coefficient of the specimens is beyond 0.9 and the specimens can bear certain load when destruction happens, which can play a better seismic behavior.

4.5. Ductility Capacity. Ductility capacity is an important parameter for evaluating structure seismic capacity.

The ductility coefficient μ is defined as the ratio of limit displacement Δ_u to yielding displacement Δ_y ; the ultimate displacement is the corresponding displacement values when the bearing capacity drops to 85% of peak value, and the yield displacement is determined according to equivalent energy method [20]. The ductility coefficients of the specimens are shown in Table 3.

From Table 3, the ductility coefficient of the prefabricated nodes is between 2.5 and 3.4 and the previous test's ductility coefficient of the cast in situ reinforced concrete frame node is around 2.0 and 5.5 [21, 22]. In this test, the ductility coefficients of the prefabricated nodes are in the scope, showing the prefabricated joint has good deformation. Although the shear failure occurs in node core area, RC-01 exhibits better ductility under the constraint of high strength spiral stirrup, which demonstrates that the high strength spiral stirrup has a satisfactory effect on concrete.

4.6. Energy Dissipation. When the structure enters the elastic-plastic stage, the component's energy dissipating capacity determines the seismic performance of the structure to a great extent and in the test, how much energy the component can be absorbed is reflected by the area surrounded by load-displacement curve. In this paper, the component's energy dissipation is evaluated by equivalent viscous coefficient h_e . The calculation formulas of equivalent

TABLE 3: Load characteristic values and displacement ductility of specimens.

Specimen number		Yield load P_y/kN	Yield displacement Δ_y/mm	Limit load P_u/kN	Ultimate displacement Δ_u/mm	Ductility factor μ
RC-01	Front	193.07	36.26	227.02	132.91	3.67
	Back	-194.51	-38.39	-232.22	-134.07	3.49
#PAN-01	Front	178.17	52.88	238.57	143.67	2.73
	Back	-181.16	-50.84	-256.12	-141.66	2.79
#PAN-02	Front	164.75	53.15	230.93	141.13	2.66
	Back	-180.91	-50.24	-233.97	-146.83	2.92
#PAN-03	Front	175.72	48.26	234.51	149.47	3.10
	Back	-185.20	-57.05	-247.91	-145.67	2.55
#PAN-04	Front	180.63	55.23	242.66	148.54	2.69
	Back	-160.56	-42.21	-211.84	-141.47	3.35
#PAN-05	Front	175.01	54.47	232.70	146.39	2.69
	Back	-167.47	-47.66	-237.11	-142.75	3.00
#PAN-07	Front	-201.46	50.30	255.515	145.12	2.89
	Back	-199.78	-53.76	-254.04	-140.85	2.62
#PAN-08	Front	199.06	56.06	269.87	142.04	2.53
	Back	-192.31	-53.19	-258.73	-139.86	2.63

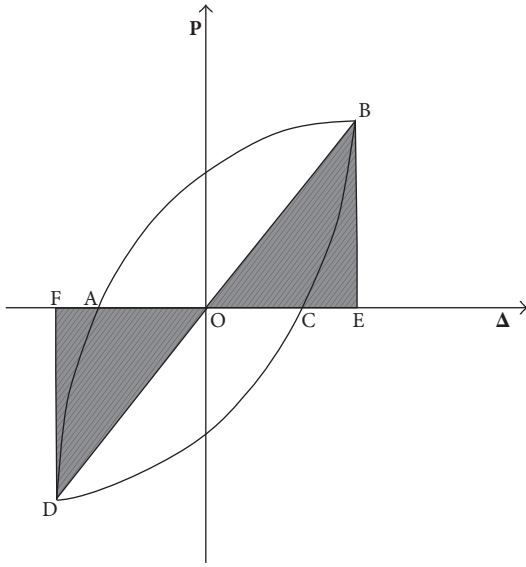


FIGURE 11: Hysteresis loop energy.

viscous coefficient can be seen in (2), where S_{ABCD} is the area of hysteretic loop; S_{OBE} and S_{ODF} are areas within OBE and ODF, as shown in Figure 11.

$$h_e = \frac{1}{2\pi} \frac{S_{ABCD}}{S_{OBE} + S_{ODF}}. \quad (2)$$

Figure 12 shows the equivalent viscous damping coefficient of all specimens; during the initial loading, the prefabricated node is in the elastic stage; it has good deformation restoring capacity and smaller energy consumption. After the non-prestressed reinforcement yielded, the residual deformation

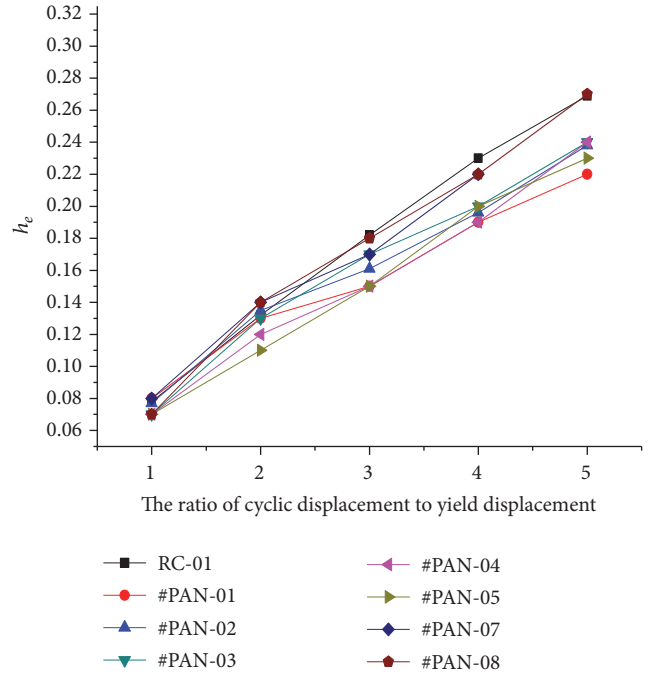


FIGURE 12: Equivalent viscous damping coefficient.

appears and equivalent viscous coefficient increases obviously. The equivalent viscous coefficient of the cast-in-place concrete node is about 0.10 when reaching peak load [23]. The equivalent viscous coefficient of each prefabricated node is between 0.22 and 0.24, showing that the energy consumption capacity of the prefabricated node is superior to standard test specimens of the cast in situ concrete. For the double stirrup

specimens, there is bigger energy consumption capacity and its equivalent viscous coefficient is about 0.27.

5. Conclusion

A new-type of fabricated beam-column connection with end plates is presented. To investigate the seismic behavior of the prefabricated node, a quasi-static test is conducted for nine real-size beam-column connections. From the experimental results, the following conclusions can be drawn.

- (1) From the seismic performance indices such as strength, ductility factor, and energy dissipation capacity, the strength degradation of the fabricated joint is not obvious, and the joint proposed in this paper exhibits favorable ductility and energy dissipation capacity.
- (2) Under the constraint of the double-layer stirrup, #PAN-07 and #PAN-08 have larger bearing capacity, ductility, and energy dissipation capacity. When the plastic hinge failure appears in the beam end, the damage area is small and drop-out of concrete protective layer is not serious. So it is suggested that the double-layer stirrup can be arranged in the hinge region to improve the seismic performance of the structure.
- (3) In this test, there are no fracture and sealing off in the weld pier head used in between ordinary reinforcement and end plate, so this connection form can achieve the purpose of force transmission under the action of load, which can be applied in practical engineering.

Conflicts of Interest

The authors declare that they have no conflicts of interest.

References

- [1] W. F. Mao, Y. T. Wu, and Y. Xiao, "Experimental research on seismic behavior of bolted steel beam to RC column connections," *Industrial Construction*, vol. 35, no. 11, pp. 1–4, 2005.
- [2] J. Wang and H. Zhang, "Seismic performance assessment of blind bolted steel-concrete composite joints based on pseudo-dynamic testing," *Engineering Structures*, vol. 131, pp. 192–206, 2017.
- [3] L.-Y. Wu, L.-L. Chung, S.-F. Tsai, T.-J. Shen, and G.-L. Huang, "Seismic behavior of bolted beam-to-column connections for concrete filled steel tube," *Journal of Constructional Steel Research*, vol. 61, no. 10, pp. 1387–1410, 2005.
- [4] J. H. Khoo, B. Li, and W. K. Yip, "Tests on precast concrete frames with connections constructed away from column," *ACI Structural Journal*, vol. 61, no. 1, pp. 18–27, 2006.
- [5] B.-S. Han, S.-W. Shin, and B.-Y. Bahn, "A model of confined concrete in high-strength reinforced concrete tied columns," *Magazine of Concrete Research*, vol. 55, no. 3, pp. 203–214, 2003.
- [6] H. H. Korkmaz and T. Tankut, "Performance of a precast concrete beam-to-beam connection subject to reversed cyclic loading," *Engineering Structures*, vol. 27, no. 9, pp. 1392–1407, 2005.
- [7] B. Marco, G. Santino, and T. Mauro et al., "Beam-column joints in continuous RC frames: comparison between cast-in-situ and precast solutions," *Engineering Structures*, vol. 127, pp. 129–144, 2016.
- [8] K. S. Al-Jabri, P. Pillay, M. B. Waris, and T. Pervez, "Modeling of composite beam-column flexible endplate joints at elevated temperature," *Composite Structures*, vol. 143, pp. 180–188, 2016.
- [9] H. Jiang, Q. Li, W. Jiang, and D.-Y. Zhang, "Study on seismic performance of connection joint between prefabricated prestressed concrete beams and high strength reinforcement-confined concrete columns," *Steel and Composite Structures*, vol. 21, no. 2, pp. 343–356, 2016.
- [10] X. Li, Y. Xiao, and W. F. Mao et al., "Experimental research on seismic behavior of reinforced concrete column-to-steel beam joints with bolted end-plate," *Journal of Hunan University: Natural Science Edition*, vol. 21, no. 2, pp. 1–5, 2007.
- [11] Q. N. Li, X. C. Zheng, and M. T. Xu et al., "Experimental research and theoretical analysis of a new connection node with steel plate hoop and bolt tendons," *Industrial Building*, vol. 43, no. 9, pp. 59–64, 2013.
- [12] B. Liu, Y. Z. Zhang, and Z. F. Jin et al., "Experimental study on Seismic Behavior of prestressed fabricated PC frame connections," *Journal of Building Structures*, vol. 26, no. 2, pp. 60–65, 2005.
- [13] M. J. N. Priestley, "The PRESSS program—current status and proposed plans for Phase III," *PCI Journal*, vol. 41, no. 2, pp. 22–40, 1996.
- [14] T. F. Dong, Z. B. Li, X. Y. Zhou, and L. F. Feng, "Experimental study on seismic performances of precast prestressed concrete beam-to-column connections with unbonded tendons," *Journal of Beijing University of Technology*, vol. 32, no. 2, pp. 144–148, 2006.
- [15] X. Y. Fu, Y. Y. Yu, J. Q. Han, and X. D. Hong, "Experimental study on seismic behavior of interior joints in prestressed concrete assembly frame," *Journal of Building Structures*, vol. 36, pp. 203–208, 2015.
- [16] GB50010-2010, *Code for Design of Concrete Structures*, China Architecture and Building Press, Beijing, China, 2010.
- [17] GB/T50081-2002, "Standard for Test Method of Mechanical Properties on Ordinary Concrete".
- [18] JGJ/T 101-2015, *Specification for Seismic Test of Buildings*.
- [19] Q. J. Pan, *Experimental Study on Seismic Capacity of Precast Prestressed Concrete Frame Structures*, Southeast University, Nanjing, China, 2006.
- [20] R. Park, "Evaluation of ductility of structures and structural assemblages from laboratory testing," *Bulletin of the New Zealand National Society for Earthquake Engineering*, vol. 22, no. 3, pp. 155–166, 1989.
- [21] D. Zenunović and R. Folić, "Models for behaviour analysis of monolithic wall and precast or monolithic floor slab connections," *Engineering Structures*, vol. 40, pp. 466–478, 2012.
- [22] G. Y. Ma and Y. P. Su, "Calculation formulas for ultimate compressive strength and strain of FRP confined concrete cylinder," *Journal of Hebei University of Science and Technology: Natural Science Edition*, no. 1, pp. 74–77, 2010.
- [23] L. Zeng, *Research on Seismic Behaviors And Design Method of Steel Reinforced High Strength And High Performance Concrete Frame Joints [Ph.D. thesis]*, Xi'an University of Architecture and Technology, Xi'an, China, 2008.

Research Article

Experimental Evaluation for the Microvibration Performance of a Segmented PC Method Based High Technology Industrial Facility Using 1/2 Scale Test Models

Sijun Kim¹ and Se Woon Choi²

¹Department of Plant Architectural Engineering, Kyonggi University, Suwon, Gyeonggi-do 16227, Republic of Korea

²Department of Architecture, Catholic University of Daegu, Gyeongsan-si, Gyeongbuk 38430, Republic of Korea

Correspondence should be addressed to Se Woon Choi; watercloud@cu.ac.kr

Received 8 December 2016; Revised 13 January 2017; Accepted 24 January 2017; Published 12 February 2017

Academic Editor: Giada Gasparini

Copyright © 2017 Sijun Kim and Se Woon Choi. This is an open access article distributed under the Creative Commons Attribution License, which permits unrestricted use, distribution, and reproduction in any medium, provided the original work is properly cited.

The precast concrete (PC) method used in the construction process of high technology industrial facilities is limited when applied to those with greater span lengths, due to the transport length restriction (maximum length of 15~16 m in Korea) set by traffic laws. In order to resolve this, this study introduces a structural system with a segmented PC system, and a 1/2 scale model with a width of 9000 mm (hereafter Segmented Model) is manufactured to evaluate vibration performance. Since a real vibrational environment cannot be reproduced for vibration testing using a scale model, a comparative analysis of their relative performances is conducted in this study. For this purpose, a 1/2 scale model with a width of 7200 mm (hereafter Nonsegmented Model) of a high technology industrial facility is additionally prepared using the conventional PC method. By applying the same experiment method for both scale models and comparing the results, the relative vibration performance of the Segmented Model is observed. Through impact testing, the natural frequencies of the two scale models are compared. Also, in order to analyze the estimated response induced by the equipment, the vibration responses due to the exciter are compared. The experimental results show that the Segmented Model exhibits similar or superior performances when compared to the Nonsegmented Model.

1. Introduction

Microvibrations pose a critical issue in high technology facilities that manufacture products which require precision fabrication, such as semiconductors, LCD, and optical microscopes. This vibration, which occurs during the product manufacturing process, amplifies production errors and causes defects and degradation in product performance. Thus, it is imperative that the vibration performance of (i) equipment and (ii) building structures where equipment which produce vibration-sensitive products is installed be assessed and controlled.

Generally, most manufacturers of vibration-sensitive equipment perform vibration testing on their equipment and provide some level of vibration specifications with their equipment [1]. However, it is common for installed equipment be selected after considering the design and construction of the structure that will support the equipment. Also,

as technologies advance with time, there are cases where the original equipment is later replaced by equipment of greater performance. As a result, generic vibration design criteria have been proposed to evaluate the vibration performance of the support structure regardless of the equipment [1–6]. The criteria take the form of a set of one-third octave band velocity spectra labeled vibration criterion curves VC-A through VC-E and are known as the BBN criterion curves [4].

This approach has been utilized in evaluating the vibration performance of various structures [7–10]. Lee et al. [7] analytically performed a microvibration performance assessment of a thin-film transistor liquid crystal display (TFT-LCD) factory, constructed of a flat RC slab supported by long-span steel mega trusses, where vibration was generated by automated guided vehicles. Pan et al. [8] conducted vibration performance assessments through analysis and experiments using humans walking as the vibration source, for a biotechnology laboratory with floors supported by long-span RC

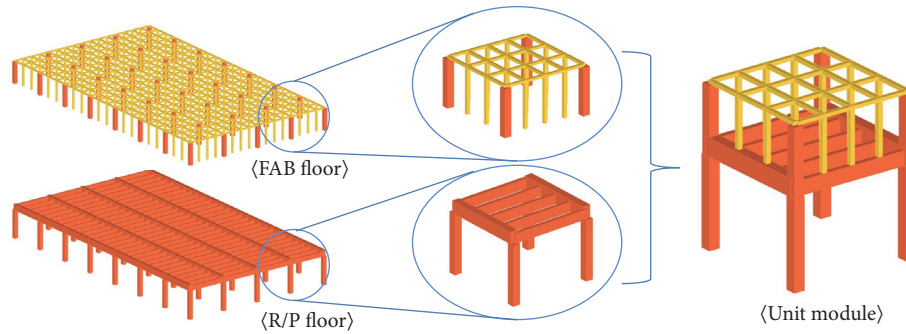


FIGURE 1: High technology industrial facility structure.

beams. Brownjohn et al. [9] performed experimental and analytical modal analysis and in-operation measurements for the evaluation of floor vibration serviceability in a factory building. Brownjohn et al. [9] advises that the vibration-sensitive products are manufactured on the floor with smaller spans is preferable.

The vibration performance of a structure involves an intricate relationship with the stiffness of the structure. Hence, to improve the vibration performance of a structure, increasing the member size can be considered. However, this method has clear limitations, since it results in increased construction costs. As an alternative approach, isolators can be applied rather than increasing the member size, and related studies have been conducted by numerous researchers to determine their effect [10–16].

On the other hand, the proper selection of appropriate structure systems can also enhance the vibration performance of structures. However, the vibration performance of a structure is affected by various structural design factors such as the (i) material (concrete, steel, and composite), (ii) supporting element of the floor (slab on grade, suspended slabs supported by columns), and (iii) floor shape (flat slab, waffle slab, etc.), and therefore the appropriate system needs to be selected by taking into consideration the characteristics of each structural system [2, 17–20].

Up until the mid-1990s, high technology facilities used the cast-in-place reinforced concrete (RC) method to construct their facilities' structure [21]. However, the vertical height of high technology facilities is often more than 8–9 m, so adopting the RC construction method would be uneconomical and lead to longer construction times, due to aerial work, floor posts, and formwork construction. The increase in construction time can be a significant disadvantage due to the rapidly changing nature of the industry, including the available technology and preferences of the consumer. As a result, construction methods employing precast concrete (PC) have been adopted since the mid-1990s [21]. The PC method manufactures structural members in a factory and assembles them onsite, minimizing onsite work and reducing construction times to ensure economic feasibility.

With the increasing size of manufacturing equipment, it becomes necessary to create longer manufacturing line span lengths in recent high technology industrial facilities. However, PC members have to be designed so that they can

be transported from the factory where they are manufactured to the construction site. According to the traffic laws of Korea, the maximum length of PC members for transportation is restricted to 15~16 m [22]. As a result, the span length of structures constructed using the PC method is generally less than 15~16 m.

Lee et al. [22] presented a segmented PC beam system for constructing high technology industrial facilities with span lengths greater than 17 m and performed simulations for verification. The proposed segmented PC beam system used the concept of the Gerber beam [23] to divide the long girder into (i) two-ended cantilevered beams and (ii) a central simple beam placed on top of the two-ended cantilevered beams in order to realize span lengths of 17 m or greater [22]. Since the vibration performance of the proposed segmented PC method had been verified by using the only simulation results, the experimental verification is required to apply the proposed method to real structures.

This study aims to experimentally evaluate the vibration performance of the segmented PC method which is verified through the simulation. To achieve this goal, the 1/2 scale model (hereafter, the Segmented Model) of high technology industrial facility using of a segmented PC method by Lee et al. [22] is manufactured, and, also, the 1/2 scale model (hereafter, the Nonsegmented Model) of typical high technology industrial facility using of a nonsegmented PC method is manufactured. By applying the same experimental methods to both scale models and comparing the results, the relative vibration performance of the Segmented Model is investigated. Impact testing and harmonic load testing are conducted to compare the natural frequencies, transfer functions, and responses of the two models.

2. Segmented PC Method Applied to High Technology Industrial Facility Structure

The structure of the high technology industrial facility dealt with in this study is composed of fabrication (FAB floor) and return plenum (R/P floor) structures as shown in Figure 1, where the entire high technology industrial facility structure is comprised of a two floor structure of unit spans (1 span \times 1 span) repeated consecutively. The FAB floor is where the fabrication and production of products occur and the R/P floor is where various equipment are installed, including

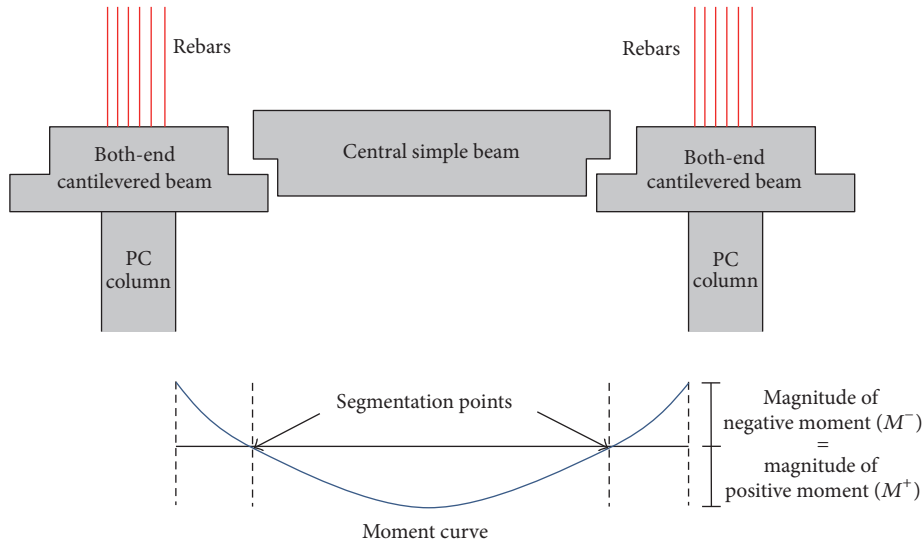


FIGURE 2: Concept of the segmented PC beam system and positions of segmentation points.

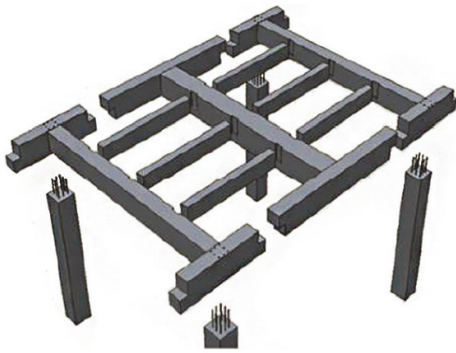


FIGURE 3: An example of a segmented PC beam system.

exhaust ducts, cables, bus ducts, utility provision, and exhaust pipes. Since the FAB floor is where precision fabrication occurs, it requires high stiffness. Thus, small columns are densely located between the FAB and R/P floors. The main columns that support the FAB floor are arranged at relatively wide intervals. Moreover, to reduce the time needed for construction, the FAB floor and small columns had steel-frame structures, while the R/P floor and main column employed structure systems constructed with PC.

In order to resolve the restriction posed by the traffic laws and to realize span lengths of 17 m and greater, the Gerber beam system with segmented PC method applied is applied to the R/P floor, as shown in Figure 2. By placing the cantilevered PC beam on top of the column and connecting the central PC beam to both ends of the cantilevered PC beam, this enables a structure with a large span length of 17 m or more. The floor structure plan of the R/P floor was constructed by segmenting the girder in the longitudinal direction as shown in Figure 3, and the remaining members smaller than or equal to 15 m in length were fabricated into single members and constructed.

The magnitudes of the positive and negative moments of the continuous beam under the gravity loads vary depending on the positions of segmentation points. Since the cross-sectional size of a beam is generally determined by the magnitudes of moments, the cross-sectional size of a segmented beam can be decreased by controlling the positions of segmentation points. For this reason, it is recommended that segmentation points are positioned where the magnitudes of the positive and negative moments of the continuous beam are the same or similar as shown in Figure 2 to reduce the magnitudes of moments.

3. Law of Similarity

Although an experimental test on a real-size structure is the most accurate method of identifying and analyzing the vibration characteristics of a structure, it is not effective when considering the spatial limitations and costs involved, so generally a scale model is manufactured and experimented on. Defining the accumulation effect on a real structure as a physical ratio is known as the law of similarity, and this law is commonly applied to scale model experiments [24].

The law of similarity determines the physical value sought from the experiments based on dimensional analysis. For a generic dynamics problem according to time, the basic dimensions of length (L), mass (M), and time (T) are selected, while the remaining physical parameters are derived as a combination of the basic dimensions [24]. For example, when defining the scale factor of the real structure to the scale model as “ S ,” the scale relationship between the two structures is derived as shown in Table 1.

In general, research on the dynamic experiments using law of similarity has been conducted, and most of the laws of similarity selected have been based on acceleration. However, using acceleration as the basis means that the scale factor for the mass becomes S^2 and the mass of the scale model is

TABLE I: Law of similarity.

Parameter	Range	Scale factor		
		Mass basis	Time basis	Acceleration basis
Length	L	S	S	S
Mass	M	S^3	S	S^2
Time	T	S	1	$S^{0.5}$
Acceleration	LT^{-2}	1/S	S	1
Force	MLT^{-2}	S^2	S^2	S^2
Damping	MT^{-1}	S^2	S	$S^{3/4}$
Natural frequency	T^{-1}	1/S	1	1/S ^{0.5}

reduced to S^3 . In order to compensate for these values, an additional mass has to be attached to the model. The scale factor of this study is 0.5 ($S = 1/2$) where the additional mass for the acceleration basis becomes equal to the mass of the scale model, making the manufacturing of the test specimen difficult.

With respect to using a time basis, there is an advantage in that the natural frequency of the original structure and the scale model can be the same, but the additional mass with regard to the scale factor S becomes large, as in the case of the acceleration basis, which again makes it difficult to manufacture the test specimen. Therefore, in this study, a scale model with mass basis applied, so that no additional mass is necessary, is prepared for the experimentation.

4. Experimental Vibration Performance Evaluation

4.1. Test Specimen Preparation. In order to assess the vibration performance of the long-span segmented PC structure, a Segmented Model is manufactured as shown in Figure 4, and vibration experimentation is conducted. Meanwhile, a Nonsegmented Model by the conventional PC method is also manufactured under the same scale condition (mass basis, $S = 0.5$), as shown in Figure 5. The conventional PC method applied high technology industrial facility is based on a 14.4 m span length facility structure which is designed as a plasma display panel (PDP) fabrication facility. Vibration experiments are conducted using the same conditions for both the Nonsegmented and Segmented Models, and the relative vibration performance of the long-span segmented PC structure is evaluated by comparing the experiment results. Table 2 shows the design specifications of the Nonsegmented and Segmented Models.

4.2. Experiment Method

4.2.1. Vibration Characteristics Testing Using Impact Load. First, in order to obtain the dynamic properties of the scaled models, such as natural frequency, impact testing was performed using an impact hammer. The experimental method involves measuring the response at a random location on the structure where an impact hammer is used to apply impact,



FIGURE 4: Test specimen photograph of Segmented Model.



FIGURE 5: Test specimen photograph of Nonsegmented Model.

as shown in Figure 6. When an impact hammer excites the structure, the sensor in the impact hammer measures the impact force $f(t)$ and the accelerometer sensor installed at the location point intended to measure the response records the response $x(t)$ that is induced by the impact hammer. Impact force $f(t)$ and response $x(t)$ are data displayed in the time domain which can be shown in the frequency domain when (1) and (2) are used. Also, the response $X(\omega)$ and excitation force $F(\omega)$ defined in the frequency domain can be expressed as a linear relationship with the transfer function $H(\omega)$ as shown in (3). The transfer function $H(\omega)$ is a unique

TABLE 2: Specifications of Nonsegmented and Segmented Models.

Category		Segmented	Nonsegmented
Member dimensions (unit: mm)	R/P floor beam	500 × 800	400 × 600
		250 × 450	350 × 600
		650 × 800	700 × 800
		700 × 850	
	Main column	600 × 600	500 × 500
	FAB floor beam	H-200 × 150 × 6 × 9	H-200 × 150 × 6 × 9
Steel frame column		H-150 × 150 × 7 × 10	H-150 × 150 × 7 × 10
	Slab	Thickness: 90	Thickness: 90
Span		9000 mm × 7500 mm	7200 mm × 7200 mm
Story height		First floor: 4500 mm	First floor: 4500 mm
		Second floor: 2750 mm	Second floor: 2750 mm
Material properties		27 MPa concrete	27 MPa concrete
		500 MPa rebar	500 MPa rebar
		400 MPa section steel	400 MPa section steel

TABLE 3: Equipment specifications used in the vibration characteristics test.

Equipment	Model	Function
SignalCalc Mobilyzer	Data Physics Co. Model: DP440	Vibration measurement and analysis system
Impact Hammer	Type 8210	Transfer function measurement and mode analysis
Accelerometer	Dytran 3191A	Vibration measurement precision sensor
Modal Analyzer	Star Modal Ver 5.1	Natural frequency

property of the structure representing the magnitude of the response with respect to the unit excitation force. Table 3 shows the equipment specifications used in the vibration test.

$$F(\omega) = \frac{1}{2\pi} \int_{-\infty}^{\infty} f(t) e^{-j\omega t} dt \quad (1)$$

$$X(\omega) = \frac{1}{2\pi} \int_{-\infty}^{\infty} x(t) e^{-j\omega t} dt \quad (2)$$

$$X(\omega) = H(\omega) F(\omega). \quad (3)$$

4.2.2. Response Experiment Using Harmonic Loads. High technology industrial facilities are excited by a variety of causes such as motors, impact, and human walking. However, it is realistically hard to set up vibration environment equivalent to the real vibration conditions at the scale experiment procedure. In this study, among the various exciting causes, a motor is considered as the excitation force, and the resulting responses of two scale models are compared. There are a number of fabrication equipment and air conditioning equipment operated by motors on the FAB and R/P floors. The power, voltage, and pole number of a motor employed in this study are 0.2 kW, 380 V, and 2 P, respectively. The excitation frequencies of 20 Hz, 40 Hz, and 60 Hz are employed.

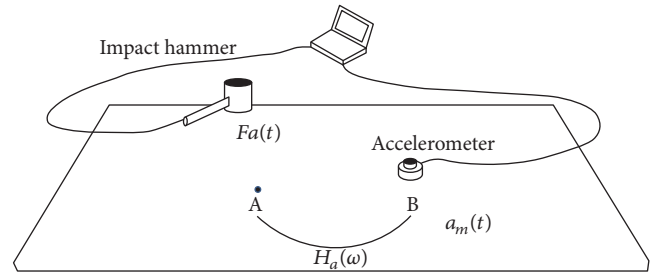


FIGURE 6: Impact hammer excitation experiment setup.

4.3. Results and Discussion. The excitation and measurement locations of two tests are shown in Figures 7–10. Since dimensions and plans of two models are different, excitation and measurement locations of two models are different. To compare the results between two models despite these differences, in this study, the averaged values are used.

The results from the impact test are shown in Tables 4 and 5 and Figure 11. The averaged results of the dynamic characteristics experiment for the FAB floor are summarized in Table 4. The frequencies of the 1st, 2nd, and 3rd resonance responses for the frequency domain are found to be 94%, 93.9%, and 91.5%, respectively, for the Segmented Model when compared to the Nonsegmented Model. The results show that the resonance response of the Segmented Model occurs at a lower frequency domain than the resonance response of the Nonsegmented Model.

The magnitudes of the 1st, 2nd, and 3rd resonance responses shown as the velocity value in the frequency domain are 54.2%, 55.8%, and 78.9%, respectively, for the Segmented Model when compared to the Nonsegmented Model. The response magnitude for the Segmented Model was significantly less than that of the Nonsegmented Model.

The averaged results of dynamic characteristics experiment for the R/P floor are summarized in Table 5. The averaged values of the 1st, 2nd, and 3rd resonance responses of the Segmented Model are 96.4%, 92.5%, and 104.9%, respectively,

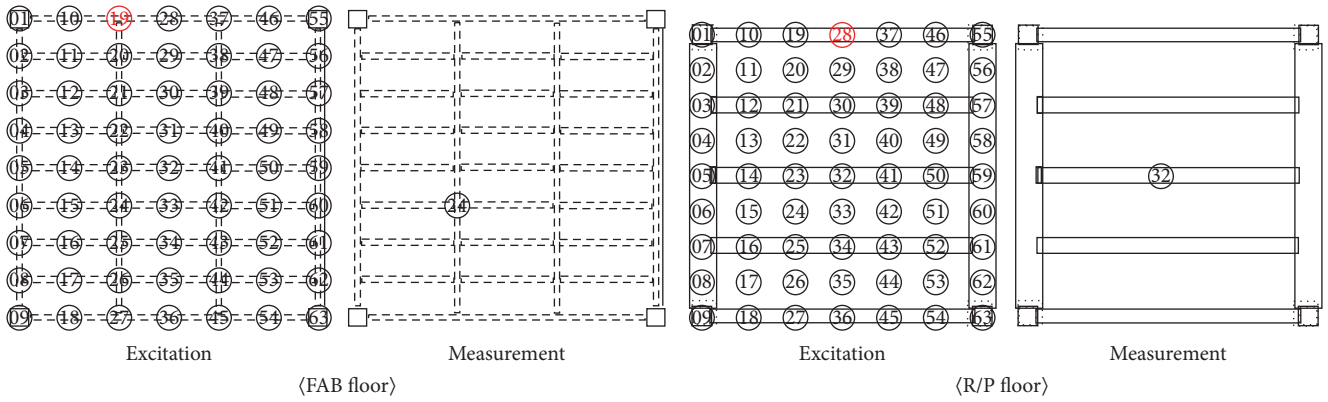


FIGURE 7: Excitation and measurement locations in the impact test of Nonsegmented Model.

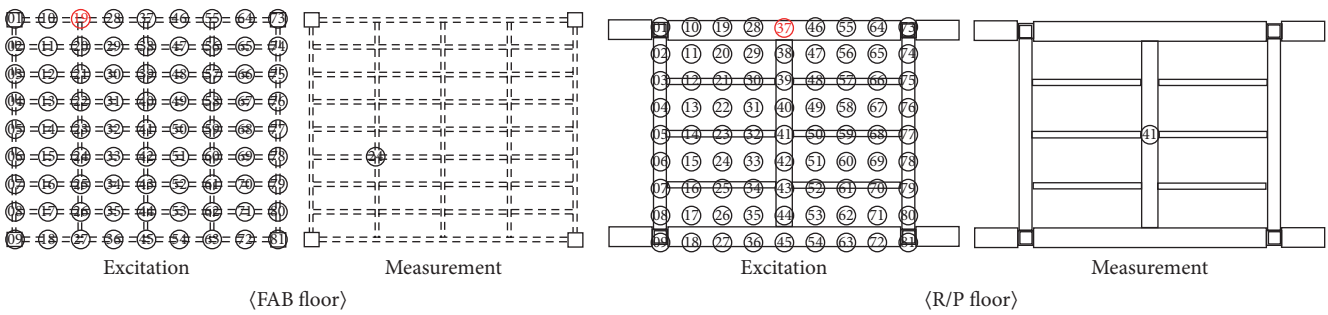


FIGURE 8: Excitation and measurement locations in the impact test of Segmented Model.

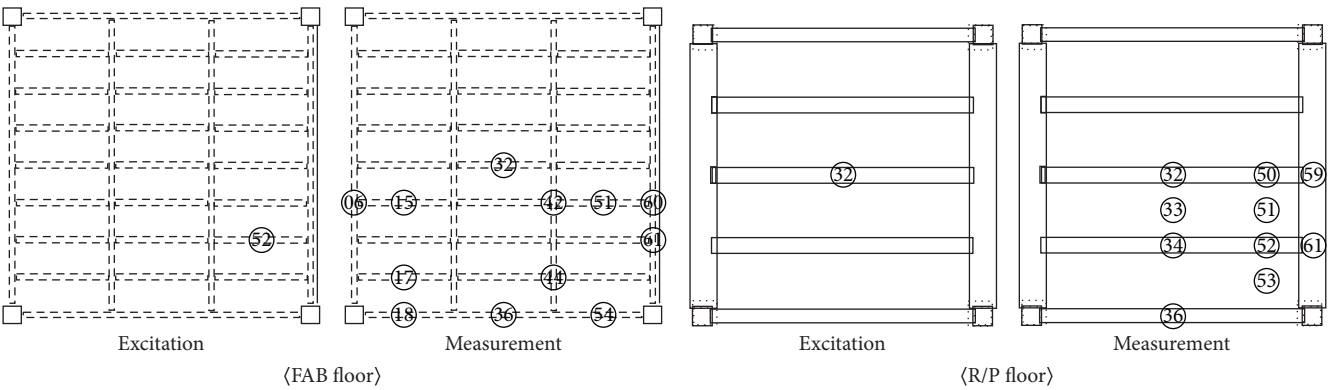


FIGURE 9: Excitation and measurement locations in the harmonic test of Nonsegmented Model.

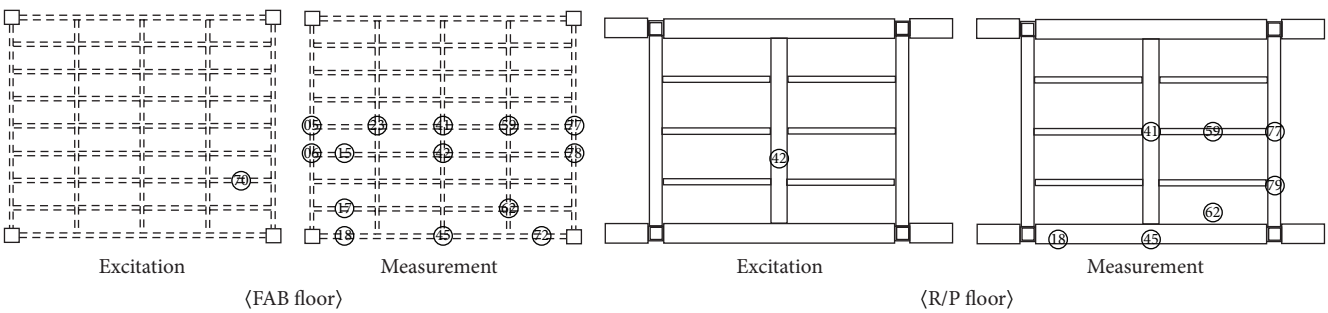


FIGURE 10: Excitation and measurement locations in the harmonic test of Segmented Model.

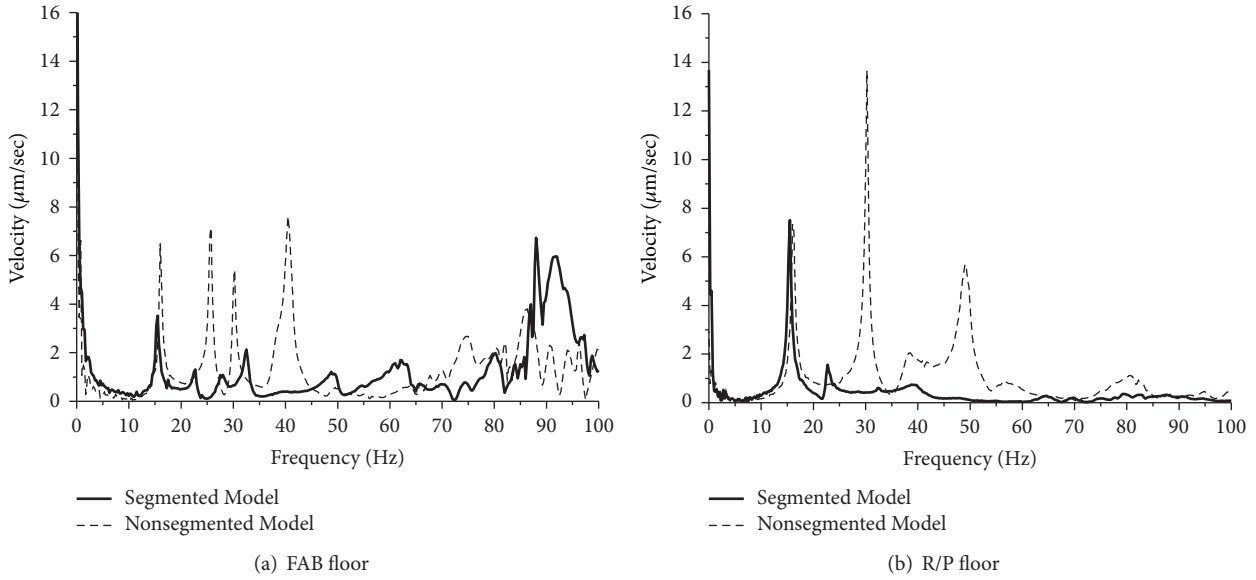


FIGURE 11: Comparison of transfer functions of two models by the impact tests.

TABLE 4: Comparison of natural frequency and response magnitude by the impact test on FAB floor.

Mode	Frequency (Hz)			Response (um/Ns)		
	Nonsegmented Model	Segmented Model	Ratio (%)	Nonsegmented Model	Segmented Model	Ratio (%)
1st	16.2	15.2	94.0	13.1	7.1	54.2
2nd	25.8	24.3	93.9	6.1	3.4	55.8
3rd	33.3	30.4	91.5	5.2	4.1	78.9

TABLE 5: Comparison of natural frequency and response magnitude by the impact test on R/P floor.

Mode	Frequency (Hz)			Response (um/Ns)		
	Nonsegmented Model	Segmented Model	Ratio (%)	Nonsegmented Model	Segmented Model	Ratio (%)
1st	16.3	15.7	96.4	13.5	6.3	46.3
2nd	29.1	26.9	92.5	4.9	0.9	17.8
3rd	38.6	40.5	104.9	3.5	0.8	23.8

when compared with those of the Nonsegmented Model. The 1st and 2nd resonance responses of the Segmented Model occur in a somewhat low frequency range compared to the Nonsegmented Model while the 3rd response occurs in a somewhat high frequency range.

The magnitudes of the 1st, 2nd, and 3rd resonance responses are 46.3%, 17.8%, and 23.8%, respectively, for the Segmented Model, revealing that the resonance response magnitudes of the Segmented Model are significantly lower than those of the Nonsegmented Model.

Figure 11 shows examples of transfer functions of the Nonsegmented Model and Segmented Model obtained from the impact tests. Figure 11 is made based on the results of impact tests that excitation locations for FAB and R/P

floors of Nonsegmented Model are 19 and 28 in Figure 7, respectively, and those for FAB and R/P floors of Segmented Model are 19 and 37 in Figure 8, respectively. Since the values in Tables 4 and 5 are the values averaging results from multiple impact tests while Figure 11 is based on the result from the specific impact test, the frequency values and peak responses can be different. It is confirmed that the response magnitudes of the Segmented Model tend to be smaller than those of the Nonsegmented Model.

The averaged results of harmonic tests are summarized in Table 6. The averaged responses of FAB floor for the excitation frequencies of 20 Hz, 40 Hz, and 60 Hz are 48.4%, 32.5%, and 81.2%, respectively. The averaged responses of R/P floor for the excitation frequencies of 20 Hz, 40 Hz, and 60 Hz are

TABLE 6: Comparison of responses of two Models by the harmonic tests.

Floor	Response of Nonsegmented Model (um/Ns)			Response of Segmented Model (um/Ns)			Ratio (%)		
	Excitation frequency (Hz)			Excitation frequency (Hz)			Excitation frequency (Hz)		
	20	60	60	20	60	60	20	60	60
FAB	21.9	210.8	740.5	10.6	68.5	601.3	48.4	32.5	81.2
R/P	20.4	825.5	415.4	9.2	277.8	94.6	45.1	33.7	22.8

45.1%, 33.7%, and 22.8%, respectively. It is confirmed that responses of Segmented Model are smaller than those of Nonsegmented Model.

5. Conclusion

In this study, to resolve the application limitation of the precast concrete (PC) method in high technology industrial facilities caused from the transport length restriction set by traffic laws, a structural system with a segmented PC system is introduced and the vibration performance of the segmented PC system is evaluated by the experimental test using the models scaled based on the mass basis law of similarity which does not require additional mass.

Using the mass basis law of similarity (scale factor $S = 0.5$), a Segmented Model is manufactured using the segmented method to produce a width of 9000 mm, depth of 7500 mm, and height of 7250 mm. In order to assess the relative vibration performance of the Segmented Model, a Nonsegmented Model is additionally manufactured, and the nonsegmented PC method, which is widely applied to conventional high technology industrial facilities, is applied to produce the Nonsegmented Model with a width of 7200 mm, depth of 7200 mm, and height of 7250 mm. The cross-sectional dimension of a girder in the original structure (14.4 m \times 14.4 m) for Nonsegmented Model is 1400 mm \times 1600 mm, and the cross-sectional dimension of a girder in the original structure (18 m \times 15 m) for Segmented Model is 1400 mm \times 1700 mm.

Compared to the span length and the height of cross section of a girder of Nonsegmented Model, those of Segmented Model are increased by 25% and 6.25%, respectively. The amount of increase in span length is larger the amount of increase in the dimension of cross section. This results in the decrease of stiffness of a structure. Although the stiffness of Segmented Model is smaller than that of Nonsegmented Model, it is shown that microvibration responses of Segmented Model at low frequency range are smaller than those of Nonsegmented Model. It is thought that the increased masses of Segmented Model compared to those of Nonsegmented Model affect responses. According to Newton's second law, if the magnitude of the applied force is same, the increased mass of the structure leads to the reduction in the response of the structure caused by the force.

Competing Interests

The authors declare that there is no conflict of interests regarding the publication of this paper.

Acknowledgments

This research was supported by Basic Science Research Program through the National Research Foundation of Korea (NRF) funded by the Ministry of Education (NRF-2014R1A1A2059874).

References

- [1] K. A. Salyards and R. J. Firman III, "Review of generic and manufacturer design criteria for vibration-sensitive equipment," in *Proceedings of the 27th Conference and Exposition on Structural Dynamics (IMAC XXVII)*, Society for Experimental Mechanics (SEM), Orlando, Fla, USA, February 2009.
- [2] E. E. Ungar, D. H. Sturz, and C. H. Amick, "Vibration control design of high technology facilities," *Sound and Vibration*, vol. 24, no. 7, pp. 20–27, 1990.
- [3] H. Amick, "On generic vibration criteria for advanced technology facilities: with a tutorial on vibration data representation," *Journal of the Institute of Environmental Sciences*, vol. 40, no. 5, pp. 35–44, 1997.
- [4] C. G. Gordon, "Generic criteria for vibration-sensitive equipment," in *Vibration Control in Microelectronics, Optics, and Metrology*, vol. 1619 of *Proceedings of SPIE*, pp. 71–85, International Society for Optical Engineering (SPIE), February 1991.
- [5] H. Amick, M. Gendreau, and C. G. Gordon, "Facility vibration issues for nanotechnology research," in *Proceedings of the Symposium on Nano Device Technology*, Hsinchu, Taiwan, 2002.
- [6] H. Amick, M. Gendreau, T. Busch, and C. G. Gordon, "Evolving criteria for research facilities: vibration," in *Buildings for Nanoscale Research and Beyond*, vol. 5933 of *Proceedings of SPIE*, September 2005.
- [7] C.-L. Lee, Y.-P. Wang, and R. K. L. Su, "Assessment of vibrations induced in factories by automated guided vehicles," *Proceedings of the Institution of Civil Engineers—Structures and Buildings*, vol. 166, no. 4, pp. 182–196, 2013.
- [8] T.-C. Pan, X. You, and C. L. Lim, "Evaluation of floor vibration in a biotechnology laboratory caused by human walking," *Journal of Performance of Constructed Facilities*, vol. 22, no. 3, pp. 122–130, 2008.
- [9] J. M. W. Brownjohn, T.-C. Pan, C. Middleton, S. C. Tan, and G. Yang, "Floor vibration serviceability in a multistory factory building," *Journal of Performance of Constructed Facilities*, vol. 30, no. 1, Article ID 04014203, 2016.
- [10] M. Ismail, J. Rodellar, and F. Ikhouane, "An innovative isolation bearing for motion-sensitive equipment," *Journal of Sound and Vibration*, vol. 326, no. 3, pp. 503–521, 2009.
- [11] Y. L. Xu, Z.-F. Yu, and S. Zhan, "Experimental study of a hybrid platform for high-tech equipment protection against earthquake and microvibration," *Earthquake Engineering and Structural Dynamics*, vol. 37, no. 5, pp. 747–767, 2008.

- [12] Y. L. Xu, Z. C. Yang, J. Chen, H. J. Liu, and J. Chen, "Microvibration control platform for high technology facilities subject to traffic-induced ground motion," *Engineering Structures*, vol. 25, no. 8, pp. 1069–1082, 2003.
- [13] Y. L. Xu and A. X. Guo, "Microvibration control of coupled high tech equipment-building systems in vertical direction," *International Journal of Solids and Structures*, vol. 43, no. 21, pp. 6521–6534, 2006.
- [14] E. I. Rivin, "Vibration isolation of precision equipment," *Precision Engineering*, vol. 17, no. 1, pp. 41–56, 1995.
- [15] Y. Q. Ni, Z. G. Ying, and Z. H. Chen, "Micro-vibration suppression of equipment supported on a floor incorporating magneto-rheological elastomer core," *Journal of Sound and Vibration*, vol. 330, no. 18-19, pp. 4369–4383, 2011.
- [16] H. P. Gavin and A. Zaicenco, "Performance and reliability of semi-active equipment isolation," *Journal of Sound and Vibration*, vol. 306, no. 1-2, pp. 74–90, 2007.
- [17] H. Amick, S. Hardash, P. Gillett, and R. J. Reaveley, "Design of stiff, low-vibration floor structures," in *Vibration Control in Microelectronics, Optics, and Metrology*, Proceedings of SPIE, pp. 180–191, International Society for Optics and Photonics, February 1992.
- [18] A. Pavic and P. Reynolds, "Vibration serviceability of long-span concrete building floors. Part 1: review of background information," *Shock and Vibration Digest*, vol. 34, no. 3, pp. 191–211, 2002.
- [19] C. J. Middleton and J. M. W. Brownjohn, "Response of high frequency floors: a literature review," *Engineering Structures*, vol. 32, no. 2, pp. 337–352, 2010.
- [20] C. Q. Howard and C. H. Hansen, "Vibration analysis of waffle floors," *Computers and Structures*, vol. 81, no. 1, pp. 15–26, 2003.
- [21] KICT, *Development of the Prefabricated System of the RC Building Structures*, Korea Institute of Civil Engineering and Building Technology, Goyang, Republic of Korea, 1999.
- [22] S. S. Lee, H. M. Chun, J. G. Kim, and K. Hong, "Suggestions of segmented PC frame systems for the long span floor of anti-vibration industrial buildings," *Journal of Architectural Institute of Korea (Structural Division)*, vol. 26, no. 11, pp. 13–20, 2010.
- [23] H. J. Cowan and P. R. Smith, *Dictionary of Architectural and Building Technology*, Spon Press, New York, NY, USA, 4th edition, 2004.
- [24] H. Harris and G. Sabnis, *Structural Modeling and Experimental Techniques*, CRC Press, 2nd edition, 1999.

Research Article

The Absolute Deviation Rank Diagnostic Approach to Gear Tooth Composite Fault

Guangbin Wang, Wenhui Deng, Xiaoyang Du, and Xuejun Li

*Hunan Provincial Key Laboratory of Health Maintenance for Mechanical Equipment,
Hunan University of Science & Technology, Xiangtan 411210, China*

Correspondence should be addressed to Guangbin Wang; jxxwgb@126.com

Received 17 October 2016; Accepted 7 December 2016; Published 9 January 2017

Academic Editor: Luca Collini

Copyright © 2017 Guangbin Wang et al. This is an open access article distributed under the Creative Commons Attribution License, which permits unrestricted use, distribution, and reproduction in any medium, provided the original work is properly cited.

Aiming at nonlinear and nonstationary characteristics of the different degree with single fault gear tooth broken, pitting, and composite fault gear tooth broken-pitting, a method for the diagnosis of absolute deviation of gear faults is presented. The method uses ADAMS, respectively, set-up dynamics model of single fault gear tooth broken, pitting, and composite fault gear tooth broken-pitting, to obtain the result of different degree of broken teeth, pitting the single fault and compound faults in the meshing frequency, and the amplitude frequency doubling through simulating analysis. Through the comparison with the normal state to obtain the sensitive characteristic of the fault, the absolute value deviation diagnostic approach is used to identify the fault and validate it through experiments. The results show that absolute deviation rank diagnostic approach can realize the recognition of gear single faults and compound faults with different degrees and provide quick reference to determine the degree of gear fault.

1. Introduction

Gearbox, as one of the core parts of mechanical transmission system, is extremely prone to various faults due to the long run under harsh working environment. As a matter of fact, the fault does not often appear alone; the gear failures of broken teeth and pitting usually easily lead to broken teeth-pitting composite failures [1–4]. In recent years, many scholars are dedicated to extraction and recognition research of gear fault feature, and it has made a great achievement. Kar and Mohanty [5] use multiresolution Fourier transform to diagnose the gearbox under different load. Lei and Tang [6] set up planetary gearbox vibration signal simulation model based on analysis of the transmission mechanism to obtain different gear fault vibration response signal and compared it with the different normal and fault signal features in order to recognize the planetary gearbox failures. Chen and Yu [7], respectively, make analysis to the envelope order harmonic components and impact components, based on morphological differences of component and the measured speed signal between rolling bearings and gears contained in wind turbine gearbox composite failure vibration signals and its effectively separated gears fault feature under variable speeds

from rolling bear. Zhan et al. [8] used the autoregressive model to analyze the residual signal of the gears containing the impact components. It was proved that the order of the AR model was correlated with the load. By satisfying the response statistic based on the AR model error signal, an AR model suitable for the diagnosis of variable load gear condition can be obtained.

The paper puts forward the absolute deviation rank diagnostic approach to broken teeth-pitting composite fault, and it took single broken teeth fault, pitting, and composite broken teeth-pitting fault as the research object, using ADAMS to establish gear teeth broken-pitting compound fault dynamics model and single failure dynamic model. It obtained the single fault and multifault frequency value in the meshing frequency and multiple frequency after the Fourier transformation to simulation data. The absolute value deviation diagnostic approach is proposed based on the normal state of the meshing frequency and the absolute value of frequency multiplication, and the frequency multiplication of different degrees and different types of faults is obtained. The fault sensitive features are determined and verified by experiments.

2. Based on ADAMS Dynamic Model of Gear Tooth Broken-Pitting

It is a key point to calculate the meshing stiffness of gears when it builds dynamic model of gear transmission system in ADAMS [9]. Many scholars have a deep research [10] and they all considered that it can effectively simulate the gear bending and torsional deformation through adding auxiliary gear and torsional spring [11–14].

Assuming that the gear drive is described by n generalized coordinates q , after introducing the contact constraint condition, its dynamic equation is expressed as [15]

$$M\ddot{q} + Kq + \lambda\phi_q^T = Q + F \quad (1)$$

$$\phi(q, t) = 0,$$

where M and K are the generalized mass matrix and the generalized stiffness matrix; ϕ is the constraint equation; ϕ_q is the Jacobian matrix of the constraint equation; λ is the Lagrange multiplier; Q is the generalized force matrix; and F is the contact force.

According to the contact mechanics theory, the contact force is reduced to the equivalent spring-damping model. The generalized expression is

$$F = K\delta^n + C(\delta)\dot{\delta}, \quad (2)$$

where K is the equivalent contact stiffness of meshing tooth profile elasticity; δ is the deformation of the meshing point; n is a nonlinear elasticity exponent and $n \geq 1$; $C(\delta)$ is a deformation-based contact damping polynomial that describes the energy loss during gear meshing; $\dot{\delta}$ is the tooth profile deformation speed.

The moment of inertia and the effective area of contact will change, resulting in a change in stiffness while the gears are in motion. Therefore, calculate the equivalent stiffness values of the gears under different faults, and input ADAM to achieve the simulation analysis. The equivalent stiffness of the gear meshing is calculated as [16]

$$K = \frac{1}{k_h} + \frac{1}{k_b} + \frac{1}{k_a} + \frac{1}{k_s} + \frac{1}{k_f}, \quad (3)$$

where k_h is the failure of the Hertz stiffness; k_b is bending stiffness; k_a is radial stiffness, k_s is shear stiffness; k_f is tooth base stiffness.

The meshing Hertz stiffness of the same material is

$$k_h = \frac{\pi EL}{4(1-\nu^2)}, \quad (4)$$

where E is the elastic potential energy, L is the axial thickness of the gear, and ν is Poisson's ratio.

Tooth base stiffness k_f is

$$\frac{1}{k_f} = \frac{\cos^2 \alpha}{EL} \left\{ L^* \left(\frac{u_f}{s_f} \right)^2 + M^* \left(\frac{u_f}{s_f} \right) + P^* (1 + Q^* \tan^2 \alpha) \right\}, \quad (5)$$

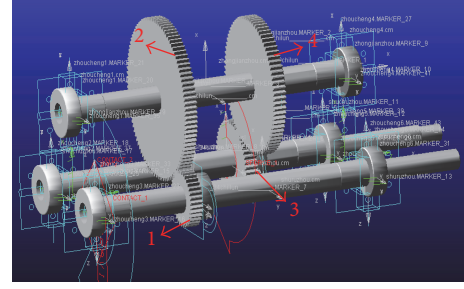


FIGURE 1: Dynamic model of gear transmission system.

where X^* represents the coefficients L^* , M^* , P^* , and Q^* . $h_f = r_f/r$, and r_f is the root diameter. The remaining parameters are described in [10].

The bending stiffness and shear stiffness are

$$\frac{1}{k_b} = \int_{-\alpha_1}^{\alpha_2} \frac{\{1 + \cos \alpha_1 [(\alpha_2 - \alpha) \sin \alpha - \cos \alpha]\}^2 (\alpha_2 - \alpha_1) \cos \alpha}{2EI_{xc}} d\alpha \quad (6)$$

$$\frac{1}{k_s} = \int_{-\alpha_1}^{\alpha_2} \frac{1.2(1+\nu)(\alpha_2 - \alpha) \cos \alpha \cos^2 \alpha_1}{2EA_{xc}} d\alpha,$$

where L is the axial thickness of the gear; ν is Poisson's ratio; R_{b1} is the base circle radius of the pinion. α_2 is the pressure angle of the faulty contact point; α is the pressure angle.

I_{xc} and A_{xc} are the effective moment of inertia and the cross-sectional area distance from the tooth root x , respectively, when the gear is faulted.

$$I_{xc} = \frac{1}{12} \cdot R_{b1} \{ [\sin \alpha_2 + (\alpha_2 + \alpha) \cos \alpha - \sin \alpha] - q \sin \nu \}^3 L \quad (7)$$

$$A_{xc} = \{ R_{b1} [\sin \alpha_2 + (\alpha_2 - \alpha) \cos \alpha - \sin \alpha] - q \sin \nu \} \cdot L.$$

As shown in Figure 1, the dynamic model of gear transmission system was built with normal state in ADAMS [17].

The gear transmission system was designed for double-stage driving. It concludes three shafts which contain input shaft, intermediate shaft, output shaft, and two pairs of gears where gear 1 meshed with 2 and gear 3 meshed with 4.

It will generate gear bending, torsional, and contact deformation in the mesh movement, and the contact deformation of the tooth surface can cause the change of meshing stiffness and damping. Then, based on the dynamic model of the gear transmission system in Figure 1, the fault geometry is implanted in the solid model of the gear transmission system, which can effectively simulate the dynamic effects of gear tooth breakage and pitting failure through the contact algorithm in ADAMS software. It established dynamics model of single fault to broken teeth, pitting, and broken teeth-pitting composite fault through changing the geometry in the three-dimensional entity model. Specifically, as shown in

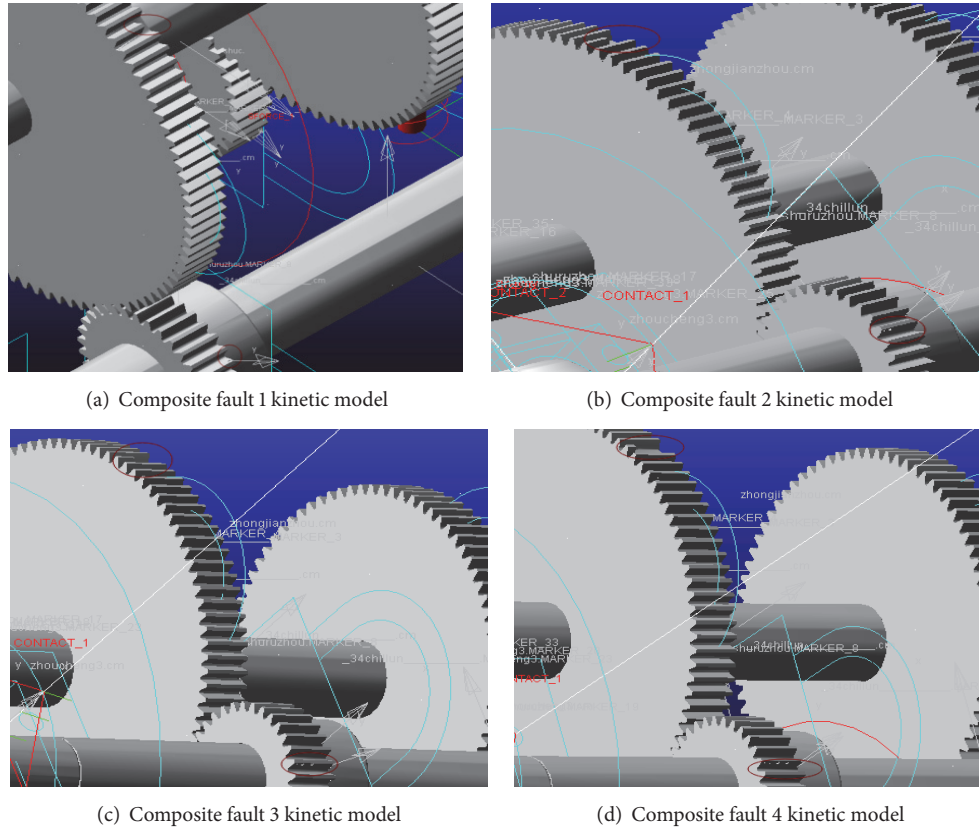


FIGURE 2: Dynamics model of the gear broken teeth-pitting compound fault.

Figure 2, four different degrees of broken gear failure include 1/5 broken teeth, 2/5 broken teeth, 3/5 broken teeth, and 4/5 broken teeth; four different kinds of gear pitting failure include pitting 1 which is to form a circle with a diameter of 4 mm, pitting 2 which is based on pitting 1 to form a diameter of 5 mm circle, pitting 3 which is based on pitting 2 more than a diameter of 6 mm circle, and pitting 4 which is in pitting 3 on the basis of more than a diameter of 7 mm circle. The composite fault is obtained by combining the broken tooth with the pitting failure, composite failure 1 is the combination of the broken tooth 1 and the pitting corrosion 1, and then the compound fault of different degrees can be obtained by analogy.

3. The Time-Frequency Statistics Analysis of Gear Failure

There are four different degrees of broken teeth-pitting compound fault simulated with three kinds of load and three types of speed, where the load in size is 0 N·m, 975 N·m, and 1790 N·m and the motor in speed is 10 Hz, 20 Hz, and 30 Hz. The statistical analysis includes the peak-peak value and the root-mean-square value, in which the peak-peak value is defined as the difference between the single peak maximum value and the single peak minimum value and is positive. The root mean square (RMS) value is named as the effective

value representing the energy of vibration signal, and it is an important index to judge whether the machine running state is normal or not in mechanical fault diagnosis, and the statistical results are shown in Figures 3–6.

Comparing four different degrees of composite fault analysis data with speed peak-peak value, we can see from Figures 3–6 that the vibration signal amplitude value increased with the degree of gear composite fault and the speed of values becomes more obvious as the growing of load during the speed from 600 RPM to 1800 RPM; the trend is upward as a whole. The skewness about vibration signal significantly increased when speed crosses around 1200 RPM; that is to say, the vibration of gear system increased along with the deepening of fault degree. Since the RMS reflects the energy change, we can know that the larger RMS value, the greater energy of the system and the greater the impact vibration of gears system.

According to Figure 7, the peak-peak value of the compound fault increased with the augment of the rotating speed under the same load 1790 N·m, and the amplitude value increased with the augment of the fault degree. The RMS value of the composite fault in different degree increased with the augment of the rotational speed, and the RMS value of the amplitude changes little in different complex failure when it works in rotating speed 600~1200 RPM. The RMS value increases with the augment of the rotational speed when the rotating speed is 1200~1800 RPM, which indicates the greater

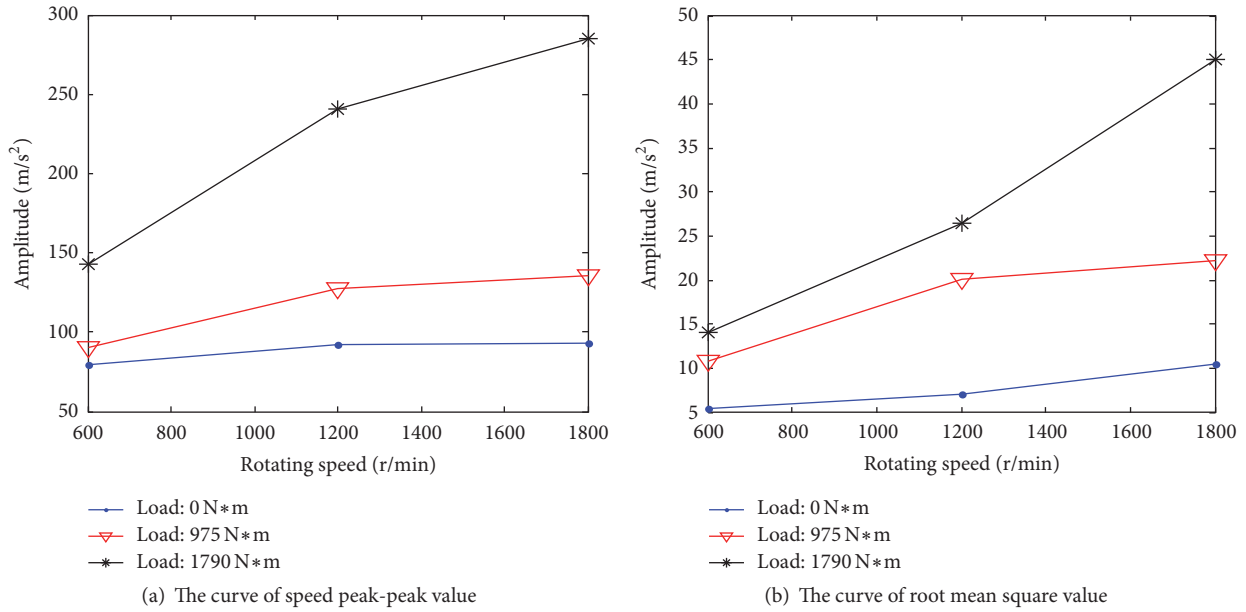


FIGURE 3: Broken teeth-pitting compound fault 1.

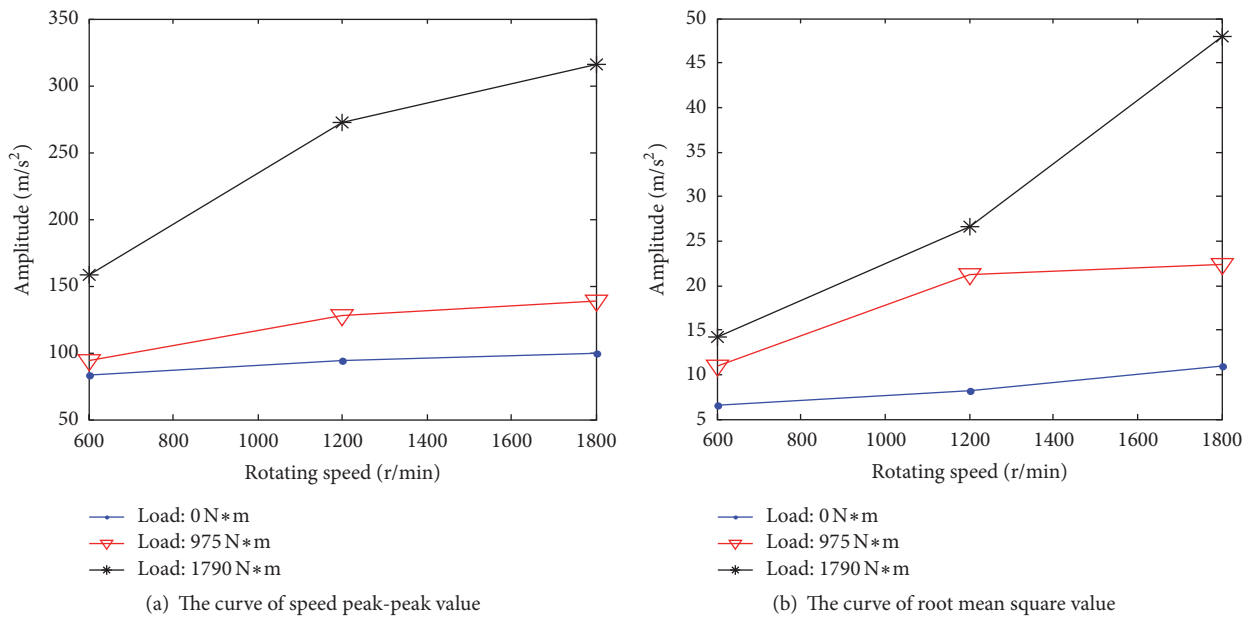


FIGURE 4: Broken teeth-pitting compound fault 2.

vibration impact of the gear system with the expanding fault degree and increasing speed.

From the analysis above, we can know the greater impact strength while the gear is meshing, and it followed with the growth of the rotating speed when it is under the same degree of broken teeth composite fault and speed; the bigger load, the greater impact strength in gear mesh when it is under the same degree of broken teeth and load; the greater load leads to worse broken teeth composite fault and greater impact strength in the gear mesh when it is under the same rotating speed and load.

4. Based on Gear Tooth Broken-Point Erosion Composite Fault of the Absolute Deviation Rank Diagnostic Approach

Based on simulation results, the frequency domain graph about gear teeth broken, gear pitting single failure, and broken teeth-pitting composite failures is obtained. The fault characteristics can be observed directly from the simulation curve, and the type of fault can be easily identified under the condition of known fault type and fault degree, since the original signal obtained from spot test includes racket

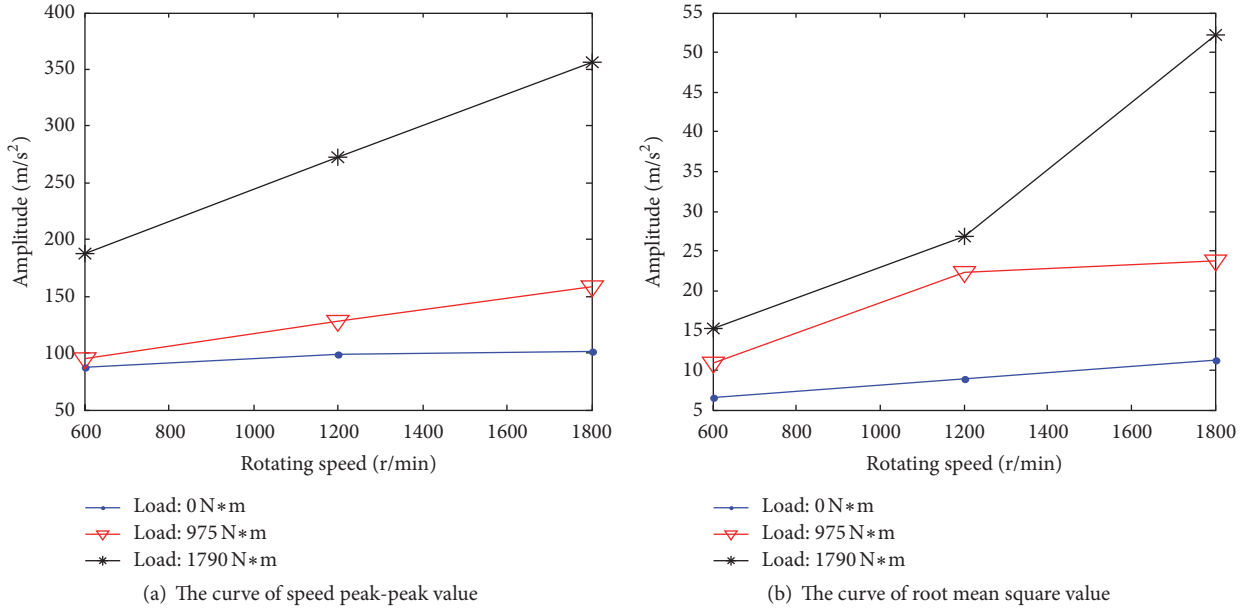


FIGURE 5: Broken teeth-pitting compound fault 3.

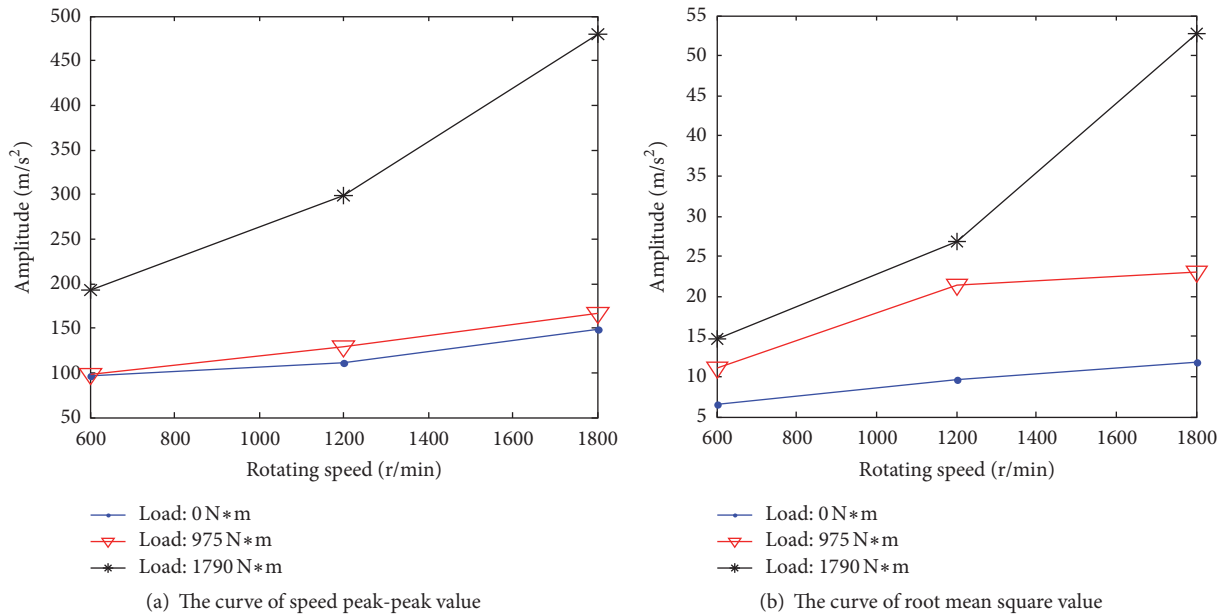


FIGURE 6: Broken teeth-pitting compound fault 4.

interference signal and it is hard to identify its fault type and degree and to found out its characteristic rules from the time-frequency diagram.

Therefore, the data is comprehensively analyzed based on the simulation results. Firstly, according to the type of fault and the degree of failure to classify, with the numbers 1 to 14, the specific situation is shown in Table 1.

Secondly, in order to realize the identification and monitoring of fault types, as shown in Table 2, the obtained simulation results are classified according to the tooth broken, pitting, and tooth broken-pitting corrosion.

According to the result of Table 2, it assumes a normal model as a benchmark on the basis of gear failure simulation, selecting vibration amplitude of sensitive feature, and the corresponding feature frequency as the identification of the fault parameters. Each of the simulated fault characteristic frequency amplitudes is compared with normal amplitude and takes it as an absolute deviation calculation; the results are shown in Table 3.

The absolute deviation formula is

$$|\Delta_i| = \frac{(a_i - a_i^n)}{a_i^n} \times 100\%, \quad (8)$$

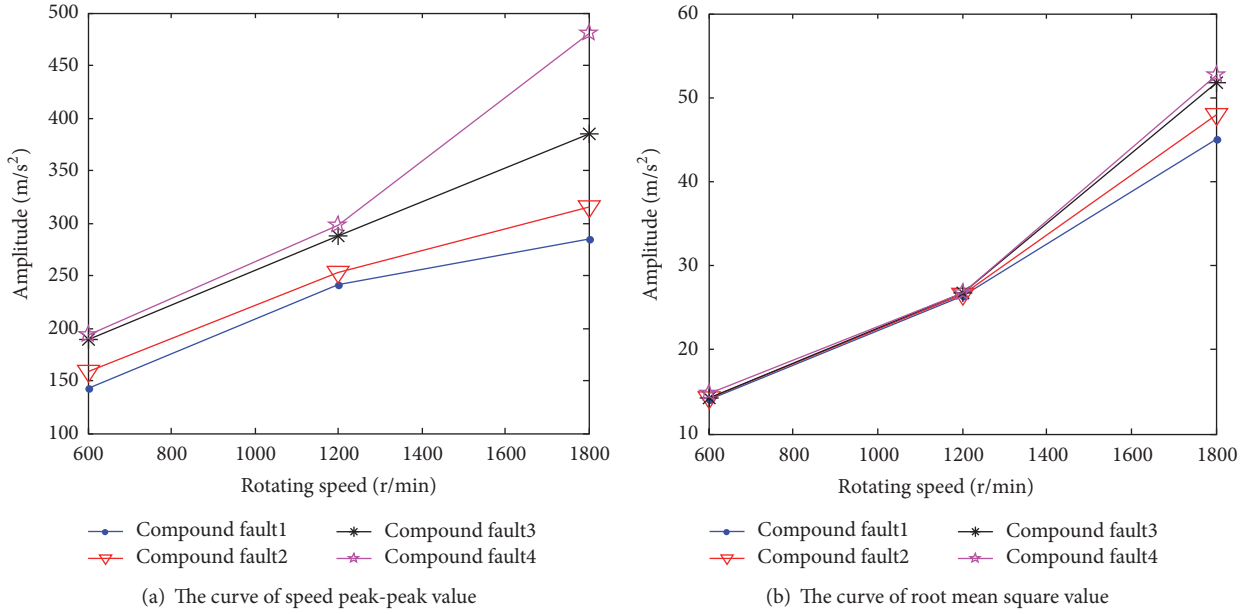


FIGURE 7: The curve of compound fault on load 1790 N·m.

TABLE 1: The code of simulation faults model.

Number	Fault type	Fault degree
1	Normal model	Nonfault
2	1/5 broken teeth	Seriousness
3	2/5 broken teeth	Seriousness
4	3/5 broken teeth	Seriousness
5	4/5 broken teeth	Seriousness
6	Total broken teeth	Seriousness
7	Point erosion 1	Slight
8	Point erosion 2	General
9	Point erosion 3	Seriousness
10	Point erosion 4	Seriousness
11	Compound fault 1	General
12	Compound fault 2	Seriousness
13	Compound fault 3	Seriousness
14	Compound fault 4	Seriousness

where a_i ($i = 1, 2, 3, 4, 5$) represents the vibration signal of the fault model in mesh and multiple frequency amplitude and a_i^n is the responding frequency amplitude of the normal model.

In order to quickly extract the fault features from three different fault types, it is more intuitive to judge the fault type of the gears in the actual operation so as to achieve the purpose of fault recognition. After we got the calculation results of absolute deviation and divided the absolute deviation into several grades, where setting the absolute deviation as less than 1 as grade 0, setting the absolute deviation within the range of 1~4 as grade I, setting the absolute deviation within the range of 4~7 as grade II, setting the absolute deviation within the range of 7~10 as grade III, setting the absolute

deviation within the range of 10~13 as grade IV, and setting the absolute deviation over 13 as grade V, then Table 3 can be rewritten as Table 4.

Table 4 is the results of the broken teeth, pitting, and broken teeth-pitting compound fault compared with normal model after classification and treatment, in order to more intuitively analyze each of absolute deviation rank values differences to identify the type of fault. Table 4 can be changed as pillars diagram, setting the absolute deviation rank 0 as 1 and setting the absolute deviation rank I as 2, and the rest is analogized in sequence, so Table 4 can be changed as in Figure 8.

We can see from Figure 8 and Table 4 that the absolute deviation of each fault type in the amplitude of the characteristic frequency is different. We can calculate its absolute deviation to identify the fault for the broken teeth because of little change in meshing frequency amplitude; there exists I rank deviation in second-time frequency amplitude and the same applies to the one-time frequency amplitude, which suggests that the feature frequency amplitude is sensitive fault parameters of broken teeth. There are three I rank deviations and one II rank deviation in the first-three-time frequency, which indicate that it is the point erosion fault sensitive parameters. There are three II rank deviations and one II rank deviation in double frequency amplitude, which are fault sensitive parameters for broken teeth-point erosion compound fault.

From Figure 8 and Table 4 absolute deviation level can be drawn to a fault and its different degree of sensitivity of the characteristic frequency can be analyzed by the corresponding characteristic frequency amplitude changes in the absolute deviation of the table to determine whether the level of the existence is of a gear failure.

TABLE 2: The fault simulation data.

Number	Fault type	Different fault of vibration amplitude in mesh frequency and multiple frequency				
		286 Hz	572 Hz	858 Hz	1144 Hz	1430 Hz
1	Normal model	23310	70770	40960	11970	9438
2	1/5 broken teeth	23190	72690	41260	12340	9021
3	2/5 broken teeth	23180	72050	41220	12200	9231
4	3/5 broken teeth	23150	71950	41220	12550	9040
5	4/5 broken teeth	23130	72120	41790	12850	9094
6	Total broken teeth	23300	68380	39720	12530	9305
7	Point erosion 1	22050	67400	38990	11210	8328
8	Point erosion 2	22630	79110	40410	9656	10040
9	Point erosion 3	22530	80410	40900	10090	9653
10	Point erosion 4	22550	81120	40890	10310	9856
11	Compound fault 1	23570	73470	41260	11890	9329
12	Compound fault 2	22280	67420	37130	9816	8892
13	Compound fault 3	21930	61100	39320	10510	9356
14	Compound fault 4	22020	70210	37660	10500	8163

TABLE 3: The absolute deviation of different fault types vibration frequency amplitude.

Number	Fault type	Different fault of absolute deviation in mesh frequency and multiple frequency (100%)				
		$ \Delta_1 $	$ \Delta_2 $	$ \Delta_3 $	$ \Delta_4 $	$ \Delta_5 $
1	Normal model	0	0	0	0	0
2	1/5 broken teeth	0.51	2.71	0.73	3.09	4.42
3	2/5 broken teeth	0.56	1.81	0.63	1.92	2.19
4	3/5 broken teeth	0.69	1.67	0.63	4.85	4.22
5	4/5 broken teeth	0.77	1.91	2.03	7.35	3.64
6	Total broken teeth	0.04	3.38	+	4.68	1.43
7	Point erosion 1	5.41	4.76	4.81	6.35	11.76
8	Point erosion 2	2.92	11.78	1.34	19.33	6.38
9	Point erosion 3	3.35	13.62	0.15	15.71	2.28
10	Point erosion 4	3.26	14.62	0.17	13.87	4.43
11	Compound fault 1	1.12	3.82	0.73	0.67	1.15
12	Compound fault 2	4.42	4.73	9.35	17.99	6.14
13	Compound fault 3	5.92	13.66	4.00	12.20	0.87
14	Compound fault 4	5.53	0.79	8.06	12.28	13.51

5. Experimental Verification

It takes fault simulation test bench of the American Quest Spectra company as object, and the vibration signal was collected by PULSE acquisition system. The end of the gearbox output axle connected to the brake, which changes the braking torque by adjusting the current with the electromagnetic brake and the sensor layout as shown in Figure 9.

Setting experimental conditions, the speed of the motor respectively is 10 Hz, 20 Hz, and 30 Hz, the current electromagnetic brake is set to 55 mA, where the brake torque is 1790 N·m, and sampling frequency of acquisition system is 16384 Hz, the acquisition time is 10 s, and pulley transmission ratio is 1:3.56.

Four different degrees of broken teeth, pitting single fault, and broken teeth-pitting composite failure are obtained by PULSE acquisition system. The vibration signals of different degrees of fault are obtained by experiment, the frequency amplitude in meshing frequency, and multiple frequency place to be obtained after engaging Fourier transform and the results are shown in Table 5.

The calculation was carried out with absolute deviation for the experimental data, and the obtained results are divided into several levels, where setting the absolute deviation as less than 1 as grade 0, setting the absolute deviation within the range of 1 to 4 as grade I, setting the absolute deviation within the range of 4 to 7 as grade II, setting the absolute deviation within the range of 7~10 as grade III, setting the absolute

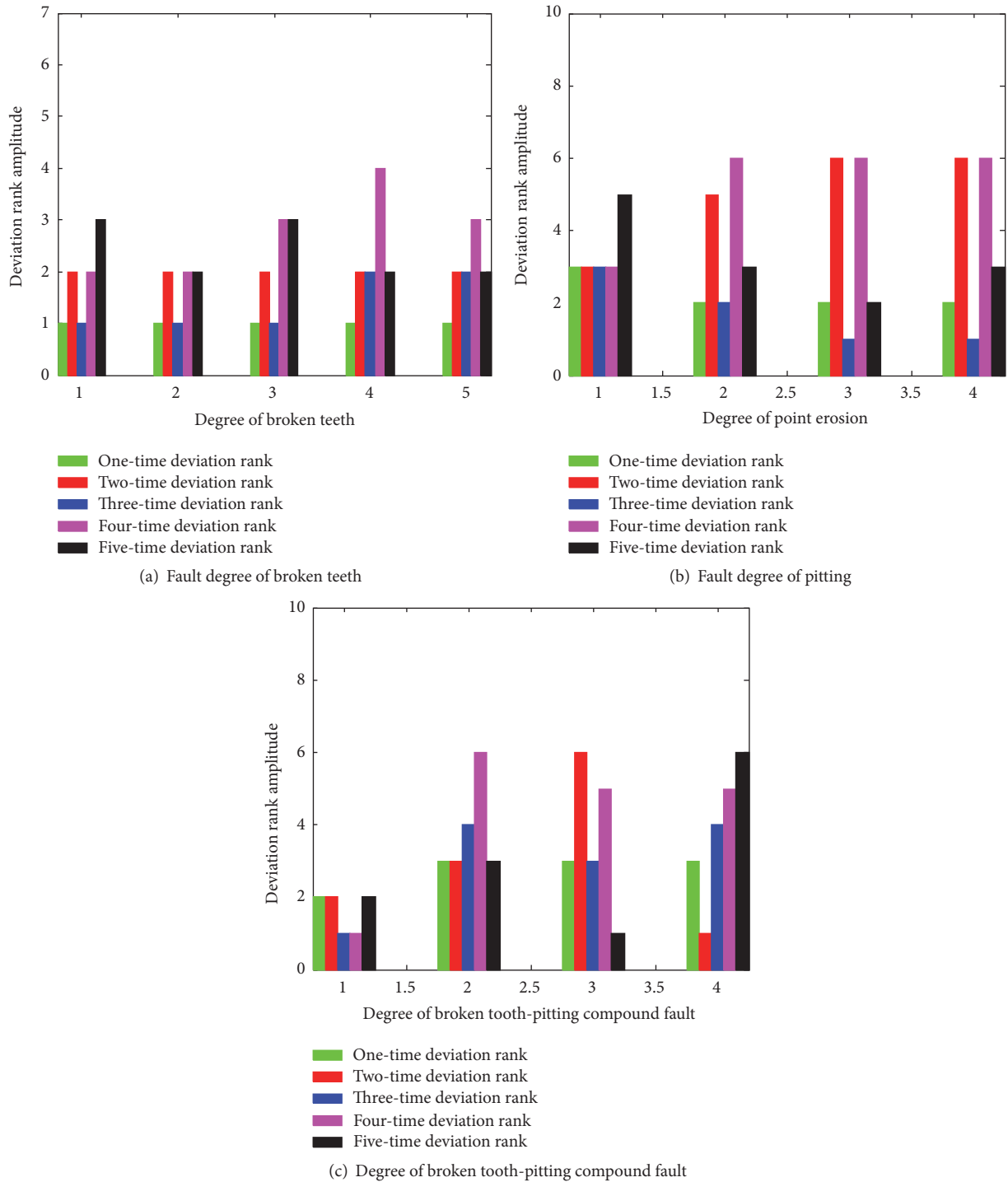


FIGURE 8: The relationship of absolute deviation rank between different fault degree and magnitude.

deviation within the range of 10 to 13 as grade IV, and setting the absolute deviation over 13 as grade V. Then Table 3 can be rewritten as Table 6.

The obtained consequences from simulation about different fault types of vibration frequency and amplitude absolute deviation level data are consistent with experimental data. It proved that this conclusion is correct. And it can accurately

reflect the sensitive degree of fault type and provide quick reference to determine the fault degree for gear diagnosis.

6. Conclusion

In this paper, the different degree of broken teeth, pitting single fault, and broken teeth-pitting composite fault are

TABLE 4: The absolute deviation rank of different fault types vibration frequency amplitude.

Number	Fault type	Different fault of absolute deviation rank in mesh frequency and multiple frequency				
		$ \Delta_1 $	$ \Delta_2 $	$ \Delta_3 $	$ \Delta_4 $	$ \Delta_5 $
1	Normal model	0	0	0	0	0
2	1/5 broken teeth	0	I	0	I	II
3	2/5 broken teeth	0	I	0	I	I
4	3/5 broken teeth	0	I	0	II	II
5	4/5 broken teeth	0	I	I	III	I
6	Total broken teeth	0	I	I	II	I
7	Point erosion 1	II	II	II	II	IV
8	Point erosion 2	I	IV	I	V	II
9	Point erosion 3	I	V	0	V	I
10	Point erosion 4	I	V	0	V	II
11	Compound fault 1	I	I	0	0	I
12	Compound fault 2	II	II	III	V	II
13	Compound fault 3	II	V	II	IV	0
14	Compound fault 4	II	0	III	IV	V

TABLE 5: The fault experimental data.

Number	Fault type	Different fault of vibration amplitude in mesh frequency and multiple frequency				
		290 Hz	580 Hz	870 Hz	1160 Hz	1450 Hz
1	Normal model	2231	4127	2713	1073	2286
2	1/5 broken teeth	2236	4239	2732	1113	2383
3	2/5 broken teeth	2243	4200	2729	1094	2345
4	3/5 broken teeth	2246	4190	2725	1126	2397
5	4/5 broken teeth	2249	4215	2785	1157	2365
6	Total broken teeth	2251	4268	2809	1125	2341
7	Point erosion 1	2360	4341	2841	1145	2558
8	Point erosion 2	2291	4672	2756	1279	2437
9	Point erosion 3	2309	4684	2719	1246	2351
10	Point erosion 4	2322	4734	2726	1224	2392
11	Compound fault 1	2266	4284	2738	1079	2318
12	Compound fault 2	2335	4325	2974	1260	2430
13	Compound fault 3	2368	4695	2835	1208	2304
14	Compound fault 4	2379	4160	2936	1219	2593

TABLE 6: The level of absolute deviation of different fault types vibration frequency amplitude.

Number	Fault type	Different fault of absolute deviation rank in mesh frequency and multiple frequency				
		$ \Delta_1 $	$ \Delta_2 $	$ \Delta_3 $	$ \Delta_4 $	$ \Delta_5 $
1	Normal model	0	0	0	0	0
2	1/5 broken teeth	0	I	0	I	II
3	2/5 broken teeth	0	I	0	I	I
4	3/5 broken teeth	0	I	0	II	II
5	4/5 broken teeth	0	I	I	III	I
6	Total broken teeth	0	I	I	II	I
7	Point erosion 1	II	II	II	II	IV
8	Point erosion 2	I	IV	I	V	II
9	Point erosion 3	I	V	0	V	I
10	Point erosion 4	I	V	0	V	II
11	Compound fault 1	I	I	0	0	I
12	Compound fault 2	II	II	III	V	II
13	Compound fault 3	II	V	II	IV	0
14	Compound fault 4	II	0	III	IV	V

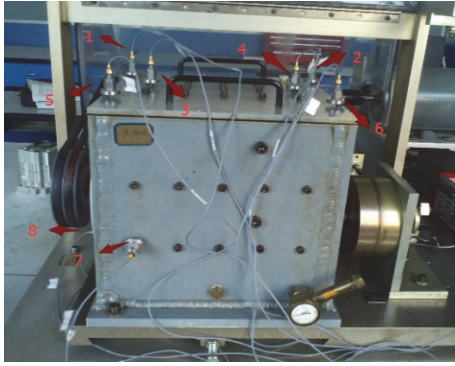


FIGURE 9: Sensor arrangement.

taken as research project. The results show that the method can get different degrees and different types of faults in the frequency doubling of meshing frequency by using the absolute deviation rank diagnostic approach for the gear broken teeth-pitting composite fault, and it is proved to be the most sensitive feature. According to the analysis of the corresponding characteristic frequency amplitude in the table to judge whether there is a fault in the gear, on the basis of the conclusion, the characteristics of the fault signal can achieve the purpose of identification about the different degree of broken teeth-pitting compound fault to broken teeth and pitting single fault.

Competing Interests

There is no conflict of interests regarding the publication of this paper.

Acknowledgments

Financial support from National Natural Science Foundation of China (51575178, 51175170, and 51375162) and financial support from China Scholarship Fund (201408430118) are appreciated.

References

- [1] W. J. Staszewski, K. Worden, and G. R. Tomlinson, "Time-frequency analysis in gearbox fault detection using the Wigner-Ville distribution and pattern recognition," *Mechanical Systems and Signal Processing*, vol. 11, no. 5, pp. 673–692, 1997.
- [2] H. Li, Y. Zhang, and H. Zheng, "Application of Hermitian wavelet to crack fault detection in gearbox," *Mechanical Systems and Signal Processing*, vol. 25, no. 4, pp. 1353–1363, 2011.
- [3] G. Bin, X. Li, J. Wu, and J. Gao, "Virtual dynamic balancing method without trial weights for multi-rotor series shafting based on finite element model analysis," *Journal of Renewable and Sustainable Energy*, vol. 6, no. 4, Article ID 042014, 2014.
- [4] P. N. Saavedra and C. G. Rodriguez, "Accurate assessment of computed order tracking," *Shock and Vibration*, vol. 13, no. 1, pp. 13–32, 2006.
- [5] C. Kar and A. R. Mohanty, "Vibration and current transient monitoring for gearbox fault detection using multiresolution Fourier transform," *Journal of Sound and Vibration*, vol. 311, no. 1-2, pp. 109–132, 2008.
- [6] Y. Lei and W. Tang, "ASTFA-BSS method and its application in the composite gearbox fault diagnosis," *Journal of Mechanical Engineering*, vol. 50, no. 17, pp. 61–68, 2014.
- [7] X. Chen and D. Yu, "Gear box composite fault diagnosis method based on morphological component analysis and order tracking," *Journal of Aerospace Power*, vol. 29, no. 1, pp. 225–232, 2014.
- [8] Y. Zhan, V. Makis, and A. K. S. Jardine, "Adaptive state detection of gearboxes under varying load conditions based on parametric modelling," *Mechanical Systems and Signal Processing*, vol. 20, no. 1, pp. 188–221, 2006.
- [9] P. Velex and P. Sainsot, "An analytical study of tooth friction excitations in errorless spur and helical gears," *Mechanism and Machine Theory*, vol. 37, no. 7, pp. 641–658, 2002.
- [10] F. Chaari, T. Fakhfakh, and M. Haddar, "Analytical modelling of spur gear tooth crack and influence on gearmesh stiffness," vol. 28, no. 3, pp. 461–468, 2009.
- [11] A. Saxena, B. Wu, and G. Vachtsevanos, "A methodology for analyzing vibration data from planetary gear systems using complex morlet wavelets," in *Proceedings of the American Control Conference (ACC '05)*, pp. 4730–4735, Portland, Ore, USA, June 2005.
- [12] S. Wang, M. Huo, C. Zhang et al., "Effect of mesh phase on wave vibration of spur planetary ring gear," *European Journal of Mechanics - A/Solids*, vol. 30, no. 6, pp. 820–827, 2011.
- [13] W. Kim, J. Y. Lee, and J. Chung, "Dynamic analysis for a planetary gear with time-varying pressure angles and contact ratios," *Journal of Sound and Vibration*, vol. 331, no. 4, pp. 883–901, 2012.
- [14] G. Bin, Z. Jiang, X. Li, and B. S. Dhillon, "Weighted multi-sensor data level fusion method of vibration signal based on correlation function," *Chinese Journal of Mechanical Engineering*, vol. 24, no. 5, pp. 899–904, 2011.
- [15] Z. Fang, G. Shu, K. He et al., "Multi-body contact dynamic modeling of gear transmission," *Journal of Mechanical Transmission*, vol. 33, no. 1, pp. 15–19, 2009.
- [16] L. Cui, C. Kang, L. Gao, F. Zhang, and S. Su, "Research on the vibration response and dynamic model a spur gear system with fault," *Journal of Vibration and Shock*, vol. 33, no. 1, pp. 15–19, 2009.
- [17] D. R. Salgado and J. M. Del Castillo, "A method for detecting degenerate structures in planetary gear trains," *Mechanism and Machine Theory*, vol. 40, no. 8, pp. 948–962, 2005.